

UNIVERSITÀ DEGLI STUDI DI NAPOLI FEDERICO II

SCUOLA POLITECNICA E DELLE SCIENZE DI BASE
AREA DIDATTICA SCIENZE MATEMATICHE FISICHE E NATURALI

DIPARTIMENTO DI FISICA “ETTORE PANCINI”



LAUREA MAGISTRALE IN FISICA

Ricerca di nuove risonanze ad alta
massa nel canale $ZZ \rightarrow llqq$
nell'esperimento ATLAS ad LHC

Searches for new high mass resonances decaying

in $ZZ \rightarrow llqq$ channel with the ATLAS experiment at LHC

Relatori:

Prof. Leonardo Merola
Dott.ssa Elvira Rossi

Candidato:

Antonio Giannini
Matricola: N94/300

ANNO ACCADEMICO 2015/2016

*"O frati," dissi, "che per cento milia
perigli siete giunti a l'occidente,
a questa tanto picciola vigilia*

*d'i nostri sensi ch'è del rimanente
non vogliate negar l'esperienza,
di retro al sol, del mondo senza gente.*

*Considerate la vostra semenza:
**fatti non foste a viver come bruti,
ma per seguir virtute e canoscenza".***

*DANTE, Inferno
Canto XXVI vv. 112-120*

Contents

Introduction	4
1 The Standard Model and Beyond	6
1.1 Elementary Particles	6
1.1.1 The Fermions	6
1.1.2 Forces and Carrier Particles: the Bosons	7
1.2 The Standard Model	8
1.2.1 Quantum Electrodynamics (QED)	9
1.2.2 Quantum Chromodynamics (QCD)	11
1.2.3 The Electroweak Theory	13
1.3 Spontaneous Symmetry Breaking and the Higgs Mechanism	15
1.3.1 The spontaneous symmetry breaking: a complex field	15
1.3.2 The Higgs field	18
1.3.3 Gauge boson masses	19
1.3.4 Fermion masses	20
1.4 Higgs boson mass constrains	21
1.4.1 Theoretical Constrains	21
1.4.2 Experimental Constrains before LHC	23
1.4.3 Search and discovery of the Higgs boson at LHC	26
1.5 Beyond the Standard Model	31
1.5.1 New heavy particle decaying into diboson final states	31
1.5.2 Heavy Higgs bosons/Scalar resonances	31
1.5.3 Two-Higgs-Doublet models (2HDM)	32
1.5.4 Heavy Vector Triplet	33
1.5.5 Bulk Randall-Sundrum Model	34
2 CERN, the LHC and the ATLAS Experiment	35
2.1 The Large Hadron Collider and the Run-I	35
2.1.1 LHC: the Run-II	38
2.2 The ATLAS Detector	41
2.2.1 ATLAS Coordinate System	42
2.2.2 ATLAS Magnets	43
2.2.3 The Inner Detector	44
2.2.4 The Calorimetric System	46
2.2.5 The Muon Spectrometer	48
2.2.6 The ATLAS Trigger	49
2.2.7 Monte Carlo Generators in ATLAS Event Simulation	55
3 Physics Objects Reconstruction in ATLAS	57
3.1 Data quality	57
3.2 ID Tracks	57
3.3 Primary vertices	60
3.4 Electrons	62

3.4.1	Electron reconstruction	62
3.4.2	Electron identification	62
3.4.3	Electron scale factors and energy corrections	64
3.5	Muons	65
3.5.1	Muon reconstruction and identification	65
3.6	Jets	68
3.6.1	Jet reconstruction	69
3.6.2	Jet calibration	71
3.6.3	Jet selection	73
3.6.4	Jet energy resolution	74
3.7	b -tagging	75
3.7.1	b -tagging algorithms	75
3.8	Missing transverse energy	79
4	Search for diboson resonances in the $llqq$ final state	81
4.1	Introduction	81
4.2	Data and MonteCarlo samples	82
4.3	Object definition: particle reconstruction and identification	83
4.3.1	Overlap removal	85
4.4	$ZZ \rightarrow llqq$ channel: the event selection	85
4.4.1	Trigger	85
4.4.2	$Z \rightarrow ll$ preselection	87
4.4.3	$Z \rightarrow q\bar{q}$ selection	87
4.4.4	Mass constraint	93
4.5	Vector boson fusion process: a dedicated selection	93
4.5.1	VBF selection optimization	94
4.6	Background	96
4.6.1	Z control region	96
4.6.2	Top control region	100
4.6.3	Diboson backgrounds	100
4.7	Event Categorization	100
4.7.1	Event Prioritization and Recycling	103
4.7.2	Details of event categorization	103
4.7.3	Data-MC comparison by Region	104
4.8	Systematics	109
4.8.1	Experimental uncertainties	109
4.8.2	Background Modeling Uncertainties	115
4.8.3	Signal uncertainties	115
4.8.4	Summary of uncertainties	116
4.9	Statistic procedure: the profile likelihood fit	116
4.10	Results	118
	Conclusions	126
	Ringraziamenti	136

Introduction

In July 2012 the experiment ATLAS and CMS announced the discovery of a new particle with a mass of approximately 125 GeV [1, 2] compatible with the Higgs boson. This discovery represents a nodal point in the understanding of electroweak symmetry breaking. Successive studies [3, 4, 5, 6] have shown that the properties of the new particle are consistent with the expectations of the Standard Model (SM) Higgs boson. Although, the current experimental results cannot exclude the possibility that the new particle is part of an extended Higgs sector or other extensions of the SM. Many of these models predict the existence of diboson resonances. In models with an extended Higgs sector such as the two-Higgs-doublet model (2HDM) [7] and the electroweak-singlet (EWS) model [8], a heavy spin-0 neutral Higgs boson can decay to a pair of Z bosons. In models with warped extra dimensions [9, 10], a spin-2 graviton is expected to decay to ZZ .

My thesis work has been devoted to the search of heavy resonances decaying into a ZZ pair with one of the two Z decaying to a pair of light charged leptons (electrons or muons, referred to as ℓ), $Z \rightarrow \ell\ell$, and the other decaying to a pair of quarks, $Z \rightarrow qq$. This leads to the $ZZ \rightarrow \ell\ell qq$ decay mode. The analysis has been restricted in the diboson mass range 300 – 5000 GeV/ c^2 , within the context of Standard Model extensions with an extended Higgs sector (heavy spin-0 neutral Higgs boson) and warped extra dimensions (spin-2 Randall-Sundrum graviton).

A heavy resonance will appear as a resonant structure in the invariant-mass distributions of the $\ell\ell qq$ final state, thus this invariant mass is used as the final discriminant for the signal-background separation. For the heavy scalar interpretations, the analysis has also been separated into Higgs production modes (gluon-gluon fusion (ggF) and vector boson fusion (VBF)).

Both the ATLAS and CMS Collaborations have searched for heavy resonances in ZV ($V = W, Z$) decays in the $\sqrt{s} = 7$ and 8 TeV datasets [11, 12, 13, 14, 15] and in the $\sqrt{s} = 13$ TeV datasets [17, 16, 18, 19] but only with 2015 data.

For my thesis, I analyzed proton-proton collision data recorded during 2015 and the beginning of 2016 by the ATLAS experiment at LHC with a center of mass energy $\sqrt{s} = 13$ TeV. The integrated luminosity used in this study has been 13.2 fb^{-1} , larger than the previous ATLAS searches.

This thesis is organized as follows:

- Chapter 1: The first chapter gives an overview of the Standard Model and its extensions (Beyond Standard Model (BSM)). In particular an overview of the Two-Higgs-Doublet model and the Randall-Sundrum graviton model is presented.
- Chapter 2: The second chapter illustrates the characteristics of the LHC and of the ATLAS apparatus. The present status of the data taking (Run-II) is also reported.
- Chapter 3: In the third chapter the particle identification and detection techniques used in the ATLAS experiment are described. The reconstruction of leptons and jets are given with more details as they have been widely used in this thesis.
- Chapter 4: In chapter 4 the analysis is presented. A discussion on the various background and a full description of the categorization of events are given. The resulting invariant mass distributions are shown and the determination of confidence levels for the exclusion of a heavy Higgs boson and Randall-Sundrum graviton, over the full range of masses considered, is discussed.

¹To simplify the notations, antiparticles are not explicitly labelled.

A summary of this thesis is given in the conclusive section (4.10).

Chapter 1

The Standard Model and Beyond

The Standard Model (SM) of particle physics is a non-abelian gauge theory that describes the strong and electroweak interaction.

Proposed at the end of the 60's, it obtained many experimental confirmations and it is the model used currently to study the high energy physics.

This chapter summarizes the relevant theoretical aspects used into the presented analyses. It starts with an introduction, *-particles and forces-*, arriving to a description of the Standard Model Higgs boson and the efforts to find it. Some models beyond Standard Model are also presented.

1.1 Elementary Particles

Nowadays the known physical world is described in a big proportion in terms of fundamental matter particles and their interactions thanks to the SM. It describes all known particles and three of the four known fundamental interactions, that is the electromagnetic, weak and strong interactions. Within the SM the particles are classified by their spin as either:

- half-integer spin particles, called fermions, obeying Fermi-Dirac statistics. These form the matter particles;
- integer spin particles called bosons. These particles obey Bose-Einstein statistics and their exchange between the fermions describes the fundamental interactions.

1.1.1 The Fermions

The fermions are categorized into two types, the quarks and the leptons. The quarks are given a baryon number $B = 1/3$. The leptons are assigned a lepton number $L = 1$ and do not interact strongly. Fermions are categorized in three families or generations. Figure 1.1 lists the quarks and leptons and other basic properties [26]; both leptons and quarks families consists of a doublet of particles.

The first generation of quarks consists of the up (u) quark with $+2/3$ electric charge (in units of electron charge, e) and the down (d) quark with $-1/3$ electric charge. The 3 other generations consist of a u -type and a d -type quark but are successively heavier than the first generation. The second generation consists of the strange (s) and charm (c) quarks while the third generation consists of the bottom (b) and top (t) quarks. Quarks carry color charge and each of them comes in three distinct color states (red, green or blue).

Each doublet of leptons is composed of an electrically charged lepton and its corresponding neutral neutrino. As with quarks, the mass of the charged leptons in the doublet increases with generation. The first generation consists of the electron (e) and its neutrino (ν_e), the second the

muon (μ) and its neutrino (ν_μ) and the third the tau (τ) and its neutrino (ν_τ). Each quark and lepton have a corresponding anti-particle, denoted with a bar. Anti-particles have the same mass of the corresponding particle but opposite quantum numbers (for example opposite electric charge). In nature quarks are only found within composite hadrons, composed of either three quarks making a baryon or in quark anti-quark states called mesons.

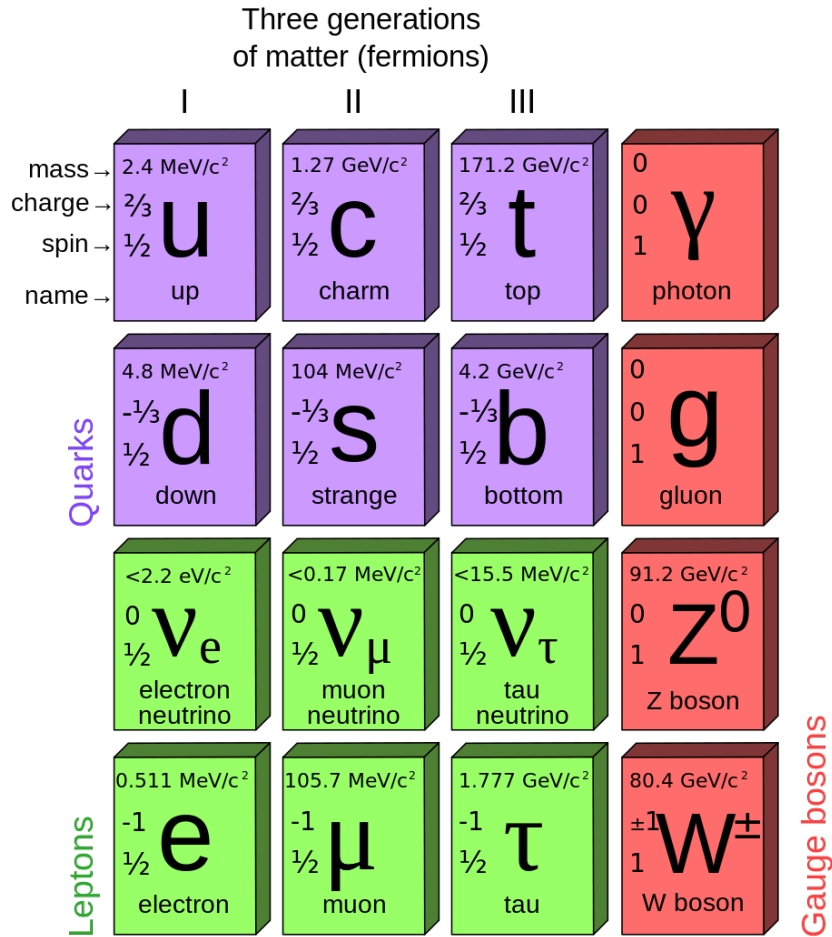


Figure 1.1: Standard Model of Elementary Particles.

1.1.2 Forces and Carrier Particles: the Bosons

Interactions between the fermions are mediated by the absorption and emission of integer spin particles called bosons. This gives rise to four fundamental forces, represented in the Figure 1.2. The electromagnetic force makes the electron bind to nuclei and more generally, molecule formation underpinning Chemistry and it is mediated by the photon (γ). The strong force is responsible for holding nuclei together and is mediated by eight massless gluons (g). The weak force explains decay and is mediated by exchange of W and Z bosons. Gravity is responsible for galactic formation and it is the weakest of all the forces and is negligible at the energy scales considered in particle physics. According to the present knowledge of modern physics all the fundamental forces are described by a quantum field theory except for the gravity. Efforts in this direction are performed and different models predicting a new particle describing the quantum of this interaction, the *graviton*, exists; however, experimental evidences haven't been found yet.

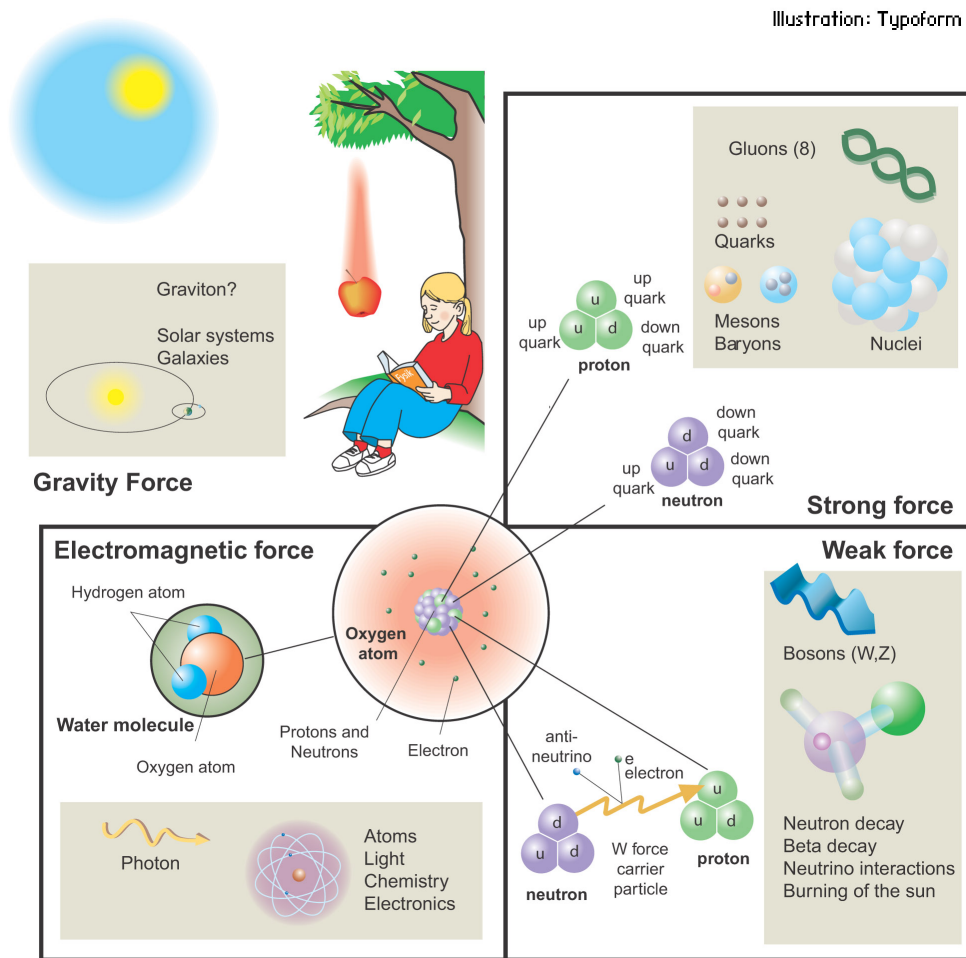


Figure 1.2: Artistic representation of the fundamental forces in Nature.

1.2 The Standard Model

The SM is a theoretical framework of quantum field theory [27] in which the elementary particles are the quanta of the underlying fields and the interactions are a consequence of the principle of local gauge invariance. As yet attempts to incorporate gravity using this approach have failed.

The time-line of the SM becoming an unified theory of the forces that it describes started with the development of the quantum field theory of electromagnetic interactions, called Quantum Electrodynamics.

Subsequently in the 1960's an electroweak theory was developed unifying the electromagnetic and weak interactions.

Finally the electroweak theory was unified with the theory of the strong interactions (Quantum Chromodynamics) giving what is understood as the SM today.

The first step to build a quantum field theory is doing the quantization of the fields; this means that the field operators, that are function of the space-time coordinate, are wrote as linear combination of operators that create or destroy a particle acting on a state vector of the system.

These operators obey to dynamical equation descending from a Lagrangian L by a variational principle.

Usually L is wrote as an integral over the space coordinate of a *Lagrangian density* \mathcal{L} ; this is a function of the fields $\phi_j(x)$ and of their gradients $\frac{\partial\phi_j(x)}{\partial x_\mu} \equiv \partial_\mu\phi_j(x)$:

$$\mathcal{L}(t, \mathbf{x}) = \mathcal{L}(\phi_j(x), \partial_\mu\phi_j(x)). \quad (1.1)$$

The dynamical equation for the fields are obtained from the *Euler-Lagrange equation*:

$$\frac{\partial\mathcal{L}}{\partial\phi_j} - \frac{\partial}{\partial x^\mu} \left(\frac{\partial\mathcal{L}}{\partial\left(\frac{\partial\phi_j}{\partial x_\mu}\right)} \right) = 0 \quad (j = 1, 2, \dots) \quad (1.2)$$

that are a consequence of a variational principle. The interaction between the fields are introduced requiring an invariance of the theory under a local gauge symmetry group; starting from the Lagrangian \mathcal{L}_0 for the free fields, the request of the invariance for the total Lagrangian \mathcal{L} produce the interaction term \mathcal{L}' :

$$\mathcal{L} = \mathcal{L}_0 + \mathcal{L}'. \quad (1.3)$$

Then a set of *Feynman rules* correspond to the particular Lagrangian of the theory; using systematically the Feynman rules is possible writing the matrix elements of the processes involving the particle interactions.

So, under the construction of the Standard Model there is a symmetry principle; the gauge invariance guarantees the mathematical coherence and the prediction of the theory, that is its renormalizability.

The symmetry group used for the Stander Model is:

$$SU(3)_C \otimes SU(2)_L \otimes U(1)_Y, \quad (1.4)$$

where:

- $SU(3)_C$ is the non-abelian group of the color symmetry, that describes the strong interactions between quarks, through an octet of massless boson, the gluons, according to the rules of the QCD;
- $SU(2)_L \otimes U(1)_Y$ is the gauge group of the weak isospin that describes the electroweak interaction (EW), obtained starting from two gauge groups, $SU(2)_L$ for the weak interaction, and $U(1)_Y$ for the electromagnetic interaction, as results in the *Glashow, Weinberg and Salam model*. The electroweak interaction is mediated by four bosons, three of them with mass, W^\pm, Z^0 , and one massless, the photon γ .

The Standard Model Lagrangian can be written as the sum of two contributes: the contribute of the quantum chromodynamics, that describes the strong interactions, and the contribute of the electroweak model, that describes the electromagnetic and weak interactions:

$$\mathcal{L}_{SM} = \mathcal{L}_{QCD} + \mathcal{L}_{EW}. \quad (1.5)$$

1.2.1 Quantum Electrodynamics (QED)

All quantum electromagnetic interactions consist of the interaction of charged fermions with the quantum of the electromagnetic field, the photon. A basic form of this interaction is shown in Figure 1.3. It shows the interaction of charged fermions, a electron pair with a photon γ to produce a muon pair. As with all interactions, the strength is characterized by a coupling constant associated to each vertex. The electromagnetic force couples to electric charge and so this defines the strength of electromagnetic interactions. This vertex corresponds to the basic building block from which all QED processes can be represented. Complete QED processes represented in this way are called

Feynman diagrams ¹. Feynman diagrams with the smallest number of vertices for a given process to occur are referred to as tree-level or leading-order whereas diagrams with a higher number of vertices are called higher order diagrams. A detailed picture of any QED process can be obtained by summing over all possible internal states and this corresponds to summing over all Feynman diagrams of all orders.

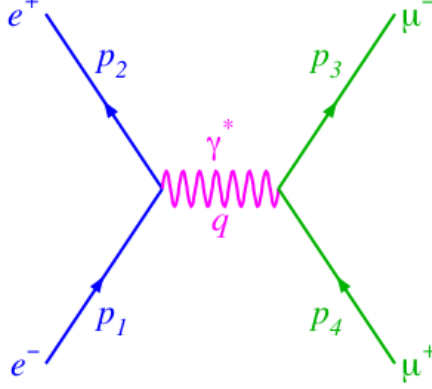


Figure 1.3: Feynman diagram of a muon pair production with a γ virtual mediator.

As said previously, it is convenient to use the Lagrangian formalism to describe the interactions of fermions within the SM, whereby such interactions can be described in terms of an action involving a Lagrangian acting on the fermion fields. The dynamics of non-interacting massive fermion fields is described by the Dirac equation [28] and as such the relevant Lagrangian is the Dirac Lagrangian:

$$\mathcal{L} = i\bar{\psi}\gamma^\mu\partial_\mu\psi - m\bar{\psi}\psi, \quad (1.6)$$

where:

$$\bar{\psi} = \psi^\dagger\psi^0, \quad (1.7)$$

and γ^μ are the Dirac matrix acting on the space 4×4 of the Dirac spinors, and they satisfy the anticommutation algebra rules:

$$\{\gamma^\mu, \gamma^\nu\} = \gamma^\mu\gamma^\nu + \gamma^\nu\gamma^\mu = 2g^{\mu\nu} \quad (1.8)$$

where $g^{\mu\nu}$ is the metric tensor.

In 1954 Yang and Mills [29] proposed a framework for theories involving the exchange of vector bosons, such as those in QED. The Lagrangian in a Yang-Mills theory is invariant under transformations that are a function of space and time. This local gauge symmetry provides an accurate description of physical interactions and is therefore a desirable property of the SM theories.

A local gauge transformation in QED can be represented as a transformation under the symmetry group $U(1)$ corresponding to all unitary matrices of dimension 1×1 . Therefore the local gauge group of QED is called $U(1)$. A generic transformation of this group can be written as:

$$\begin{aligned} \psi(x) &\longrightarrow \psi'(x) = e^{iq\theta(x)}\psi(x) \\ \bar{\psi}(x) &\longrightarrow \bar{\psi}'(x) = e^{-iq\theta(x)}\bar{\psi}(x). \end{aligned} \quad (1.9)$$

¹Given a quantum field theory, represented by a Lagrangian as a function of one or more fields, each one different by the others, it's possible to expand the Green functions as a serie of infinite terms; each one of these terms is composed by few types of elementary objects that are found at all of the orders; therefore, associating to these elementary objects a "pictorial" representation, it's possible build the terms of the infinite expansion in a very simple way. The picture obtained at an assigned order is called *Feynman diagram* while the associations done between the analytic terms and the pictorial representation are called *Feynman rules* and these characterizes completely the theory. Finally, starting from the Green function, it's possible calculate all the observables of the theory, such as cross sections and decaying widths.

$$\begin{array}{l}
\alpha \longrightarrow \beta \quad \rightarrow \quad \left(\frac{i}{\not{p} - m + i\varepsilon} \right)_{\beta\alpha} \\
\mu \text{ (wavy) } \nu \quad \rightarrow \quad \frac{-i\eta_{\mu\nu}}{p^2 + i\varepsilon} \\
\begin{array}{c} \beta \\ \nearrow \\ \alpha \end{array} \text{ (solid) } \mu \text{ (wavy) } \quad \rightarrow \quad -ie\gamma_{\beta\alpha}^{\mu} (2\pi)^4 \delta^{(4)}(p_1 + p_2 + p_3)
\end{array}$$

Figure 1.4: Feynman rules for QED.

In order to ensure this symmetry is retained, a new massless vector field $A_{\mu}(x)$ must be introduced which is identified as the photon field. The request of invariance for the Lagrangian so implies the introduction of this new field and gives also its transformation rule:

$$A_{\mu}(x) \rightarrow A_{\mu}(x) - \partial_{\mu}\theta(x) \quad (1.10)$$

it's then convenient introduce the *covariant derivative*:

$$\mathcal{D}_{\mu} \equiv \partial_{\mu} + iqA_{\mu}(x) \quad (1.11)$$

that is related to the presence of the interactions with the field $A_{\mu}(x)$. This gives rise to the QED Lagrangian:

$$\mathcal{L} = i\bar{\psi}\gamma^{\mu}\mathcal{D}_{\mu}\psi - m\bar{\psi}\psi \quad (1.12)$$

which is then observed to be invariant under transformations of the local gauge group $U(1)$ and to contain interaction terms. It's important to observe that the invariance request implies the theory introduces naturally the gauge field A_{μ} . Finally, the QED Lagrangian is completed adding the kinetic energy term of the free field $A_{\mu}(x)$, that describes the free propagation of photons; this term is local gauge invariant directly:

$$\begin{aligned}
\mathcal{L} &= i\bar{\psi}\gamma^{\mu}\mathcal{D}_{\mu}\psi - m\bar{\psi}\psi - \frac{1}{4}F^{\mu\nu}F_{\mu\nu} = \\
&= i\bar{\psi}\gamma^{\mu}\partial_{\mu}\psi - m\bar{\psi}\psi - j^{\mu}A_{\mu} - \frac{1}{4}F^{\mu\nu}F_{\mu\nu}
\end{aligned} \quad (1.13)$$

where $F^{\mu\nu}(x)$ is the electromagnetic tensor; in the last line the interaction term is put in evidence, it represents the interaction between the Dirac particle and the classical electromagnetic field. Using this Lagrangian the QED Feynman rules are obtained and these are shown in figure 1.4.

The requirement that the physical system remains invariant under local gauge transformations results in the conservation of electron charge, as confirmed by experiment.

Using different symmetry groups, the same principle may be extended to the strong and weak interactions.

1.2.2 Quantum Chromodynamics (QCD)

Quantum Chromodynamics (QCD) is the quantum field theory describing the strong interactions between quarks and gluons inside the hadrons. The strong force couples to colour charge, so only

the coloured gluons and quarks are involved in strong interactions. The most basic QCD interaction vertex, involving the interaction of quarks q with a gluon g is shown in Figure 1.5. The local gauge group of QCD is $SU(3)_C$ corresponding to the unitary group of 3×3 matrices with determinant 1. The three dimensional nature of this group is a consequence of there being three quark colours (C) and as such the quark fields transforming in the vector space of colour. To preserve local gauge invariance of the Dirac Lagrangian eight massless fields must be introduced which correspond to the eight gluons. These fields are also vector fields because the gluons have an intrinsic colour charge.

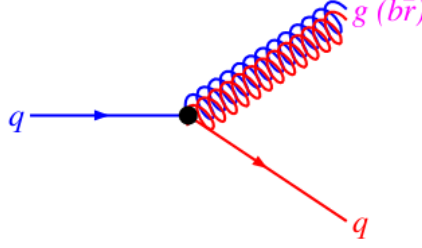


Figure 1.5: The fundamental quark-gluon vertex of QCD.

The $SU(3)_C$ group is an example of a non-abelian group, because its generators do not commute. This is a consequence of gluons carrying a colour charge and leads to self interaction terms in the QCD Lagrangian. This behaviour gives rise to diagrams whereby gluons are coupling to other gluons. This does not occur in QED as photons do not carry electric charge. Same further consequences arise from this property, making QED and QCD intrinsically different.

In the QCD description the quarks take part as color triplet, that is three spinorial fields, $\psi_j^f(x)$ with $j = 1, 2, 3$ color index, correspond to each flavor f :

$$\psi^f(x) = \begin{pmatrix} \psi_1^f(x) \\ \psi_2^f(x) \\ \psi_3^f(x) \end{pmatrix}. \quad (1.14)$$

The QCD free Lagrangian is therefore:

$$\mathcal{L} = \sum_{f=1}^6 \bar{\psi}^f (i\gamma^\mu \partial_\mu - m_j) \psi^f. \quad (1.15)$$

A generic transformation of the local gauge group $SU(3)_C$ is:

$$\psi_j^f(x) \rightarrow \psi_j^{\prime f}(x) = e^{ig_s \vec{\lambda} \cdot \vec{\theta}(x)} \psi_j^f(x), \quad (1.16)$$

where λ_i are the 8 Gell-Mann matrix and $g_s = (4\pi\alpha_s)^{\frac{1}{2}}$ is the strong coupling constant. Then the invariance of the Lagrangian under transformations of $SU(3)_C$ is required; in order to obtain this condition 8 gauge gluon field, $G_\mu^a(x)$, are introduced and a covariant derivative related to this interaction is defined:

$$\mathcal{D}_\mu = \partial_\mu + ig_s \frac{\lambda_a}{2} G_\mu^a \quad (1.17)$$

using this instead of the traditional derivative ∂_μ the Lagrangian 1.15 results gauge invariant. Adding then the kinetic energy term for each gluon as $-\frac{1}{4} G_{\mu\nu}^a G_{\mu\nu}^a$, where:

$$G_{\mu\nu}^a = \partial_\mu A_\nu^a - \partial_\nu A_\mu^a - g_s f_{abc} A_\mu^b A_\nu^c \quad (1.18)$$

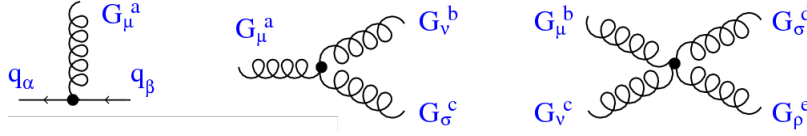


Figure 1.6: QCD rules.

the final QCD Lagrangian is:

$$\mathcal{L} = \sum_f \left[\bar{\psi}^f (i\gamma^\mu \partial_\mu - m) \psi^f - g_s \bar{\psi}^f \gamma^\mu G_\mu^a(x) \frac{\lambda_a}{2} \psi^f \right] - \frac{1}{4} G_{\mu\nu}^a(x) G_a^{\mu\nu}(x) \quad (1.19)$$

where the index $f = 1, 2, \dots, 6$ specifies the quark flavor and $a = 1, 2, \dots, 8$ the gluon fields.

The terms in the Lagrangian 1.19 produce autointeractions between the gluon fields, generating new vertices that doesn't exist in QED, figure 1.6. New aspects appear in the description of the strong interaction, such as the *asymptotic freedom* and the *color confinement*, that make QED and QCD intrinsically different.

Asymptotic freedom refers to the fact that the strength of the strong force (i.e. the coupling strength) increases with increasing distance. This is because in QCD both quark anti-quark loops and gluon-gluon loops contribute to the higher order processes. However, although quark anti-quark loops, like loops in QED, lead to a net reduction in coupling strength with increasing distance the opposite is true for gluon-gluon loops. Because there are more gluons than quarks, the effect from the gluon-gluon loops outweighs that from the quark anti-quark loops and as such gives rise to a net increase in coupling strength with increasing distance. A consequence of asymptotic freedom is that no free quarks or gluons, unlike leptons and photons, are observed in nature and this is why we only observe colourless hadrons in the form of baryons or mesons.

1.2.3 The Electroweak Theory

In analogy to QED and QCD, the quantum field theory of weak interactions is determined by requiring local gauge invariance of the appropriate Lagrangian. The local gauge group of the weak interaction under which the Lagrangian must be invariant is $SU(2)_L$ in the vector space of weak isospin I , where the L subscript refers to the fact that the fermions whose interactions the Lagrangian describes are left-handed (left-handed and right-handed are referred to states that are eigenstates of the chirality). All left-handed fermions experience the weak interaction and are arranged into pairs or fermion doublets. For the leptons these doublets consist of the same generations shown in Figure 1.1, corresponding to the physical (mass) eigenstates. The weak interaction does not couple to the quark mass eigenstates, u, s, d , but instead, linear combinations of them, u', s', d' , which are determined by the CKM matrix [30].

Flavour changing neutral current reactions are not allowed in the SM. In the original formulation of the SM, neutrinos only experience the weak interaction and so are not predicted to have a right-handed component. In 1968 Glashow, Salam and Weinberg [7, 8, 9] successfully extended the theory of weak interactions to encompass the electromagnetic interaction by using the gauge group:

$$SU(2)_L \otimes U(1)_Y. \quad (1.20)$$

Here Y is called *weak hyper-charge* and is related to electric charge Q by $Q = Y + I_3$ where I_3 is the 3rd component of weak isospin. This showed that the electromagnetic and weak forces can be viewed as two components of a single force, called the electroweak force at high energy. In this case preserving local gauge invariance requires four massless fields be introduced. Mixing of these

four fields gives the electroweak bosons γ , W^+ , W^- , Z^0 ². The non-abelian nature of the $SU(2)_L$ group gives rise to self interaction terms and allows W and Z bosons to couple to each other. The $U(1)_Y$ group is however abelian and as such the absence of photon-photon couplings in QED is maintained.

All the fermions of the Standard Model are sensitive to the electroweak interaction. The spinorial fields of the fermions can be written as sum of left-handed and right-handed component using a projection operator:

$$\psi_{L,R} = \frac{1}{2} (1 \mp \gamma^5) \psi. \quad (1.21)$$

The experimental observations show that the weak interaction doesn't preserve the parity. In particular, only the left-handed component of the fundamental fermions take parts to the weak charge-current process and, therefore, these are represented by doublet obeying to the weak isospin symmetry. Whereas the neutral-current processes are related also to the right-handed component of the fermions and these are represented by singlet.

The preserved charge associated to the subgroup $U(1)_Y$, as said, is the weak hypercharge Y . The hypercharge Y and the isospin I satisfies the *Gell-Mann-Nishima relation*, that related these to the electric charge, that is a physical observable:

$$Q = I_3 + \frac{Y}{2}. \quad (1.22)$$

The values of the quantum numbers of the fermions in the EW theory are reported in table 1.1.

The generic transformation of the $SU(2)_L \otimes U(1)_Y$ group is:

$$\begin{aligned} \psi_L(x) &\rightarrow \psi'_L(x) = e^{i\alpha^a(x) \cdot T_a + i\beta(x)Y} \psi_L(x) \\ \psi_R(x) &\rightarrow \psi'_R(x) = e^{i\beta(x)Y} \psi_R(x) \end{aligned} \quad (1.23)$$

where $\alpha^a(x)$ e $\beta(x)$ are local phases and T_a e Y are the generators of the $SU(2)_L$ and $U(1)$ groups. Requiring the invariance for the Lagrangian, four new vectorial field are introduced and the interactions terms are included in the covariant derivative defined as:

$$\mathcal{D}_\mu = \partial_\mu + i\frac{g}{2}W_\mu^a T_a + i\frac{g'}{2}B_\mu Y \quad (1.24)$$

where g e g' are the coupling constant of the two interactions. So, the invariant Lagrangian under $SU(2)_L \otimes U(1)_Y$ group is:

$$\mathcal{L}_\mu = \sum_j i\bar{\psi}_L^j \gamma^\mu \mathcal{D}_\mu \psi_L^j + \sum_k i\bar{\psi}_R^k \gamma^\mu \mathcal{D}_\mu \psi_R^k - \frac{1}{4}W_{\mu\nu}^a W_a^{\mu\nu} - \frac{1}{4}B_{\mu\nu} B^{\mu\nu} \quad (1.25)$$

where the sums over j e k is on all doublet and singlet states written in table 1.1 and:

$$W_{\mu\nu}^a = \partial_\mu W_\nu^a - \partial_\nu W_\mu^a - g'\epsilon_{abc}W_\mu^b W_\nu^c \quad (1.26)$$

$$B_{\mu\nu} = \partial_\mu B_\nu - \partial_\nu B_\mu. \quad (1.27)$$

are the tensor associated to the four fields.

²The discovery of the W and Z bosons was considered a major success for CERN. First, in 1973, neutral current interactions were observed with the huge *Gargamelle* bubble chamber. The discovery of the W and Z bosons themselves had to wait for the construction of a particle accelerator powerful enough to produce them. Build the Super Proton Synchrotron, unambiguous signals of W bosons were seen in January 1983 during a series of experiments made possible by *Carlo Rubbia* and *Simon van der Meer*. The actual experiments were called UA1 (led by Rubbia) and UA2 (led by Pierre Darriulat), and were the collaborative effort of many people. Van der Meer was the driving force on the accelerator end (stochastic cooling). UA1 and UA2 found the Z boson a few months later, in May 1983. Rubbia and van der Meer were awarded the 1984 Nobel Prize in Physics.

	Generation			Quantum numbers			
	1	2	3	I	I_3	Y	Q[e]
Leptons	$\begin{pmatrix} \nu_e \\ e^- \end{pmatrix}_L$	$\begin{pmatrix} \nu_\mu \\ \mu^- \end{pmatrix}_L$	$\begin{pmatrix} \nu_\tau \\ \tau^- \end{pmatrix}_L$	1/2	1/2	-1	0
	e_R^-	μ_R^-	τ_R^-	1/2	-1/2	-1	-1
				0	0	-2	-1
Quarks	$\begin{pmatrix} u \\ d \end{pmatrix}_L$	$\begin{pmatrix} c \\ s \end{pmatrix}_L$	$\begin{pmatrix} t \\ b \end{pmatrix}_L$	1/2	1/2	1/3	2/3
	u_R	c_R	t_R	1/2	-1/2	1/3	-1/3
	d_R	s_R	b_R	0	0	4/3	2/3
				0	0	-2/3	1/3

Table 1.1: Overview on the quantum numbers of the Standard Model fermions in the GWS model. The right-handed neutrinos don't take part to the SM interaction and they are not considered here.

1.3 Spontaneous Symmetry Breaking and the Higgs Mechanism

A combination of the theories of the electroweak and strong interactions may be done to form a unified theory of all the fundamental forces apart from gravity. The corresponding local gauge group is $SU(3)_C \otimes SU(2)_L \otimes U(1)_Y$ and the associated Lagrangian, the SM Lagrangian. However as with the individual theories, the fields which must be included in order to preserve local gauge symmetry, these are identified with the γ , W^+ , W^- , Z and gluons, are each required to be massless. The same is true for the fermions which under $SU(2)_L$ must be massless. Experimentally, however, it has been shown that the W^+ , W^- , Z and fermions are indeed massive. So, the Lagrangian need new terms that haven't disobey the gauge invariance in order to describe the massive contribute.

The mechanism of *spontaneous electroweak symmetry breaking* applied to a *non-abelian* theory was introduced by Peter Higgs [31] in 1964, and independently by Robert Brout and Francoise Englert [32], and Gerald Guralnik, C. R. Hagen, and Tom Kibble[33],[34]. It provides a solution to the massless fields and it is commonly known as the Higgs mechanism.

The Higgs mechanism solve the problem of the masses giving mass terms that are invariant under $SU(2)$ group adding these to the Lagrangian. The basic idea is that while the Lagrangian is gauge invariant the fundamental state isn't invariant necessarily. The spontaneous symmetry breaking of the fundamental state is a consequences of the existence of a new scalar field, the *Higgs field*.

1.3.1 The spontaneous symmetry breaking: a complex field

The basic idea behind *spontaneous symmetry breaking* is discussed in the following by means of adding to the theory a scalar field.

Consider, firstly, a real scalar field $\phi(x)$ with the Lagrangian equation 1.28:

$$\mathcal{L} = T - V(\phi) = (\partial_\nu \phi)(\partial^\nu \phi) - \frac{1}{2}\mu\phi^2 - \frac{1}{4}\lambda\phi^4 \quad (1.28)$$

where $V(\phi)$ is a self-interaction potential of the field ϕ , represented in figure 1.7, and μ and λ are two free parameters. In order for this Lagrangian to be invariant under global gauge transformations (the associated gauge group is $U(1)$), i.e. symmetric under $\phi \rightarrow -\phi$, and there to exist a vacuum state with positive and finite energy, λ must be positive. Imposing $\lambda > 0$, two solutions for μ^2 exist:

- $\mu^2 > 0$ describes a scalar field with mass μ . ϕ is a self-interacting field with coupling λ . The ground state vacuum expectation value here is $\phi = 0$; satisfying mirror symmetry.

- $\mu^2 < 0$ describes a case where the mass term has the wrong sign for ϕ since the relative sign between the kinematic and the potential energy is now positive.

The potential has two minima which satisfy equation 1.28, that are:

$$\phi = 0 \quad (1.29)$$

and:

$$\phi = \pm \sqrt{\frac{\mu}{\lambda}} \quad (1.30)$$

that can be written as:

$$\phi = \pm v \quad \text{where} \quad v = \sqrt{\frac{\mu}{\lambda}}. \quad (1.31)$$

Perturbative expansion about the minimum allows to write ϕ like:

$$\phi(x) = v + \eta(x) \quad (1.32)$$

where $\eta(x)$ represents quantum fluctuations and the field has been translated to $\phi = +v$. The configuration $\phi = -v$ is easily achieved through mirror symmetry.

Doing the corresponding substitution into the mentioned Lagrangian, we have:

$$\mathcal{L} = \frac{1}{2}(\partial_\nu \eta)(\partial^\nu \eta) - \lambda v^2 \eta^2 - \lambda v \eta^3 - \frac{1}{4} \lambda \eta^4 + \text{const}. \quad (1.33)$$

Now the mass term of the field η has a correct sign,

$$m_\eta = \sqrt{2\lambda v^2} = \sqrt{-2\mu^2}. \quad (1.34)$$

The higher order terms (η^3 and η^4) correspond to the self-interactions in η , similar to ϕ^4 in 1.28. This new Lagrangian gives us an accurate picture of physics for scalar particles. It now has a mass term because of the way it was generated, i.e. ϕ was expanded as a function of η around the $\phi = +v$.

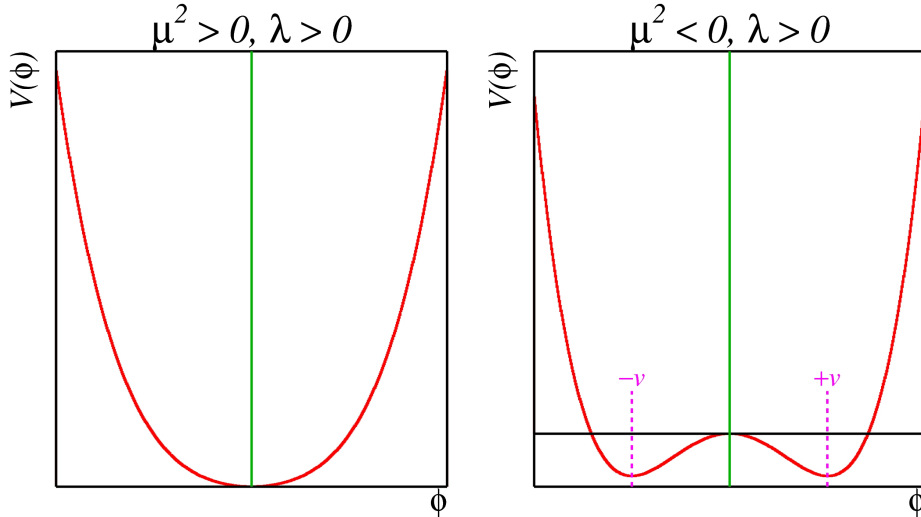


Figure 1.7: The potential $V(\phi) = \frac{1}{2}\mu^2\phi^2 + \frac{1}{4}\lambda\phi^4$ for $\mu^2 > 0$, and for $\mu^2 < 0$ where $\lambda > 0$ in both cases.

Spontaneous symmetry breaking corresponds to the choice in selecting the ground state $\phi = +v$. In physics, spontaneous symmetry breaking occurs when a system belonging to a particular symmetry group goes into a vacuum state that is not symmetric.

Taking into account the previous statement, a look into the spontaneous breaking of a global symmetry is going to be useful in order to describe a Lagrangian for which the mass of gauge bosons can be generated.

Repeating the above procedure for a complex scalar field:

$$\phi(x) = \frac{\phi_1(x) + i\phi_2(x)}{\sqrt{2}}, \quad (1.35)$$

which is invariant under the phase transformation $\phi \rightarrow e^{i\alpha}\phi$, the Lagrangian is:

$$\mathcal{L} = (\partial_\nu \phi)^* (\partial^\nu \phi) - \mu^2 \phi^* \phi - \lambda (\phi^* \phi)^2. \quad (1.36)$$

By substituting the field $\phi = \frac{1}{\sqrt{2}}(\phi^1 + i\phi^2)$ into equation 1.36, becomes

$$\mathcal{L} = \frac{1}{2}(\partial_\nu \phi_1)^2 + \frac{1}{2}(\partial_\nu \phi_2)^2 + \frac{1}{2}\mu^2(\phi_1^2 + \phi_2^2)^2. \quad (1.37)$$

the potential $V(\phi)$ in this case is represented in figure 1.8. After minimizing the potential, we can look at the cases $\lambda > 0$, $\mu^2 < 0$. The minima for $v(\phi)$ exist in a plane ϕ_1 , ϕ_2 , with radius v such that:

$$v^2 = \phi_1^2 + \phi_2^2 \quad (1.38)$$

where $v^2 = -\frac{\mu^2}{\lambda}$, that translates ϕ to a minimum energy position.

In a simple case, the particular choice of the fundamental state could be:

$$\begin{aligned} \phi_1 &= v \\ \phi_2 &= 0 \end{aligned} \quad (1.39)$$

then it's possible expanding the Lagrangian about the vacuum in terms of the fields η and ϵ :

$$\phi(x) = \sqrt{\frac{1}{2}(v + \eta(x) + i\epsilon(x))} \quad (1.40)$$

that if it is included into the equation 1.36, becomes:

$$\mathcal{L} = \frac{1}{2}(\partial_\nu \epsilon)^2 + \frac{1}{2}(\partial_\nu \eta)^2 + \mu^2 \eta^2 + \text{const} + \text{higher orders} \quad (1.41)$$

where the third term has the form of a mass term for η with a mass of:

$$m_\eta = \sqrt{-2\mu^2}. \quad (1.42)$$

As for ϵ there is not apparent mass term, the theory classifies it as a massless scalar Goldstone boson [35, 36, 37], that are bosons that appear in modes which exhibit spontaneous symmetry breaking.

The request that the Lagrangian must be invariant under $U(1)$ gauge transformations in ϕ can be satisfied by transforming:

$$\phi(x) \rightarrow e^{i\alpha(x)}\phi(x) \quad (1.43)$$

and replacing ∂_μ with a covariant derivative, $\mathcal{D}_\mu = \partial_\mu - ieA_\mu$. The gauge field A_μ transforms as:

$$A_\mu \rightarrow A_\mu + \frac{1}{e}\partial_\mu \alpha, \quad (1.44)$$

where A_μ couples to the Dirac particle charge $-e$. Then, the Lagrangian is written as

$$\mathcal{L} = \mathcal{D}_\mu \phi^* \mathcal{D}_\mu \phi - \mu^2 \phi^* \phi - \lambda (\phi^* \phi)^2 - \frac{1}{4} F_{\mu\nu} F^{\mu\nu} \quad (1.45)$$

now, acting the spontaneous symmetry breaking choosing the fundamental state as before and expanding the field around this, the Lagrangian becomes:

$$\begin{aligned} \mathcal{L} = & \frac{1}{2} \partial_\nu \eta \partial^\nu \eta - \lambda v^2 \eta^2 + \frac{1}{2} \partial_\nu \epsilon \partial^\nu \epsilon - ev A_\mu \partial^\mu \epsilon + \\ & + \frac{1}{2} e^2 v^2 A_\mu A^\mu - \frac{1}{4} F_{\mu\nu} F^{\mu\nu} + \text{interaction terms} \end{aligned} \quad (1.46)$$

where $v = \pm \sqrt{-\frac{\mu^2}{\lambda}}$.

So, from spontaneous symmetry breaking we have a massless Goldstone boson ϵ , a massive scalar η and a massive vector A_μ with their masses:

$$\begin{aligned} m_\epsilon &= 0, \\ m_\eta &= \sqrt{2\lambda v^2}, \\ m_A &= ev. \end{aligned} \quad (1.47)$$

By having generated a mass for the gauge field, we still need to solve de problem relative to the generation of a massless Goldstone boson. Giving mass to A_μ , the number of degrees of freedom is taking from four, two scalar field and a massless vector field, to five, two scalar field and a vector field with mass, requiring that we deduce that all the fields must not correspond to distinct particles.

Approximating ϕ to the lowest order in ϵ , that is:

$$\phi(x) = \frac{1}{\sqrt{2}}(v + \eta(x) + i\epsilon(x)) \approx \frac{1}{\sqrt{2}}(v + \eta(x))e^{i\frac{\epsilon(x)}{v}} \quad (1.48)$$

and substituting different fields h , θ , A_μ , where h is real obviously:

$$\phi(x) \longrightarrow \sqrt{\frac{1}{2}}(v + h(x))e^{i\frac{\theta(x)}{v}}; \quad (1.49)$$

that gives to the Lagrangian the following form:

$$\begin{aligned} \mathcal{L} = & \frac{1}{2}(\partial_\mu h)^2 - \lambda v^2 h^2 - \lambda v h^3 - \frac{1}{4}\lambda h^4 + \\ & + \frac{1}{2}e^2 v^2 A_\mu^2 + \frac{1}{2}e^2 A_\mu^2 h^2 + v e^2 A_\mu^2 h - \frac{1}{4}F_{\mu\nu} F^{\mu\nu} \end{aligned} \quad (1.50)$$

It is possible to see that the Goldstone boson does not appear in the equation and the extra degree of freedom corresponds to the ability to make gauge transformations. The Lagrangian describes two interactive massive particles A_μ and h . A_μ is a vector gauge boson and h is a massive scalar known as the Higgs particle. With this mathematical computation, the Goldstone boson now represents a longitudinal polarization for the massive gauge boson, this is known as the Higgs Mechanism.

1.3.2 The Higgs field

The Higgs field is composed by a weak isospin doublet of complex scalar fields with hypercharge $Y = 1$:

$$\phi = \begin{pmatrix} \phi^+ \\ \phi^0 \end{pmatrix} = \frac{1}{\sqrt{2}} \begin{pmatrix} \phi_1 + i\phi_2 \\ \phi_3 + i\phi_4 \end{pmatrix} \quad (1.51)$$

so it contains four real scalar fields ϕ_i . This fields is sentive to the potential:

$$V(\phi) = \mu^2 \phi^\dagger \phi + \lambda (\phi^\dagger \phi)^2 = \mu^2 \phi^2 + \lambda \phi^4. \quad (1.52)$$

the Lagrangian of the Higgs sector is then:

$$\mathcal{L}_H = (\mathcal{D}_\mu \phi)^\dagger (\mathcal{D}^\mu \phi) - V(\phi) \quad (1.53)$$

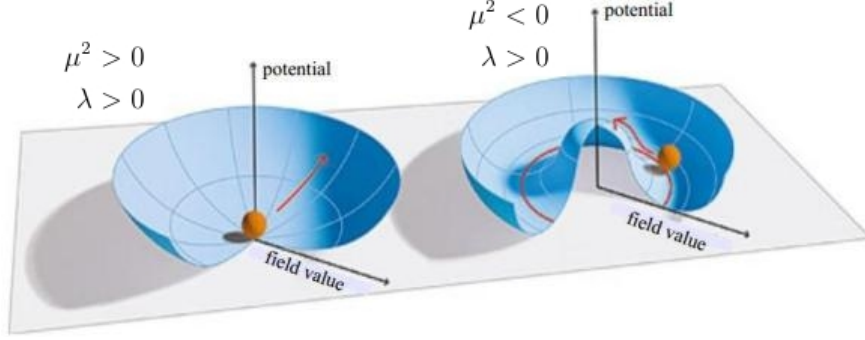


Figure 1.8: Schematic representation of the Higgs potential $V(\phi)$. The interesting case is with the conditions $\lambda > 0$ e $\mu^2 < 0$.

where \mathcal{D}_μ is defined by the equation 1.24.

Choosing the conditions $\lambda > 0$, that is an essential condition for the vacuum stability, and $\mu^2 < 0$, the potential drawn in figure 1.8 is obtained. There is an infinity of generate states with the minimal energy satisfying the condition:

$$\phi_0^2 = -\frac{\mu^2}{2\lambda} \equiv v^2 \quad (1.54)$$

where v is theoretical unknown and experimental fixed to the value 246 GeV ; then it's possible to choose one of these degenerate states as solution:

$$\phi_1 = \phi_2 = \phi_4 = 0, \quad \phi_3^2 = -\frac{\mu^2}{2\lambda} = v^2. \quad (1.55)$$

Then the fluctuations of ϕ around the selected vacuum state:

$$\phi_0 = \begin{pmatrix} 0 \\ v \end{pmatrix} \quad (1.56)$$

can be written as:

$$\phi = \begin{pmatrix} 0 \\ \frac{1}{\sqrt{2}}(v + H(x)) \end{pmatrix} \quad (1.57)$$

acting the spontaneous symmetry breaking mechanism with this particular fundamental state the mass terms wanted are obtained.

1.3.3 Gauge boson masses

The Lagrangian after the electroweak gauge invariance request is:

$$\mathcal{L} = (\mathcal{D}_\mu \phi)^\dagger (\mathcal{D}^\mu \phi) - V(\phi) - \frac{1}{4} W_{\mu\nu}^a W_a^{\mu\nu} - \frac{1}{4} B_{\mu\nu} B^{\mu\nu}. \quad (1.58)$$

Considering the kinetic part, it's possible reconstructing the physical fields, the fields W^\pm are defined as:

$$W_\mu^\pm = \frac{1}{\sqrt{2}}(W_\mu^1 \mp iW_\mu^2) \quad (1.59)$$

while the neutral Z field and the photon field are orthogonal:

$$Z_\mu = \frac{g'W_\mu^3 - gB_\mu}{\sqrt{g'^2 + g^2}} \quad (1.60)$$

and:

$$A_\mu = \frac{g'W_\mu^3 + gB_\mu}{\sqrt{g'^2 + g^2}}. \quad (1.61)$$

introducing the *weak mixing angle* θ_W :

$$\begin{aligned} \cos \theta_W &= \frac{g'}{\sqrt{g'^2 + g^2}}, \\ \sin \theta_W &= \frac{g}{\sqrt{g'^2 + g^2}} \end{aligned} \quad (1.62)$$

the Z and A field are written as:

$$\begin{aligned} Z_\mu &= -B_\mu \sin \theta_W + W_\mu^3 \cos \theta_W \\ A_\mu &= B_\mu \cos \theta_W + W_\mu^3 \sin \theta_W. \end{aligned} \quad (1.63)$$

The boson masses are represented by the quadratic terms that come from the Lagrangian 1.58:

$$\begin{aligned} M_W &= \frac{gv}{2} \\ M_Z &= \frac{v}{2} \sqrt{g'^2 + g^2} \end{aligned} \quad (1.64)$$

while the photon is still massless. The boson masses and the mixing angle are related by the equation:

$$\frac{M_W}{M_Z} = \cos \theta_W. \quad (1.65)$$

1.3.4 Fermion masses

The last step is to add the fermion masses that is still out of the theory. Fermion mass terms could be added considering the interaction between the scalar field ϕ and the fermions. Considering the Lagrangian for the Yukawa terms:

$$\mathcal{L}_{\text{Yukawa}} = -G_\ell^{ij} \bar{L}_L^i \phi \ell_R^j - G_d^{ij} \bar{Q}_L^i \phi d_R^j - G_u^{ij} \bar{Q}_L^i \phi_C u_R^j + h.c. \quad (1.66)$$

where \bar{L}_L^i e \bar{Q}_L^i represented the isospin doublet of the leptons and quarks and ℓ_R^j , d_R^j , u_R^j the singlet for the leptons and the up and down states of the quarks. In the third term:

$$\phi_C = i\sigma_2 \phi^* \quad (1.67)$$

is the conjugate doublet in the sense of $SU(2)_L$ of the doublet ϕ .

The matrix G_ℓ^{ij} , G_d^{ij} e G_u^{ij} define the coupling constant and the mixing of the quarks generation, infact the weak interaction engistates are overlaps of the masses engistates. Acting the spontaneous symmetry breaking and substituting the value of ϕ as written in 1.57 the fermion mass values are obtained. For instance, the mass term for the electron field is reported:

$$\mathcal{L}_e = -\frac{G_e}{\sqrt{2}} v (\bar{e}_L e_R + \bar{e}_R e_L) - \frac{G_e}{\sqrt{2}} (\bar{e}_L e_R + \bar{e}_R e_L) H = \quad (1.68)$$

$$= -m_e \bar{e} e - \frac{m_e}{v} \bar{e} e H \quad (1.69)$$

where $m_e = \frac{G_e v}{\sqrt{2}}$ is the electron mass. The coupling constant G_e is not fixed and the actual electron mass isn't predicted. The Lagrangian has also an interaction term that couples the Higgs field to the electron field and this term is proportional to the electron mass.

The masses of the other fermions are generated in the same way except for the neutrinos that are considered massless according to the Standard Model.

In particular, about quarks, the coupling isn't diagonal considering the fields, this implies that the masses matrix aren't diagonal and the no-diagonal condition remain after the spontaneous symmetry breaking; to obtain diagonal matrix id need to act four unitary transformations, that transform the interaction engistate in the mass engistates. These transformations have effect in the current; in the case of charge current, these transformations put in evidence a violation of the charge conjugation symmetry and of the parity symmetry (CP).

1.4 Higgs boson mass constrains

In the Standard Model there are four types of gauge vector bosons, W , Z , photon γ and gluon, and twelve types of fermions, six quarks and six leptons [22, 23, 24, 25]. These particles have been observed experimentally. At present, all the data obtained from the many experiments in particle physics are in agreement with the SM. We already know that the Higgs boson, according to the SM, is the responsible for giving masses to all the particles. In this sense the Higgs particle occupies a unique position. But the theory itself does not predict the Higgs boson mass, so, in order to understand how the Higgs's search have been perform during the last decades, lets make a review of the theoretical and experimental constrains to such a value, including the most recent LHC's results, where the discovery of a new Higgs-like boson have boosted this already exciting research.

1.4.1 Theoretical Constrains

As mentioned earlier, the Higgs boson mass is not predicted by the SM, nevertheless there are several theoretical ways to define boundaries to the Higgs mass value. Such a constrains have been classified as follow:

Unitarity

Define as the requirement that the total scattering probability for a process, obtained from integrating over all contributing Feynman diagrams, remains less than 1. The theory of electroweak interaction of Fermi violates unitarity at the electroweak scale $\sqrt{s} \approx G_\mu^{-\frac{1}{2}}$ because it assumes point-like interactions. The introduction of massive intermediate bosons resolves the problem for low energy. However, certain processes involving the longitudinal components of the vector bosons are expected to violate unitarity at tree-level. An example of such a process is $W^+W^- \rightarrow W^+W^-$ longitudinal scattering (figure 1.9) which gets contributions from Z and γ , leading to its cross section increasing at high energy in proportion to the square of the centre of mass energy or \sqrt{s} [47]. Unitarity can be restored by adding Higgs exchange diagrams, establishing an upper bound on the Higgs mass of $2v\sqrt{\pi} \approx 800$ GeV.

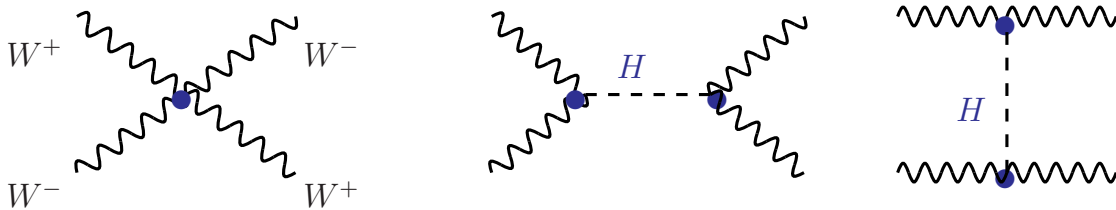


Figure 1.9: Some Feynman diagrams that contribute to the $W^+W^- \rightarrow W^+W^-$ scattering.

Triviality

Referring to section 1.3, the mass of the Higgs boson is given by $m_h = \sqrt{-2\mu^2} = v\sqrt{2\lambda}$. This represents the leading order expression and will be modified once higher order corrections are accounted for, examples of which are shown in figure 1.10. These corrections give rise to divergences which can be accounted for using a renormalisation procedure. After applying this renormalisation it becomes evident that the Higgs self-coupling λ diverges with increasing energy scale. Assuming the Higgs self-coupling is larger than the top quark Yukawa coupling, it varies with energy like $\lambda^2 \ln(Q^2)$. Since it is assumed that the SM is valid at all energies, λ must be zero. This implies that the SM is valid up to a cut-off energy scale (Λ) at which new physics will begin to appear. In order that it produces meaningful predictions at energies below this cut-off the perturbativity of the SM theory must be maintained and as such the Higgs self coupling must remain finite (figure

1.10). Since the Higgs coupling is proportional to the square of the Higgs mass, an *upper limit* on its value is predicted, depending on Λ . This is called the triviality bound on the mass of the Higgs boson. Like an example, a cut-off energy of 10 TeV the upper limit imposed by this constraint gives a $m_h \approx 500$ GeV.

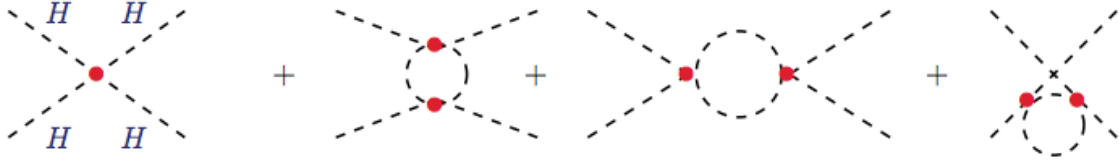


Figure 1.10: Feynman diagrams for the three level of the self-interaction at one loop of the Higgs boson.

Vacuum stability

A *lower constraint* on the Higgs boson mass is derived by assuming the top quark Yukawa coupling is larger than the Higgs self-coupling. This implies low Higgs masses, $m_h < m_t$, where the coupling to top and weak bosons becomes large. In this scenario, the Higgs potential will develop a global minimum at large energy scales, thereby creating an unstable vacuum and preventing spontaneous symmetry breaking. Imposing the same cut-off energy scale Λ at which the SM is valid to, a lower constraint on the Higgs boson mass is imposed in order to maintain vacuum stability. For a cut-off energy scale of the electroweak scale ($\Lambda = 10^3$) $m_h \approx 70$ GeV.

The combined effect of the triviality and vacuum stability requirements is shown in figure 1.11, showing the allowed Higgs mass window as a function of the cut-off energy scale Λ [38], where the bands represent the upper and lower limit theoretical uncertainties and enclose the allowed Higgs boson mass. The limits were derived assuming a top mass $m_t = 175 \pm 6$ GeV and strong coupling constant $\alpha_s = 0.118 \pm 0.002$.

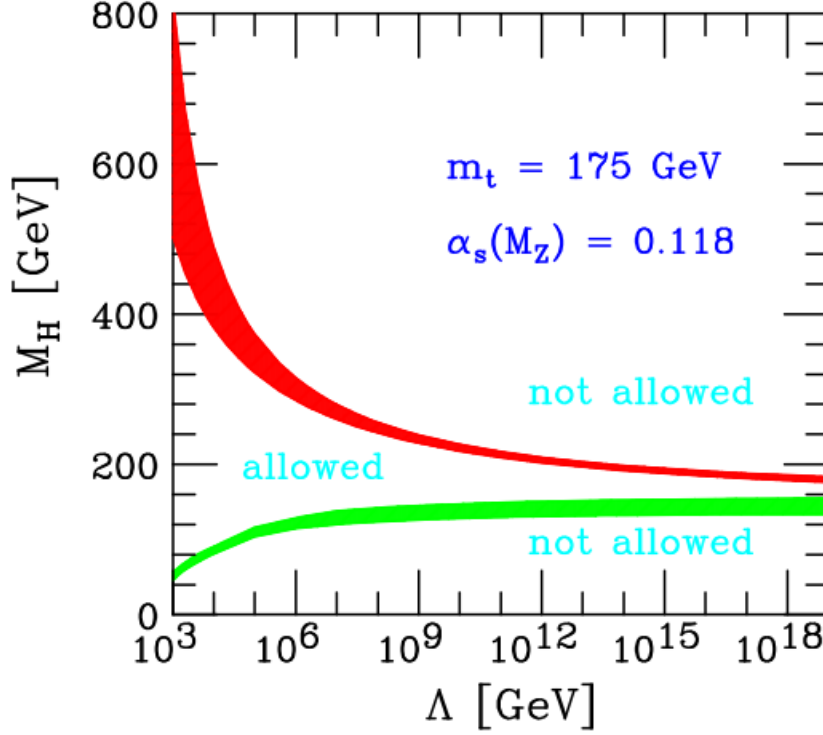


Figure 1.11: Theoretical upper and lower limits on the mass of the Higgs boson as a function of cut-off energy scale Λ . The upper limits are provided by the triviality bound and the lower limits by the vacuum stability bound.

1.4.2 Experimental Constrains before LHC

Experimental constrains on the SM Higgs mass have been established in two ways, in form of limits coming from direct Higgs searches performed at colliders like LEP at CERN and TeVatron at Fermilab, and indirect limits, arising from precision measurements of the electroweak parameters.

The LEP machine was an e^+e^- collider which was operative at CERN from 1989 to 2000. In the first phase of its operations (LEP I) it provided collision at $89 < \sqrt{s} < 93 \text{ GeV}$ to perform precision studies on the recently discovered Z boson, while in the second phase (LEP II) the search for the Higgs boson became one of its main goals, and collision where recorded at increasing energy up to $\sqrt{s} = 210 \text{ GeV}$. The LEP machine provided data to four detector experiments: ALEPH [79], DELPHI [80], L3 [81] and OPAL [82].

The main Higgs production mechanism at LEP was the Higgs-strahlung processes, in which an Higgs boson is radiated by a virtual Z boson: $e^+e^- \rightarrow Z^* \rightarrow ZH$. And all the possible detectable decay modes of H and Z have been used in the search.

While some initial hints of a Higgs signal with mass around 115 GeV was seen, in the final combined result of the search for the Higgs boson performed by the four experiments didn't show any relevant excess, and the final result is shown in Figure 1.12: the test statistics was $-2 \ln Q = -2 \ln \frac{\mathcal{L}_s}{\mathcal{L}_b}$, where \mathcal{L}_b and \mathcal{L}_s are the likelihood of the background only and signal plus background hypotheses respectively. From Figure 1.12 one can deduce that up to a Higgs mass of 114.4 GeV the observed data are consistent with the background only hypothesis.

The TeVatron is a proton-antiproton collider operating in the so called RUN II at a center of mass energy of 1.96 TeV and it has been taking data up to 2011 providing data to two detector experiments: CDF [83] and D0 [84].

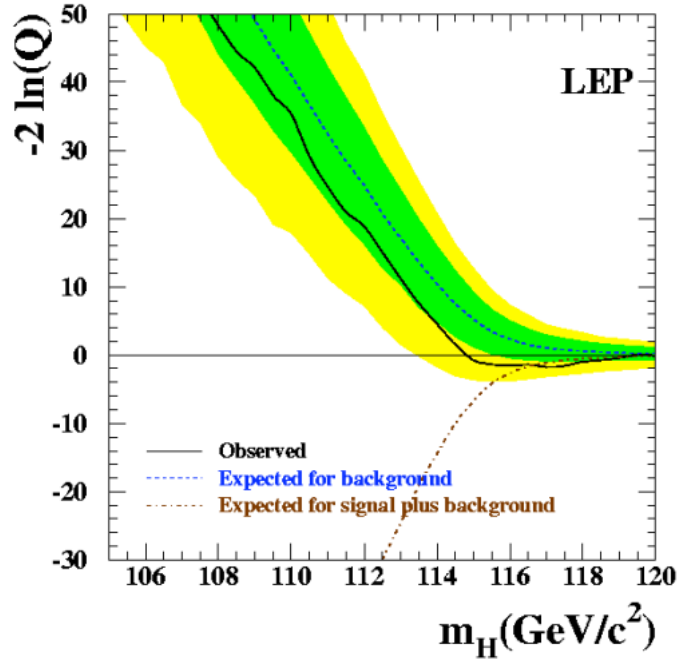


Figure 1.12: Combined results of the direct Higgs search performed by the four experiments at LEP.

The main Higgs production mechanism at the TeVatron collider was the associate production including also the W boson ($p\bar{p} \rightarrow VH, V = W^\pm, Z$), while the main decay channels include also the decay to pairs of vector bosons ($H \rightarrow ZZ^*$ and $H \rightarrow W^+W^-$) because of the wider mass range accessible at the TeVatron. The results of the combined search of CDF and D0 are shown in Figure 1.13 [85]: the 95% confidence level upper limit on the ratio of the Higgs boson production to the SM expectation is shown as a function of the Higgs boson mass.

As can be seen the observed limit goes below unity in the interval $147 < m_H < 180 \text{ GeV}$ and therefore the presence of the Higgs boson is excluded in this mass range with a 95% confidence level.

With only Higgs boson as the missing piece of the SM predictions, it is obvious to attend to predict its mass by fitting all data within the SM framework, having it as one of the free parameters. The variations of the χ^2 of this fit to the data collected by the LEP, TeVatron and SLC accelerators are shown in Figure 1.14. The main result of this fit is that the low mass region (compatible with LEP and TeVatron results) is favoured, but also the high-mass region is not excluded.

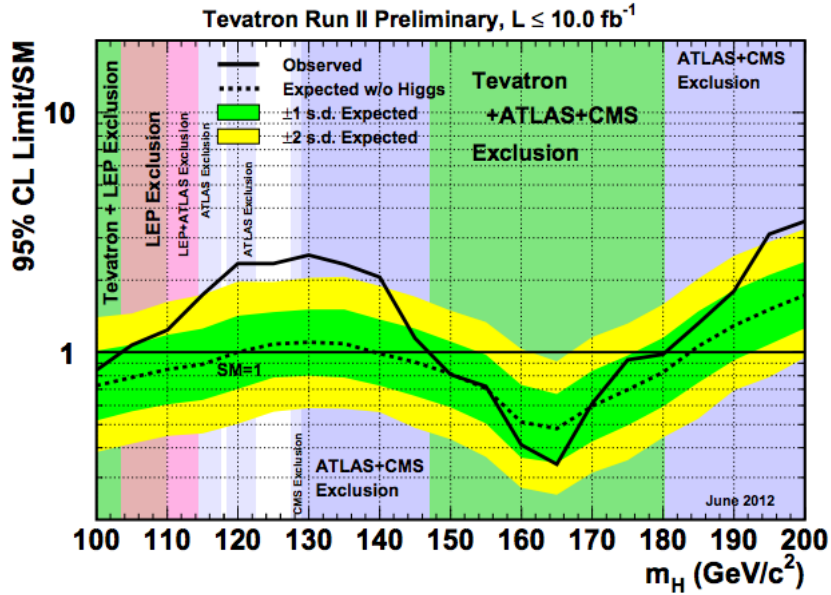


Figure 1.13: Combined results of the Higgs searches by the CDF and D0 collaborations.

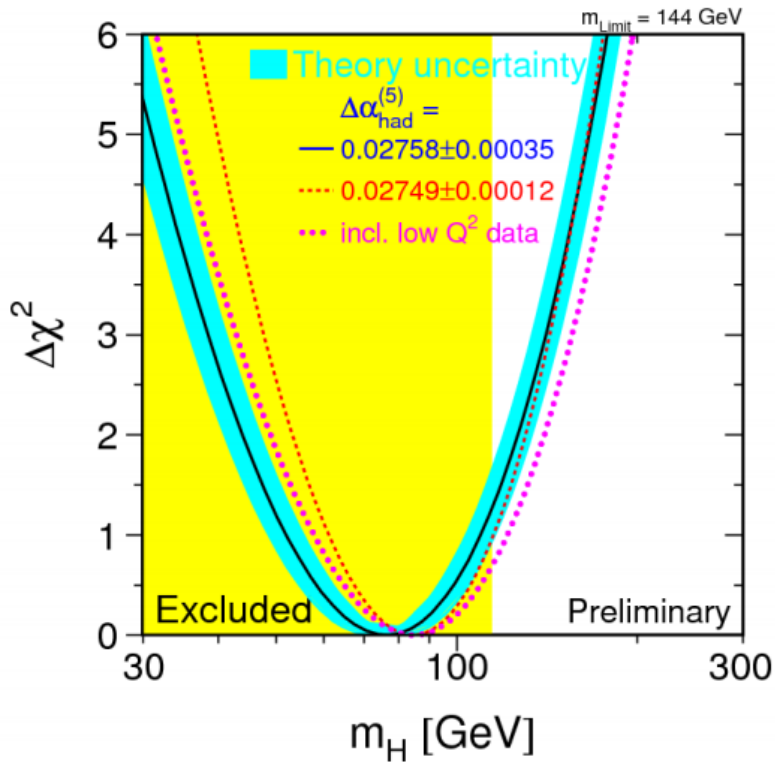


Figure 1.14: Variation of the χ^2 of the electroweak fit as a function of the Higgs boson mass.

1.4.3 Search and discovery of the Higgs boson at LHC

There are essentially four mechanisms for the single production of the SM Higgs boson at hadron collider[39]. A Higgs boson could be produced starting from gluons with production of fermions toward strong interaction, such as in the *gluon-gluon fusion* and *$t\bar{t}$ fusion*, or starting from quarks with production of weak boson, such as in the *Higgs-strahlung* and *vector boson fusion*. The Feynman diagrams of these mechanisms are shown in the Figure 1.15.

The total cross sections are displayed in Figure 1.16 for the LHC at two different center of mass energies: $\sqrt{s} = 8\text{TeV}$ and $\sqrt{s} = 14\text{TeV}$ as a function of the Higgs mass. Lets summarised below the main features of each production channel:

1. Gluon-gluon fusion $gg \rightarrow H$:

This is the dominant production process at the LHC, up to masses $M_H \approx 1\text{TeV}$. The most promising detection channels are[40] $H \rightarrow \gamma\gamma$ for $M_H \leq 130\text{GeV}$ and slightly above this mass value, $H \rightarrow ZZ^* \rightarrow 4l^\pm$ and $H \rightarrow WW^* \rightarrow ll\nu\nu$ with $l = e, \mu$, for masses below $2M_W$ and $2M_Z$ respectively. For higher masses, $M_H > 2M_Z$, it is the golden channel $H \rightarrow ZZ \rightarrow 4l^\pm$, with from $M_H > 500\text{GeV}$ can be complemented by $H \rightarrow ZZ \rightarrow \nu\nu l^+ l^-$, $H \rightarrow WW \rightarrow 4l^\pm$ and –our dissertation analysis– $H \rightarrow ZZ \rightarrow l^+ l^- q\bar{q}$ to increase statistics.

2. Vector boson WW/ZZ fusion:

This process has the second largest cross section at the LHC. For several reasons, the interest in this process has grown: it has a large enough cross section one can use cuts, forward-jet tagging, mini-jet veto for low luminosity as well as triggering on the central Higgs decay products[42] which render the background comparable to the signal, therefore allowing precision measurements.

3. Associated production with a vector boson (Higgs-strahlung) $q\bar{q} \rightarrow HV$:

The associated production with gauge bosons, with $H \rightarrow b\bar{b}$ and possibly $H \rightarrow WW^* \rightarrow l^+ \nu jj$, is the most relevant mechanism at TeVatron[41] ($gg \rightarrow H \rightarrow WW \rightarrow l\nu l\nu$ being important for Higgs masses close to 160GeV). At the LHC, this process plays only a marginal role; however, the channels $HW \rightarrow l\nu\gamma\gamma$ and eventually $lvb\bar{b}$ could be useful for the measurement of Higgs couplings.

4. Associated production with $t\bar{t}$ ($t\bar{t}$ fusion) $pp \rightarrow t\bar{t}H$

Higgs boson production in association with top quarks, with $H \rightarrow \gamma\gamma$ or $b\bar{b}$, can be observed at the LHC and direct measurement of the top Yukawa coupling, as well as an unambiguous determination of the CP violation of the Higgs boson can be possible, in spite that $pp \rightarrow t\bar{t}H \rightarrow t\bar{t}b\bar{b}$ may be subject to a too large jet background[43].

The discovery of this new particle has been made public with a press conference held at CERN on July 4th 2012, and it is based on the analysis and the combination of both the 2011 and 2012 datasets, studied independently by the two collaborations (ATLAS and CMS).

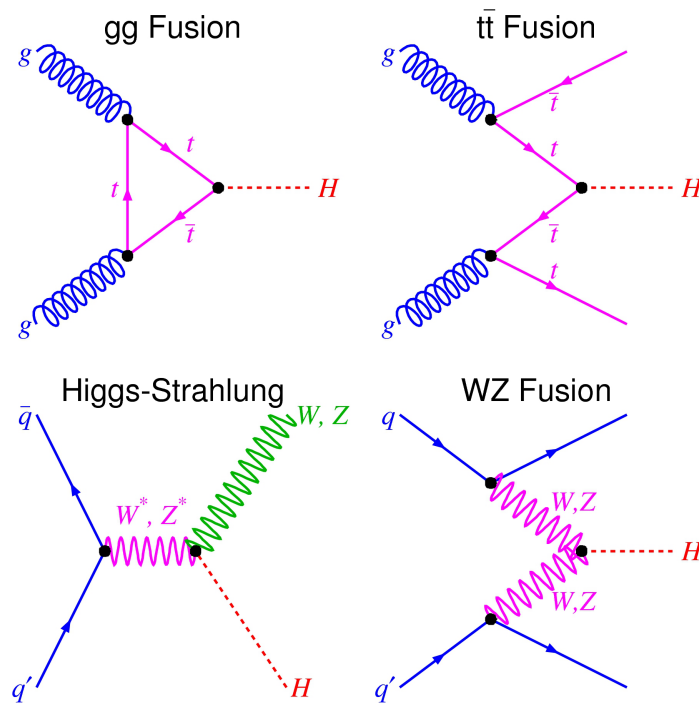


Figure 1.15: The most important processes for Higgs production at hadron colliders. Gluon fusion, vector boson fusion, Associative production with W and an example of the diagrams having associative production with a top pair.

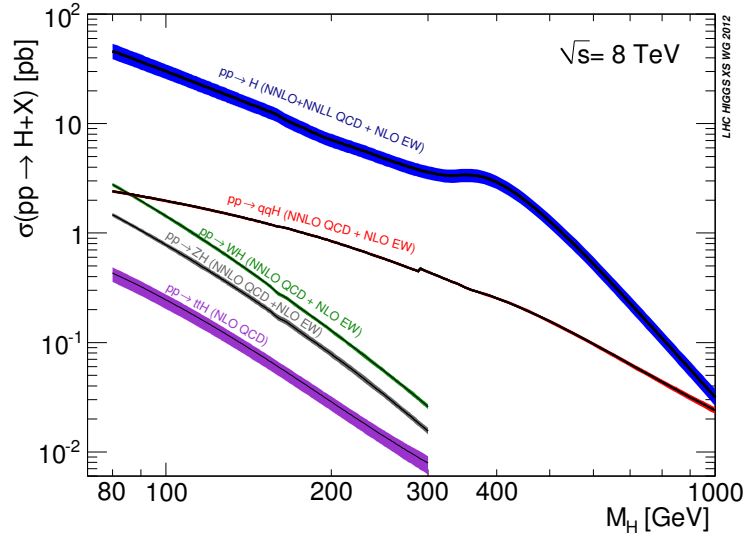
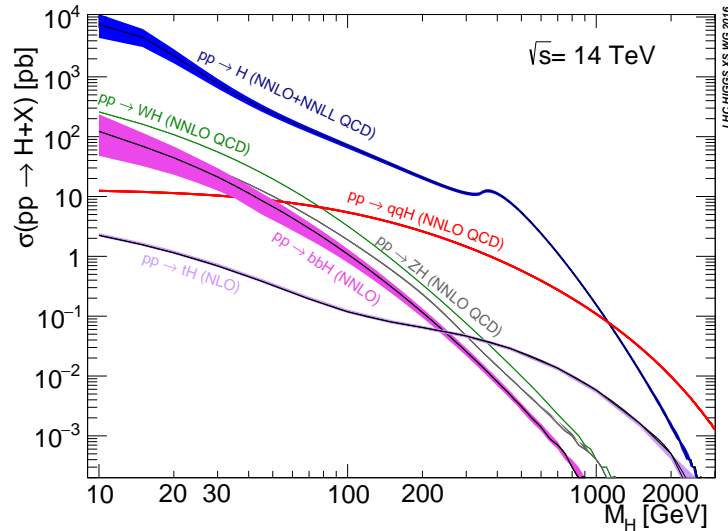
(a) Production cross sections at $\sqrt{s} = 8$ TeV.(b) Production cross sections at $\sqrt{s} = 14$ TeV.

Figure 1.16: Standard Model Higgs boson production cross sections at (a) $\sqrt{s} = 8$ TeV and (b) $\sqrt{s} = 14$ TeV. Transition for VBF at $M_H = 300$ GeV at 8 TeV is due to change from ZWA to complex-pole-scheme.

Figure 1.17 shows the evolution of the p -value³ of the combined Higgs search in the ATLAS experiment as a function of time (i.e. available integrated luminosity): the dashed lines stand for the expected p -value distributions while the solid lines represent the observed ones.

The p -value is basically the probability that, given a certain hypothesis (e.g. the background-only hypothesis), the data have fluctuations greater than the observed ones. The aim of such a measurement is to exclude at 5σ the background-only hypothesis.

³Given a null hypothesis, the p -value represents the probability of getting the results observed considering the null hypothesis true. According to the scientific community an observation characterized by a p -value less than 5σ can be referred as a discovery.

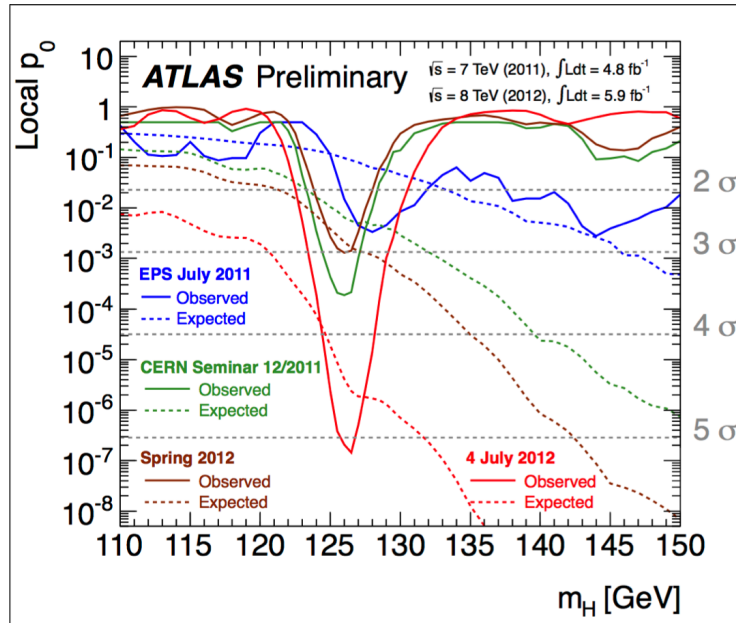


Figure 1.17: Evolution of the p -value measured in the combined Higgs boson search by the ATLAS experiment as a function of time. 2012 results include the full 2011 data sample combined with the amount of data collected in 2012 (at $\sqrt{s} = 8$ TeV) up to the closure for the reference public document.

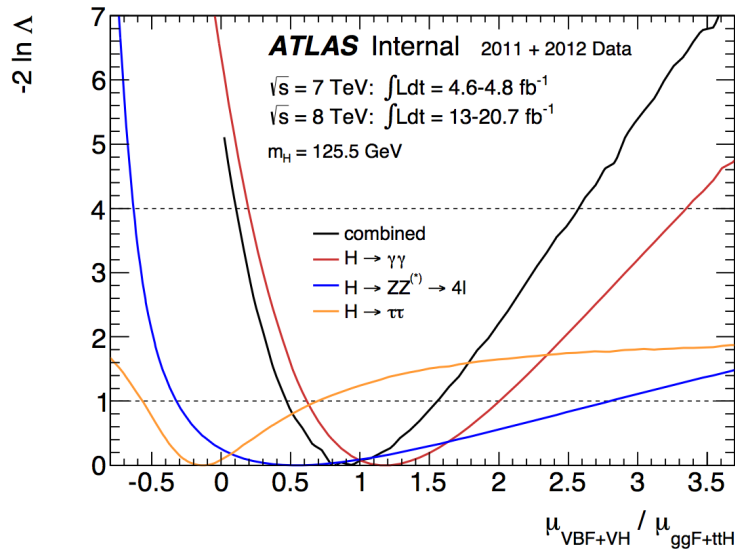


Figure 1.18: Likelihood curves for the ratio $\mu_{VBF+VH} / \mu_{ggF+t\bar{t}H}$ from the $H \rightarrow \gamma\gamma$, $H \rightarrow ZZ^* \rightarrow 4l$ and $H \rightarrow \tau^+\tau^-$ channels and their combination for a Higgs boson mass hypothesis of $m_H = 125.5$ GeV. The branching ratios and possible non-SM effects coming from the branching ratios cancel in $\mu_{VBF+VH} / \mu_{ggF+t\bar{t}H}$, hence the different measurements from all three channels can be compared and combined.

In March 2013 such a observation of a new particle in the search for the Standard Model (SM) Higgs boson at the LHC, reported by the ATLAS[1] and CMS[2] Collaborations, has been update into a combined signal strength value for low mass resolution channels $H \rightarrow WW^* \rightarrow l\nu l\nu$, $H \rightarrow \tau^+\tau^-$ and $H \rightarrow b\bar{b}$ [44]. The mass, signal strength and couplings measurements have been updated using up to $4.8fb^{-1}$ of pp collision data at $\sqrt{s} = 7$ TeV and about $21fb^{-1}$ at $\sqrt{s} = 8$ TeV for the two channels $H \rightarrow \gamma\gamma$ [45] and $H \rightarrow ZZ^* \rightarrow 4l$ [46]. The Figure 1.18 shows the Likelihood curves for the ratio different channels and their combination for a Higgs boson mass hypothesis of $m_H = 125.5$ GeV.

1.5 Beyond the Standard Model

Despite being able to explain with high precision most of the experimental data that has been produced until now, the SM suffers from several theoretical problems:

- no dark matter candidate is provided by the SM;
- it does not explain the gravitational interaction;
- the level of CP violation is not sufficient to explain the matter anti-matter asymmetry seen in the universe;
- it does not explain the hierarchy problem, i.e. why gravity is so weak compared to the other interactions;
- fine tuning is required to deal with divergences in the Higgs sector.

Because of these reasons and indeed others not discussed, it is a widely held opinion within the scientific community that the SM is an effective theory which we currently probe at low energy. The general theory will begin to become accessible when the predictions of the SM start to become incorrect. More precise determination of the free parameters of the SM will allow the scale at which this happens to be better understood.

Several beyond the SM theories exist which describe the SM predictions at low energy. Perhaps one of the most popular is supersymmetry which suggests a new symmetry between fermions and bosons and provides solutions to a number of the problems associated with SM. This model commonly provides a dark matter candidate and it also provides a solution to divergences in the Higgs sector.

1.5.1 New heavy particle decaying into diboson final states

Many models beyond the Standard Model of particle physics predict heavy particles that could decay into diboson final states. Below a description of a subset of the models predicting a heavy diboson resonance is given.

1.5.2 Heavy Higgs bosons/Scalar resonances

The Standard Model of particle physics was made consistent by the introduction of the Higgs mechanism, which gave a theoretical explanation for the fact that the elementary particles can be massive while preserving the gauge invariance of the theory itself. The Higgs mechanism implied the existence of a new scalar particle, the Higgs boson. After decades of searching, a new particle was discovered in 2012 that seems to be consistent with the expected Higgs boson. However, a single Higgs boson is only the simplest possible theoretical model. Since the original proposal of the Higgs mechanism, numerous extensions have been proposed that can be tested at the LHC, like the *electroweak singlet model* [110] and the *2 Higgs-doublet model* [111]. All these models predict the existence of additional bosons beyond the single one required by the minimal Higgs mechanism.

The analysis, in which my work takes part, tests basic extensions of the Standard Model which introduce an additional Standard-Model-like neutral CP-even spin-0 resonance in the mass range $300 \text{ GeV}/c^2 < m_H < 1000 \text{ GeV}/c^2$ with either: a narrow width, similar to its lightweight analogue, and thus its experimental signature will be dictated by the resolution of the detector; or a large width, tested with values of 5%, 10%, and 15% of the mass of the resonance. Interference effects between the signal and the ZZ background as well as the Higgs at 125 GeV are neglected in this search for the ZZ background (which is small) and the signal shapes and cross sections. Interference effects are model dependent and, in the EWS, neglecting them weakens the given limits [112].

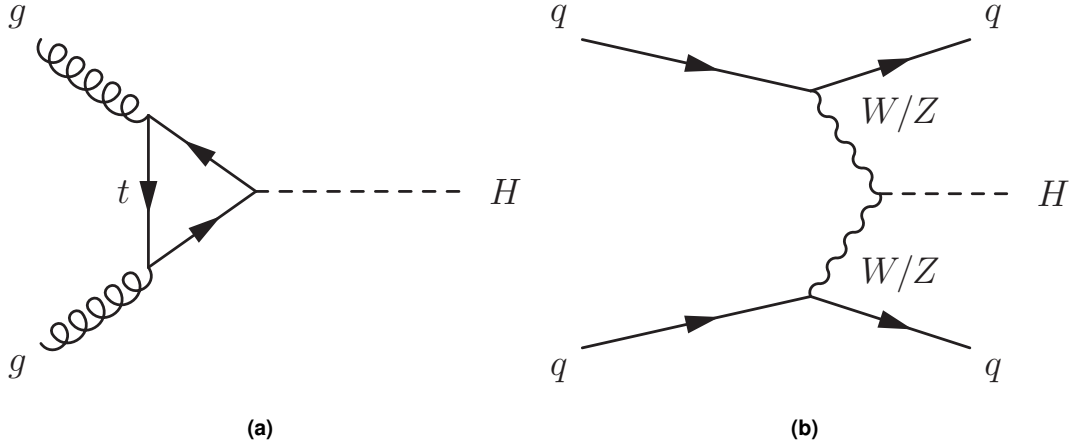


Figure 1.19: Higgs production mode: (a) gluon-gluon fusion (ggF) and (b) vector boson fusion (VBF).

The two main Higgs production modes, gluon-gluon fusion (ggF) and vector boson fusion (VBF), are considered in this work. The corresponding Feynman diagrams are shown in Figure 1.19. The relative ratio of production rate between these two modes are model dependent, and some typical cross sections for a SM-like narrow width Higgs at different masses are shown in Table 1.2. Given that these two production modes lead to distinct features of kinematics, especially the jet multiplicities, dedicated event selection categorizations are defined for ggF and VBF separately.

Table 1.2: Higgs production rates for ggF and VBF, calculated from PowhegBox [120].

m_H (GeV)	σ_{ggF} (pb)	σ_{VBF} (pb)
300	6.65	1.22
500	3.08	0.47
1000	0.089	0.085

1.5.3 Two-Higgs-Doublet models (2HDM)

In this form the SM, the Higgs mechanism constitutes only a minimal configuration to implement the breaking of the electroweak symmetry and the generation of particle masses. A simple extension of the SM Higgs sector is given by the addition of a second complex Higgs doublet, giving rise to five Higgs bosons:

- two CP-even scalar fields h and H ,
- one pseudoscalar A (CP-odd),
- and two charged fields H^\pm .

These Two-Higgs-Doublet models (2HDM) are phenomenologically interesting since they can explain the generation of the baryon asymmetry in the universe [8] and are an important ingredient of axion models that are designed to explain the dark matter content of the universe [96].

Finally, the minimal supersymmetric SM [97] contains two Higgs doublets as well. Four different types of 2HDMs can be distinguished, depending on the different coupling of the two scalar fields h and H to fermions and weak gauge bosons. In type-I models all quarks couple to just one of the Higgs doublets, while in type-II models the right-handed up-type quarks couple to one Higgs

doublet and the right-handed down-type quarks to the other doublet. Type-III and type-IV models differ only from type-I and type-II models in their couplings to the leptons.

Recent detailed reviews on 2HDMs can be found in Refs. [98, 99]. Since the discovery of the new boson at the LHC, 2HDMs have attracted much attention in phenomenological studies [100, 101, 102, 103, 104], which provide a strong incentive for dedicated experimental investigations in this direction. Searches for generic 2HDMs have been performed by the CDF collaboration at the TeVatron [105, 106]. The rate of the Higgs-like boson at 125 GeV in the two-photon channel provides also constraints on 2HDMs [107], mainly reducing the parameter space of type-II models. The analysis presented investigates the possibility that the boson observed by the ATLAS and CMS experiments at a mass of 125 GeV originates from a Higgs boson that is part of a 2HDM. In particular, it is assumed that the observed particle is the low mass Higgs h of the 2HDM.

1.5.4 Heavy Vector Triplet

Searches for heavy vector particles are theoretically well-motivated since the existence of these new particles is predicted by many extensions of the SM. In order to obtain as much information as possible about such new particles, their couplings to quarks, leptons, SM gauge and Higgs bosons have to be investigated. All of these couplings are present, and in principle sizeable, for a *colourless electroweak triplet heavy vector* with zero hypercharge, which we refer to as HVT, and we thus choose this as a motivated representative to study. The phenomenological features of such a triplet can be concisely described within the HVT setup introduced in Ref. [113]. An HVT consists of two essentially degenerate states: an electrically charged, V^\pm , and a neutral one, V^0 . The couplings of the HVT to all SM particles are given in terms of the new coupling g_V , which parameterizes the interaction strength between the heavy vectors. This makes the setup extremely versatile since it can capture the features of many, weakly and strongly coupled, concrete models.

The relevant parameter space of an HVT with a given mass is two-dimensional consisting of two parameter combinations which describe its couplings to fermions and to SM gauge bosons. The HVT model under consideration is a simplified version with an universal coupling C_F of V to fermions. The coupling of the HVT to fermions scales as $g^2/g_V c_F$, where g is the SM $SU(2)_L$ gauge coupling and c_F is a free parameter which can be fixed in each explicit model. Concerning the HVT coupling to SM bosons, note that it couples dominantly to the longitudinal components of the gauge bosons and to the Higgs, while the coupling to transverse gauge bosons is generally suppressed. Moreover, couplings to identical neutral bosons are absent – in the case of ZZ the coupling is not included, in the case of HH the coupling is forbidden. Contrary to the coupling to fermions, the HVT coupling to SM bosons scales as $g_V c_H$. The parameter c_H , analogously to c_F , has to be fixed in each individual model and takes values of order one. In a very large class of explicit models of heavy vectors, the parameters c_H and c_F can be computed and the result test the compatibility of the concrete model with the experimental search.

Diboson final states, both neutral W^+W^- , ZH , and charged $W^\pm Z$, $W^\pm H$, where H is the SM Higgs boson, are particularly interesting in strongly coupled models where the branching ratio into diboson final states is enhanced. Note that the HVT coupling to two SM bosons comes from a gauge invariant coupling to the electroweak triplet Higgs current, with strength $g_V c_H$, and thus all the couplings to the aforementioned final states are expected to be equal. In particular the HVT framework predicts the same branching ratios for the four processes:

$$\text{BR}(V^\pm \rightarrow W^\pm Z) = \text{BR}(V^\pm \rightarrow W^\pm H) = \text{BR}(V^0 \rightarrow W^\pm W^\pm) = \text{BR}(V^0 \rightarrow ZH). \quad (1.70)$$

Other neutral diboson final states are either suppressed or forbidden.

This relation is of primary importance in the HVT framework since it allows us to gain a higher sensitivity by combining not only neutral and charged channels, but also eventually channels involving the Higgs boson. For more details on the theory, please refer to the literature (Ref [113]).

The HVT also couples to fermions. Here it is important to note that the triplet couples to the fermionic current. Therefore, what needs to be compared is the sum of the widths (or equivalently the sum of the BRs) of all quark and lepton final states. For example, the sum of the widths into

$\ell\ell$ and $\nu\nu$ is the same as the width into $\ell\nu$. For the quark sector, the mixing has to be taken into account and the sum of all charged quark final states is equal to the sum of all neutral quark final states. Hence equation 1.70 is true in general.

1.5.5 Bulk Randall-Sundrum Model

The Randall–Sundrum (RS1) framework [114] attempts to explain the hierarchy problem by introducing large extra dimensions in which SM fields can propagate. This leads to a tower of Kaluza–Klein (KK) excitations of SM fields, notably including KK excitations of the gravitational field that appear as TeV – scale spin-2 Gravitons (G^*) [115].

In some RS1 models the graviton has sizable couplings to all SM fields, which do not propagate significantly into the extra dimension (bulk). This leads to large production rates in both gluon-gluon (gg) and quark-quark (qq) fusion modes, and substantial decay rates to diphotons and dileptons. In the “bulk RS” scenario considered here, however, the SM fields are permitted to propagate into the bulk, where they are localized. The bulk RS model avoids the constraints on other RS scenarios arising from flavor physics and electroweak precision tests, at the cost of suppressing the couplings of the G^* to light fermions, which leads to significantly reduced production rates from qq fusion and lower branching fractions to leptons and photons. The gg fusion production mode therefore dominates in the bulk RS model, with the G^* -gluon coupling suppressed by a factor $k/\bar{M}_{\text{Planck}}$, where k is the curvature scale of the extra dimension and \bar{M}_{Planck} is the reduced Planck mass. The value of $k/\bar{M}_{\text{Planck}}$ is typically of order 1, and along with the mass of the G^* is the only free parameter in this simplified model. The decays of the G^* in this scenario are dominated by $G^* \rightarrow t\bar{t}$, $G^* \rightarrow HH$, and $G^* \rightarrow V_L V_L$, with branching fractions that depend on mass.

Chapter 2

CERN, the LHC and the ATLAS Experiment

Founded in 1954, the CERN laboratory is located on the Franco-Swiss border near Geneva. It was one of Europe's first joint ventures and now has 20 member states. The name CERN is derived from the acronym for the French *Conseil Européen pour la Recherche Nucléaire*, or European Council for Nuclear Research, a provisional body founded in 1952 with the mandate of establishing a world-class fundamental physics research organization in Europe. At that time, pure physics research concentrated on understanding the inside of the atom, hence the word "nuclear". At this moment, the understanding of matter goes much deeper than the nucleus, and the main area of research at CERN is particle physics – the study of the fundamental constituents of matter and the forces acting between them.

At CERN, the European Organization for Nuclear Research, physicists and engineers are probing the fundamental structure of the universe. They use the world's largest and most complex particle accelerator to study the basic constituents of matter or the fundamental particles. The particles are made to collide together at close to the speed of light. The process gives the physicists clues about how the particles interact, and provides insights into the fundamental laws of nature.

The instruments used at CERN are purpose-built particle accelerators and detectors. Accelerators boost beams of particles to high energies before the beams are made to collide with each other. Detectors –like ATLAS– observe and record the results of these collisions.

2.1 The Large Hadron Collider and the Run-I

The Large Hadron Collider (LHC), conceptualised around a quarter of century back, is built in a circular tunnel 27 km in circumference. The tunnel is buried around 50 m to 175 m underground. It located between the Swiss and French borders .

The first beams were circulated successfully on 10th September 2008. Unfortunately on 19th September a serious fault developed damaging a number of superconducting magnets. The repair required a long technical intervention. The LHC beam did not see beam again before November 2009. First collisions took place on 30th March 2010 with the rest of the year mainly devoted to commissioning. The 2011 was the first production year with 5 fb⁻¹ delivered to both ATLAS and CMS. The 2012 started with over 6 fb⁻¹ delivered by the time of the summer conferences. Data that allowed for the announcement of the discovery of a Higgs-like particle on 4th July 2012 mentioned in the previous chapter (section 1.4.3).

It is a proton-proton (pp) collider, and the collision were delivered at $\sqrt{s} = 7 TeV$ in 2010 and 2011, while they are being collected at $\sqrt{s} = 8 TeV$ during 2012. One of the crucial parameters for the discovery power of a particle collider is the *instantaneous luminosity*, \mathcal{L} , since it is proportional to the event rate $\frac{dN}{dt}$:

$$\frac{dN}{dt} = \mathcal{L} \cdot \sigma \quad (2.1)$$

where σ is the cross section of the considered process. The instantaneous luminosity of a particle accelerator depends on its intrinsic features:

$$\mathcal{L} = \frac{N_p^2 f k}{4\pi R^2} \quad (2.2)$$

where N_p is the number of protons in each bunch, f is the revolution frequency of the protons in the accelerating ring, k is the number of bunches circulating in the beam and R is the mean radius of the proton distribution on the plane orthogonal to the beam direction.

The instantaneous luminosity delivered by the LHC in 2011 reached the value of $3,65 \cdot 10^{33} cm^{-2}s^{-1}$ at its maximum, where the design peak luminosity was $10^{34} cm^{-2}s^{-1}$. This high luminosity is reached with 1380 (2808 from the design) bunches per beam, each of them containing 10^{11} protons. The bunches have very small transverse spread, about $15 \mu m$ in the transverse direction, and the longitudinal length is about $7 cm$. In the design of the LHC the bunches should have crossed every $25 ns$, giving a collision rate of $40 MHz$, while the actual bunch spacing reached in 2011 and 2012 is of $50 ns$. These parameters achieved in 2011 and 2012 allowed an integrated luminosity showed in Figure 2.1.

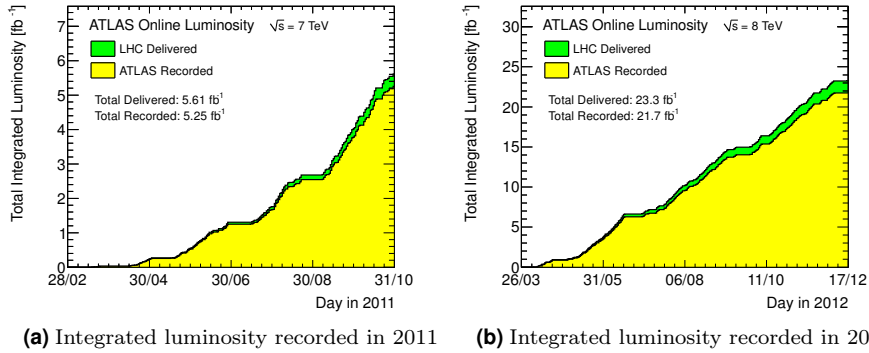


Figure 2.1: The integrated luminosity as a function of time delivered by LHC (green) and recorded by ATLAS (yellow) in 2011 and 2012.

Part of the acceleration chain and the different positions of the LHC's experiments are showed in Figure 2.2: after their production and an of $1.4 GeV$, the Super Proton Synchrotron raises their energy up to $450 GeV$ before injecting them into the LHC. Once there, the protons are accelerated in the two opposite directions up to the colliding energy of $3.5 TeV$ (2011) or $4 TeV$ (2012) per beam.

Since LHC accelerates two beams of same sign particles, two separate accelerating cavities and two different magnetic fields are needed: LHC is equipped with 1232 superconducting magnets and 16 radiofrequency cavities which bend and accelerate the proton beams in the two parallel beam lines in the machine. The magnetic field used to bend such energetic proton beams is of $8.3 T$ and to reach such a magnetic fields the superconducting magnets are cooled down to $1.9 K$ and a $13 kA$ current circulates inside them.

The LHC provides collisions in four collision points along its circumference where detector experiments located:

Feature	design value	actual value
beam energy [TeV]	7	4
bunch spacing [ns]	25	50
peak luminosity [$cm^{-2}s^{-1}$]	10^{34}	8×10^{33}
mean number of interaction per bunch crossing	23	20
number of bunches	2808	1380
protons per bunch	1.15×10^{11}	1.67×10^{11}
bunch transverse dimensions [μm]	15	~ 30

Table 2.1: Main features of the LHC. The first column contains the values as in the LHC design, the second column contains the actual value of the features. The actual features include both 2011 and 2012 runs

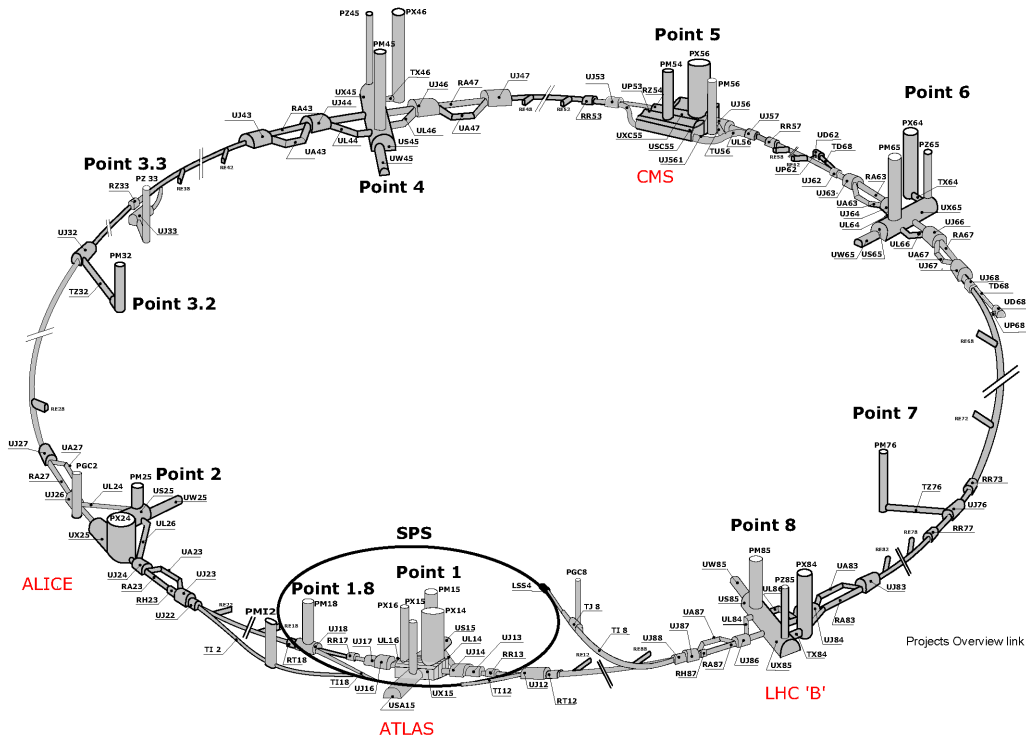


Figure 2.2: The LHC particles accelerator, in which it is possible to see the SPS and the different beam's collision points with their corresponding experiment.

- ALICE (*A Large Ion Collider Experiment*),
- ATLAS (*A Toroidal Lhc ApparatuS*),
- CMS (*Compact Muon Solenoid*),
- LHCb (*Large Hadron Collider beauty*).

ATLAS and CMS are multi-purpose detectors, while ALICE and LHCb are focused on more specific studies: (See Figure 2.2) ALICE focuses on the quark-gluon plasma produced in heavy-ions collisions¹, while LHCb focuses on the study of CP violation processes occurring in b and c hadron decays.

¹The LHC is able to accelerate and collide lead ions at $\sqrt{s} = 2.76 TeV$ per nucleon, and ions collisions are foreseen each year in the LHC program. Not part of our actual studies.

2.1.1 LHC: the Run-II

During the 2015 a second phase of event production at LHC, called *Run-II*, started. During the Run-II the LHC will reach its design energy collision, 14TeV , and the purpose of the program is to collect data corresponding about to 100fb^{-1} during 2015 – 2018. The Run-II started in *May* 2015. An initial phase of collision with 50ns bunch spacing and 1fb^{-1} in luminosity took place; the data collected were dedicated to control the performances of the magnet and of the alignment of the spectrometer.

Just after the commitioning phase the beams, characterized by 25ns bunch-spacing, circulated in the accelerator and produced collisions at $\sqrt{s} = 13\text{TeV}$ with a peak luminosity of $5,0 \cdot 10^{33}\text{cm}^{-2}\text{s}^{-1}$.

Also during the 2016 LHC produced collisions and the collection of data is going on again. The energy is still $\sqrt{s} = 13\text{TeV}$ while the peak luminosity was $12,1 \cdot 10^{33}\text{cm}^{-2}\text{s}^{-1}$. The figures 2.5a and 2.5b represent the peak luminosity as a function of the day of running during 2015 and 2016. The total integrated luminosity as a function of the days of running during 2015 and 2016 are represented in figures 2.4a and 2.4b; up to the end of *September* 2016 the total integrated luminosity is $4,2\text{fb}^{-1}$ for 2015 data and $29,7\text{fb}^{-1}$ for 2016 data. At the end of June, beams were maintained in the accelerator for a record 37 consecutive hours. But the main indicator of success for the operators is luminosity, the measurement of the number of potential collisions in a given time period. On *29 June*, peak luminosity exceeded $10^{34}\text{cm}^{-2}\text{s}^{-1}$. This represents a success for the LHC operators because it corresponds to the ultimate objective defined by those who originally designed the LHC machine.

Feature	design value	actual value
beam energy [TeV]	7	6,5
bunch spacing [ns]	25	25
peak luminosity [$\text{cm}^{-2}\text{s}^{-1}$]	$10^{34}\text{cm}^{-2}\text{s}^{-1}$	$12,1 \cdot 10^{33}\text{cm}^{-2}\text{s}^{-1}$
mean number of interaction per bunch crossing	19	23
number of bunches	2808	2220
protons per bunch	$1,15 \cdot 10^{11}$	$1,18 \cdot 10^{11}$
bunch transverse dimensions [μm]	$16\mu\text{m}$	μm

Table 2.2: Capabilities of the LHC during the Run-II. The first column contains the values as in the LHC design, the second column contains the actual value of the features.

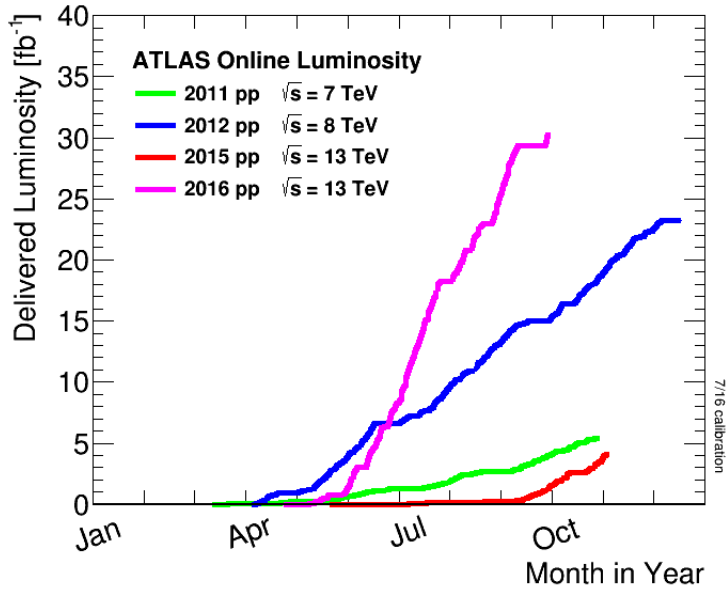
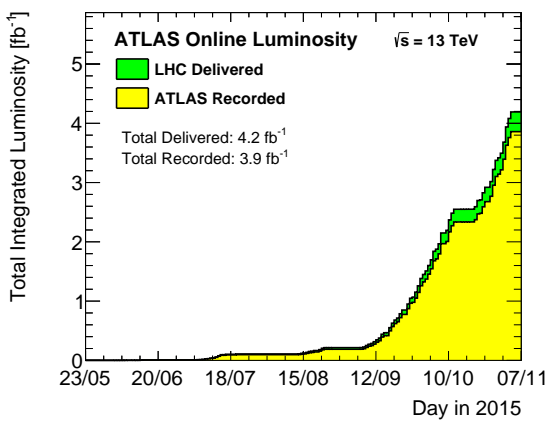
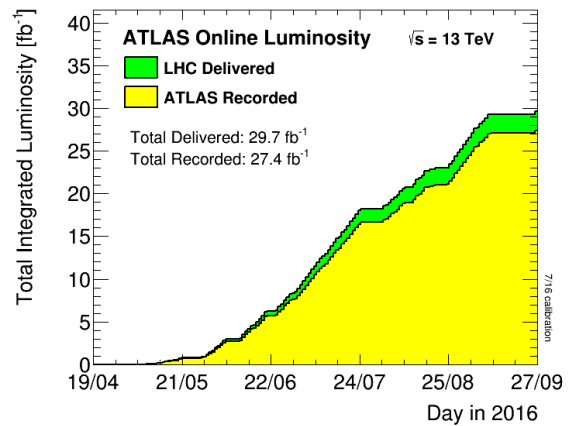


Figure 2.3: Comparison between integrated luminosity on LHC during the different years of operations.

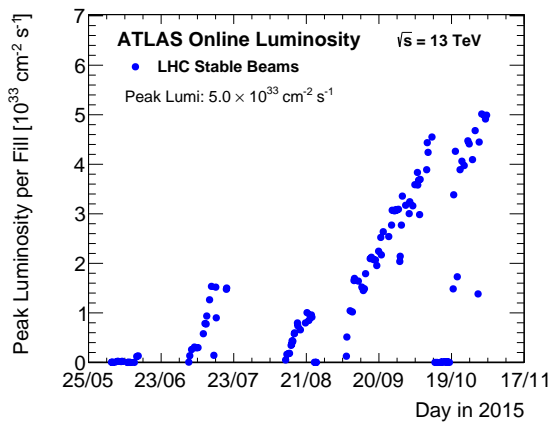


(a) Integrated luminosity recorded in 2015.

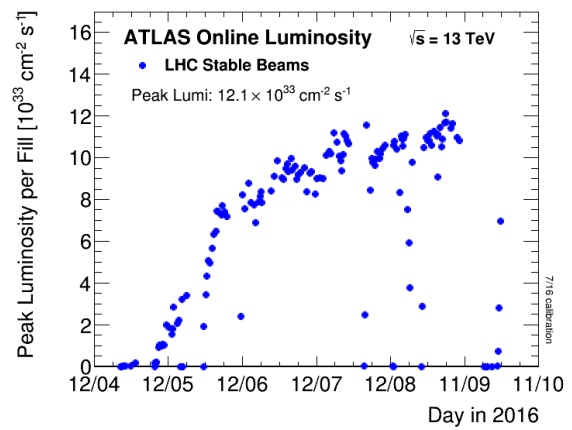


(b) Integrated luminosity recorded in 2016.

Figure 2.4: The run-II integrated luminosity as a function of time delivered by LHC (green) and recorded by ATLAS (yellow) in 2015 and 2016.



(a) Peak luminosity recorded in 2015.



(b) Peak luminosity recorded in 2016.

Figure 2.5: The LHC luminosity during run-II.

2.2 The ATLAS Detector

The ATLAS detector is one of the four main experiments recording the collisions provided by the LHC. It is 20 *m* tall and 45 *m* long and weights more than 7000 *tons*.

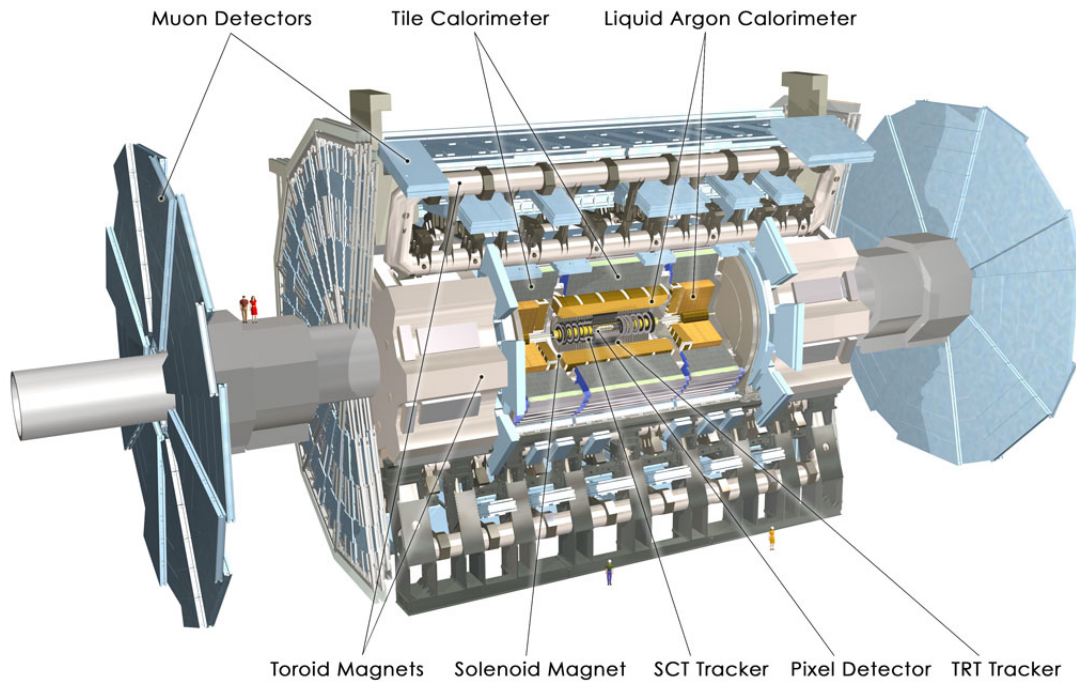


Figure 2.6: The ATLAS Detector: all the subdetectors it is composed of are shown.

The structure has a cylindrical shape centred at the interaction point with its axis along the beam line, and it is composed of several concentric subdetectors which measure different features of the particles generated in the pp collision as they fly from the center of the detector to the outer part, as shown in Figure 2.7. From the innermost to the outermost layer, the ATLAS experiment is composed of (see Figure 2.6):

- An inner tracking system to detect charged particles and measure their momentum and direction.
- A solenoidal superconducting magnet providing a uniform magnetic field along the beam axis in which the inner detector is immersed.
- An electromagnetic calorimeter to measure the energy deposited by electrons and photons.
- An hadronic calorimeter to measure the energy deposited by hadrons.
- A muon spectrometer, that is a tracking system for the measurement of muons as they travel throughout all the detector and are the only particles reaching the outer part.
- An air-cored superconducting toroidal magnet system which provide the magnetic field to the muon spectrometer.

In the following sections details about the structure of the subdetectors are be given, as well as some insight about how they work and their performances.

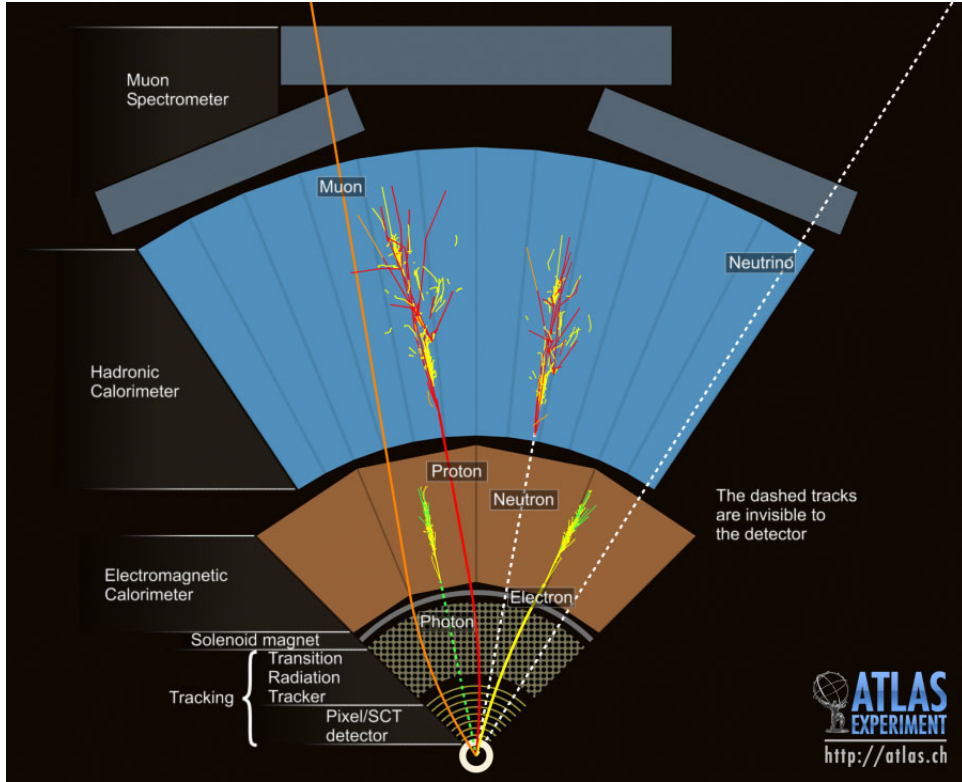


Figure 2.7: Schema of the detection of the particles produced in a proton collision while they travel through the several layers of the ATLAS detector.

2.2.1 ATLAS Coordinate System

The ATLAS coordinate system is a cartesian right-handed coordinate system, with the nominal collision point as the origin (Figure 2.8), the z axis is along the beam line and the $x - y$ plane is the plane perpendicular to the beam line.

The x axis points to the center of the LHC ring, while the y axis goes upwards. The azimuthal angle ϕ is defined around the beam axis, while the polar angle θ is the angle from the z axis in the $y - z$ plane. The θ variable is not invariant under boosts along the z axis, and so instead of the θ angle the *pseudorapidity*² η is used:

$$\eta = -\ln \left[\tan \left(\frac{\theta}{2} \right) \right]. \quad (2.3)$$

Since at an hadronic collider the real colliding particles are the partons inside the protons, we can say that the actual center of mass energy is unknown in each collision:

$$\hat{s} = x_1 \cdot x_2 \cdot s \quad (2.4)$$

where \hat{s} is the effective collision energy, x_1 and x_2 are the fractions of momentum carried by the two colliding partons and s is the colliding energy of the two protons. Because of this, the total momentum along the beam axis before the collision is unknown, while the total momentum in the transverse plane (i.e. the $x - y$ plane) is known to be zero and hence we can apply the momentum and energy conservation laws only on the transverse plane (because we know what is the initial total momentum).

²Actually the real boost-invariant variable is the *rapidity* y : $y = \frac{1}{2} \ln \frac{E+p \cos \theta}{E-p \cos \theta}$. In the ultra-relativistic limit the rapidity y can be substituted with the pseudorapidity η .

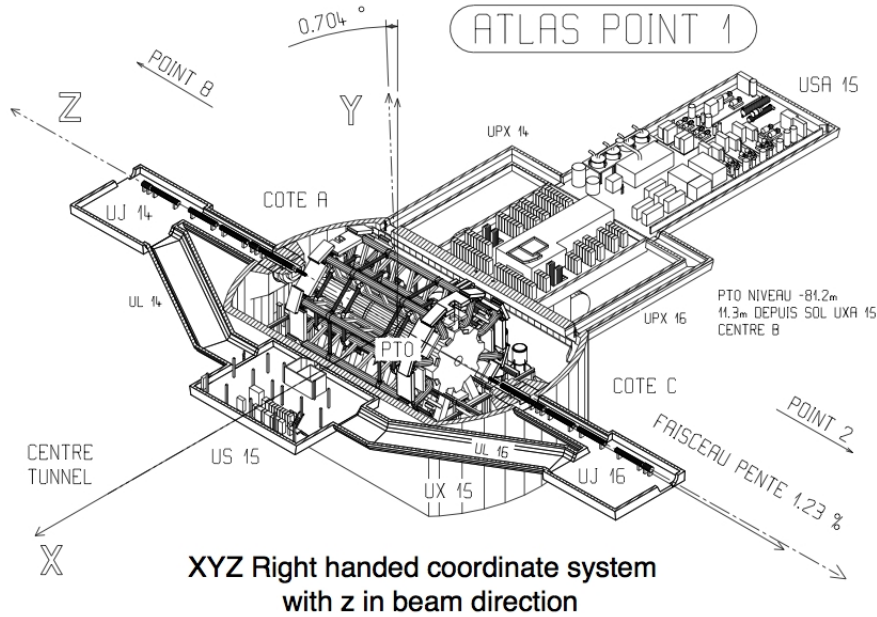


Figure 2.8: Reference system used in ATLAS.

For this reason transverse quantities are considered, and they will be denoted with the "T" subscript (e.g. p_T stands for transverse momentum, that is the projection of the momentum on the $x - y$ plane).

2.2.2 ATLAS Magnets

The ATLAS detector is equipped with two magnetic systems: a superconducting solenoid [87], providing a magnetic field to the inner tracking system, and a system of air-core superconducting toroidal magnets [88, 89] located in the outer part of the detector as shown in Figure 2.9.

The solenoid covers the central region of the detector, provides an uniform magnetic field of approximately $2T$ along the z axis bending tracks of the particles in the transverse plane in order to let the inner tracking system measure their transverse momentum.

The solenoid is located between the inner detector and the electromagnetic calorimeter and its dimensions (its width, particularly) have been optimized in order to minimize the amount of dead material (only 0.83 radiation lengths) in front of the calorimetric system.

The toroid is one of the peculiarities of the ATLAS detector: it is located outside of the calorimetric system covers the region $|\eta| < 3$ (considering all its subparts), and provides a magnetic field whose peak intensities are $3.9T$ in the central region of the detector and $4.1T$ in the forward region.

The aim of such a toroid is to have a large lever arm to improve the measurement of the muon transverse momentum, and it is built "in air" in order to minimize the muon multiple scattering within the detector.

The ATLAS double magnetic system has been designed to provide two independent measurements of the muon transverse momentum in the inner detector and in the muon spectrometer, thus ensuring good muon momentum resolution from few GeV up to the TeV scale.

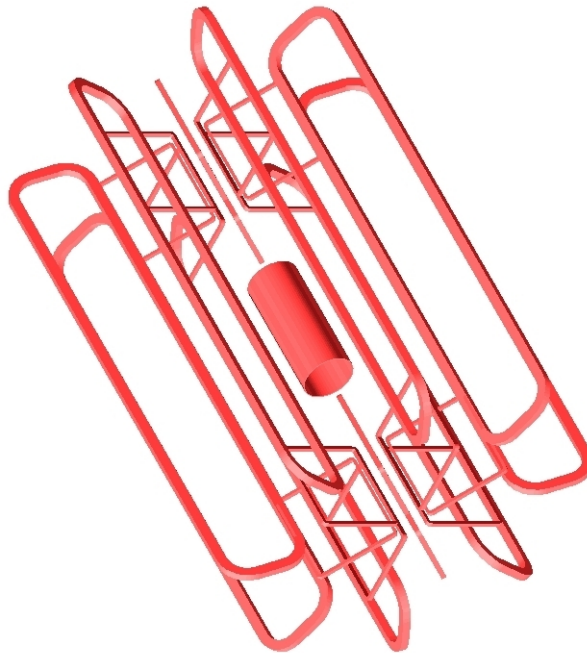


Figure 2.9: The magnetic system of the ATLAS detector: the inner cylinder is the superconducting solenoid, while the external parts are the coils of the toroid.

2.2.3 The Inner Detector

The ATLAS Inner Detector tracker (ID), shown in Figure 2.10, is composed by three concentric cylindrical subdetectors. Its axis is centred on the z axis and it is approximately 6 m long and its diameter 2.30 m , covering the region ($|\eta| < 2.5$).

The three sub-detector into the ID are:

- **Pixel Detector:** it is composed of three layers of silicon pixels. It provides high-precision track measurement, since the spatial resolution on the single hit is $\sim 10\ \mu\text{m}$ in the ϕ coordinate and $\sim 115\ \mu\text{m}$ along the z coordinate.
- **Semiconductor Tracker (SCT):** it is the second high-precision detector of the ATLAS inner tracker. It is composed of eight layers of silicon strips with a spatial resolution on the single hit of $17\ \mu\text{m}$ in ϕ and $580\ \mu\text{m}$ along z . The Pixel Detector and the Semiconductor Tracker together provide on average eight high-precision hits per track.
- **Transition Radiation Tracker (TRT):** it is composed of straw tubes chambers. The resolution of such a detector is lower than the previous one ($\sim 130\ \mu\text{m}$ per straw), but it is compensated by the high number of points per track (36 on average) that it can provide.

The aim of the ATLAS ID is to measure the tracks of the charged particles produced in the pp collision and all the related features: p_T , η , ϕ , the eventual secondary vertexes due to long-lived particles.

The momentum is measured by measuring the track curvature in the magnetic field provided by the superconducting solenoid described in the previous section. To estimate the expected resolution the *sagitta method* can be used: the magnetic field bends the trajectory of the charged particles in the ϕ coordinate because of Lorentz's force:

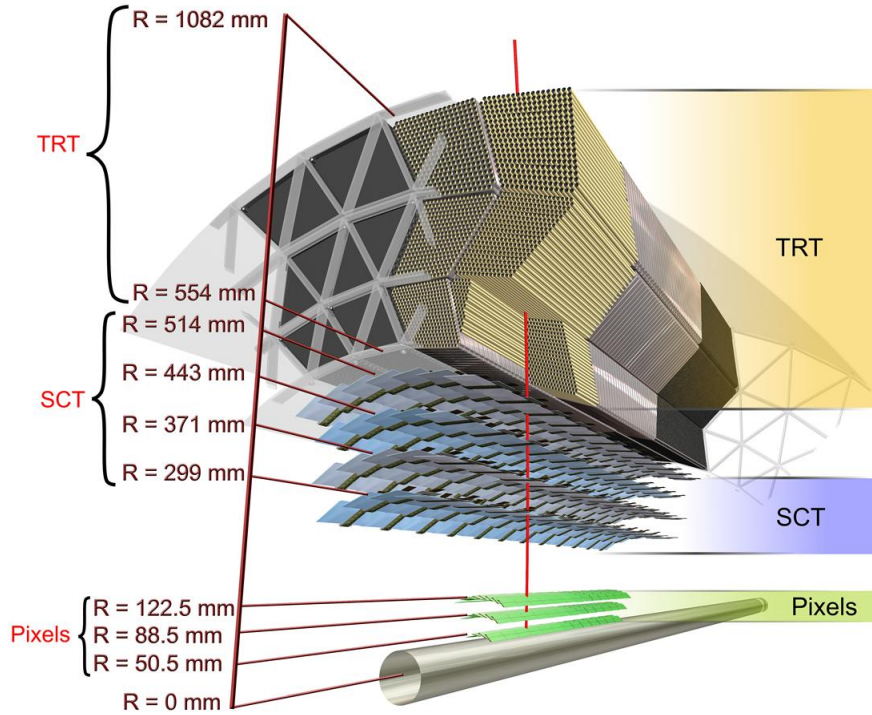


Figure 2.10: The ATLAS Inner Detector tracker: the three subdetectors (the Pixel Detector, the Semiconductor Tracker and the Transition Radiation Tracker) are shown as well as their radial dimensions.

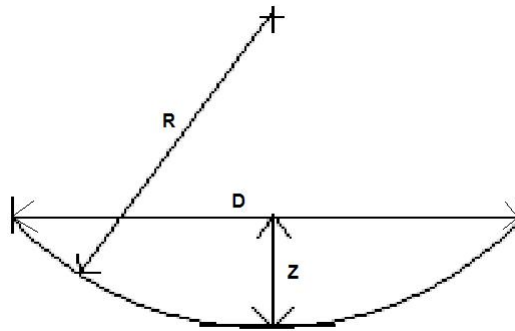


Figure 2.11: The sagitta of a track is the maximum distance between the track itself (that is an arc of a circle) and the straight segment having the same starting and ending points.

$$\vec{F}_L = q\vec{v} \times \vec{B} \quad (2.5)$$

where q is the charge of the particle, \vec{v} is its velocity and \vec{B} is the magnetic field. The resolution of the momentum measurement depends on many detector-related parameters:

$$\frac{\Delta p}{p^2} = \frac{8}{0.3 \cdot B \cdot L^2} \Delta s \quad (2.6)$$

where B is the magnetic field expressed in Tesla, L is the length of the reconstructed track expressed in meters, while Δs is (see Figure 2.11):

$$\Delta s = \frac{\epsilon}{8} \sqrt{\frac{720}{N+4}} \quad (2.7)$$

where N is the number of measured points on the track and ϵ is the resolution on the measurement of the points.

From formulas 2.7 and 2.6 it is possible to see how it is crucial to have a strong magnetic field, an high number of points per track and a good spatial resolution on these points in order to have a good resolution on the track p_T .

2.2.4 The Calorimetric System

In an high-energy physics experiment the calorimeters are used to measure the energy of photons, electrons (the electromagnetic calorimeter), hadronic jets (hadronic calorimeter) and the missing E_T (due to undetected particles like neutrinos) which is measured thanks to the tightness of the calorimetric system.

The ATLAS calorimeter has a cylindrical shape centered around the interaction point with its axis lying on the ATLAS z axis. It is long about 13 m and the external radii of the electromagnetic and hadronic calorimeters are 2.25 m and 4.25 m respectively.

The ATLAS calorimeters are represented in Figure 2.12 and the absorption lengths as a function of η are shown in Figure 2.13.

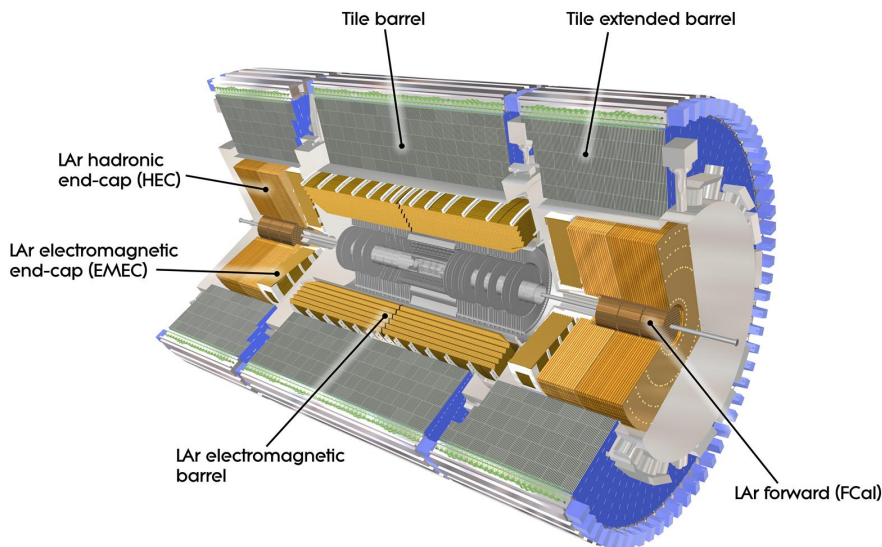


Figure 2.12: The ATLAS calorimetric system: the electromagnetic calorimeter made of liquid Argon and Lead and the hadronic calorimeter, whose composition varies as a function of η .

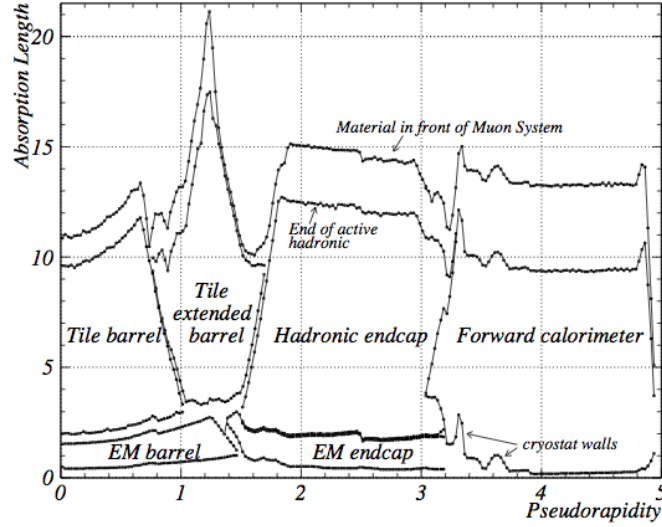


Figure 2.13: Amount of material in terms of absorption length in the ATLAS calorimetric system as a function of η .

The Electromagnetic Calorimeter

The Electromagnetic Calorimeter of the ATLAS experiment covers the region up to $|\eta| < 3.2$. The structure of the Electromagnetic Calorimeter has a special feature, how you can see in Figure 2.14: it has an accordion structure made of lead (whose thickness varies as a function of η in order to maximise the energy resolution) which is immersed in liquid Argon, which is the active material of the calorimeter. This structure confers to the calorimeter very high acceptance and symmetry in the ϕ coordinate.

In the central region $|\eta| < 2.5$ the radial coordinate the electromagnetic calorimeter has three sampling channels in order to maximize particle identification power (see Figure 2.14).

The calorimeter is segmented in cells of variable dimensions as a function of η as well as its thickness ($> 24X_0$ in the central region and $> 26X_0$ in the forward region): in the central region the segmentation is $\Delta\eta \times \Delta\phi = 0.025 \times 0.025$.

The ATLAS EM calorimeter energy resolution is parametrized as:

$$\frac{\Delta E}{E} = \frac{10\%}{\sqrt{E[\text{GeV}]}} \oplus 1\% \quad (2.8)$$

Where 10% is the sampling term and 1% is the constant inter-calibration term. The η resolution is:

$$\frac{40 \text{ mrad}}{\sqrt{E[\text{GeV}]}} \quad (2.9)$$

The Hadronic Calorimeter

The Hadronic Calorimeter covers the region $|\eta| < 4.5$, and it is realized with a variety of techniques as a function of η like it is possible to check in Figure 2.12.

The central region ($|\eta| < 1.7$) it is made of alternating layers of iron (used as absorber) and scintillating tiles as active material, and its thickness offers about 10 interactions lengths λ at $\eta = 0$. It is segmented in $\Delta\eta \times \Delta\phi = 0.1 \times 0.1$ pseudo-projective towers pointing to the interaction point.

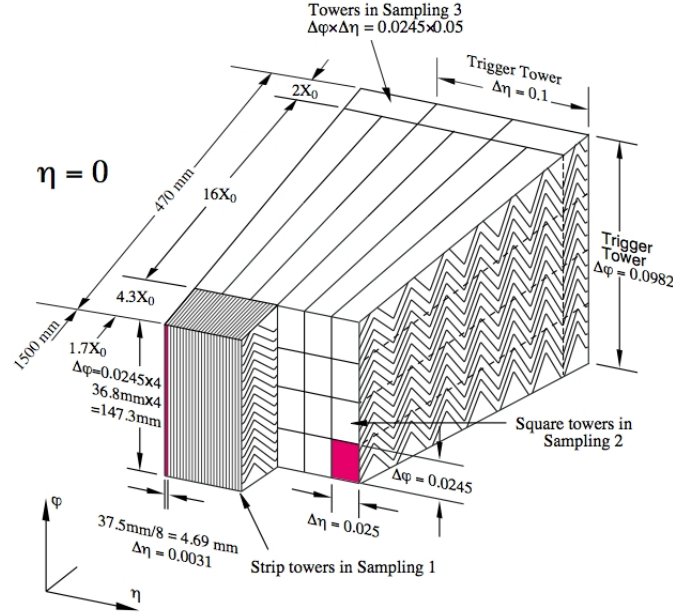


Figure 2.14: The accordion structure of the electromagnetic calorimeter and its radial segmentation.

The "endcap" region ($1.7 < |\eta| < 3.1$) is equipped with a liquid Argon and lead, as the Electromagnetic Calorimeter, while the forward region ($3.1 < |\eta| < 4.5$) is equipped with liquid Argon, but the accordion structure is replaced by a concentric rods and tubes made of copper. This variety of materials and structures is due to the different radiation hardness required in the different parts of the detector.

2.2.5 The Muon Spectrometer

The ATLAS Muon Spectrometer (MS) is instrumented with both trigger and high-precision chambers immersed in the magnetic field provided by the toroidal magnets which bends the particles along the η coordinate, and it allows to measure the muons p_T in the region $|\eta| < 2.7$ using the sagitta method described in section 2.2.3. Here the length of the lever arm plays a leading role on the p_T resolution. The MS is shown in Figure 2.15.

The chambers used to reconstruct the muon track are of several types depending on the η region, in order to face the different rate conditions present in the different parts of the detector. In the central region ($|\eta| < 2$) Monitored Drift Tubes (MDTs) are used. The MTD chambers are composed of aluminium tubes of 30 mm diameter and 400 μm thickness, with a 50 μm diameter central wire. The tubes are filled with a mixture of Argon and CO_2 at high pressure (3 bars), and each tube has a spatial resolution of 80 μm .

At higher pseudo-rapidity ($2 < |\eta| < 2.7$) the higher granularity of the Cathode Strip Chambers (CSC) are used. CSC chambers are multiwire proportional chambers in which the readout is performed using strips forming a grid on the cathode plane in both orthogonal and parallel direction with respect to the wire. The spatial resolution of the CSC is about 60 μm .

As shown in Figure 2.15, in the central region the MS is arranged on a three layer –or stations– cylindrical structure which radii are 5, 7.5 and 10 m; while in the forward region the detectors are arranged vertically, forming four disks at 7, 10, 14 and 21 – 23 m from the interaction point.

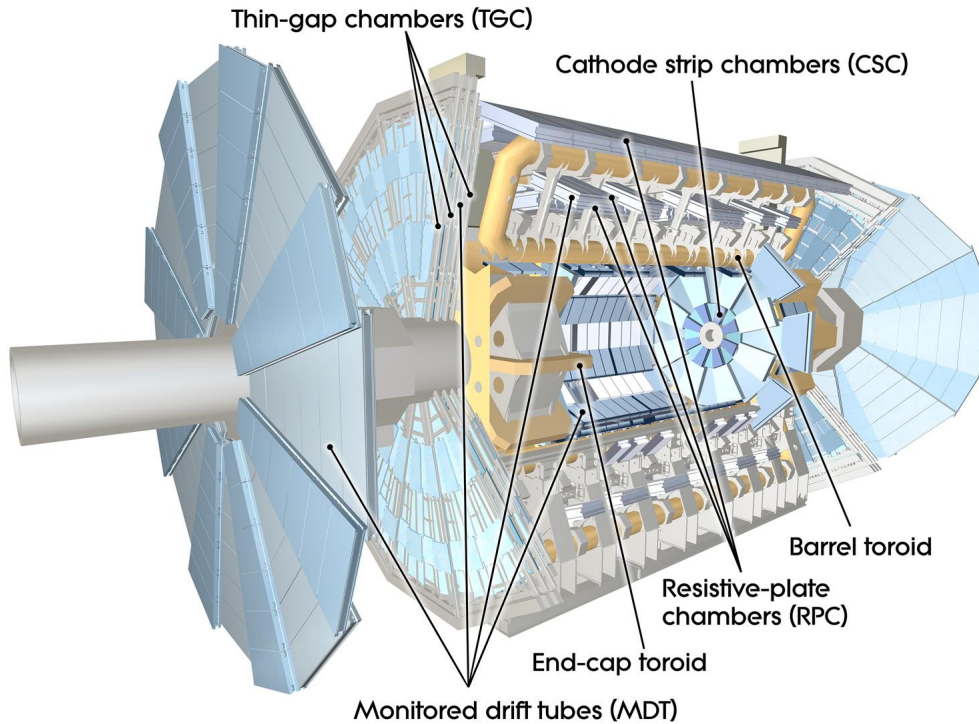


Figure 2.15: The ATLAS Muon Spectrometer.

The other chambers installed on the spectrometer are used for the trigger (see next section for details). The chambers used for the muon trigger are Resistive Plate Chambers (RPC) in the central region ($|\eta| < 1.05$) and Thin Gas Chambers (TGC) in the forward region.

These detectors provide very high time resolution ($\mathcal{O}(\text{ns})$) even if the spatial resolution is not so high ($\mathcal{O}(\text{cm})$).

The spectrometer has been designed to measure the muon p_T up to 1TeV with an error of less than 10%; this feature was required to optimize the Higgs boson discovery potential.

2.2.6 The ATLAS Trigger

The LHC is designed to provide collisions at a frequency of 40MHz and, since the average dimension of an ATLAS event is $\sim 1.5\text{MB}$, a recording rate of $\sim 60\text{TB}$ per second would be needed, while the current technology allows to record data at about 300MB/s . To deal with this environment and knowing that the interesting physics at LHC occurs at very low rate, as shown in Figure 2.17, the events to be recorded can be selected without losing the relevant information.

This selection is performed on-line by the ATLAS trigger and data acquisition system [90]. The ATLAS trigger is designed to rapidly inspect the events detected by the ATLAS detector and choose whether record or discard the event after having compared its main features with a set of predefined thresholds contained in the trigger menu. In case that the trigger decides to discard an event, then the event is not recorded and lost forever.

The ATLAS trigger system has a three level structure: each level refines the measurements of the previous level introducing also new selection criteria and combining the information from different subdetectors, as shown in Figure 2.16.

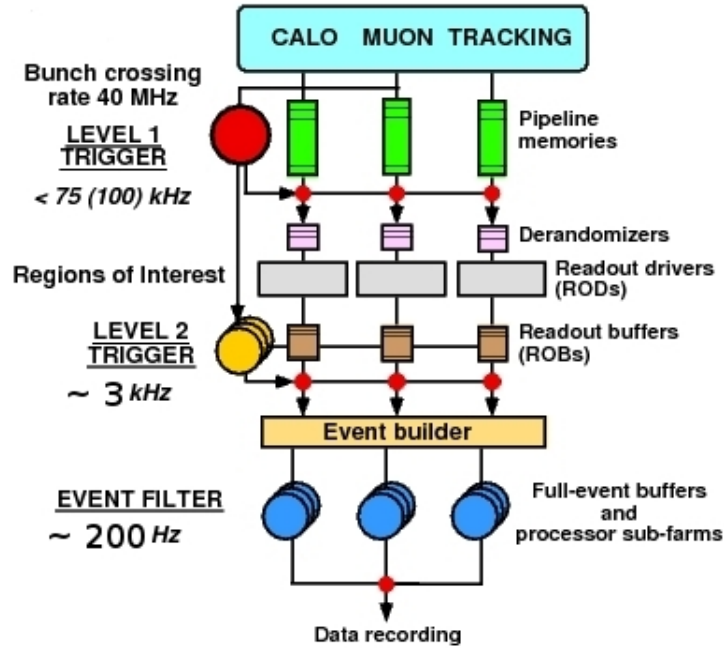


Figure 2.16: Main structure of the ATLAS trigger system: it is made of three levels, each improving the measurement of the previous levels also combining informations from different subdetectors.

The first level of the ATLAS trigger (L1 or LVL1) is completely hardware-based and it makes use of only the data collected by the calorimetric system and the muon spectrometer: the L1 trigger only looks for high- p_T muons candidates or calorimetric objects (electrons/ γ , jets) by means of fast and rough measurements performed by ad-hoc detectors in the Muon Spectrometer (RPC, TGC) and simplified object identification in the calorimeter.

Event rate and decision stages

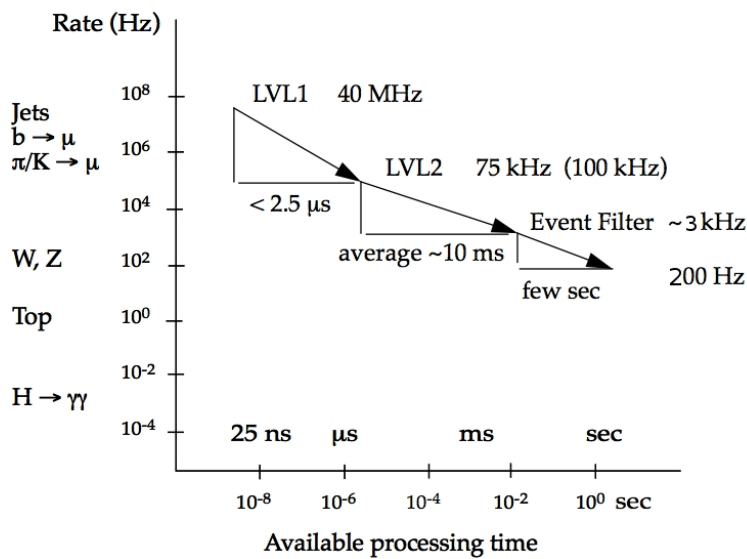


Figure 2.17: The event rate at which interesting physics occur –referred to LHC design parameters– and the processing time of each trigger level.

The L1 is designed to take a decision on the event in $2.5 \mu\text{s}$ and its output is a list of so-called *Regions of Interest* (RoI), which are $\eta - \phi$ regions of the detector in which interesting activity has been detected, and the output rate is about 100 kHz .

The second level of the ATLAS trigger (L2 or LVL2) is completely software-based. It takes as input the RoIs provided by the L1, and refines the measurement into these regions: data of the precision chambers are used in the Muon Spectrometer (MDT, CSC) as well as the data from the ID, while the measurement of the calorimetric objects is refined using higher level algorithms.

Moreover the data of the different subdetectors are combined together in order to obtain better object reconstruction/identification (e.g. the ID and the MS tracks are combined for the muons, ID and calorimetric informations are combined to discriminate between electrons and photons). The L2 takes its decision in $\mathcal{O}(10\text{ms})$ and its output rate is about 3 kHz .

The third level of the ATLAS trigger (Event Filter, EF) is completely software-based and forms, together with the L2, the High Level Trigger (HLT). At this stage a full reconstruction of the detector is performed (the measurement is not restricted to the RoIs), and the algorithms run at the EF are mostly the off-line reconstruction algorithms adapted to the on-line environment. The decision of the EF is taken in $\mathcal{O}(1\text{s})$ and the output rate is about 400 Hz .

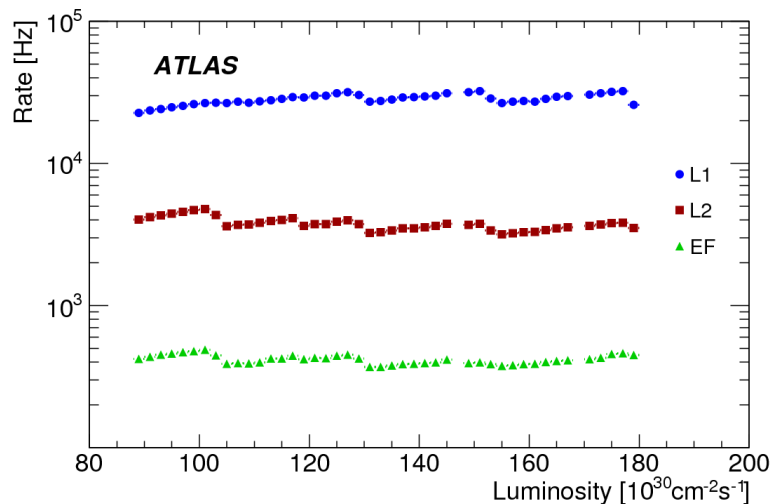


Figure 2.18: Total trigger rates at each level of the ATLAS trigger.

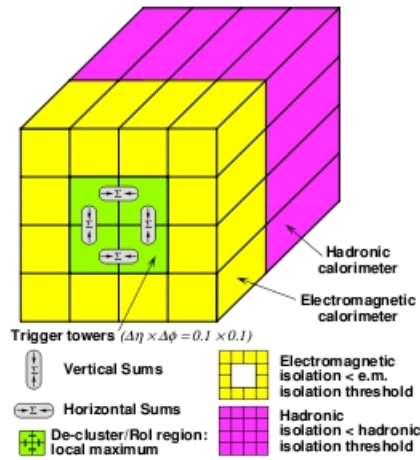


Figure 2.19: The L1 trigger for calorimetric objects in the Electromagnetic Calorimeter: the green area represents the RoI cluster, the yellow area is the region used for the isolation requirements, and the pink area is the region used for the hadronic isolation.

Figure 2.18 shows the total trigger rate for all the three levels as a function of the instantaneous luminosity: how can be seen the trigger rates are kept stable. This happens thanks to changes in the prescales and in the trigger menu –on-line into the ATLAS Control Room–, where higher thresholds or quality criteria on the trigger objects are required as the luminosity increases.

Electron Trigger

The electron trigger follows the three level ATLAS trigger structure, in which the measurements and the selections are refined at each stage. At the first level the electron trigger makes use only of the calorimeters, and hence no distinction between electrons and photons is possible since they are both identified as "calorimetric objects". In particular the L1 trigger measurement is a real calorimetric measurement even if it is done with reduced granularity, represented in Figure 2.19:

Once a relevant amount of energy is detected, the total energy in a little 2×2 cluster is measured (green area), and the isolation with respect to electromagnetic (yellow area) and hadronic activity (pink area, e.g. due to electrons coming from heavy quark decay) is computed. If these three parameters (E_T , electromagnetic and hadronic isolation) fulfil the requirements, then the electromagnetic calorimeter is accepted as a good calorimetric object and its RoI is propagated to the L2.

The L2 trigger basically refines the calorimetric measurement, accessing the full granularity of the calorimeters and studying the shape of the energy deposit (e.g. π^0/γ separation), and includes the data of the inner tracking system. At this level a "calorimetric object" may become an electron if an ID track consistent with it is found. Since the measurements are more precise at this level, tighter conditions on the quality and the kinematic features of the electron candidates can be required.

At the end of the chain the EF further refines the measurements performed at the L2 on the electron candidates, running algorithms very similar to the off-line ones and having access to the data of all the subdetectors with full granularity.

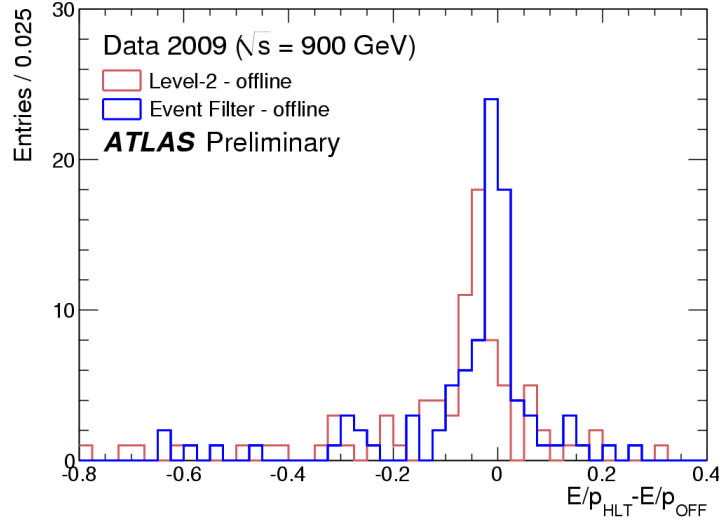


Figure 2.20: E/p distribution found by the HLT and the off-line for the electron trigger. The distributions are shown for L2 and EF separately.

The distribution of the difference between the off-line and the value measured at different trigger levels of the E/p variables for electrons is shown in Figure 2.20. This shows how the EF measurement (blue line) is better than the L2 measurement (red line), since the former is allowed to use reconstruction algorithms very similar to the off-line ones thanks to the large processing time available (see Figure 2.17), while the latter has to rely on simplified algorithms.

Muon Trigger

The L1 muon trigger relies on the temporal and geometric correlation of the hits left by a muon on the different layers of RPC detectors installed in the muon spectrometer, as shown in Figure 2.21.

When a muon coming from the interaction point crosses the RPC detectors, it leaves hits on each of them: starting from the hit on the central station (also known as *pivot* plane, RPC2 in Figure 2.21) a "correlation window" (several windows are opened for several p_T thresholds) is opened on the RPC1 layer.

If a good hit (i.e. hits in both η and ϕ and in time with the hit on the pivot plane) is found on the RPC1 layer then a low- p_T muon candidate is found. The same algorithm is applied using the RPC3 plane to look for high- p_T muon candidates. Once a muon candidate is found, the RoI is propagated to the L2.

At the L2 the muon track is reconstructed for the first time: there are algorithms which reconstruct the muon tracks in the ID and in the MS separately and then combine them in order to determine of p_T , η and ϕ . At this level the p_T measurement is not done by a fit, but *look-up tables* are used: the p_T estimation is done starting from the relation

$$\frac{1}{s} = A_0 \cdot p_T + A_1 \quad (2.10)$$

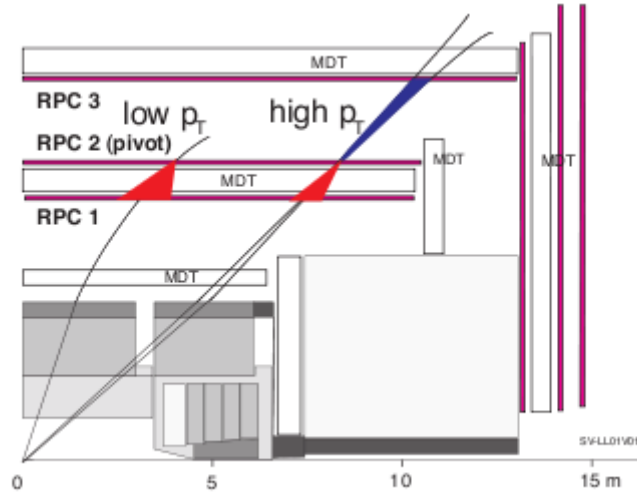


Figure 2.21: L1 muon trigger algorithm: a muon coming from the interaction point leaves hits on the three layers of RPC detectors installed in the muon spectrometer. The position of the different hits is correlated as a function of the muon p_T .

where s is the sagitta of the muon track and A_0 and A_1 are two constant values needed to take into account the magnetic field and the energy loss in the calorimeters respectively. A look-up table is basically a table whose columns and rows represent the $\eta - \phi$ segmentation of the ATLAS detector, and in each cell a (A_0, A_1) pair is contained. For each muon candidate, given η , ϕ and s , a fast estimation of the p_T is possible. This method is used since at the L2 there is not enough time to perform a real fit to precisely measure the track p_T . Once the full track is reconstructed (from the ID to the MS), the calorimetric activity around it is measured, in order to apply the isolation requirements.

At the EF the muon reconstruction algorithms perform again the operations performed by the L2 algorithms, but now the full detector with its full granularity can be accessed, and a real fit of the muon track is performed.

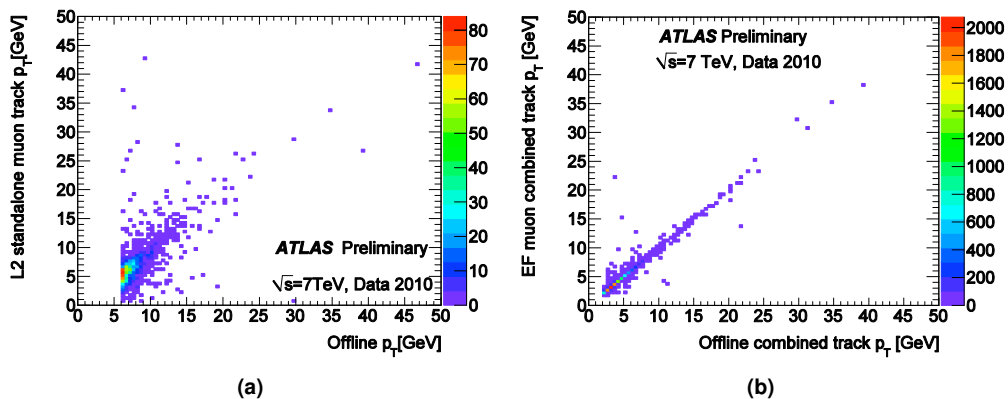


Figure 2.22: Correlation between the muon p_T reconstructed at several trigger levels (level 2 in (a) and event filter in (b)) and the off-line reconstruction.

Figure 2.22 shows the correlation between the muon p_T reconstructed at different trigger levels and the off-line reconstruction: in Figure 2.22a the correlation between the L2 stand alone p_T is shown, while in Figure 2.22b the correlation between the EF combined p_T measurement and the

off-line one is shown.

As can be seen the EF measurement is much more accurate and precise compared to the one performed at L2. The corresponding plot for L1 is not shown since at L1 the muon p_T is not really measured, but, as explained above, only a threshold is available.

2.2.7 Monte Carlo Generators in ATLAS Event Simulation

Adding to the real events recorded by the ATLAS detector, the use of the Monte Carlo simulations is essential for the different physics programs.

During the preparation phase of an experiment, simulation provides the environment to develop and understand the detector, to develop analysis strategies, to estimate the sensitivity to different physics processes, to develop and validate object reconstruction algorithms, to optimize the trigger menus, and so on. During the running phase of an experiment, simulation is used to compare predictions of theoretical models against the real data. The event simulation and reconstruction is performed in the Athena framework[52], who is in charge of the following processes:

- *Event generation*: corresponds to the phase of proton-proton (pp) collision events generation. It takes care of the production and decay of particles in a given process. Several event generators are available.
- *Detector simulation*: is the simulation of interactions between the generated particles and the detector.
- *Digitization*: corresponds to the simulation of the detector readout, or better says, the conversion of energy deposited in the detector to times, currents and voltages for readout electronics. The output format of the simulation is identical to the real detector output format.
- *Reconstruction*: in this step a set of object reconstruction algorithms are applied. These algorithms are applied to both simulation and real data in exactly the same way. This phase is better described in Chapter ??.

There are two kinds of Monte Carlo (MC) generators, the so-called *multi-purpose MC* generators which handle all the event generation steps, and the *specialized MC* generators that handle only some specific steps of the MC generation chain.

The kinematic distributions for a given process may differ between different Monte Carlo generators. Depending on the problem under study, one generator may be more suitable than others and the comparison between different generators is always encouraged.

The Monte Carlo generators used into this Higgs search analysis are listed below, together with their main characteristics.

- *Pythia*: is a multi-purpose Monte Carlo generator for event simulation in pp , e^+e^- and ep colliders. Pythia simulates non-diffractive proton-proton collisions using a $2 \rightarrow n$ ($n \leq 3$) matrix element at LO to model the hard subprocess, and uses p_T -ordered parton showers to model additional radiation in the leading-logarithmic approximation. The hadronisation model used is the Lund string model. MPIs are also simulated[48].
- *Herwig*: is a general purpose Monte Carlo generator, which uses a LO $2 \rightarrow 2$ matrix element supplemented with angular-ordered parton showers in the leading-logarithm approximation. The cluster model is used for the hadronisation. The underline is modelled using an external package called Jimmy [49, 50, 51].

- Herwig++: is based on the event generator Herwig, but redesigned in the C++ programming language (Herwig is programmed in Fortran). The generator contains a few modelling improvements. It also uses angular-ordered parton showers, but with an updated evolution variable and a better phase space treatment. The cluster model is also used for hadronisation. The UE are described using a multiple partonic interactions model[53, 54].
- Alpgen: is a specialized tree matrix-element generator for hard multi-parton processes $2 \rightarrow n$ ($n \leq 9$) in hadronic collisions. It is interfaced to Herwig to produce angular-ordered parton showers in leading-logarithmic approximation or Pythia to produce p_T -ordered parton showers. Parton showers are matched to the matrix element with the MLM matching scheme. The hadronisation process is simulated with Herwig, using the cluster model. MPIs are modelled using Jimmy[55].
- MC@NLO: is a Fortran package which allows to match NLO QCD matrix elements consistently into a parton shower framework. In order to reproduce the NLO corrections fully, some of the configurations have negative weights. The shower and hadronization can be implemented using Herwig or Herwig++. The NLO expansion of the hard emissions needs to be evaluated for each showering program used[56, 57].
- Powheg: is a parton-level Monte Carlo generator. It allows to interface NLO calculations with a parton shower framework. It generates the hardest emission first, with NLO accuracy independently of the parton shower generator used. It can be interfaced with several parton shower generators as Herwig, Pythia, etc[58].

Chapter 3

Physics Objects Reconstruction in ATLAS

The outputs of the digitization process of the detector signals generated by the particles produced in real/simulated pp collisions are processed by a serie of algorithms in order to built physics objects up. This step is not done in real time and thus is known as off-line event reconstruction. The result is a set of physics objects with four-momenta that can be used directly in physics analyses. The reconstruction of tracks, primary vertices, electrons, muons, neutrinos and jets as well as the trigger chains used in the different analyses of this thesis will be described in the following sections.

3.1 Data quality

The events where some of the relevant ATLAS subdetectors were not properly operational can not be used for physics analyses. In ATLAS, each subsystem is in charge of setting its own data quality and integrity flags for each Luminosity Block (LB) ¹. This information can be used to create a list of LB usable for analyses, called Good Runs List (GRL). Each analysis uses a GRL to reject those events affected by issues in the relevant subdetectors.

A special case during the 2011 created an exception in the data quality assessment was the LAr hole issue. The information of six front end boards in the LAr calorimeter was lost due to a problem with their controller board. It created a "hole" in the detector data collection that affected approximately 948.6 pb^{-1} of data. In release 16 of the ATLAS software, this issue was not modelled in the simulation. Instead of removing all the events affected, as would have been the procedure using a GRL, it was decided to remove only those events where the object reconstruction was affected by the issue. In release 17 of the ATLAS software, the issue was simulated in the Monte Carlo samples used. Therefore, no correction for the acceptance loss was needed.

3.2 ID Tracks

Tracks represent the trajectory of charged particles inside the detector. They are reconstructed using information from the ID, documented in Section 2.2.3. A precise track reconstruction is important to achieve a high vertex reconstruction efficiency and high precision in the particle momentum measurement.

In ATLAS, tracks are parametrized by five parameters defined at the track's trajectory point closest (unless otherwise stated) to the center of the beam-spot: d_0 , and z_0 (radial and longitudinal impact parameters), ϕ and θ (azimuthal and polar angle) and $\frac{\text{sign}(q)}{p_t}$ (Figure 3.1). The beam spot

¹A luminosity block is the unit of time for data-taking and lasts about two minutes.

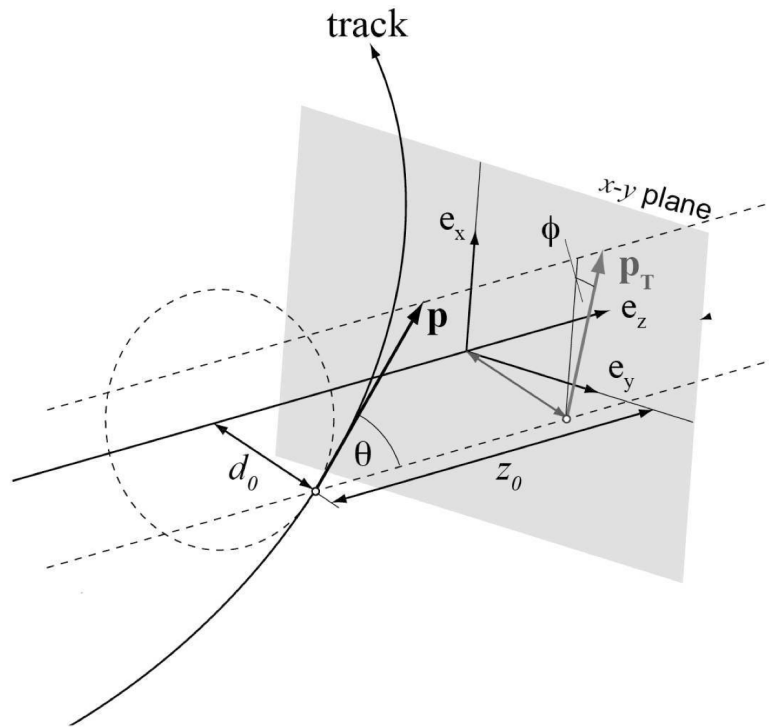


Figure 3.1: A track can be parametrized at one given point by its position, transverse momentum and charge. The position at any other point can be calculated if the magnetic field and the detector material is known.

is the region where both beams interact, which does not correspond exactly to the geometrical center of the ATLAS detector.

Lets summarized the three main steps of the track reconstruction[59]:

- **Track finding:** assignment of ID hits to track candidates.
- **Track fit:** determination of track parameters and their errors. Provides track's fit quality variables.
- **Test of track hypothesis:** check the track candidate quality and the overlap with others tracks candidates.

In ATLAS the track finding and fit steps are merged. The hits from the pixel detector and the SCT are transformed into three-dimensional space points. Just after, the inside-out algorithm[60] take action. It consists in adding the three-dimensional space points one by one moving away from the interaction point to form a "road". It uses a combinatorial Kalman filter[61]. The Kalman filter algorithm adds three-dimensional space points iteratively and fits simultaneously the track candidate. Cuts on the quality of the fit are applied to eliminate poor quality tracks and to avoid overlaps with others tracks candidates. The selected tracks are extended into the TRT and fitted again to get the final values of the track parameters.

The mean energy loss in the detector material, the multiple scattering, the Bremsstrahlung effect and the changes in the magnetic field along the track trajectory are taken into account during the track fitting process. The inside-out algorithm provides the best reconstruction efficiency of primary charged particles directly produced in a pp collision or from decays or interaction of particles with a short lifetime ($< 3 \times 10^{-11}$ s).

In order to better reconstruct secondary charged particles, produced in the interaction of primaries (with a lifetime $> 3 \times 10^{-11}$ s), or conversion candidates an additional track finding algorithm, called outside-in, is applied. The track finding process starts with TRT segments not used by the inside-out algorithm. They are then extended to the SCT and pixel detector.

During 2011 data taking the detector occupancy increased significantly. Under these conditions the possibility of having incorrect hits assignments and more fake tracks from random hit combinations increase. The performance of the track reconstruction at ATLAS has been recently studied in the 2011 high pile-up environment[61].

The efficiency remains almost unchanged. However, the fraction of combinatorial fake tracks increases with the average number of pp collisions per bunch crossing at the time of the recorded event $\langle \mu \rangle$. The figure 3.2 shows the comparison of the mean number of interactions during Run-I and Run-II operations.

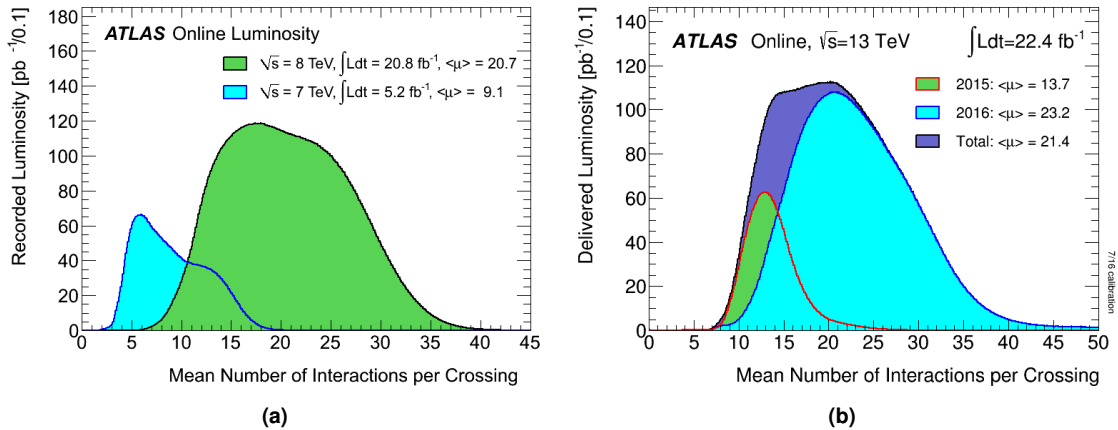


Figure 3.2: Shown is the luminosity-weighted distribution of the mean number of interactions per crossing for the (a) Run-I and (b) Run-II pp collision data recorded.

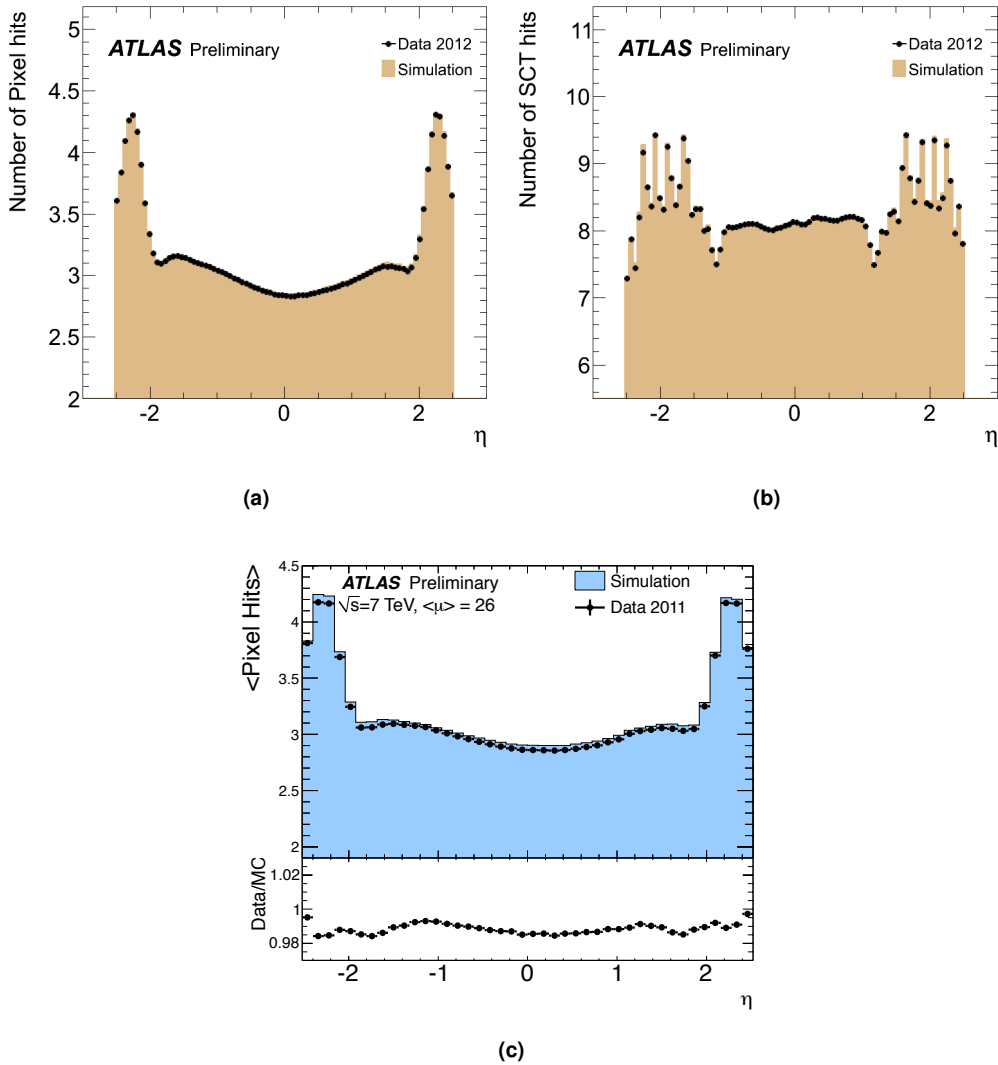


Figure 3.3: (a) 2012 data and simulation comparison of Pixel hits vs η , (b) 2012 data and simulation comparison of SCT hits vs η and (c) the number of pixel, SCT and TRT hits as a function of η for tracks with 2011 data.

3.3 Primary vertices

Two different kinds of vertices can be present in an event:

- **the primary vertices (PV)** which correspond to the collision point of beam particles. They are characterized by having many associated tracks-particle, thus a high track multiplicity. In a selected event usually there is one hard-scatter PV, while the rest are associated, by conventions, to pile-up interactions.
- **the secondary vertices** correspond to decay of short-lived particles, which decay at a measurable distance from the PVs. The track multiplicity for secondary vertices is lower.

In general, the PV reconstruction is done in three steps:

- **vertex finding:** assignment of reconstructed tracks to PV candidates.

- **vertex fit:** reconstruction of the PV position, calculation of its error matrix, estimation of the fit quality and optional refit of the associated track's parameters to constrain them to originate from the corresponding PV and not from the beam spot.
- **est of vertex hypothesis:** check the vertex candidate quality and the overlaps with others vertices candidates.

Into the ATLAS experiment, the PV reconstruction is done using an iterative vertex finding algorithm[62]. First, a vertex seed is found by looking for the maximum of the z_0 tracks distribution. An iterative χ^2 fit is used to fit the seed and the surrounding tracks. The matrix errors of the tracks are properly taken into account during the vertex fit. Tracks incompatible with the PV candidate (displaced by more than 7σ from the vertex) are used to seed a new PV. This procedure is repeated until no unassociated tracks are left or no additional vertex can be found. PVs are required to have at least two associated tracks. The same track can be associated to multiple vertices. The PV with the largest sum of squared transverse momenta $\sum p_T^2$ of the tracks is chosen as the hard-scatter PV. Figures 3.3 and 3.4 show the performance of ATLAS relative to reconstructions tracks, pixel and vertex detector-variables.

In high pile-up environment, the increasing number of fake tracks increases the probability to reconstruct a fake vertex. Furthermore, the common presence of nearby interactions increases the probability of reconstructing only one vertex out of several. Studies using 2011 data have shown that the PV efficiency reconstruction decreases with increasing $\langle \mu \rangle$ [61]. Some quality criteria are applied to the tracks used in the PV reconstruction process. They vary from one analysis to the other.

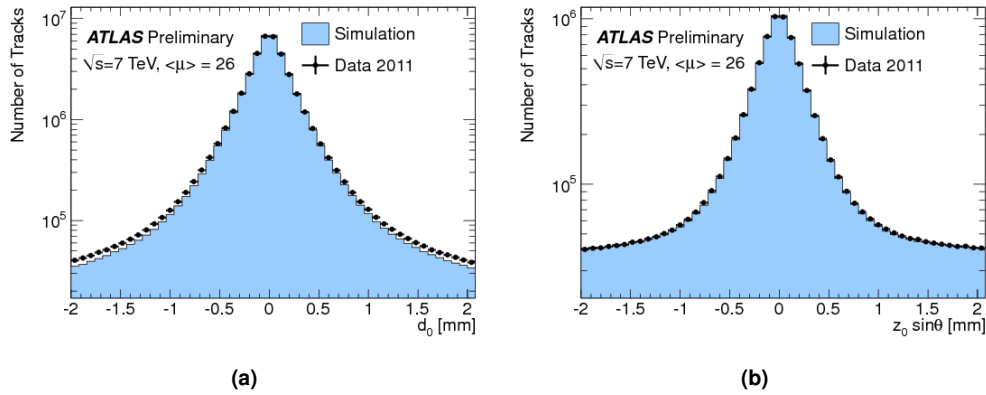


Figure 3.4: (a) The impact parameter distributions with respect to the primary vertex of tracks and the corresponding simulation sample, (b) the impact parameter distributions with respect to the primary vertex of tracks and the corresponding simulation sample. The simulation in each of the plots has been reweighted to match the p_T spectrum of the data.

3.4 Electrons

3.4.1 Electron reconstruction

The distinguishing signature of an electron is a curved track in the inner detector and a narrow shower in the EM calorimeter. Electrons can be produced in the hard-scatter interaction, but also inside jets or in photon conversions. Then, there is a probability of misclassifying narrow jets or photons as electrons. During the electron reconstruction and identification, several criteria are applied to determine if a given energy deposit and associated track were produced in the hard-scatter interaction or not. The electrons in the central region ($|\eta| < 2.47$) are reconstructed using an algorithm that combines the information from the EM calorimeter and the ID. Other algorithms reconstruct electrons in the forward region using only information from the EM calorimeter. In this thesis only electrons in the central region will be used[63]. Therefore, the reconstruction of electrons in the forward region will not be discussed[64].

Electron reconstruction in ATLAS in the central region is done using the sliding-window algorithm[65]. It searches for clusters in the middle layer of the EM calorimeter with a total $E_T > 2.5$ GeV. The window used to define the clusters has a size of 3×5 in middle layer cell units ($\Delta\eta \times \Delta\phi = 0.025 \times 0.025$). If the seeded cluster is matched to a pair of tracks originating from a reconstructed photon conversion vertex, it is tagged as a converted photon. Otherwise, if the algorithm is able to match a track from the ID with the seeded cluster, it is tagged as an electron candidate.

The matching is done in an $\Delta\eta \times \Delta\phi$ window of 0.05×0.10 , to account for bremsstrahlung losses. The track momentum is required to be compatible with the cluster energy. In case that several tracks are matched to the EM cluster, the tracks with hits in the silicon detectors are preferred and the closest in ΔR is chosen. In addition, information from the TRT can be used to enhance the separation of electron candidates from pions. The final clusters are built around the seeded clusters matched with a track, by including all cells from different EM calorimeter layers located inside a rectangle centred on the seed position. The rectangle size depends on the position in the calorimeter of the seeded clusters (barrel or endcap). The energy of the cluster is calibrated to the EM energy scale, which was derived from MC based corrections to account for energy loss in passive material, test-beam measurements, and measurements of $Z \rightarrow ee$ decays for final calibration[66, 67].

3.4.2 Electron identification

Electrons can be distinguished from hadrons since EM showers deposit most of their energy in the second layer of the EM calorimeter. The width of electron showers is narrower than for hadrons. The ratio of the transverse energy reconstructed in the first layer of the hadronic calorimeter to the transverse energy reconstructed in the EM calorimeter, known as **hadronic leakage** or R_{had} , is smaller for electrons than for hadrons. Also the ratio of the energy reconstructed in the EM calorimeter to the track momentum $\frac{E}{p}$ can be used as a discriminant variable, since it is smaller for charged hadrons (Figure 3.5).

The most difficult task is to distinguish electrons from π^0 's and η 's. They decay into two photons which form two close EM showers indistinguishable in the second EM calorimeter layer. In this case, the first layer of the EM calorimeter can be used due to its high granularity, to identify the two maximum in the π^0 or η shower corresponding to the two photons.

In ATLAS, there are six different series of cuts used in the electron identification process that provide good separation between electrons and jets faking electrons: *loose*, *loose++*, *medium*, *medium++*, *tight* and *tight++*[65].

In general, each cut adds to the previous some additional requirements. The "++" menu was incorporated starting from release 17, in order to accomplish the trigger bandwidth restrictions for high luminosity. The discriminating variables used are defined using calorimeter and ID information.

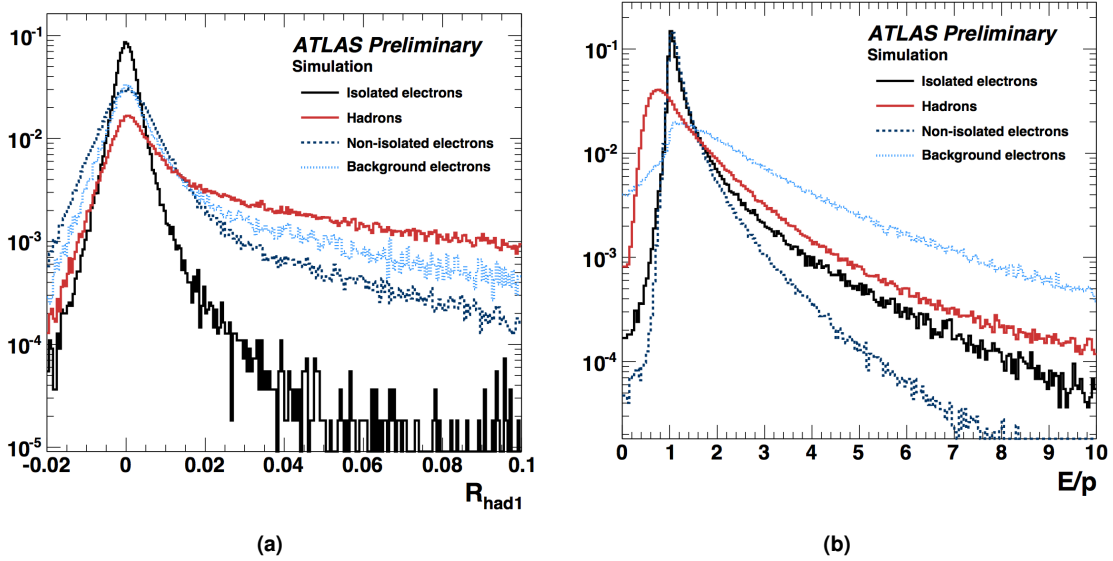


Figure 3.5: Example of some electron identification variables: (a) "hadronic leakage" R_{had} , (b) ratio of the energy reconstructed in the EM calorimeter to the track momentum $\frac{E}{p}$.

- **Loose:** is based on calorimeter information only. It requires electron candidates with $|\eta| < 2.47$ with low hadronic leakage and cuts on shower shape variables, derived from the energy deposits in the second layer of the EM calorimeter. The loose criteria provides a high identification efficiency (close to 95%). But the expected background rejection (the jet rejection), is low, about 500, i.e. one in 500 jets will pass the Loose selection.
- **Loose++:** adds additional cuts to the loose selection. It adds requirements related to the matched track: at least 1 hit in the pixel detector, at least 7 hits from both the pixel and SCT and the distance in $|\eta|$ between the cluster and the extrapolated track in the first EM layer has to be smaller than 0.015. Its efficiency, measured in $Z \rightarrow ee$ events, is close to the loose one (93% – 95%) with a higher expected rejection of about 5000[68].
- **Medium:** adds additional criteria related to the shower shape calculated using the first EM layer and to the deviation in the energies of the largest and second largest deposits in this layer, allowing discrimination against π^0 's and η 's. In addition, the absolute value of the transverse impact parameter of the track, $|d_0|$, is required to be lower than 5mm and the distance in $|\eta|$ between the cluster and the extrapolated track in the first EM layer lower than 0.01. Its efficiency is of about 88%[68] and has a rejection higher than the one achieved by the loose++ selection.
- **Medium++:** requires at least one hit in the B-layer (first pixel detector layer) to reject electrons from photon conversions. Tracks having a low fraction of high-threshold TRT hits are rejected to decrease the contamination from charged hadrons. $|\Delta\eta|$ between the cluster and extrapolated track in the first EM layer is lowered to 0.005. It has an efficiency of around 85%, with a expected rejection closer to 50000.
- **Tight:** requires that $|\Delta\phi|$ and $|\Delta\eta|$ between the cluster and the matched track has to be less than 0.02 and 0.005, respectively. A requirement on $\frac{E}{p}$ is introduced. The $|d_0|$ requirement is tightened (to be less than 1 mm), as well as the fraction of high-threshold TRT hits. The identification efficiency is around 75%, with a rejection higher than the medium++ one.
- **Tight++:** only adds asymmetric $\Delta\phi$ track-cluster matching cuts. It has an efficiency slightly better than the one for tight selection and a slightly better rejection too.

To suppress the background due to non-prompt leptons, e.g. from decays of hadrons (including heavy flavour) produced in jets, the leptons in the event are usually required to be isolated. A calorimeter isolation, a track isolation or both can be applied. The calorimeter isolation is estimated using the energy in a cone of $R = 0.2$ centred around the electron after the subtraction of the energy associated with the electron itself (**EtCone20**).

Track isolation is calculated using the scalar sum of tracks p_T in a cone of $\Delta R = 0.3$ centred around the electron without including the electron p_T itself (**PtCone30**). The calorimeter isolation variables usually include a correction for the increase in the energy of the electron in the isolation cone with electron p_T (transverse shower leakage) and for additional energy deposits from pile-up events.

3.4.3 Electron scale factors and energy corrections

The smearing or scaling of the reconstructed objects at the analysis level is a common procedure. They are used to match the object energy in simulation to the one in data, to match the object energy to a known quantity or to implement an uncertainty in the analysis. The smearing process consists in changing the object energy distribution using random numbers from a given distribution, usually a Gaussian. In the case of electrons, the EM electron cluster energy in data was corrected by applying energy scales as a function of η , ϕ and E_T to match the Z boson peak mass. They were obtained from $Z \rightarrow ee$, $J/\Psi \rightarrow ee$ or $\frac{E}{p}$ studies using isolated electrons from $W \rightarrow e\nu$. The cluster energy was smeared in Monte Carlo samples to match the energy resolution in data and to adjust the width of the Z peak.

<i>Loose</i>
Middle-layer shower shapes: R_η, w_2 Hadronic leakage: R_{had1} (R_{had} for $0.8 < \eta < 1.37$)
<i>Loose++</i>
Shower shapes: $R_\eta, R_{had1}(R_{had}), w_2, E_{ratio}, w_{s,tot}$ Track quality $ \Delta\eta < 0.015$
<i>Medium</i>
Pass <i>Loose</i> selection Strip-layer shower shapes: $w_{s,tot}, E_{ratio}$ Track quality $ \Delta\eta < 0.01$ $ d_0 < 5mm$
<i>Medium++</i>
Shower shapes as <i>Loose++</i> , but at tighter values Track quality $ \Delta\eta < 0.005$ $N_{BL} \geq 1$ for $ \eta < 2.01$ $N_{Pix} > 1$ for $ \eta > 2.01$ Loose TRT HT fraction cuts $ d_0 < 5mm$
<i>Tight</i>
Pass <i>Medium</i> selection $ \Delta\eta < 0.005$ $ d_0 < 1mm$ Track matching: $ \Delta\phi $ and E/p High TRT HT fraction $N_{BL} \geq 1$ Pass conversion bit
<i>Tight++</i>
Shower shapes as <i>Medium++</i> , but at tighter values Track quality $ \Delta\eta < 0.005$ $N_{BL} \geq 1$ for all η $N_{Pix} > 1$ for $ \eta > 2.01$ Tighter TRT HT fraction cuts $ d_0 < 1mm$ E/p requirement $ \Delta\phi $ requirement Conversion bit

Table 3.1: Summary of the variables used in the Loose, Loose++, Medium, Medium++, Tight and Tight++ operating points[69].

3.5 Muons

3.5.1 Muon reconstruction and identification

Muon reconstruction has been uploaded during Run-II [108]. Muon reconstruction is first performed independently in the ID and MS. The information from individual subdetectors is then combined to form the muon tracks that are used in physics analyses.

Muon reconstruction in the MS starts with a search for hit patterns inside each muon chamber to form segments. In each MDT chamber and nearby trigger chamber, a Hough transform is used to search for hits aligned on a trajectory in the bending plane of the detector. The MDT segments are reconstructed by performing a straight-line fit to the hits found in each layer. The RPC or TGC hits measure the coordinate orthogonal to the bending plane. Segments in the CSC detectors

are built using a separate combinatorial search in the η and ϕ detector planes.

Muon track candidates are then built by fitting together hits from segments in different layers. The algorithm used for this task performs a segment-seeded combinatorial search that starts by using as seeds the segments generated in the middle layers of the detector where more trigger hits are available. The search is then extended to use the segments from the outer and inner layers as seeds. The segments are selected using criteria based on hit multiplicity and fit quality and are matched using their relative positions and angles.

The hits associated with each track candidate are fitted using a global χ^2 fit. A track candidate is accepted if the χ^2 of the fit satisfies the selection criteria.

The combined ID–MS muon reconstruction is performed according to various algorithms based on the information provided by the ID, MS, and calorimeters. Four muon types are defined depending on which subdetectors are used in reconstruction:

- Combined (CB) muon: track reconstruction is performed independently in the ID and MS, and a combined track is formed with a global refit that uses the hits from both the ID and MS subdetectors. Most muons are reconstructed following an outside-in pattern recognition, in which the muons are first reconstructed in the MS and then extrapolated inward and matched to an ID track. An inside-out combined reconstruction, in which ID tracks are extrapolated outward and matched to MS tracks, is used as a complementary approach.
- Segment-tagged (ST) muons: a track in the ID is classified as a muon if, once extrapolated to the MS, it is associated with at least one local track segment in the MDT or CSC chambers. ST muons are used when muons cross only one layer of MS chambers, either because of their low p_T or because they fall in regions with reduced MS acceptance.
- Calorimeter-tagged (CT) muons: a track in the ID is identified as a muon if it can be matched to an energy deposit in the calorimeter compatible with a minimum-ionizing particle. This type has the lowest purity of all the muon types but it recovers acceptance in the region where the ATLAS muon spectrometer is only partially instrumented to allow for cabling and services to the calorimeters and inner detector. The identification criteria for CT muons are optimized for that region ($|\eta| < 0.1$ and a momentum range of $15 < p_T < 100 \text{ GeV}$).
- Extrapolated (ME) muons: the muon trajectory is reconstructed based only on the MS track and a loose requirement on compatibility with originating from the IP. The parameters of the muon track are defined at the interaction point, taking into account the estimated energy loss of the muon in the calorimeters. In general, the muon is required to traverse at least two layers of MS chambers to provide a track measurement, but three layers are required in the forward region. ME muons are mainly used to extend the acceptance for muon reconstruction into the region $2.5 < |\eta| < 2, 7$, which is not covered by the ID.

Muon identification is performed by applying quality requirements that suppress background, mainly from pion and kaon decays, while selecting prompt muons with high efficiency and/or guaranteeing a robust momentum measurement. Several variables offering good discrimination between prompt muons and background muon candidates are studied.

For CB tracks, the variables used in muon identification are:

- q/p significance, defined as the absolute value of the difference between the ratio of the charge and momentum of the muons measured in the ID and MS divided by the sum in quadrature of the corresponding uncertainties;
- ρ defined as the absolute value of the difference between the transverse momentum measurements in the ID and MS divided by the p_T of the combined track;
- normalized χ^2 of the combined track fit.

Four muon identification selections (*Medium, Loose, Tight and High- p_T*) are provided to address the specific needs of different physics analyses. Loose, Medium and Tight are inclusive categories in that muons identified with tighter requirements are also included in the looser categories.

Medium muons The Medium identification criteria provide the default selection for muons in ATLAS. This selection minimizes the systematic uncertainties associated with muon reconstruction and calibration. Only CB and ME tracks are used. The former are required to have ≥ 3 hits in at least two MDT layers, except for tracks in the $|\eta| < 0,1$ region, where tracks with at least one MDT layer but no more than one MDT hole layer are allowed. The latter are required to have at least three MDT/CSC layers, and are employed only in the $2.5 < |\eta| < 2,7$ region to extend the acceptance outside the ID geometrical coverage. A loose selection on the compatibility between ID and MS momentum measurements is applied to suppress the contamination due to hadrons misidentified as muons.

Loose muons The Loose identification criteria are designed to maximise the reconstruction efficiency while providing good-quality muon tracks. They are specifically optimized for reconstructing Higgs boson candidates in the four-lepton final state. All muon types are used. All CB and ME muons satisfying the Medium requirements are included in the Loose selection. CT and ST muons are restricted to the $|\eta| < 0,1$ region. In the region $|\eta| < 2,5$ about 97.5% of the Loose muons are combined muons, approximately 1.5% are CT and the remaining 1% are reconstructed as ST muons.

Tight muons Tight muons are selected to maximize the purity of muons at the cost of some efficiency. Only CB muons with hits in at least two stations of the MS and satisfying the Medium selection criteria are considered. The normalized χ^2 of the combined track fit is required to be < 8 to remove pathological tracks. A two-dimensional cut in the ρ and q/p significance variables is performed as a function of the muon p_T to ensure stronger background rejection for momenta below 20 GeV where the misidentification probability is higher.

High- p_T muons The High- p_T selection aims to maximize the momentum resolution for tracks with transverse momentum above 100 GeV . The selection is optimized for searches for high-mass Z' and W' resonances. CB muons passing the Medium selection and having at least three hits in three MS stations are selected. Specific regions of the MS where the alignment is suboptimal are vetoed as a precaution. Requiring three MS stations, while reducing the reconstruction efficiency by about 20%, improves the p_T resolution of muons above 1.5 TeV by approximately 30%.

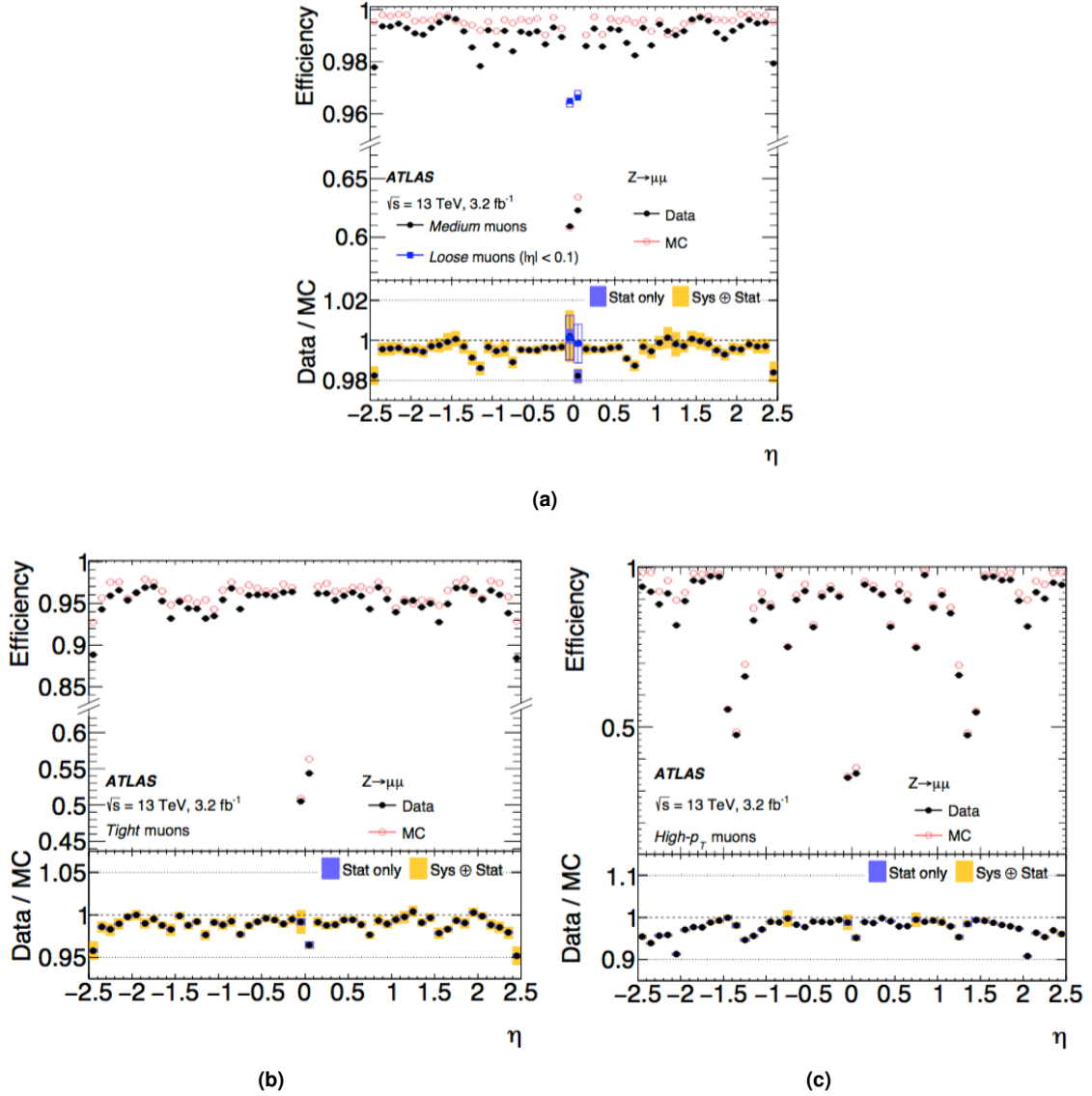


Figure 3.6: Muon reconstruction efficiency as a function of η measured in $Z \rightarrow \mu\mu$ with $p_T > 10 \text{ GeV}$ shown for (a) Medium, (b) Tight and (c) High- p_T muon selection. In addition, the (a) plot also shows the efficiency of the Loose selection (squares).

3.6 Jets

At high energy pp collisions the presence of partons is overwhelming. Due to colour confinement the partons hadronize. While the resulting bunch of particles passes through the ATLAS detector, they produce tracks in the ID and energy deposits inside the calorimeters. These detector signals allow the reconstruction of track jets (reconstructed using track information) and calorimeter jets (reconstructed using calorimeter information). This section will then focus in explaining the jet reconstruction process for calorimeter jets only. It consists in three steps: the definition of calorimeter signals, the use of a jet reconstruction algorithm to group the calorimeter signals and finally the jet calibration which corrects the jet energy and momentum for the effects of ATLAS calorimeters non-compensation, dead material, leakage, out of cone and other thresholds effects.

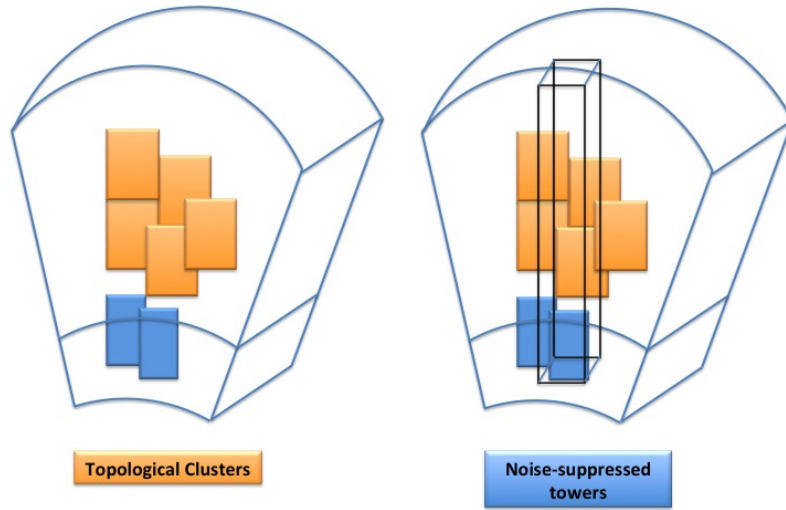


Figure 3.7: Representation of how cells may build a topological cluster (left) and how noise suppressed towers are built from those cells (right).

3.6.1 Jet reconstruction

Inputs to calorimeter jet reconstruction

In a first step, calorimeter cells are combined and the resulting clusters will be used as inputs for the jet reconstruction algorithm. ATLAS provides two different cells clustering algorithms and therefore two types of inputs to jet reconstruction:

- **Topological clusters or topoclusters** are a dynamically formed combination of cells around seed cells that exceed a given signal-to-noise ratio threshold. The seeds are defined to be the cells with $|E_{cell}/\sigma_{cell}^{noise}| > 4$, where E_{cell} is the cell energy and σ_{cell}^{noise} is the RMS of the cell noise distribution. Subsequently, their neighbouring cells are included if their signal-to-noise ratio exceeds a second threshold $|E_{cell}/\sigma_{cell}^{noise}| > 2$ [70].

Finally all cells neighbouring the formed topoclusters are added to the topocluster. Topoclusters are defined as massless. Their energy is obtained summing up the energy of all the cells included. Their direction is calculated from weighted averages of the pseudorapidity and azimuthal angles of the constituent cells relative to the nominal ATLAS coordinate system. The weight used is the absolute cell energy. Because of calorimeter noise fluctuations cluster can have a negative energy. Negative energy clusters are rejected entirely from the jet reconstruction since they do not have physical meaning.

- **Noise Suppressed Towers** are constructed by projecting calorimeter cells onto a grid with tower bin size $\Delta\eta \times \Delta\phi = 0.1 \times 0.1$. When cells larger than 0.1 exist, like in the third layer of the tile calorimeter, they are splitted between towers, and so is their energy, in a proportional manner. The towers are built using only cells belonging to topological clusters. Therefore, the same noise suppression is used in both cases. Towers are also defined to be massless and their energy and direction are calculated in the same way as for topoclusters. Negative energy towers are rejected entirely from the jet reconstruction[70]. The difference between towers and clusters is illustrated in Figure 3.7.

Jet reconstruction algorithms

Jet reconstruction algorithms allow to associate the energy deposits in the calorimeters to a jet. A good jet algorithm should give a stable and precise description of QCD interactions during the pp collision and therefore has to fulfill certain conditions:

- Collinear safety, which means that the splitting of one particle into two collinear particles has no effect on the reconstruction.
- Infrared safety, which means that the presence of additional soft particles between jet components does not affect the jet reconstruction.
- Effects of resolution and other detector effects (e.g. noise) should affect the jet reconstruction as little as possible.
- Invariance under Lorentz boosts along z coordinate.
- Minimum computer resources used.

The jet reconstruction algorithm used in this analysis is called the anti- k_T algorithm[71], which is a sequential recombination algorithm. Sequential recombination algorithms take topoclusters or towers as input and combines them to form jets according to a distance parameter defined below. For all inputs i , and pairs ij two different distances are defined:

$$d_{ij} = \min(p_{T,i}^{2p}, p_{T,j}^{2p}) \frac{\Delta R_{ij}^2}{R^2} \quad (3.1)$$

$$d_i = p_{T,i}^{2p}, \quad (3.2)$$

where p_T is the transverse momentum of the input i ,

$$\Delta R_{ij} = \sqrt{(y_i - y_j)^2 + (\phi_i - \phi_j)^2} \quad (3.3)$$

is the distance between a pair of inputs in the $y - \phi$ space, y is the rapidity and R and p are parameters of the algorithm. d_{ij} represent the distance between a pair of inputs i and j , while d_i the distance between the input i and the beam axis in the momentum space. The algorithm calculates $\min(d_i, d_{ij})$. If $\min(d_i, d_{ij}) = d_i$, the input i is said to form a jet and is removed from the list of inputs. If $\min(d_i, d_{ij}) = d_{ij}$, the inputs i and j are combined into one single input using the E-scheme (sum of four-momentum of each input). The combined input is put into the list of possible inputs, while i and j are removed. The algorithm proceeds until no inputs are left, which means that all inputs in the event will end in a jet. The parameter p defines the kind of algorithm (Figure 3.8):

- $p = 1$: k_T algorithm[72]
- $p = 0$: Cambridge/Aachen algorithm[73]
- $p = -1$: anti- k_T algorithm[71]

While R characterizes the size of the jet in the $y - \phi$ space. The anti- k_T algorithm works in the inverse transverse momentum space and has three main advantages. First, it clusters nearby particles, ensuring infrared safety. Second, soft inputs prefer to cluster with hard inputs instead of clustering with other soft particles. Third, the anti- k_T algorithm is seedless and all hard inputs within $\Delta R_{ij} < R$ will be combined into one jet, ensuring the collinear safety. In this analysis, the ratio parameter $R = 0.4$ was used.

The topoclusters and towers are defined massless. However, their distribution inside the reconstructed jet leads the jet to have a given mass. In Monte Carlo simulations track jets and calorimeter jets are reconstructed as in real data. In addition, two other kinds of jets can be defined in simulation:

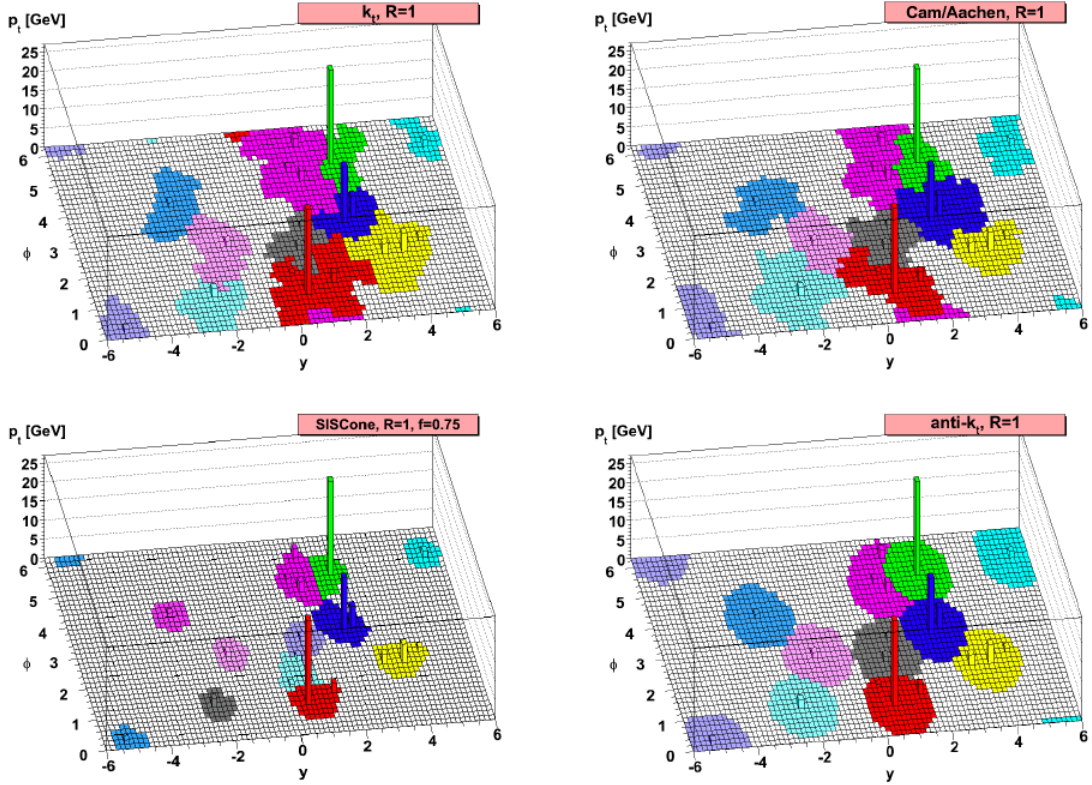


Figure 3.8: Shape output of the different reconstruction jet algorithms for the same event.

- **Parton jet** refers to the parton at the matrix-element level which causes the particle shower due to the fragmentation process.
- **Particle or truth jet** which is reconstructed from stable particles (particles with a lifetime greater than 10 ps) produced by the hadronization models of the different Monte Carlo generators, before any detector simulation. This mainly includes electrons, photons, pions, kaons, protons and neutrons and their antiparticles. Neutrinos and muons are not included, since they do not leave any significant signal in the calorimeter.

A schematic view of the different types of jets is shown in Figure 3.9. The jet reconstruction efficiencies were determined from data with a tag-and-probe method, using track jets, where the efficiency was defined as the fraction of probe track jets matching a corresponding calorimeter jet[74]. The difference between data and simulation is found to be small and within the uncertainties. Therefore, no scale factors were needed.

3.6.2 Jet calibration

The energy of the reconstructed jets does not correspond to the initial energy carried by the particles. Reconstructed jets need therefore to be calibrated to the correct energy scale. In general, the reference scale in the jet calibration process is given by the truth jets. Jets are initially reconstructed at the electromagnetic (EM) scale, which is the basic calorimeter signal scale for the ATLAS calorimeters. This means that the calorimeter signals are calibrated to properly reproduce the energy lost in the calorimeter by an electron, if the energy deposit came from an electron. The EM scale was obtained using test-beam measurements for electrons in the barrel[66, 67, 75] and the endcap calorimeters[76]. It has been validated using muons from test-beams and in cosmic-rays. The energy scale of the electromagnetic calorimeters has been corrected using the invariant mass of

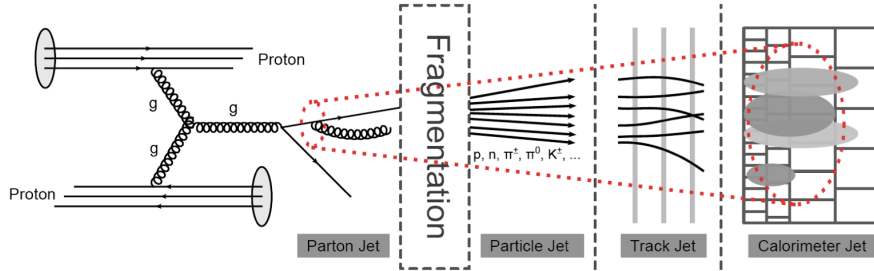


Figure 3.9: Schematic view of the different types of jets. Colorful particles, produced at the interaction point, create a bunch of colorless particles due to fragmentation. These particles will produce detector signals in the Inner Detector and Calorimeter, which can be reconstructed as track and calorimeter jets.

$Z \rightarrow ee$ events[65]. This EM scale calibration provides a very good description for energy deposits produced by electrons and photons, but not for deposits from hadronic particles like protons, neutrons, pions or kaons. This difference results from the fact that the EM scale calibration does not account for various detector effects:

- Calorimeters non-compensation: partial measurement of the energy deposited by hadrons.
- Dead material: energy losses in inactive or non instrumented regions of the detector.
- Leakage: energy deposits from particles which are not totally contained in the calorimeters.
- Out of cone: loss of energy deposits from particles inside the particle jet that are not included in the reconstructed jet.
- Thresholds effects: signal losses due to inefficiencies in calorimeter clustering and jet reconstruction.

ATLAS has developed several calibration schemes with different levels of complexity and different sensitivity to systematic effects[70], which made them complementary in the way they contribute to the understanding of the jet energy scale measurement:

- **EM+JES calibration** is a Monte Carlo-derived jet calibration scheme used in ATLAS for the first analyses. EM+JES applies a simple jet-by-jet correction that restores the reconstructed jet energy to the particle jet energy. In this scheme each jet at the EM scale is scaled by a correction factor which is a function of the reconstructed jet energy and η . In addition to this energy correction a pile-up and a jet origin correction are also applied[70].
- **Global Sequential (GS) Calibration** is a Monte Carlo-derived jet calibration, which uses longitudinal and transverse properties of the jet structure sequentially to improve the resolution, while leaving the jet energy scale unchanged. In this scheme jets are found from clusters or towers, then the EM+JES calibration is applied and finally they are scaled by a jet-by-jet correction factor which depends on the jet p_T , η and several longitudinal and transverse jet properties.
- **Global Cell Energy-Density Weighting Calibration (GCW)** attempts to compensate for the different calorimeter response to hadrons and electromagnetic particles by weighting each jet constituent cell. The weights, which depend on the cell energy density and the calorimeter layer only, are determined by minimizing the energy fluctuations between the reconstructed and particle jets in Monte Carlo simulation. Jets are found from topoclusters or towers at the EM scale, then cells are weighted and a final jet energy scale correction is applied to ensure that good linearity response is achieved[77].

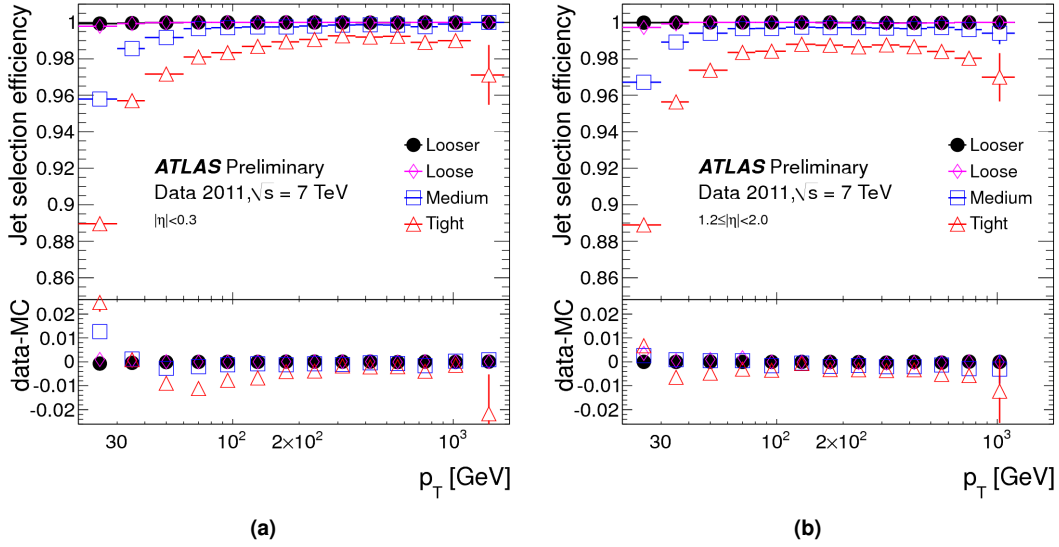


Figure 3.10: Jet quality selection efficiency for anti- k_T jets with $R = 0.4$ as a function of p_T in two η example-ranges, for the four sets of selection criteria.

- **Local Cluster Weighting Calibration (LCW)** uses properties of topoclusters (such as their energy, depth in the calorimeter, cell energy density, fractional energy deposited in the calorimeter layer and energy measured around it) to calibrate them individually before applying jet reconstruction. These weights are determined from Monte Carlo simulations of charged and neutral pions. Similarly to the GCW scheme, a final correction of the jet energy is applied[77].

The EM+JES calibration is used for first physics analysis, due to its simplicity. The others calibration schemes are presently commissioned by ATLAS. The corrections applied by each calibration schemes as well as the inputs used have been validated using data from pp collision at a center-of-mass energy of $\sqrt{s} = 7$ TeV[70].

3.6.3 Jet selection

In ATLAS jets can be reconstructed with different quality criteria: *Looser*, *Loose*, *Medium* and *Tight* [91].

Since the noisy channels of the calorimeter and its electronics can lead to fake energy deposits not due to particles going through the calorimeter (which can be reconstructed as fake jets), many quality criteria on the features of the recorded pulse are applied in order to discriminate between real and fake jets candidates. The four jet categories differ for the cuts applied on the calorimetric variables of the signal.

The Looser selection was designed to provide an efficiency above 99.8% with a fake rejection as high as possible while the Tight selection was designed to provide a much higher fake rate jet rejection with an inefficiency not larger than a few percent. The two other sets of cuts correspond to intermediate fake rejections and jet selection efficiencies. Efficiencies of the four jet reconstruction categories are shown in Figure 3.10 as a function of the jet p_T .

As explained above the jets in ATLAS are reconstructed using solely the calorimeter, however tracks reconstructed in the ID can be associated to a jet. Tracks are associated to jets using a simple geometrical matching criterion: the radial distance:

$$\Delta R = \sqrt{(\eta_{\text{jet}}^{\text{PV}} - \eta_{\text{track}}^{\text{PV}})^2 + (\phi_{\text{jet}}^{\text{PV}} - \phi_{\text{track}}^{\text{PV}})^2} \quad (3.4)$$

is calculated for each track, where $\eta_{\text{jet}}^{\text{PV}}$ and $\phi_{\text{jet}}^{\text{PV}}$ are the pseudorapidity and the azimuthal angle of the jet with respect to the primary vertex, and $\eta_{\text{track}}^{\text{PV}}$ and $\phi_{\text{track}}^{\text{PV}}$ are the pseudorapidity and the azimuthal angle of the track at the perigee² with respect to the PV.

Any track for which the condition $\Delta R < 0.4$ is satisfied are considered as matching the jet, and therefore are associated to it.

3.6.4 Jet energy resolution

The procedure adopted to measure the jet energy resolution is explained in detail in [92]. It basically relies on the assumption that in events containing only two jets, the p_{T} 's of the two jets shall be balanced because of the momentum conservation in the transverse plane. Starting from this assumption the jet energy resolution can be measured studying the asymmetry observed between the jet p_{T} 's in such a configuration. To perform this measurement, jets in the same rapidity y region are chosen in order to minimize additional detector effects that may introduce secondary effects. The jet energy resolution is thus obtained in $p_{\text{T}} \times \eta$ bins. Given the above, the fractional jet energy resolution can be parametrized as (following the parametrization of the energy resolution for the calorimeter):

$$\frac{\sigma_{p_{\text{T}}}}{p_{\text{T}}} = \frac{N}{p_{\text{T}}} \oplus \frac{S}{\sqrt{p_{\text{T}}}} \oplus C \quad (3.5)$$

Where N , S , and C are the noise, stochastic and constant terms respectively. Once the measurement according to the method mentioned above is performed (and validated with Monte Carlo simulations), the distribution of the results can be built in each η bin and a fit with the functional form in equation 3.5 can be done. Some results of such a measurement is shown in Figure 3.11 for a specific rapidity bin.

In the rapidity bin $0.0 < |y| < 0.8$ shown in Figure 3.5, a $\sigma(p_{\text{T}})/p_{\text{T}}$ of about 15% is reached for jets having $p_{\text{T}} = 40$ GeV, while at $p_{\text{T}} = 500$ GeV $\sigma(p_{\text{T}})/p_{\text{T}} \sim 7\%$. Once a measurement of the jet energy resolution is obtained, it is possible to link any measured jet falling in a given $\eta - p_{\text{T}}$ region to its corresponding resolution.

²The perigee of a track is defined as point of closest approach to the beam axis

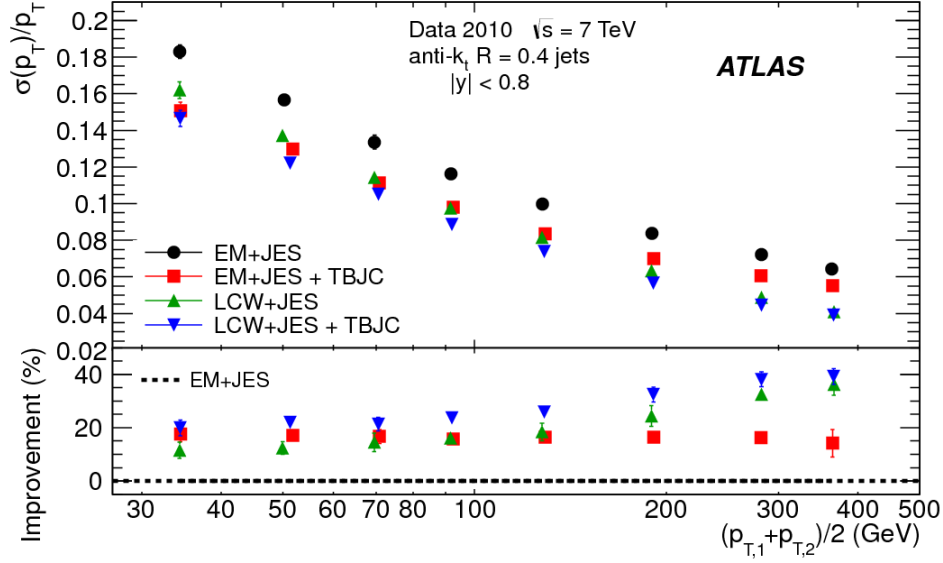


Figure 3.11: Fractional jet p_T resolutions, measured in data for anti- k_t jets with $R = 0.4$ and for four jet calibration schemes: EM+JES, EM+JES+TBJC, LCW+JES and LCW+JES+TBJC. The lower panel of the figure shows the relative improvement for the EM+JES+TBJC, LCW+JES and LCW+JES+TBJC calibrations with respect to the EM+JES jet calibration scheme, used as reference (dotted line). The errors shown are only statistical.

3.7 b -tagging

The performance of the current ATLAS b -tagging algorithms has been optimized ahead of the 2016 Run-2 data taking. The inputs to the b -tagging algorithms are the trajectories of charged particles (tracks) reconstructed in the Inner Detector (ID). In order to have better track and vertex reconstruction performance at the higher luminosities expected during Run 2, a fourth pixel layer, the insertable B-layer (IBL), has been added to ATLAS. This inclusion leads to significantly improved b -tagging performance, mostly in the low and medium jet p_T region, compared to that achieved at Run 1.

3.7.1 b -tagging algorithms

The B hadron formed by the bottom quark has a relatively long lifetime of about 1×10^{-12} s and can travel around 3mm before decaying. The identification of b -jets is very important for example in the discrimination of top quark analysis backgrounds with only light jets in the final state. b -tagging algorithms exploit the fact that a certain number of tracks point to a secondary vertex instead of pointing to the reconstructed primary vertices as shown in Figure 3.12 and that impact parameters of these tracks are large. Thus b -tagging relies on the ID track reconstruction and for such reason it can be only applied to jets with $|\eta| < 2.5$. Moreover ID tracks are required to pass some quality criteria that depend on the different b -tagging algorithms.

Various b -tagging algorithms can be defined, based on these discriminating variables, on secondary vertex properties and on the presence of leptons within b -jets, and for each jet they usually give as output a weight reflecting the probability that the input jet originates from a b -quark. There are basically three kinds of b -tagging algorithms[78]. The one used in this analysis is based on the measurement of the *impact parameter* (see Figure 3.12) and on the reconstruction of the secondary vertex.

The transverse impact parameter d_0 is the distance in the transverse plane $x - y$ between the

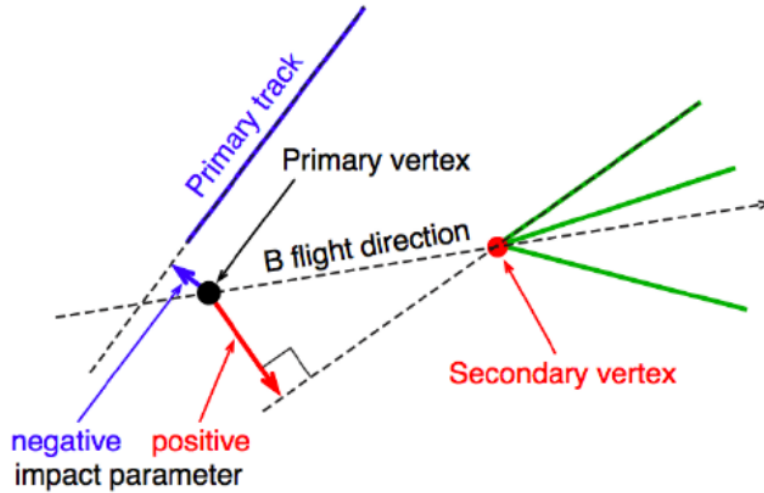


Figure 3.12: Schematic representation of a b -hadron decay and definition of the impact parameter.

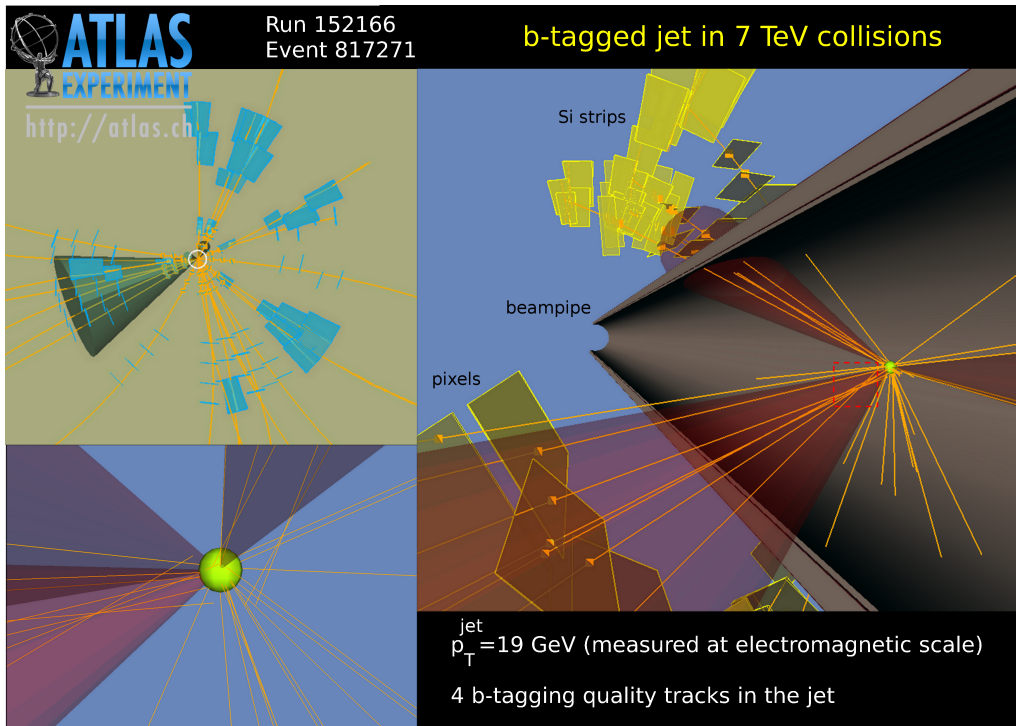


Figure 3.13: Real collision view of a b -jet candidate. The event display shows a b -jet candidate reconstructed with the anti- k_T algorithm, where the primary vertex is shown in the yellow circle and the secondary vertex in the dashed red box.

point of closest approach of a track and primary vertex, while the longitudinal impact parameter is the z -coordinate of this point (z_0). The b -tagging algorithm used in these analyses is called *MV2* (multiVariate tagger) [109]: it is based on a neural network and takes as input the output weights of three simpler tagging algorithms:

- IP3D [93], based on the d_0 significance;
- SV1 [93], based on the reconstruction of secondary vertexes;
- JetFitterCombNN [93], which performs a fit on the flight direction of the b -hadrons and then

combines the result with the output weights of IP3D and SV1.

The output of these b-tagging algorithms are combined in a multivariate discriminant, MV2, that is the output of the default algorithm used by ATLAS which provides the best separation between the different jet flavours.

Three MV2 variants are released, MV2c00, MV2c10 and MV2c20, where the names of the taggers indicate the c-jet fraction in the training; e.g. in MV2c20, the background sample is composed of 20% (80%) c- (light-flavour) jets. It is possible to modify the light versus c-jet rejection performance by changing the fraction of c-jets in the training. Given that the majority of physics analyses are presently more limited by the c-jets rather than the light-flavour jet rejection, the c-jet background fraction in the training has been chosen in such a way to enhance the charm rejection by keeping a similar light-flavour jet rejection compared to the previous approach. The c-jet fraction of the training for MV2c10 is therefore set at 7% such that the training is performed assigning b-jets as signal and a mixture of 93% light-flavour jets and 7% c-jets as background. In a second variant, denoted MV2c20, the c-jet fraction used is 15%; lastly, no c-jet contribution is present in the training is used for MV2c00.

The output of the MV2 tagger is a continuous value w_{MV2} , and it is possible to choose a threshold value \bar{w} to tag a jet as a b -jet: if $w_{MV2} > \bar{w}$ then the jet will be considered a b -jet, otherwise it will be considered a light-flavour jet. The choice of the value of \bar{w} depends on the desired b -tagging efficiency and on the desired mis-tag rate one wants to have in the analysis.

The data-Monte Carlo comparison on the output of the MV2c10 algorithm is shown in Figure 3.14b. The figure 3.14b shows the distribution of the MV2c10 multivariate discriminant applied to jets in a $t\bar{t}$ -dominated sample of events selected by requiring an opposite-sign e-mu pair and at least two jets. The data is shown by the points with error bars and the simulation by the filled areas, divided into contributions from b (red), c (green) and light (purple) flavoured jets, and normalized to the same number of jets as the data. As can be seen the data-Monte Carlo agreement is good for the considered taggers. In particular the output weight of the MV2 tagger clusters to 0 for light jets, while assumes values near to 1 for b -jets.

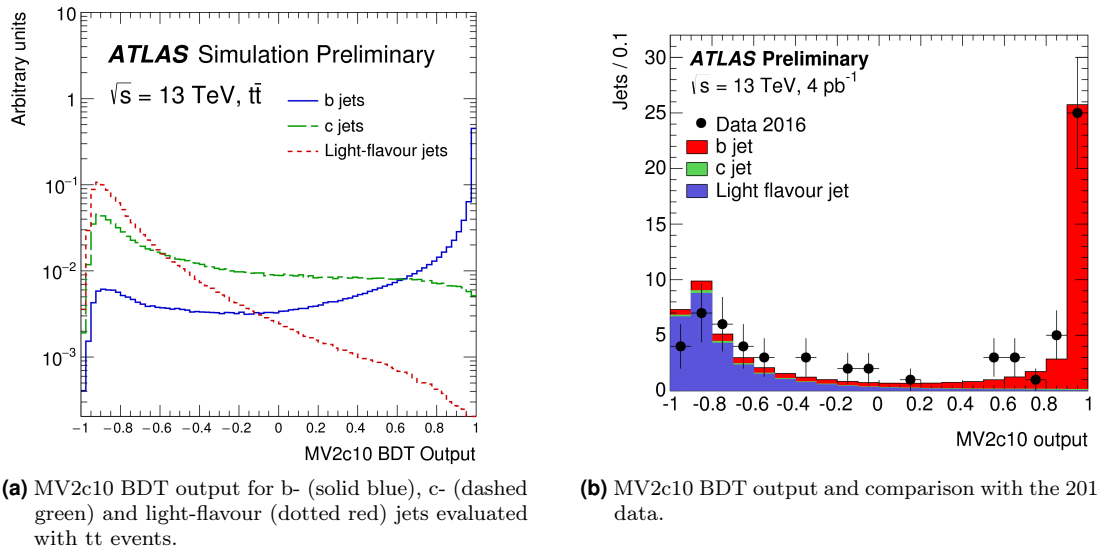


Figure 3.14: Multivariate MV2c10 discriminant used in Run-II for b-tagging.

The figures 3.15 shows the light-flavour jet and c jet rejection vs b jet efficiency curves obtained by simulation; the choose of the working point on this curve determines the b jet efficiency selection and the contamination of the the light-flavour and c jet in the analysis.

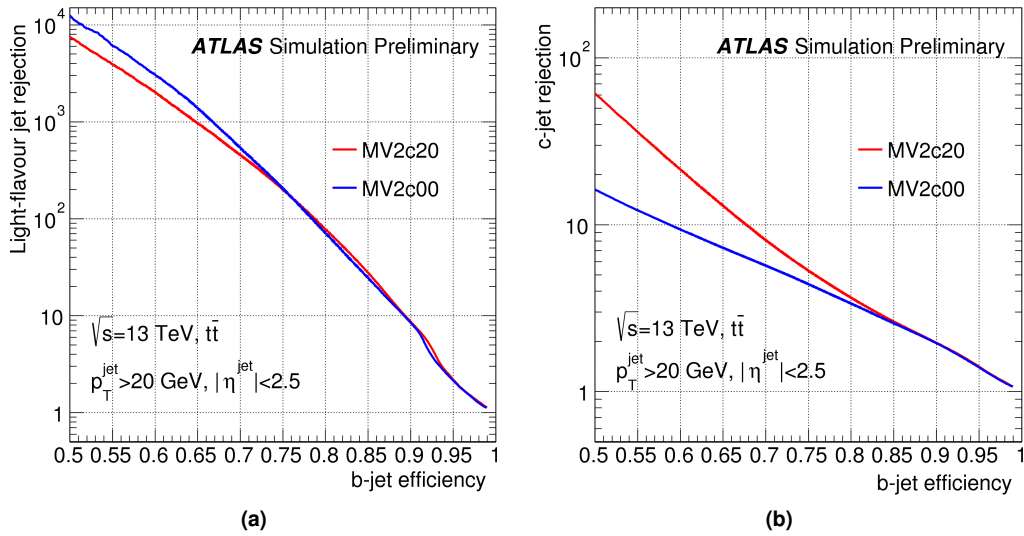


Figure 3.15: The light-flavour (a) and c-jet (b) rejection versus b-jet efficiency for the MV2c20 (red) and MV2c00 (blue) b-tagging algorithms in $t - \bar{t}$ events.

As previously said, the b-tagging performances reached in Run 2 data taking are improved in comparison with the Run 1 and this is put in evidence in figures 3.16.

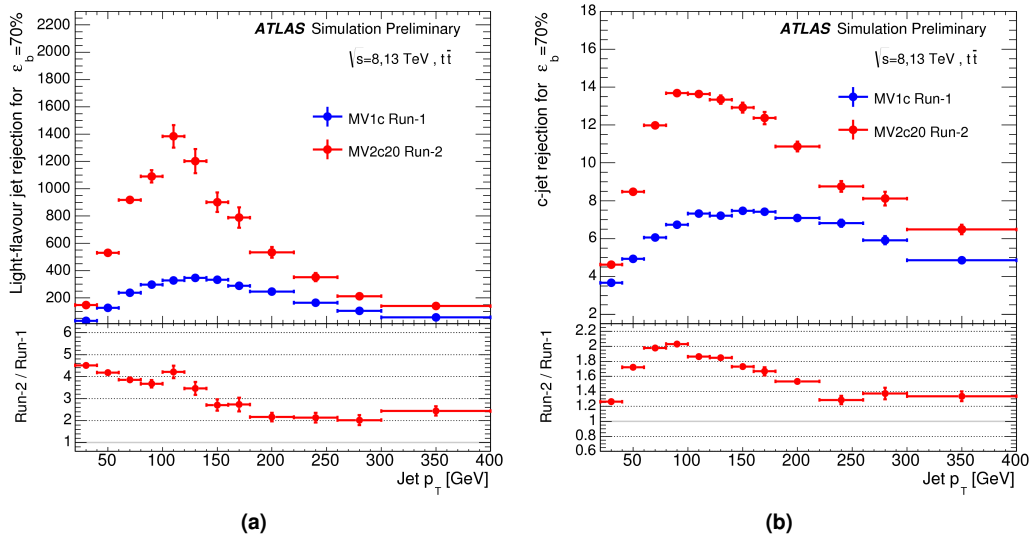
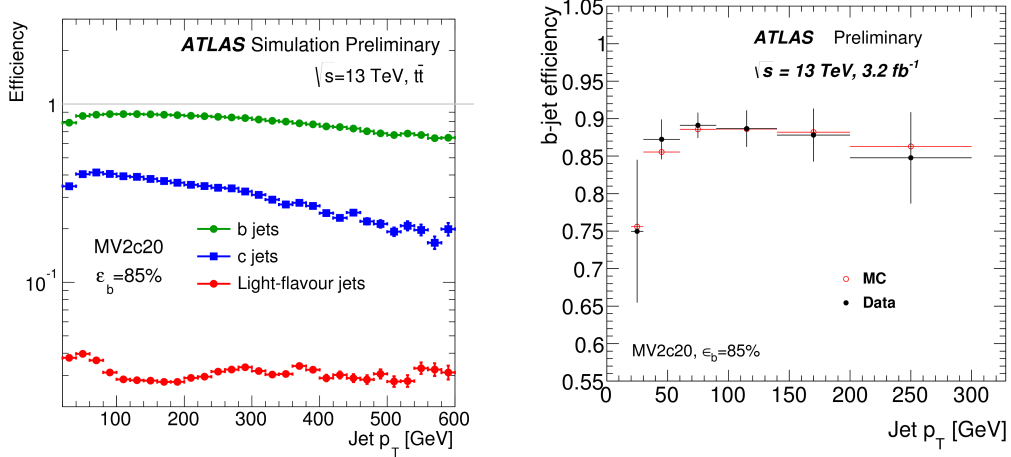


Figure 3.16: The light-flavour jet rejection (a) and c-jet rejection (b) in bins of jet p_T for the MV1c b-tagging algorithm using the Run-1 detector and reconstruction software (blue) compared to the MV2c20 b-tagging algorithm using the Run-2 setup (red). In each p_T bin the b-tagging cut value has been chosen in such a way to yield a constant b-jet efficiency of 70%.



(a) The efficiency to tag b (green), c (blue) and light-flavour (red) jets for the MV2c20 tagger with the 85% operating point.

(b) b-tagging efficiency extracted from data (black) using the $t\bar{t}$ Probability Distribution Function method and in simulation (red). Error bars indicating the combined statistical and systematic uncertainty are shown.

Figure 3.17: b-tagging efficiency for the Mv2c20 b-tagging algorithm at the 85% working point as a function of jet p_T .

3.8 Missing transverse energy

The missing transverse energy, E_T^{miss} , in a collider experiment is the energy imbalance in the transverse plane, where the energy conservation is expected. The physical source of such an imbalance typically is the presence of unseen particles such as neutrinos which go through all the detector without leaving any signal, and it is measured thanks to the tightness of the calorimetric system.

In addition many detector-related effect (such as mismeasurements of energy) can give rise to E_T^{miss} . The E_T^{miss} reconstruction algorithm starts from all the calorimetric cells belonging to topological clusters (see section 3.10) in the $|\eta| < 4.9$ range, considering their energy and also their position in θ and ϕ , as shown in equation 3.9.

The final E_T^{miss} calculation is defined as:

$$E_T^{\text{miss}} = \sqrt{(E_x^{\text{miss}})^2 + (E_y^{\text{miss}})^2} \quad (3.6)$$

where the $E_{x(y)}^{\text{miss}}$ contain contribution from both calorimetric energy deposits and corrections for the muons in the event in each transverse direction x and y :

$$E_{x(y)}^{\text{miss}} = E_{x(y)}^{\text{miss, Calo}} + E_{x(y)}^{\text{miss, Muon}} \quad (3.7)$$

where:

$$E_x^{\text{miss, Calo}} = - \sum_{i=1}^{N_{\text{cell}}} E_i \sin \theta_i \cos \phi_i \quad (3.8)$$

$$E_y^{\text{miss, Calo}} = - \sum_{i=1}^{N_{\text{cell}}} E_i \sin \theta_i \sin \phi_i \quad (3.9)$$

and the $E_{x(y)}^{\text{miss, Muon}}$ takes into account the energy muon energy deposit as it goes through the calorimetric system. The $E_{x(y)}^{\text{miss, Calo}}$ terms contain all the energy deposits in the calorimeter: all

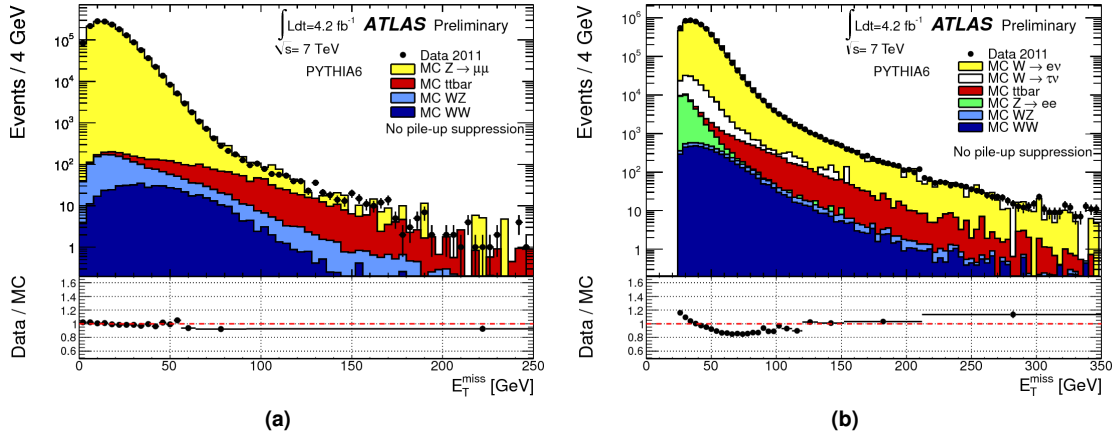


Figure 3.18: Distribution of E_T^{miss} measured in $Z \rightarrow \mu^+ \mu^-$ (a) and $W \rightarrow e \nu$ (b) events for data and Monte Carlo.

the energy deposits associated to reconstructed physics objects (electrons, photons, taus, jets) are considered as well as those that are not associate to any reconstructed object. This last contribution may suffer of contamination from noisy channels, but this is avoided by means of quality requirement on any energy deposit contributing to the E_T^{miss} calculation [94].

Figure 3.18 shows the reconstruction of E_T^{miss} in $Z \rightarrow \mu^+ \mu^-$ (Figure 3.18a) and $W \rightarrow e \nu$ (Figure 3.18b) for both data and Monte Carlo.

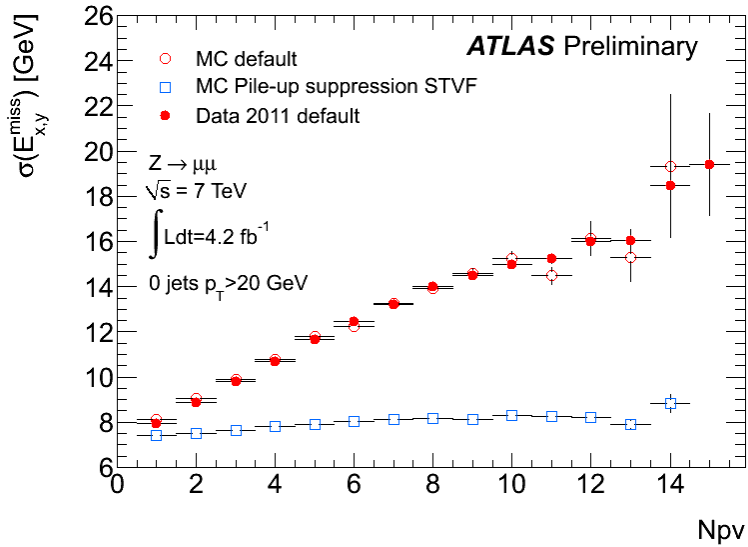


Figure 3.19: E_T^{miss} resolution as a function of the number of reconstructed primary vertexes (i.e. as a function of the pileup). The effect of the pileup suppression is shown too.

In figure 3.19 the E_T^{miss} resolution as a function of the number of reconstructed primary vertexes in each event is shown. This points out how pileup affects calorimetric measurements and the effect of pileup suppression methods.

Chapter 4

Search for diboson resonances in the $llqq$ final state

4.1 Introduction

In July 2012 the experiment ATLAS and CMS announced the discovery of a new particle with a mass of approximately 125 GeV [1, 2] compatible with the expectations of the Standard Model (SM) Higgs boson. This discovery represents a milestone in the understanding of electroweak symmetry breaking.

Although, the current experimental results cannot exclude the possibility that the new particle is part of an extended Higgs sector or other extensions of the SM. Many of these models predict the existence of diboson resonances. In models with an extended Higgs sector such as the two-Higgs-doublet model (2HDM) [7] and the electroweak-singlet (EWS) model [8], a heavy spin-0 neutral Higgs boson can decay to a pair of Z bosons. In models with warped extra dimensions [9, 10], a spin-2 graviton is expected to decay to ZZ .

Both the ATLAS and CMS Collaborations have searched for heavy resonances in ZV ($V = W, Z$) decays in the $\sqrt{s} = 7$ and 8 TeV datasets [11, 12, 13, 14, 15] and in the $\sqrt{s} = 13$ TeV datasets [17, 16, 18, 19] but only with 2015 data.

This thesis work has been focused on the search of heavy resonances decaying into a ZZ with one of the two Z decaying to a pair of light charged leptons (electrons or muons, referred to as ℓ), $Z \rightarrow \ell\ell^1$, and the other decaying to a pair of quarks, $Z \rightarrow qq$. This leads to the $ZZ \rightarrow \ell\ell qq$ decay mode. The analysis has been restricted in the diboson mass range 300 – 6500 GeV/ c^2 , within the context of Standard Model extensions with an extended Higgs sector (heavy spin-0 neutral Higgs boson) and warped extra dimensions (spin-2 Randall-Sundrum graviton). For my thesis, I analysed proton-proton collision data recorded during 2015 and the beginning of 2016 by the ATLAS experiment at LHC with a center of mass energy $\sqrt{s} = 13$ TeV. The integrated luminosity used in this study has been 13.2 fb^{-1} .

The reconstruction of the $Z \rightarrow qq$ decay proceeds in two different ways. The resolved reconstruction attempts to identify two separate small-radius jets (small- R jet, or j) of hadrons from the $Z \rightarrow qq$ decay, while the merged reconstruction uses jet-substructure techniques to identify the $Z \rightarrow qq$ decay reconstructed as a single large-radius jet (large- R jet, or simply J). The latter is expected when the resonance mass is significantly higher than the Z boson mass. In this case, the qq pair from the Z boson decay can be collimated; hadrons from the two quarks overlap in the detector and are more efficiently reconstructed as a single large- R jet (“merged selection”). In this analysis I used both reconstructions of the $Z \rightarrow qq$.

Production of heavy resonances will manifest themselves as resonant structures in the invariant-mass distributions of the $llqq$ final state. Thus for this decay mode, the invariant masses of the $\ell\ell J$ system ($m_{\ell\ell J}$) and of the $\ell\ell jj$ system ($m_{\ell\ell jj}$) are used as the final discriminants for the signal-background separations for the merged and resolved reconstructions of the $Z \rightarrow qq$ decays,

¹To simplify the notations, antiparticles are not explicitly labelled.

respectively. The main background in this analysis is from Z + jets events, with smaller backgrounds arising from top quark production, diboson (ZZ/WZ) production, and multi-jet production.

The results of the search are interpreted for a narrow width "Standard Model-like" Higgs boson. In addition limits are set using simulated Randall-Sundrum graviton samples (spin-2).

Events from the VBF Higgs boson production possess unique topologies, and hence are selected from the $H \rightarrow ZZ \rightarrow \ell\ell qq$ candidates by applying additional criteria.

My work has been mostly devoted to the optimization of the event selection and on the characterization of the VBF component and it has been part of a more general analysis for the searches of heavy resonances in diboson decays [20].

4.2 Data and MonteCarlo samples

This analysis uses data collected during the 2015 and 2016 LHC Run-2 period in pp collisions, corresponding to an integrated luminosity of 3.2 fb^{-1} in 2015 and 10.0 fb^{-1} in 2016.

Events used in the $ZZ \rightarrow \ell\ell$ search were recorded with a combination of multiple single-electron or single-muon triggers with varying E_T (electron) and p_T (muon), quality, and isolation requirements. The minimum E_T threshold for electrons is 24 GeV , while the minimum p_T threshold for muons is 20 GeV . These triggers are complemented by triggers with higher thresholds with no isolation requirement (60 GeV or 120 GeV for electrons and 50 GeV for muons).

Monte Carlo simulated events are used for the evaluation of background modelling and signal acceptance, optimisation of event selection, estimation of systematic uncertainties and the statistical analysis. They are produced using ATLAS approved event generator settings and processed with the simulation of the ATLAS detector and trigger.

Samples are processed through the full ATLAS detector simulation [117] based on GEANT4 [118].

Background processes include Z + jets, $t\bar{t}$, single top and diboson (WZ , ZZ). Events containing Z bosons with associated jets are simulated using the Sherpa 2.2 [119] generator. The Z + jets events are normalized to the NNLO cross sections and they are sliced by both the p_T ranges of Z boson (from 0 GeV to the center-of-mass energy) and the number of b and c quarks in the final state.

The generation of $t\bar{t}$ events is done with the Powheg-Box v2 [120] generator with the CT10 PDF sets in the matrix element calculation. The top quarks are decayed using MadSpin [121] preserving all spin correlations, while for all processes the parton shower, fragmentation, and the underlying event are simulated using Pythia 6.428 [122] with the CTEQ6L1 PDF sets and the corresponding Perugia 2012 tune (P2012) [123]. The top mass is set to 172.5 GeV . The cross section of $t\bar{t}$ is known to NNLO in QCD including re-summation of next-to-next-to-leading logarithmic (NNLL) soft gluon terms, and the reference value used in ATLAS is calculated using TOP++ 2.0 [124].

The generation of single top-quark events in the Wt- and s-channels is also done with Powheg-Box v2 with the CT10 PDF set. The decay of the top quarks and subsequent parton shower is performed in the same way as the $t\bar{t}$ events.

The diboson processes (WZ and ZZ) are generated with POWHEG-BOX v2 interfaced to PYTHIA 8.186 [125].

Signal samples for high mass Higgs models using the narrow width approximation (NWA) are generated at NLO for both gluon-gluon fusion (ggF) and vector boson fusion (VBF) production modes with POWHEG-BOX v2 interfaced to PYTHIA 8.186. In addition, samples for Higgs models using various, larger widths (LWA) are generated to probe BSM Higgs sector models. Widths of 5%, 10%, and 15% of the Higgs mass are generated. These MC samples are made at NLO using AMCATNLO to generate the larger width Higgs, which is subsequently decayed with MADSPIN, and finally interfaced to PYTHIA 8.186. Higgs masses of NWA and LWA Higgs samples range from 300 GeV to 1 TeV .

Signal samples for the RS Graviton and HVT are generated with MADGRAPH5-2.2.2 (MG5) [126] interfaced to PYTHIA 8.186. The RS Graviton samples are generated with $k/\bar{M}_{\text{Planck}}=1$.

Additional pp collisions generated with PYTHIA 8.186 are overlaid to model the effect of the pileup for all MC events. All simulated events are processed with the same reconstruction algorithm as the data.

4.3 Object definition: particle reconstruction and identification

Electrons are reconstructed from isolated energy clusters in the electromagnetic calorimeter matched to ID tracks, within the fiducial region of transverse energy $E_T > 25$ GeV and pseudorapidity $|\eta| < 2.47$. Electrons are identified using the likelihood identification criteria described in Ref. [138], which is based on shapes of the showers in the electromagnetic calorimeter, track quality requirements and the distributions of the track cluster matching. The levels of identification are categorized to "LooseLH", "MediumLH", and "TightLH" corresponding to 96%, 94% and 88% of identification efficiencies to signal electrons at $E_T = 100$ GeV, respectively. Candidate electrons are also required to be isolated.

Electron candidates are first pre-selected by requiring the following cuts:

- Kinematic cuts: $p_T > 7$ GeV and $|\eta| < 2.47$
- Identification:
 - "LooseLH" identification, which includes hit requirements on the tracks: 2 hits in the Pixel detector, 7 hits in Pixel or Silicon detector.
 - Requirement of a hit in the b-layer (IBL)
- Isolation: "LooseTrackOnly" isolation
- Impact parameter significance: $|d_0/\sigma(d_0)| < 5$ and $|z_0 * \sin \theta| < 0.5$ mm.

Muons are reconstructed by fitting the ID and MS tracks together, and are required to have $p_T > 25$ GeV and $|\eta| < 2.5$. Muons must pass identification requirements, based on the number of hits in the different ID and MS subsystems, and the significance of the difference $|q/p_{MS} - q/p_{ID}|$ [127], where q is the charge and p_{MS} (p_{ID}) is the momentum of the muon measured in the muon spectrometer (inner detector). Similar to electrons, muons are also classified as either "loose" or "medium", following the criteria of Refs. [128, 127].

Four identification quality levels are predefined in this tool, namely "VeryLoose", "Loose", "Medium" and "Tight", which are defined as:

- "VeryLoose": including all muons.
- "Loose": including segment tagged and calo tagged muons with $|\eta| < 0.1$.
- "Medium": including
 1. stand alone muons with $|\eta| > 2.5$ and at least three hits at precision layers;
 2. combined muons with q/p significance of less than 7 and at least two hits at precision layers. If muon $|\eta| < 0.1$, the candidates with q/p significance of less than 7, exactly one hit at precision layers and at most one hole at precision layers are also accepted as "Medium" muon.
- "Tight" : requiring the muon to be a combined muon which satisfies q/p significance of less than 5, at least two hits at precision layers and χ^2/ndf of the combination of less than 8.

The cuts imposed on the inner detector track quality (where available) are: at least 1 pixel hits, crossed dead pixel sensors are counted as hits; at least 5 SCT hits, crossed dead SCT sensors are counted as hits; less than 3 silicon holes; a successful TRT extension if the track is inside TRT acceptance.

Candidate muons are pre-selected requiring:

- Kinematic cuts: $p_T > 7$ GeV and $|\eta| < 2.5$
- Identification: "Loose" quality

- Isolation: "LooseTrackOnly" isolation
- Impact parameter significance: $|d_0/\sigma(d_0)| < 3$ and $|z_0 * \sin \theta| < 0.5$ mm.

All electrons and muons are required to be isolated using selections on the sum of track p_T in a variable-size cone around their directions (excluding the track associated to the lepton); the cone size depends on the lepton p_T . The isolation selection criteria are designed to produce a flat efficiency of 99% in the $p_T - \eta$ plane for reconstructed leptons from $Z \rightarrow \ell\ell$ decays in Z +jets events, and to minimize efficiency loss for highly boosted Z bosons in the relevant kinematic range. Furthermore, to reject leptons not originating from the primary vertex the product of the longitudinal impact parameter z_0 and the sine of the polar angle of the candidates (θ) must satisfy $|z_0 \sin(\theta)| < 0.5$ mm. In addition, the ratio of the transverse impact parameter d_0 to its uncertainty σ_{d_0} must be less than five for electrons and less than three for muons. Muon and electron are labelled as "signal" if their $p_T > 25$ GeV.

Small-R jets are built from topological clusters, formed from calorimeter cell deposits, and calibrated to the electromagnetic (EM) scale. They are reconstructed using the anti-kt algorithm with a distance parameter of $R = 0.4$. The jet four vector is then corrected for the beamspot and a jet energy scale calibration is performed. Energy- and η -dependent correction factors derived from MC simulations are applied to correct jets back to the particle level [129]. Jets are required to have $p_T > 30$ GeV and $|\eta| < 4.5$ and those with $|\eta| < 2.5$ are called 'signal' jets. To suppress contributions from pileup interactions, jets with $p_T < 60$ GeV and within the acceptance of the inner tracker ($|\eta| < 2.4$) must have a value of the jet vertex tagger, based on tracking and vertexing information [130], above 59%.

The 'signal' jets containing b -hadrons are identified using a multivariate algorithm (b -tagging) [131], which combines information such as the explicit reconstruction of secondary decay vertices and track impact-parameter significances. The chosen b -tagging algorithm has an efficiency of 70% for b -quark jets in the simulated $t\bar{t}$ events, with a light-flavour jet rejection factor of about 380 and a c -jet rejection of about 12. For this analysis, we consider our "signal" jets to be those with $|\eta| < 2.5$.

Jets in ATLAS are assigned a score from a multivariate selector to determine whether they are b -jets. The selector is known as MV2c10, along with various working points corresponding to tighter or looser selection. For this analysis, we use the 70% working point.

Hadronically decaying Z bosons can sometimes be boosted such that their constituents are no longer reconstructed as two distinct small-R jets. To make up for the loss in selection efficiency, large-R jets are considered, with additional requirements placed on them to select ones likely coming from boson decays. The jet collection used for boson tagging is anti- k_t jet [132] with a distance parameter of $R = 1.0$. The jets are found using topological clusters, formed from calorimeter cell deposits, as the input. The jet's total four-vector is evaluated by summing the four-vectors of the massless constituents.

Jet grooming refers to a series of techniques selecting a subset of a jet's constituents, with the aim of removing contributions to the jet from the underlying event or pile-up. In Run-2 the pre-recommended grooming technique is the trimming algorithm. Trimming takes the original constituents of the jet, in this case the anti- k_t $R = 1.0$ jet, and reclusters them using the k_t algorithm with a smaller distance parameter. Here, we use $R_{\text{subject}} = 0.2$, to produce a collection of sub-jets. These subjets are then discarded if they carry less than a specific fraction of the original jets p_T , f_{cut} . The optimised selection is to keep a subject if $f_{\text{cut}} > 5\%$.

Jets are required to have $p_T > 200$ GeV and $|\eta| < 2.0$, to select high transverse momentum, central jets with a good overlap between the ID tracking and the calorimeter information.

Boson tagging is applied to the large- R jets to select those from $Z \rightarrow qq$ decays. The tagging is performed through a two-step process [133, 134]. A p_T -dependent requirement is applied to the jet substructure variable $D_2^{(\beta=1)}$, which is a ratio of energy correlation functions of subjets [135, 136]:

$$D_2^{\beta=1} = \frac{e_3^{\beta=1}}{(e_2^{\beta=1})^3} = \frac{\sum_{i < j < k \in J} p_{T,i} p_{T,j} p_{T,k} R_{ij} R_{ik} R_{jk}}{\sum_{i < j \in J} p_{T,i} p_{T,j} R_{ij}} \quad (4.1)$$

where the sums are taken over the set of subjets in the large-R jet after trimming. In general, lower $D_2^{(\beta=1)}$ values are indicative of two-prong large-R jets.

The Z boson jets are then selected by requiring the large- R jet mass m_J to be in the ± 15 GeV window centered around the expected value of the boson mass from simulations. This boson tagging is approximately 50% efficient for the signals studied.

A concise summary of the key object selections used in the analysis are showed in table 4.1.

Object	Kinematics	Type, Quality	Additional
Electrons	$p_T > 7$ GeV $ \eta < 2.47$	"LooseLH" $d_0/\sigma(d_0) < 5$ $ z_0 \sin \theta < 0.5$ "LooseTrackOnly" isolation ($\epsilon \sim 99\%$)	B-layer (IBL) hit requirement
Muons	$p_T > 7$ GeV $ \eta < 2.5$	Loose quality $d_0/\sigma(d_0) < 3$ $ z_0 \sin \theta < 0.5$ "LooseTrackOnly" isolation ($\epsilon \sim 99\%$)	
Large-R Jets	$p_T > 200$ GeV $ \eta < 2.0$	anti- k_T $R = 1.0$ LCTopo Trimmed ($R_{\text{subject}} = 0.2, f_{\text{cut}} = 5\%$)	
Small-R Jets	$p_T > 30$ GeV $ \eta < 4.5$	anti- k_T $R = 0.4$ EMTopo	$JVT > 0.59$ if $p_T < 60$ GeV, $ \eta < 2.4$

Table 4.1: A concise summary of the key object selections used in the analysis.

4.3.1 Overlap removal

At the end of the object selection an overlap removal procedure is applied when two or more selected analysis objects are believed to represent the same particle. Two types of overlap removal are considered:

- Overlap removal between electrons, muons, and jets;
- Overlap removal between large-R jets and leptons: Large-R jets are removed within a cone size of 1.0 around a selected loose lepton. Two close-by electrons from a boosted Z boson can fake a hadronic large-R jet while still maintaining individually reconstructed electron constituents, so these large-R jets are removed to avoid double counting.

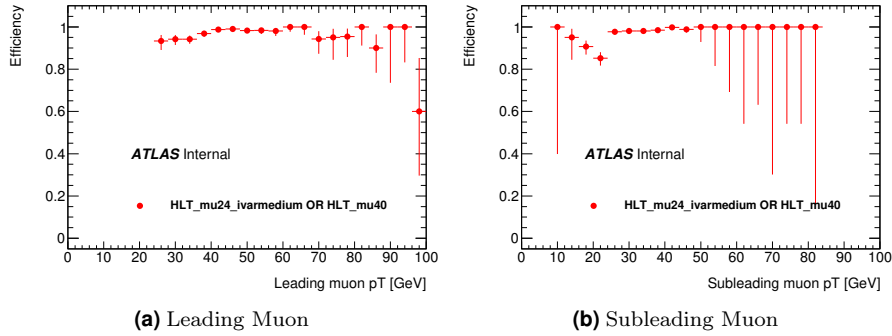
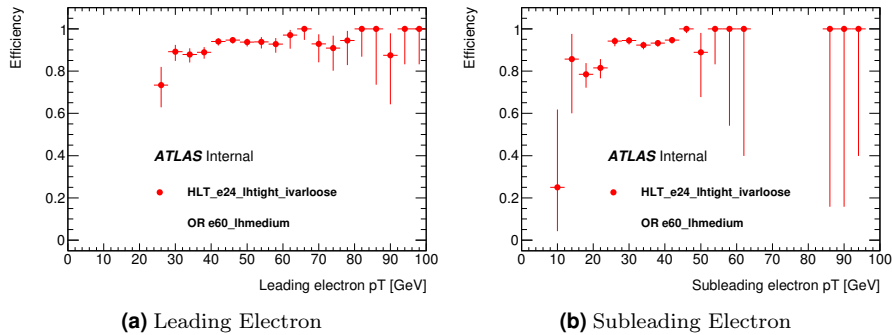
4.4 $ZZ \rightarrow \ell\ell qq$ channel: the event selection

This section describes the event selection. My work has been mostly devoted to optimize the selection of the events in order to maximize the expected significance of the signal over background. A set of preselection cuts are applied first, including trigger requirements and a dilepton system compatible with $Z \rightarrow \ell\ell$ process. Then the signal region is defined with two small-R jets or one boosted boson jet.

4.4.1 Trigger

The unrescaled single lepton triggers with the lowest momentum threshold are used in this analysis and are summarized in Table 4.2. The efficiencies of the isolated triggers are slightly lower than the non-isolated triggers. The efficiencies at the plateau of the single lepton triggers is about 95%. Figures 4.1 and 4.2 show the trigger efficiency relative to the leptons selected for analysis (as described in sec. 4.4.2) as a function of p_T for the logical OR of the single lepton triggers for data taken in run 297730. We require either lepton to pass the single lepton triggers. The lowest unrescaled single lepton triggers have the p_T threshold at 26 GeV.

Period	Electron triggers	Muon triggers
2015	HLT_e24_lhmedium_L1EM20VH HLT_e60_lhmedium HLT_e120_lhloose	HLT_mu20_loose_L1MU15 HLT_mu50
2016	HLT_e24_lhtight_nod0_ivarloose HLT_e60_lhmedium_nod0 HLT_e60_medium HLT_e140_lhloose_nod0	HLT_mu24_loose HLT_mu24_ivarloose HLT_mu40 HLT_mu50 HLT_mu24_ivarmedium HLT_mu24_imedium

Table 4.2: The list of triggers used in the analysis.

Figure 4.1: The muon trigger efficiency as a function of p_T for a) the leading muon, and b) the subleading muon for data events taken in run 297730. The efficiency for the single lepton triggers (HLT_mu24_ivarmedium and HLT_mu_40) is shown, relative to muons passing the event preselection where only one muon is required to pass the triggers.

Figure 4.2: The electron trigger efficiency as a function of p_T for a) the leading electron, and b) the subleading electron for data events taken in run 297730. The efficiency for the single lepton triggers (HLT_e24_lhtight_ivarloose, and HLT_e60_lhmedium) is shown relative to electrons that pass the event preselection, where only one electron is required to pass the triggers.

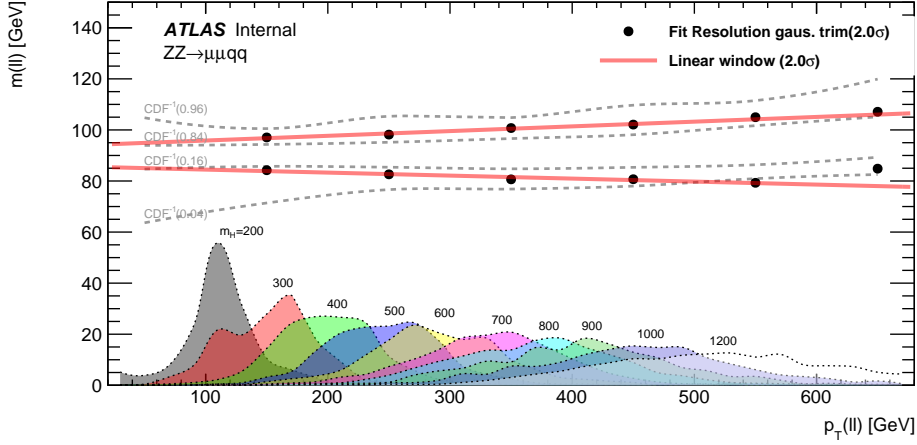


Figure 4.3: 2σ bound of fit to dimuon mass for H signal and SR cut window over the mass range of the search (to be updated). Signal PDFs are shown at bottom in the $p_T(\ell\ell)$ distribution.

4.4.2 $Z \rightarrow \ell\ell$ preselection

Events are retained for analysis if they were recorded with all detector systems operating normally and pass event- and jet-level cleaning requirements [137]. Event vertices are formed from tracks with $p_T > 400$ MeV. If an event contains more than one vertex candidate, the one with the highest $\sum p_T^2$ of its associated tracks is selected as the primary vertex. All events are required to have one primary vertex with at least two associated tracks.

The $ZZ \rightarrow \ell\ell qq$ event selection begins with the identification of the $Z \rightarrow \ell\ell$ candidate. The $Z \rightarrow \ell\ell$ candidate is selected by requiring two "loose" same flavor leptons, with at least one of them satisfying the "medium" requirement. If the event consists of two muons, they are required to have opposite charge. No such requirement, however, is applied for two electrons to minimize efficiency loss due to charge mismeasurements. The dilepton invariant mass is required to be in the range of $83 - 99$ GeV for electrons and fall within a $p_T(\ell\ell)$ -dependent window, $-0.0117p_T(\ell\ell) + 85.63 < m(\ell\ell) < .0185p_T(\ell\ell) + 94.00$ GeV for muons. Both windows are consistent with the Z boson mass, drawn in Figs. 4.3 and 4.4 showing the signal PDFs in $p_T(\ell\ell)$ and quantile functions in $m(\ell\ell)$ used for easy validation of the windows over the dilepton p_T -spectrum of the search.

The increasing mass window for muons is to ensure high selection efficiency for high p_T Z bosons as the momentum resolution of the muons from these Z boson decays is significantly degraded. The effect of widening the mass window is a gain of acceptance of about 3% for a gluon-fusion signal with $m_H = 700$ GeV and about 5% for a gluon-fusion signal with $m_H = 2200$ GeV.

4.4.3 $Z \rightarrow q\bar{q}$ selection

The reconstruction of the $Z \rightarrow qq$ decay is split into two categories: the resolved and the merged category. The resolved category contain events with two separate small-radius jets (small- R jet, or j) of hadrons from a Z , while the merged category uses jet-substructure techniques to identify the $Z \rightarrow qq$ decay reconstructed as a single large-radius jet (large- R jet, or simply J). The merged category events is expected when the resonance mass is significantly higher than the Z boson mass. In this case, the Z boson is boosted and the qq pair from its decay can be collimated and they are more efficiently reconstructed as a single large- R jet.

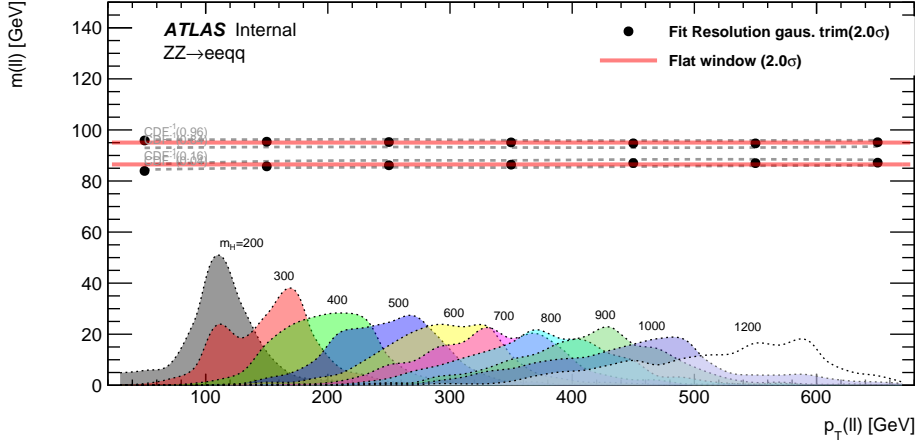


Figure 4.4: 2σ bound of fit to dielectron mass for H signal over the mass range of the search (to be updated), well within cut chosen.

Resolved category

Over most of the mass range considered in this analysis ($m_X \lesssim 700 \text{ GeV}/c^2$), the $Z \rightarrow q\bar{q}$ decay results in two well-separated jets that can be individually resolved. For this category, events are selected containing at least two jets as defined in 4.3 with a $p_T > 25 \text{ GeV}$ in addition to the $Z \rightarrow \ell\ell$ candidate described above.

For $Z \rightarrow q\bar{q}$, a relatively large fraction (21%) of signal events contains b -jets, coming from $Z \rightarrow b\bar{b}$, while those are rare in the $Z + \text{jets}$ process that forms the dominant background. This feature is exploited by dividing the two leptons plus two jets sample into a "tagged" subchannel, containing events with two b -tags, and an "untagged" subchannel, containing events with less than two b -tags. Any events with more than two b -tags are rejected.

The two jets that are selected for the rest of the analysis differ by subchannel. For events with exactly two b -tagged jets, i.e. those in the "tagged" subchannel, the two b -tagged jets are chosen to reconstruct the hadronic Z . For events in the "untagged" subchannel with 1 b -tagged jet, the b -tagged jet and the non- b -tagged jet with the highest p_T are selected; while for events with 0 b -tagged jet, the two jets with the highest p_T are selected, regardless of their b -tagged status.

After selecting the two jets of interest, the leading jet of the two is required to have $p_T > 60 \text{ GeV}$. Various distributions of the kinematics of the two leading jets after this requirement are shown in Figs. 4.5 and 4.6.

In addition, a topological cut on the momentum balance of the system is introduced to select events with two recoiling bosons. The ratio

$$\frac{\sqrt{p_T^2(\ell\ell) + p_T^2(jj)}}{m(\ell jj)} \quad (4.2)$$

is required to have a value > 0.5 for both WZ and ZZ signal region. This cut is dropped for the "tagged" subchannel in ZZ signal region to boost data and Monte Carlo statistics. The effect on the significance for that subchannel is minimal. Fig. 4.7 shows the distribution of this ratio.

The final cut is placed on the dijet mass. To select events that are consistent with a hadronically decaying Z (W) boson, we require $70(62) < m_{jj} < 105(97) \text{ GeV}$. The m_{jj} range is larger than the $m_{\ell\ell}$ range because the jet energy resolution is worse than that of leptons.

The resulting resolution of $m_{\ell jj}$ in the gluon-fusion signal samples is found to be about 4% of the resonance mass. This is slightly larger in the ZZ "tagged" subchannel due to worse b -jet resolution.

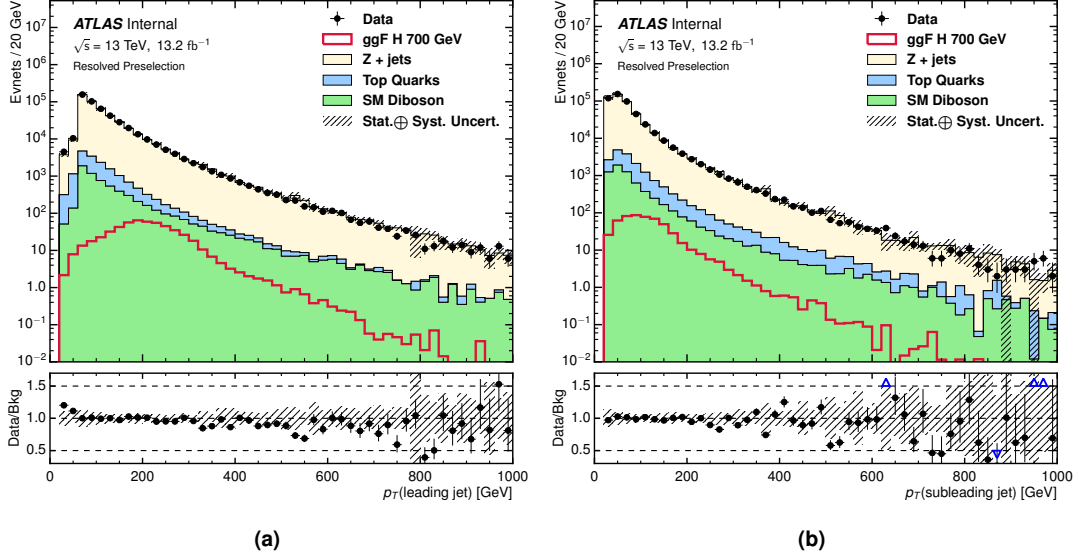


Figure 4.5: The p_T distributions for the leading (a) and subleading (b) small-R jets after requiring the leading jet $p_T > 60$ GeV in the resolved selection (inclusive, no categorization applied). The shaded area (hatching) in the bottom ratio plots represents the total uncertainty (statistical + systematic) on the distribution.

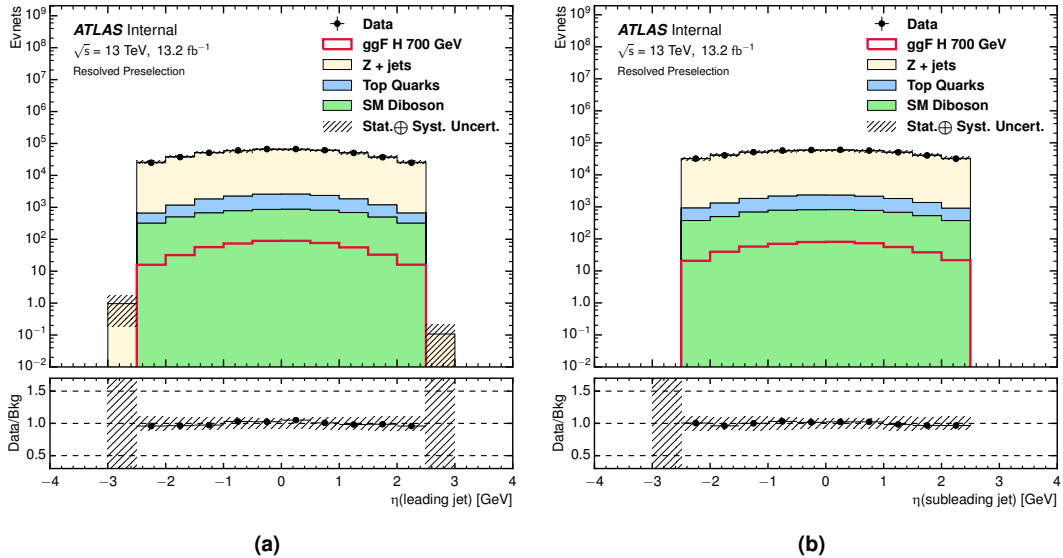


Figure 4.6: The η distributions for the leading (a) and subleading (b) small-R jets after requiring the leading jet $p_T > 60$ GeV in the resolved selection (inclusive, no categorization applied). The shaded area (hatching) in the bottom ratio plots represents the total uncertainty (statistical + systematic) on the distribution.

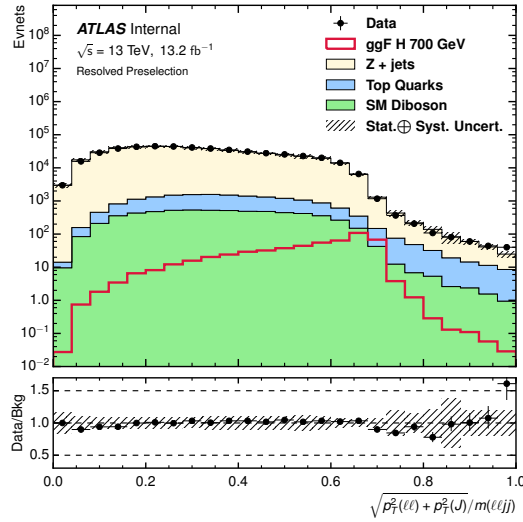


Figure 4.7: The topological ratio distribution for the two selected jets after requiring the leading jet $p_T > 60$ GeV in the resolved selection (inclusive, no categorization applied). The shaded area (hatching) in the bottom ratio plots represents the total uncertainty (statistical + systematic) on the distribution.

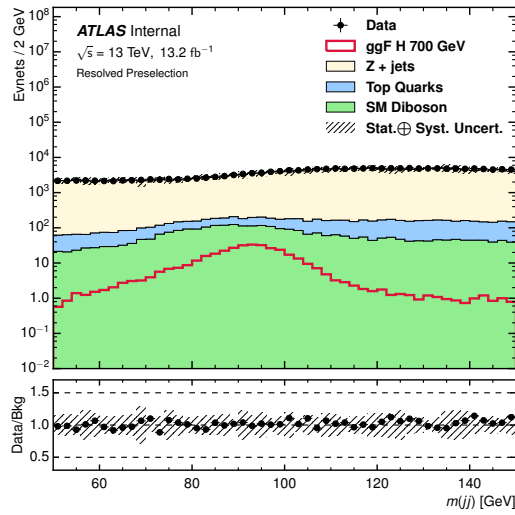


Figure 4.8: The dijet mass distribution for the two selected jets after cutting on the topological ratio in the resolved selection (inclusive, no categorization applied). The shaded area (hatching) in the bottom ratio plots represents the total uncertainty (statistical + systematic) on the distribution.

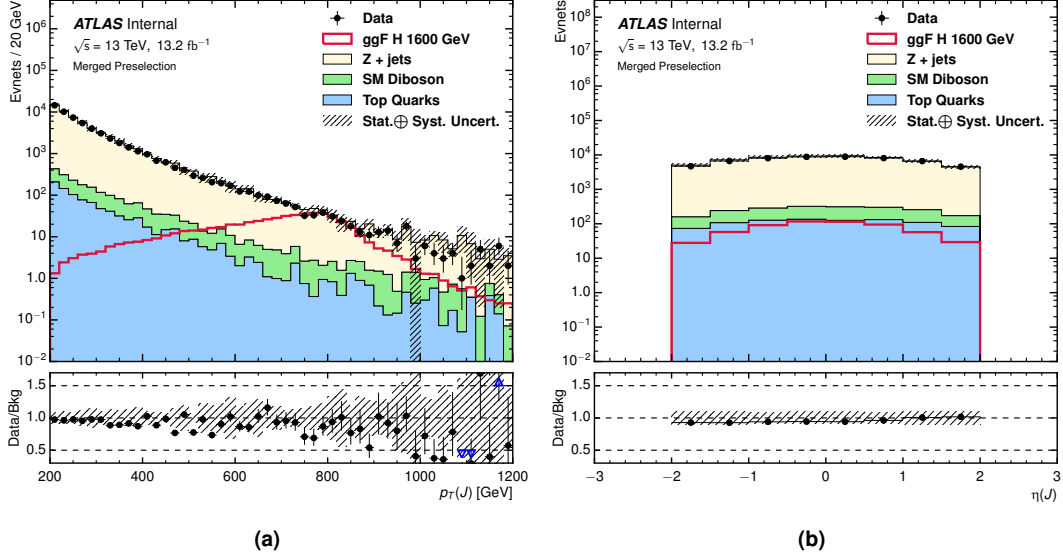


Figure 4.9: The p_T and η distributions for the leading large-R jet after requiring at least one large-R jet in the merged selection (inclusive, no categorization applied). The shaded area (hatching) in the bottom ratio plots represents the total uncertainty (statistical + systematic) on the distribution.

Merged category

For large resonance masses, namely $m_X \geq 700 \text{ GeV}/c^2$, the hadronic W/Z bosons can also often be reconstructed as a large-R jet, as explained in . For this category, events are selected containing at least one large-R jet on top of event and $Z \rightarrow \ell\ell$ preselection. Various distributions of the kinematics of the leading large-R jet are shown in Fig. 4.9.

The leading large-R jet is selected for consideration in the rest of the analysis. After selecting this jet, we make a similar momentum balance selection as in the resolved analysis. We require the ratio

$$\frac{\min[p_T(\ell\ell), p_T(J)]}{m(\ell\ell J)} \quad (4.3)$$

to have a value > 0.3 for spin-0 signals, and > 0.35 for spin-1 and spin-2 signals. Fig. 4.10 shows the distribution of this ratio.

Events are then subject to the boson tagging.

High purity and low purity merged category

To enhance sensitivity of the analysis, two signal regions (or categories) are considered to distinguish backgrounds in boosted topologies at high mass based on the energy correlation function D_2 (see details in section 4.3):

- high-purity signal region: leading large-R jet passes $D_2(J)$ cut
- low-purity signal region: leading large-R jet fails $D_2(J)$ cut.

The distributions of the tagging variables, $D_2^{(\beta=1)}$ variable and the leading large-R jet mass, are shown in Fig. 4.11. As expected, the large-R jet mass of the signal events are clustered around the mass of the vector boson while the background events have largely smooth distributions. Since we are only considering signal coming from Z bosons, we apply the Z boson trained cuts (for the boson tagging see section 4.3) for the ZZ signal region respectively.

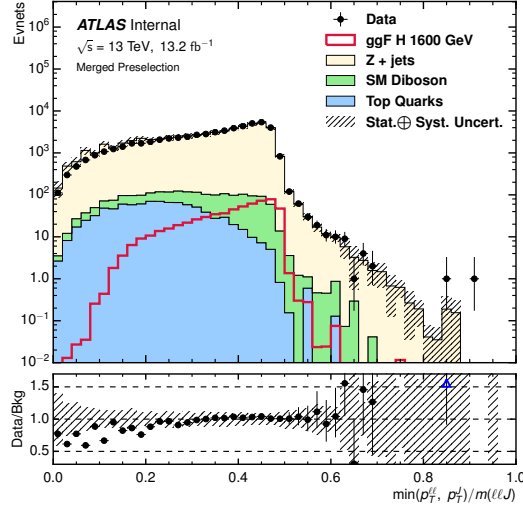


Figure 4.10: The topological ratio distribution for the leading large-R jet after requiring at least one large-R jet in the merged selection (inclusive, no categorization applied). Note that the data/MC disagreement region is the region in which the events are not selected. The shaded area (hatching) in the bottom ratio plots represents the total uncertainty (statistical + systematic) on the distribution.

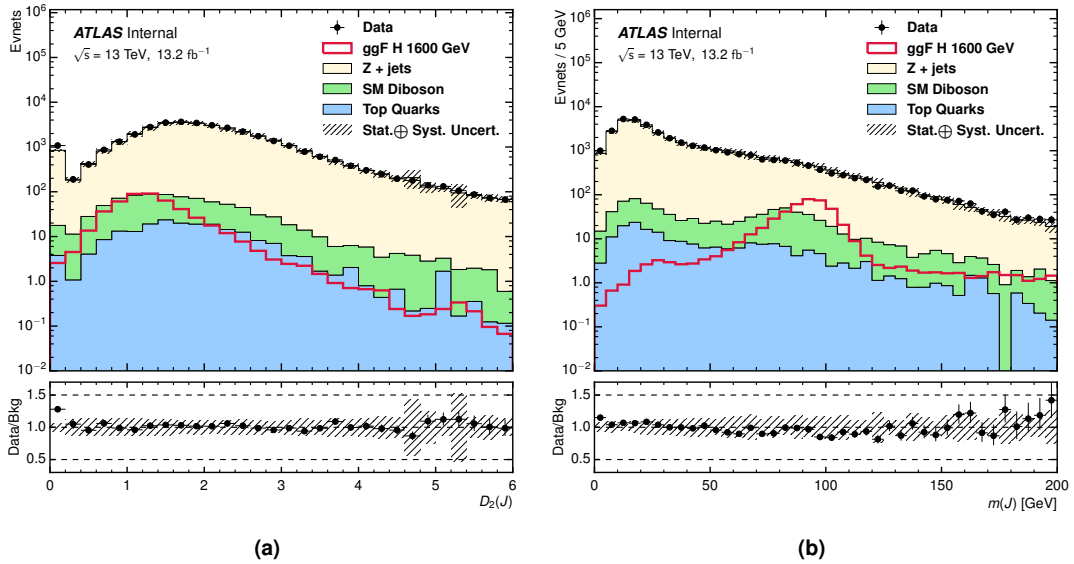


Figure 4.11: The $D_2^{(\beta=1)}$ and mass distributions for the leading large-R jet after cutting on the topological ratio in the merged selection (inclusive, no categorization applied). The shaded area (hatching) in the bottom ratio plots represents the total uncertainty (statistical + systematic) on the distribution.

Since the Z boson tagging efficiency is only 50%, signal acceptance drops significantly after applying this cut. To recover the loss of signal acceptance and without degrading the search sensitivity, a low purity merged category is introduced. The low purity category is defined as events failing the $D_2^{(\beta=1)}$ cut but passing the Z boson mass cut.

Although it is expected that sensitivity of the analysis is dominated by the high-purity region, the low-purity one is nevertheless retained because for a heavy resonance it provides improved signal efficiency with moderate background contamination (mostly Z +jets in this analysis). By adding the low-purity signal region, a clear improvement in the sensitivity of the experiment is observed as shown in Fig.4.12. The improvement is about 10% quantitatively in terms of significance in the next section.

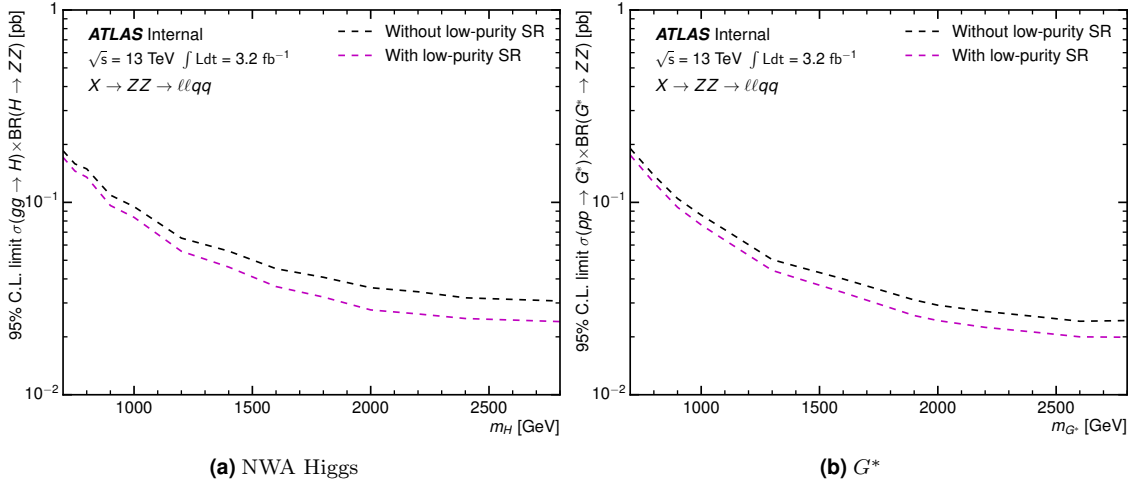


Figure 4.12: Comparison of the expected limits with and without the addition of low-purity signal region for NWA Higgs (left) and G^* (right).

Unlike in the resolved category, the merged analysis does not split events into subchannels based on the number of b -tagged jets.

The resulting resolution of m_{llj} in the gluon-fusion Higgs signal samples is found to be about 4% of the resonance mass, as in the "untagged" resolved subchannel.

4.4.4 Mass constraint

To improve the dilepton mass resolution, especially for the $\mu\mu$ channel events, the p_T of the dilepton system are scaled event-by-event by a single multiplicative factor to set the dilepton invariant mass $m_{\ell\ell}$ to the mass of the PDG Z boson (m_Z). This improves the $m_{\ell\ell j}$ resolution by about 30% at 2 TeV.

To improve the dijet mass resolution for the resolved signal region, a similar approach as for $Z \rightarrow \ell\ell$ mass constraint is applied to the dijet system. For ZZ signal region, m_{jj} is set to m_Z .

4.5 Vector boson fusion process: a dedicated selection

An important contribution to the production of scalar signals is the vector boson fusion process (VBF). In this process, two vector bosons are radiated from quarks in the colliding protons, which then produce a heavy particle through their normal interaction vertex. For the Standard Model Higgs boson, VBF production accounts for roughly 10% of the total production cross section.

VBF production is characterized by extra jets in the event. These jets are usually in the forward section of the detector, and will have a large separation in pseudorapidity between them. The two

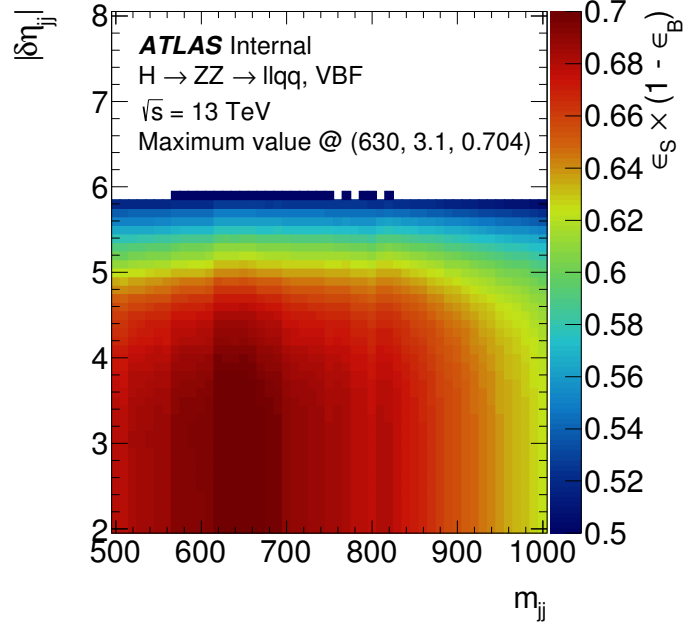


Figure 4.13: Selection optimization on the two VBF variables using signal efficiency times background rejection. The optimal cut values are found at $m_{jj}^{\text{tag}} = 630$ GeV and $|\Delta\eta_{jj}^{\text{tag}}| = 3.1$

variables used in this analysis to select VBF jets are the invariant mass of the jet pair m_{jj}^{tag} , and the absolute value of the difference between their pseudorapidities $|\Delta\eta_{jj}^{\text{tag}}|$. After having identified the two small-R or one large-R jet from the boson decay, the VBF jets are selected as the pair of remaining small-R jets that have opposite pseudorapidity signs and have the highest invariant mass. If the event has been categorized as a merged event, the two VBF jets are required to be outside of $|\Delta R| < 1.5$ of the large-R jet selected for the merged analysis. This value is chosen to ensure that there is no double counting of the jet energy between the large-R jet and the VBF jet.

The selection on VBF jets are:

- $m_{jj,\text{tag}} > 630$ GeV,
- $\Delta\eta_{jj,\text{tag}} > 3.1$.

Detailed optimization study on VBF jet selection is documented in next section.

Events failing the VBF selection are categorized as ggF, and the splitting of VBF and ggF categories is done after the final event selection described above.

4.5.1 VBF selection optimization

One of the most important task of my work has been the study on the characterization of the VBF component. Optimizations on the VBF variables were performed in two ways. The first is based on optimizing the selection efficiency of VBF signal samples times the background rejection of all backgrounds after cutting on these variables. The second is based on optimizing the estimated significance after cutting on these variables, calculated using the asymptotic formula and summed in quadrature over 50 GeVbins in the final invariant mass spectra. Values were scanned between $500 < m_{jj}^{\text{tag}} < 1000$ GeV in steps of 10 GeV and $3 < |\Delta\eta_{jj}^{\text{tag}}| < 7$ in steps of 0.1. This procedure was performed for all VBF signal samples between signal mass of 300 GeV and 2000 GeV, then averaged together. Results from this optimization can be seen in Figs.4.13 and 4.16.

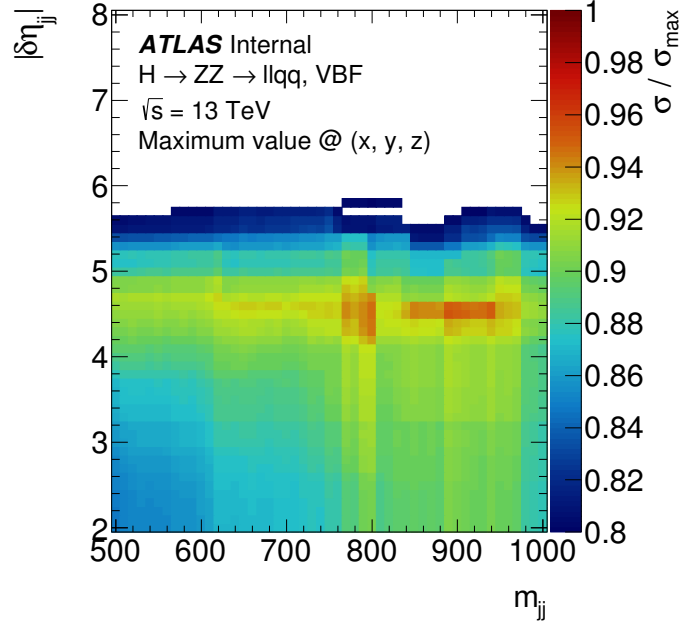


Figure 4.14: Selection optimization on the two VBF variables using estimated significance. Two clear optimal cut values are found, at $m_{jj}^{\text{tag}} = 800$ GeV and $m_{jj}^{\text{tag}} = 890$ GeV, both with $|\Delta\eta_{jj}^{\text{tag}}| = 4.5$

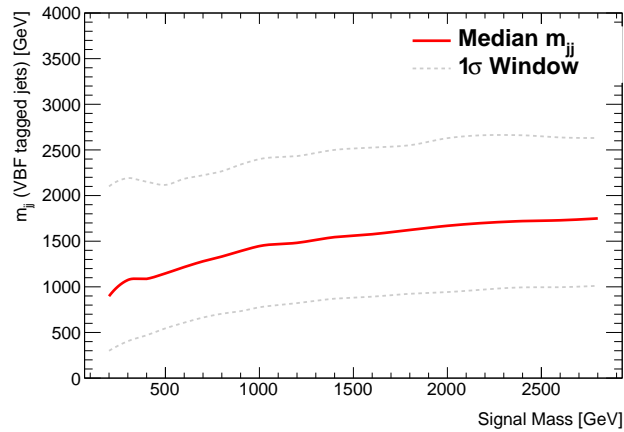


Figure 4.15: Median m_{jj} of VBF tagged jets with a one σ window, as a function of signal mass.

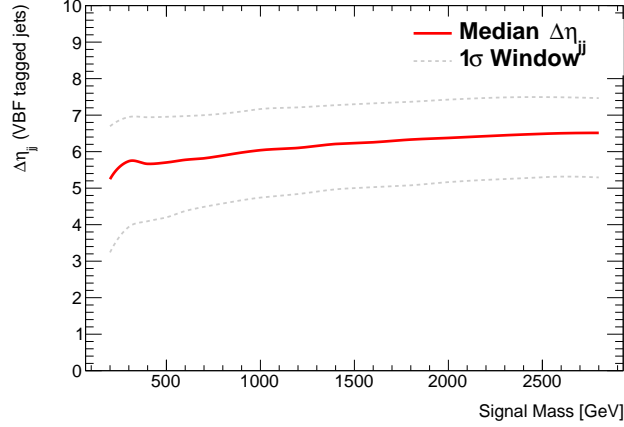


Figure 4.16: Median $\Delta\eta_{jj}$ between VBF tagged jets with a one σ window, as a function of signal mass.

4.6 Background

This section introduces the various background in this analysis. Control regions are introduced for the major backgrounds ($Z + \text{jets}$ and top processes), which are designed to constrain the overall contribution of the background in our signal regions. Additional, smaller backgrounds are estimated directly from Monte Carlo. One of my tasks was to study the $Z + \text{jets}$ background for both merged and resolved regime.

4.6.1 Z control region

To estimate the contribution of the dominant $Z + \text{jets}$ background, we use a control region where an event passes the nominal signal region selection but fails the di-jet mass cut. In particular, for the resolved analysis, we require $50 \text{ GeV} < m_{jj} < 70 \text{ GeV}$ or $105 \text{ GeV} < m_{jj} < 150 \text{ GeV}$. For the merged analysis, the leading large- R jet must pass the substructure cut, but fail the mass cut, both of which vary based on the p_T of the jet in consideration, for the high purity category, and to fail both mass and substructure cuts for the low purity category. We call this region the Z control region, or "ZCR".

The normalization of the $Z + \text{jets}$ is taken from a fit to the data in the control region, which defines a global scale factor to be applied to the signal region. In addition, the resolved $Z + \text{jets}$ background is split into six separate categories based on the truth classification of the two selected jets for the final discriminant. The categories used are:

- two truth b jets, or $Z + bb$;
- one truth b jet and one truth c jet, or $Z + bc$;
- one truth b jet and one truth light jet, or $Z + bl$;
- two truth c jets, or $Z + cc$;
- one truth c jet and one truth light jet, or $Z + cl$;
- two truth light jets, or $Z + ll$.

The "tagged" subchannel has been designed such that it is predominantly coming from the $Z + bb$ background. As such, the "tagged" Z control region will largely be used for constraining this scale factor, while the "untagged" Z control region will be used for constraining the $Z + l$ contribution.

The shape of the $Z + \text{jets}$ background in the merged category and the "untagged" subchannel are taken directly from Monte Carlo in both the Z control region and the signal region. Due to the powerful discrimination of the MV2c10 tagger against non- b -jets, truth tagging is therefore used in "tagged" subchannel for events in which either of the selected jets is not a truth-matched b -jet to ensure reasonable statistics.

Plots of the Z control region are located in section 4.7, after the description of the event categorization.

$Z + \text{jets}$ MC smoothing

The $Z + \text{jets}$ Monte Carlo background estimation suffers from low statistics in the tails of the signal region. To smooth the tails of the $Z + \text{jets}$ distributions, we use a functional form fit of the shape. Tests were performed fitting the $Z + \text{jets}$ background with different functional forms, and the chosen function was the di-jet function, which yielded the lowest χ^2 . The di-jet function is defined by equation 4.4:

$$f(m_{\ell\ell J}) = p_0 \frac{\left[1 - \left(\frac{m_{\ell\ell J}}{\sqrt{s}}\right)\right]^{p_1}}{\left(\frac{m_{\ell\ell J}}{\sqrt{s}}\right)^{p_2 + p_3 \log(m_{\ell\ell J}/\sqrt{s})}} \quad (4.4)$$

where \sqrt{s} is the centre of mass energy, p_0 , p_1 , p_2 and p_3 are free parameters, and $m_{\ell\ell J}$ is expressed in GeV.

The fitting range used varies according to the region the distributions are being fitted, due to stability and goodness of the fits. It varies between 400 to 4000 GeV.

Figure 4.17 shows the fit for the merged high purity signal region in the scalar ggF selection, as well as the residue and pull plots. We can see that the functional form can describe well the shape trend in the tails.

After the fit is performed, we use the functional form to fill the histogram in the corresponding signal region. The final smoothed histogram will take the Monte Carlo values as they are up to 400-1000 GeV (signal region dependent), where the residue of the functions start being smaller. From the chosen threshold onwards, the functional form is used to set the bin content, by taking the integral of the functional form in the range corresponding to the lower and upper values of the bin, and dividing by the bin width. We can see the resulting background in Fig. 4.18.

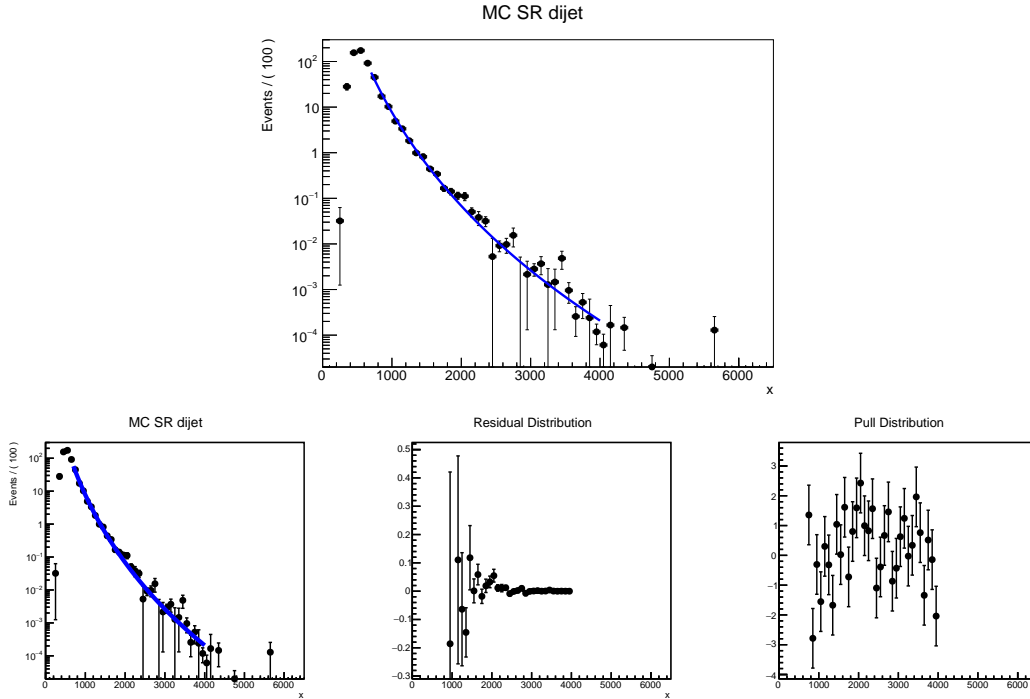


Figure 4.17: Top: Fit of the Z+jets Monte Carlo in the merged high purity ggF spin 0 signal region. Bottom: Fitting of the Z+jets Monte Carlo in the merged high purity ggF spin 0 signal region (left), the residues (centre) and pull plots (right).

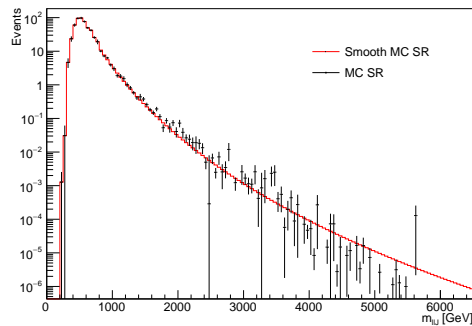


Figure 4.18: The comparison between the smoothed histogram (red) and the original MC distribution (black points), for the Z+jets signal region in the merged high purity ggF spin 0 category.

Data-driven Z +jets estimation

The Z +jets control region can also be used to estimate the background in the signal region, using the α ratio method. The data in the Z +jets control region is compared to the MC in the same control region, to check for good agreement (Fig. 4.19). Then the data in the CR is multiplied by the α ratio, defined as the ratio of the MC yields in the signal and the control region (Figs. 4.19(b)):

$$\alpha(m_{\ell\ell J}) = \frac{MC(SR)}{MC(CR)} \quad (4.5)$$

The CR data corrected by the α ratio (blue dots in Fig. 4.19 (c)) is then the data-driven background estimation of the signal region. We can then compare that estimation with the MC in the signal region.

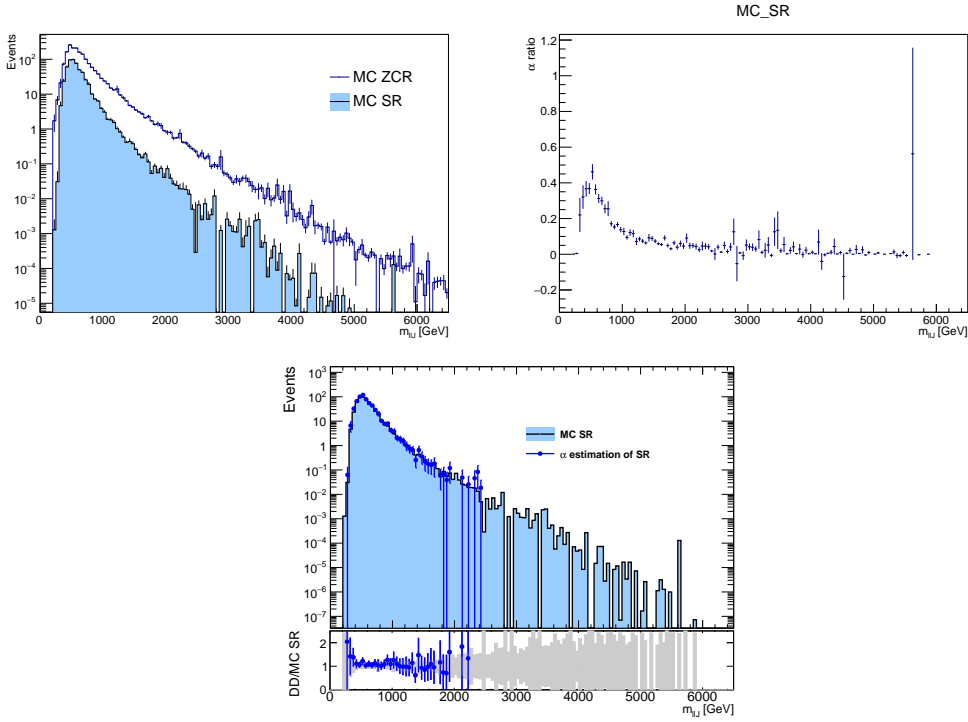


Figure 4.19: The comparison of MC in the Z +jets signal and control region (a), the α ratio (b), and the data driven background taken from the Z +jets control region compared to the MC in the ZZ signal region (c). All plots are done for the merged high purity ggF spin 0 category.

There are several advantages in using the differential ratio $\alpha(m_{\ell\ell J})$ for the background modeling of the $m_{\ell\ell J}$ distributions:

- The larger statistics available in the Z +jets control region;
- The background estimation gets insensitive to several systematic effects (e.g. the luminosity of the collected sample, pile-up corrections, etc) which cancel out in the $\alpha(m_{\ell\ell J})$ ratio;
- The $\alpha(m_{\ell\ell J})$ ratio is less sensitive to mismodeling of the matrix element calculation for the background and to theory systematics (e.g. normalization and factorization scale, PDFs, etc.) since the background composition is similar in the two regions.

For the W + jets I see very small contamination in the regions of interest so I neglected it.

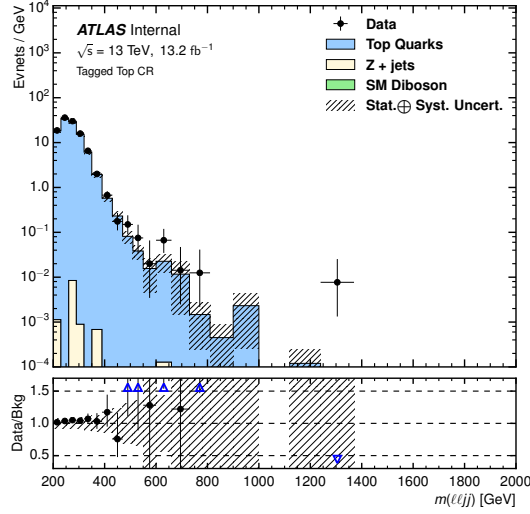


Figure 4.20: The m_{lljj} distribution in the Top control region.

4.6.2 Top control region

The subdominant background comes from single t and $t\bar{t}$ production, as leptonic W decays coming from t decays can cause events with the same final state as a diboson ZZ event. To estimate the contribution of these background, we use a control region of events with a different flavor lepton pair, namely $e\mu$. This simple requirement causes this control region to be very pure in t backgrounds. To help increase statistics in this control region, the cut on the dilepton mass is relaxed to be within the range of $76 \text{ GeV} < m_{ll} < 106 \text{ GeV}$. In addition, this control region is required to be in the "tagged" subchannel, as the top quark predominantly decays to a bottom quark. No requirement is made on the dijet mass of the event. Fig. 4.20 shows the distribution of m_{lljj} in the final Top control region.

The normalization of the t backgrounds is taken from a fit to the data in the control region, and the shape is taken from Monte Carlo.

4.6.3 Diboson backgrounds

The next largest background is from diboson WW , WZ , and ZZ production. ZZ/WZ contributes as an irreducible background in the exact final state of our signal, however is subject to a much smaller cross section than $Z + \text{jets}$ production. WW cannot have the same final state, and as such is almost completely outside of our signal and control regions.

The normalizations of these backgrounds are estimated completely from Monte Carlo. The shapes of these backgrounds for the "untagged" subchannel and the merged channel are taken from Monte Carlo directly. Similar to the $Z + \text{jets}$ background, truth tagging method is used for all the events to obtain the shape of m_{lljj} distribution in the tagged subchannel. However, the tagged distribution is normalized to the yield obtained with the direct tagging.

4.7 Event Categorization

The event selections before ggF and VBF splitting are summarized in Table 4.3 and 4.4 for resolved and merged respectively. The signal region (SR) and the control region (CR) definitions are included in the tables.

Each event used by this analysis is placed into one of $14 + 1$ categories, where the 14 are best understood as the result of 4 roughly binary classifications and the last is the top control region.

Events are classified according to the following four criteria:

- $Z \rightarrow q\bar{q}$ jet mass window (SR and ZCR)
- b -tagging (tagged and untagged) for small-R jets and W/Z -tagging (merged and low-purity) for large-R jets
- VBF jet selection criteria
- one large-R jet (merged) vs. two small-R jets (resolved)

This categorization fails to fully describe the selection process with regard to two key points: the overlapping reconstruction of calorimeter activity as two small-R jets and a single large-R jet, and the priority of small-R jet usage in the Z -mass window criteria and the VBF selection criteria. The precise details regarding the prioritization of the above selections is discussed in the following subsections in addition to the specific VBF selection criteria. The details of b -tagging of small-R jets and W/Z -tagging of large-R jets have already been discussed in Sec. 4.4.3. The signal and control regions schematic representations are shown in Figs. 4.21-4.22, for spins 0 and 2 signal hypothesis, respectively.

Selection	Resolved	
	SR	CR
Preselection	Single lepton triggers exactly 2 loose leptons, ≥ 1 medium lepton	
$Z \rightarrow \ell\ell$	$83 < m_{ee} < 99$ GeV $-0.01170p_{\text{T}}^{\ell\ell} + 85.63 < m_{\mu\mu} < 0.01850p_{\text{T}}^{\ell\ell} + 94.00$ GeV	
Opposite sign	For $\mu\mu$ channel only	
Signal jets	At least two small-R central jets Leading jet $p_{\text{T}} > 60$ GeV Subleading jet $p_{\text{T}} > 30$ GeV	
p_{T} ratio	$\frac{\sqrt{p_{\text{T}}^2(\ell\ell) + p_{\text{T}}^2(jj)}}{m(\ell\ell jj)} > 0.4$ (0.5) for spin-0 (2) in untagged regions	
$Z \rightarrow q\bar{q}$ $W \rightarrow qq'$	$70 < m_{jj} < 105$ GeV $62 < m_{jj} < 97$ GeV	$50 < m_{jj} < 62$ GeV or $105 < m_{jj} < 150$ GeV
b -tagging (ZZ only)	"tagged": 2 b -jets "untagged": 0 or 1 b -jet	

Table 4.3: Event selection summary for resolved analysis.

Selection	Merged			
	High purity		Low purity	
	SR	CR	SR	CR
Preselection	Single lepton triggers exactly 2 loose leptons, ≥ 1 medium lepton			
$Z \rightarrow \ell\ell$	$83 < m_{ee} < 99$ GeV $-0.01170p_{\text{T}}^{\ell\ell} + 85.63 < m_{\mu\mu} < 0.01850p_{\text{T}}^{\ell\ell} + 94.00$ GeV			
Opposite sign	For $\mu\mu$ channel only			
Signal jets	At least one large-R jet Leading jet $p_{\text{T}} > 200$ GeV			
p_{T} ratio	$\frac{\min(p_{\text{T}}(\ell\ell), p_{\text{T}}(J))}{m(\ell\ell J)} > 0.3$ (0.35) for spin-0 (2) signal			
$Z \rightarrow q\bar{q}$	$D_2^{(\beta=1)}(Z) \& \& m(Z)$	$D_2^{(\beta=1)}(Z) \& \& !m(Z)$	$!D_2^{(\beta=1)}(Z) \& \& m(Z)$	$!D_2^{(\beta=1)}(Z) !m(Z)$

Table 4.4: Event selection summary for merged analysis. For Z boson tagging, it's divided into two separate cuts: substructure ($D_2^{(\beta=1)}$) cut and mass (m) cut. $D_2^{(\beta=1)}(Z)$ means $D_2^{(\beta=1)}$ cut for Z boson, while $!D_2^{(\beta=1)}(Z)$ means the large-R jets should fail. Similar nomenclature applies to the mass (m) cut.

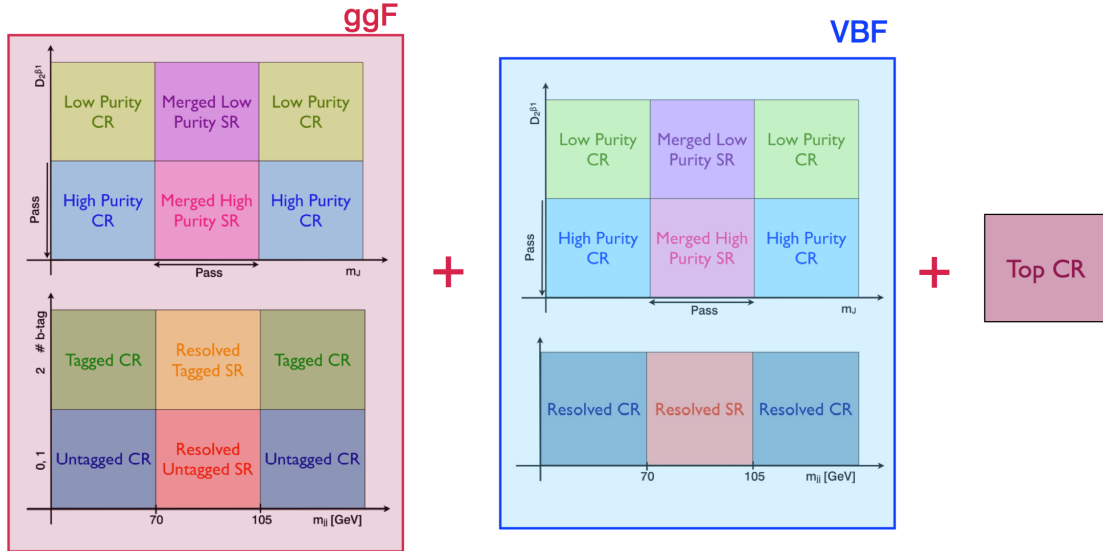


Figure 4.21: The event categories in the spin 0 analysis: the events are separate in ggF or VBF production modes. The ggF has 8 regions: 2 merged signal regions (high and low purity), 2 merged control regions (high and low purity), 2 resolved signal regions (untagged and tagged), 2 resolved control regions (untagged and tagged). The VBF has 6 regions: 2 merged signal regions (high and low purity), 2 merged control regions (high and low purity), 1 resolved signal region and 1 resolved control region (both inclusive in b-tag categories). Additionally, there is one top control region.

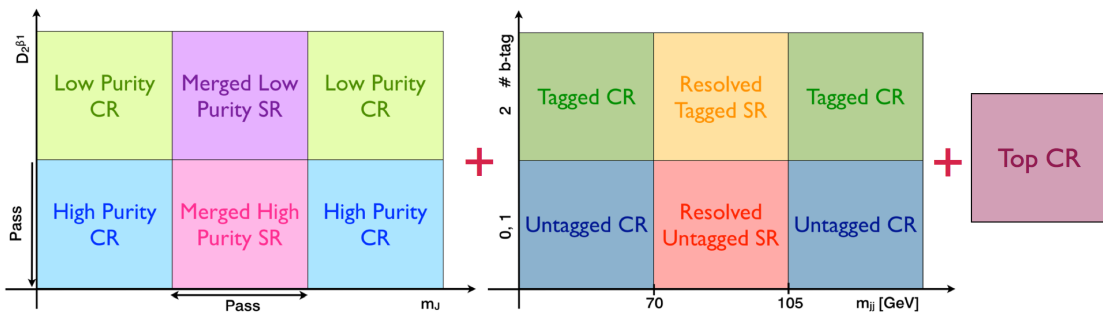


Figure 4.22: The event categories in the spin 2 analysis: There are 9 regions in total: 2 merged signal regions (high and low purity), 2 merged control regions (high and low purity), 2 resolved signal regions (untagged and tagged), 2 resolved control regions (untagged and tagged). Additionally, there is one top control region.

4.7.1 Event Prioritization and Recycling

For events which satisfy both the small-R jet preselection for the resolved regime and the large-R jet preselection for the merged regime the following is used to classify events with respect to jet regime, region, and signal category. When an event fails a given selection it is tested on the next according to its priority; this is termed “recycling”. Only upon failing all selections is an event discarded. The order of selections is as follows:

- Merged SR
- Low Purity SR
- Resolved SR
- Merged ZCR
- Low Purity ZCR
- Resolved ZCR.

The phase space considered in this search where the recycling strategy is most important is roughly in the transition region from $500 \leq m_H \leq 800$ GeV. Above and below these signal masses hadronic decays of the $Z \rightarrow q\bar{q}$ are reconstructed primarily as either merged or resolved, respectively, but small differences in signal to background significance are found over the full mass range. The recycling strategy is considered to be superior to a fixed cut strategy on the basis of saving more signal events, no matter the cut optimization. The placing of merged prior to resolved was determined by studies using signal to background optimization, see section 4.7.2, and confirmed with the 2015 expected limits under each.

For the scalar signal benchmark, when the VBF regions are also present, the events will first be tested if they pass the VBF selection criteria, and added to the ggF region otherwise. The order of selection inside each of the VBF and ggF regions follows the same order described above.

4.7.2 Details of event categorization

Another important part of my work has been the study of the event categorization and in particular to define the optimal order of all the selections. A first study has been made in categorizing an event as either ggF or VBF. Selecting ggF or VBF one must consider the order in which you select the jets that come from the $Z \rightarrow q\bar{q}$ from the resonance decay and the jets that come from the valence quarks in the colliding protons. In the categorization scheme for this analysis, the decision to first find the reconstructed Z boson, then to select the VBF jets was made for two reasons:

- the expected limits from selecting the VBF jets second was shown to be 10% stronger than the other order, and
- selecting the VBF jets second allows for the $Z \rightarrow q\bar{q}$ selection to be consistent for all signal selections, including those which do not have a ggF/VBF split.

Moreover the event categorization is important at intermediate masses of the signals where boosted and resolved topologies overlap. Studies have been performed to maximize both signal acceptance and the sensitivity using different designs of event “recycling” methods. These three schemes can be summarized as:

1. MLR: events are first passed through merged selections of high-purity signal region and subsequently those of low-purity signal region should they fail the previous one; they are then considered for the resolved selections. This “recycling” method can be represented by an arrow diagram: high-purity \rightarrow low-purity \rightarrow resolved.
2. MRL: Following the above example, the “MRL” scheme corresponds to: high-purity \rightarrow resolved \rightarrow low-purity where resolved signal regions are given higher priority than the low-purity one.

3. RML: resolved \rightarrow high-purity \rightarrow low-purity.

Spin-0 and spin-2 models were all subjected to the three “recycling” methods in an attempt to arrive at the same strategy that can be used for simplicity. Scatter plots comparing the acceptance and significance of these methods can be found for NWA Higgs and G^* models in Figs. 4.23 and 4.24.

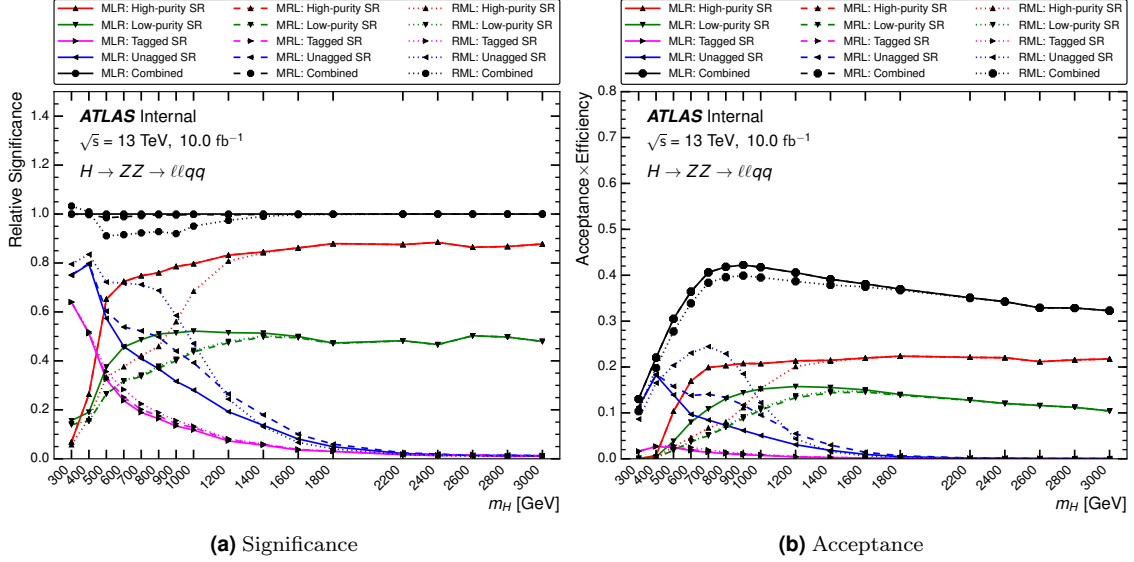


Figure 4.23: Comparison of the significance (left) and acceptance (right) assuming three different methods of event categorization for NWA Higgs samples. The significance calculated in the left plot is relative to the significance for “MRT” method at each signal mass point.

Significances were calculated as a bin-by-bin (50 GeV per bin) quadratic sum of the Asimov approximation for median significance with the uncertainties of background taken into account:

$$\sigma = \left[2 \times \left((s+b) \ln \left[\frac{(s+b)(b+\sigma_b^2)}{b^2 + (s+b)\sigma_b^2} \right] - \frac{b^2}{\sigma_b^2} \ln \left[1 + \frac{\sigma_b^2 s}{b(b+\sigma_b^2)} \right] \right) \right]^{1/2} \quad (4.6)$$

$$\sigma_{total} = \sqrt{\sum_i \sigma_i^2} \quad (4.7)$$

where σ_b is the variance of the background. In the calculations, statistical fluctuations of backgrounds were considered as part of the uncertainty and a flat dummy systematic uncertainty of 10% was also added independently to reflect the impact of systematic uncertainties to some degree. In the end, similar sensitivities were found in resolved and low-purity signal regions but inferior to the sensitivity of high-purity signal region due to the fact that it has a substructure cut for the leading large-R jet. The sequential steps (high-purity \rightarrow low-purity \rightarrow resolved) are finally chosen as the “recycling” method for event categorization.

4.7.3 Data-MC comparison by Region

The final binning is determined as a balance of communication of results to the reader, signal width, fit speed and stability, MC statistics available, and consistency between regimes. For fit stability, speed and legibility a minimum bin width of 20 GeV is chosen in all regimes and regions. In the high mass range the binning is harmonized in all plots. The binning in the range above 1500 GeV is chosen to roughly contain 90% of the narrow width higgs signal.

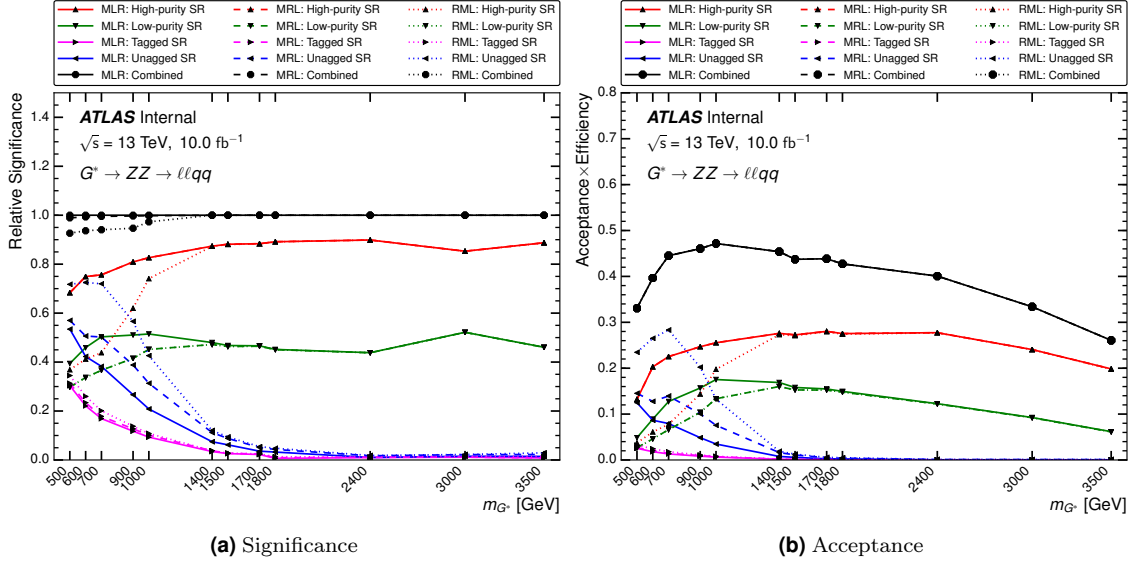


Figure 4.24: Comparison of the significance (left) and acceptance (right) assuming three different methods of event categorization for G^* samples. The significance calculated in the left plot is relative to the significance for “MRL” method at each signal mass point.

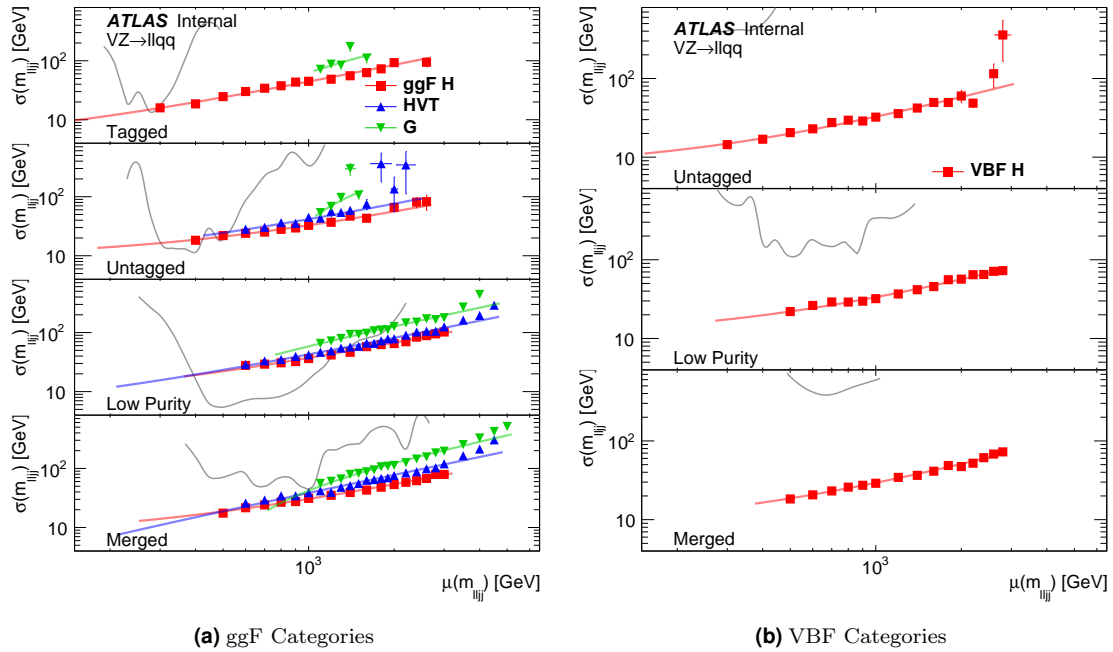


Figure 4.25: Signal resolutions evaluated with 1.7σ trimmed gaussian fit. Also shows the estimated bin width to achieve 5% statistical uncertainty on the MC.

Figure 4.25 shows the signal resolution in all categories for the 4 signal types considered in this analysis.

The final binning was determined as a compromise of several factor including the optimization of limit, signal width, statistics, and experimental resolution.

The eight ZCRs in the analysis are shown in Fig. 4.26 and Fig. 4.27. Figure 4.26 holds both merged and resolved ZCRs for ggF analysis and Fig. 4.27 shows the corresponding regions passing the additional VBF selection criteria. The agreement between data and Monte Carlo prediction is good within the statistical and systematic uncertainties. Event yields are shown in Table 4.5

	High P.	Low P.	VBF High P.	VBF Low P.	Untagged	VBF Resolv.	Tagged
Top	3.52 ± 0.69	5.90 ± 1.04	0.11 ± 0.04	0.02 ± 0.04	291.09 ± 28.29	8.85 ± 1.77	130.92 ± 5.57
Diboson	49.40 ± 6.58	51.19 ± 4.59	1.28 ± 0.39	3.13 ± 0.87	668.26 ± 39.18	13.90 ± 1.31	54.27 ± 5.67
Z	576.44 ± 21.58	1230.49 ± 32.72	18.11 ± 2.06	53.77 ± 6.56	19903.21 ± 136.56	230.26 ± 14.67	408.97 ± 17.89
Zl	–	–	–	–	15093.58 ± 594.19	–	0.80 ± 0.23
Zbb	–	–	–	–	169.38 ± 27.25	–	356.25 ± 19.91
Zbc	–	–	–	–	117.08 ± 16.56	–	20.88 ± 4.12
Zbl	–	–	–	–	1641.33 ± 242.42	–	23.53 ± 12.31
Zcc	–	–	–	–	392.04 ± 117.36	–	6.28 ± 2.54
Zcl	–	–	–	–	2489.81 ± 564.98	–	1.23 ± 1.33
Total	629.36 ± 22.09	1287.57 ± 33.95	19.51 ± 2.12	56.92 ± 6.53	20862.71 ± 137.36	253.01 ± 14.50	594.16 ± 17.53
Data	606	1270	25	59	20857	246	608

Table 4.5: Best-fit values of the global yields for the Standard Model backgrounds from the background-only ($\mu = 0$) fit, as well as the total number of data candidates in all Z -control regions.

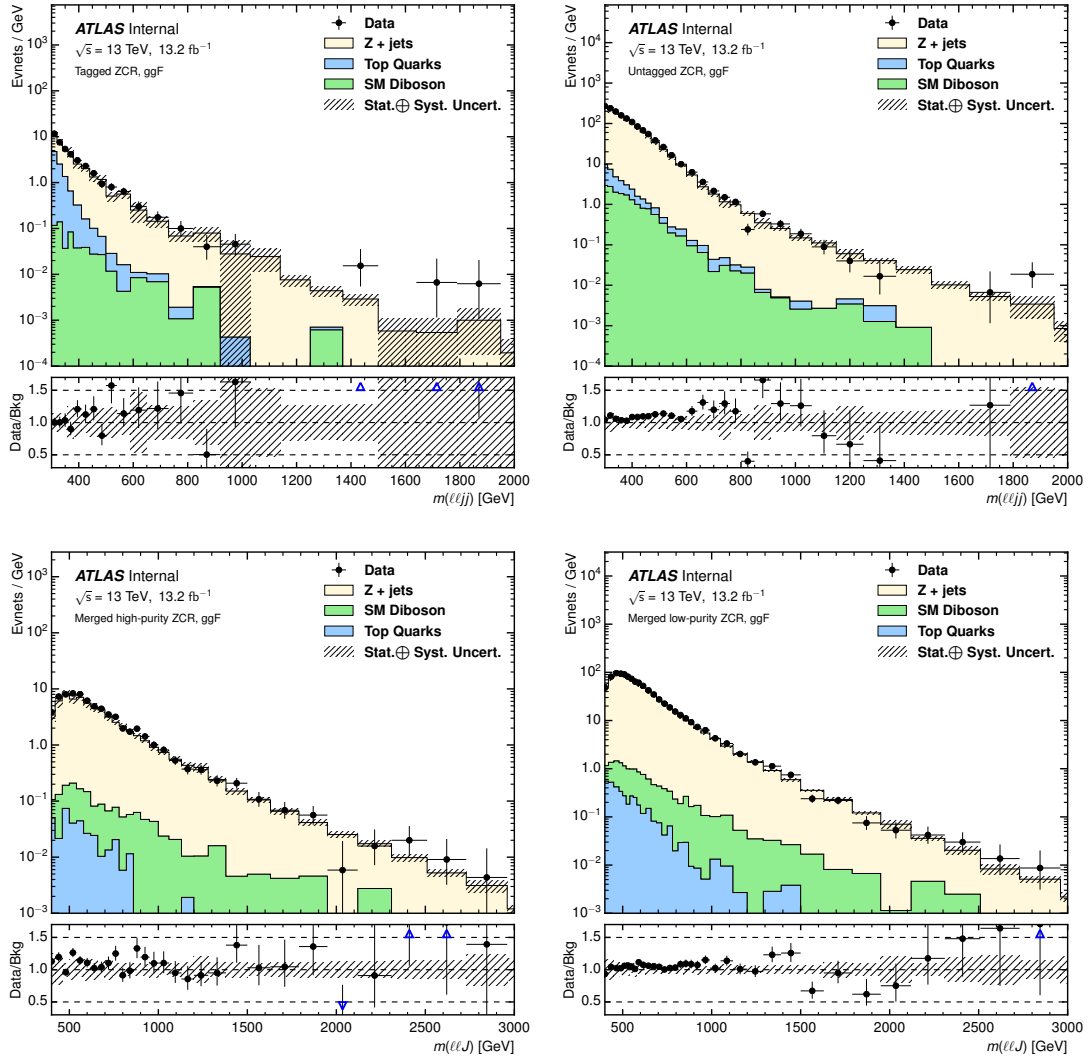


Figure 4.26: Untagged and tagged m_{lljj} distributions in the resolved regime (top) and Z-tagged and low-purity m_{llJ} distributions in the merged regime (bottom) in the Z control region after full ggF selection and categorization.

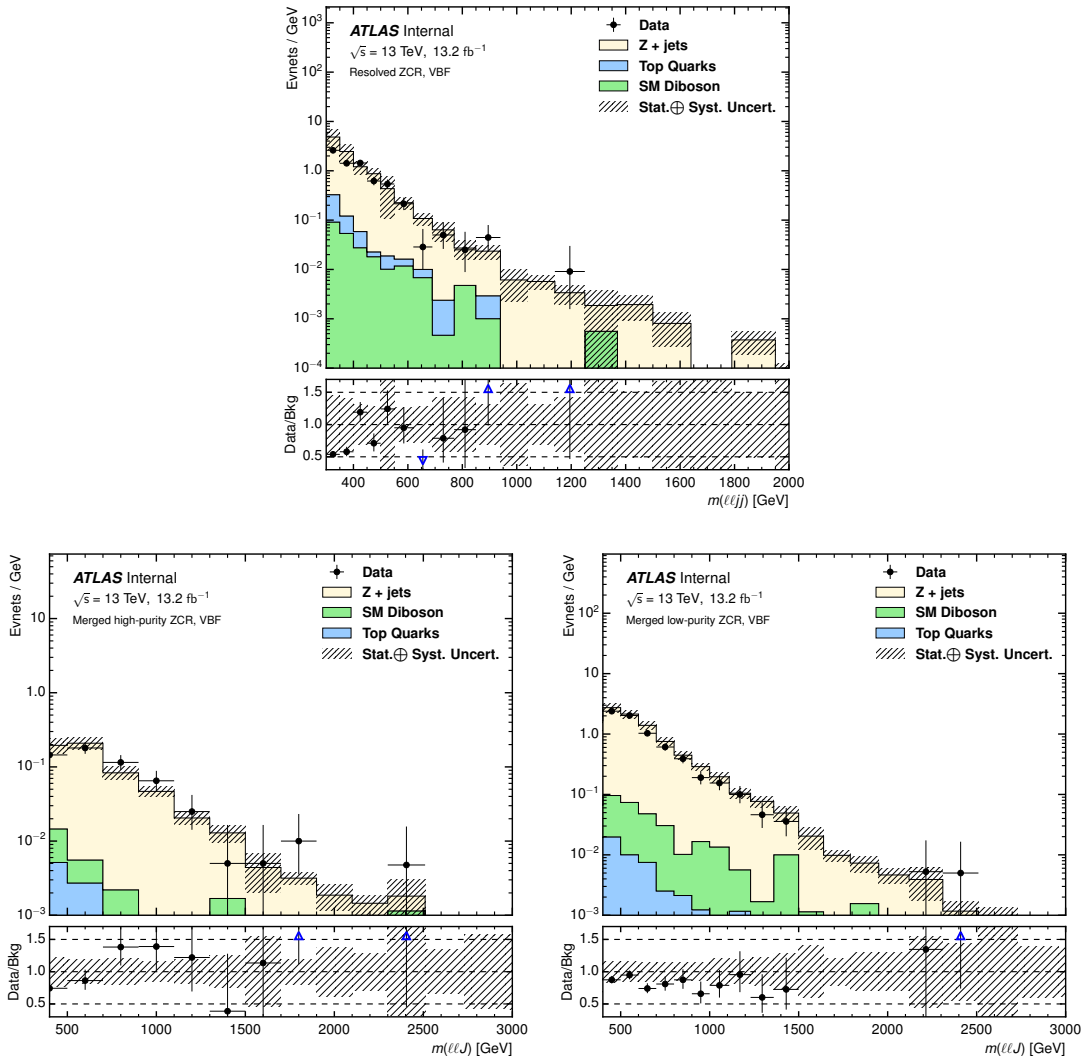


Figure 4.27: m_{lljj} distributions in the resolved regime (top) and Z-tagged and low-purity m_{llJ} distributions in the merged regime (bottom) in the Z control region satisfying VBF criteria in addition to full selection and categorization.

4.8 Systematics

This section describes the sources of systematic uncertainty considered in the analysis. These uncertainties are divided into three categories: experimental uncertainties, uncertainties on the background estimation, and theoretical uncertainties on the signal processes. In the statistical analysis each systematic uncertainty is treated as a nuisance parameter the names of which are defined below. These systematic variations are estimated on the final discriminant, the four- or three-body invariant mass.

4.8.1 Experimental uncertainties

Each reconstructed object has several sources of uncertainties, each of which is evaluated separately. Experimental systematics are applied on both signal and background Monte Carlo events. The leading instrumental uncertainty for all channels is the uncertainty on the jet energy scale (JES).

Luminosity

The uncertainty on the integrated luminosity is 2.1% for 2015 dataset and 3.7% for 2016 dataset. The combined luminosity uncertainty of 2.8% is applied to those backgrounds estimated from simulation and signal samples.

Trigger

Systematic uncertainties on the efficiency of the electron or muon triggers are evaluated using the tag and probe method [138], and are applied to those backgrounds estimated from simulation and signal samples.

Leptons

The following systematic uncertainties are applied to electrons and muons:

- Energy and momentum scales: these are also measured with Z mass line shape.
- Identification and reconstruction efficiency: the efficiencies are measured with the tag and probe method using the Z mass peak.
- Isolation: isolation requirements at the object selection level are evaluated using the leptonic Z mass peak.
- Track-to-vertex association efficiency for muons.

Figs 4.28 and 4.29 show the effect of the systematic variations on the electron energy and muon momentum scales and resolutions for the spin-0 signal sample at 1.2 TeV.

Jets

The jet energy scale and resolution are measured in situ by calculating the difference between Monte Carlo and data in various bins of kinematic phase space.

The small-R jets have a total of 19 nuisance parameters and 5 different correlation schemes, the tightest of which reduces the total number of nuisance parameters to 3. The large-R jets have 3 different correlation schemes available. Since we found that all of the schemes give equivalent results, we decided to use the tightest small-R jet scheme and the medium large-R jet scheme.

In addition to the correlations that are made between the systematics for the individual types of jets, additional correlations can be made between the small-R and large-R jet energy scale systematics. Three different schemes have been tested and they were shown to have minimal effect on the fits to the data. As such, a fully uncorrelated scheme has been kept between the two sets of systematics.

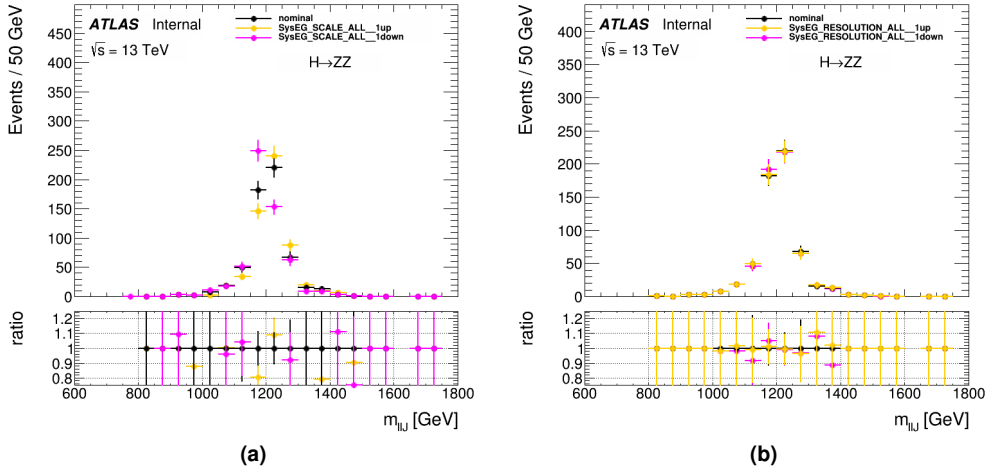


Figure 4.28: Impact of electron energy scale (a) and resolution (b) uncertainties on m_{llJ} distribution in the merged high purity signal region for spin-0 signal samples.

Figure 4.30 and 4.31 show the effect of systematic variations on small-R jet energy scale and resolution uncertainties for spin-0 signal sample at 1.2 TeV in the resolved signal region. Figure 4.32 and 4.33 show the effect of systematic variations on large-R jet energy scale and resolution uncertainties for spin-0 signal sample at 1.2 TeV in the merged high purity signal region.

The small-R jets are also susceptible to uncertainties from the b -tagging calibration. This analysis uses the tightest b -tagging systematic scheme, which assumes correlations between most of the b -tagging variables. This is due to studies that showed the looser schemes did not have enough constraining power on all of the relevant nuisance parameters, and many of them were underconstrained. All of the schemes yielded very similar expected results.

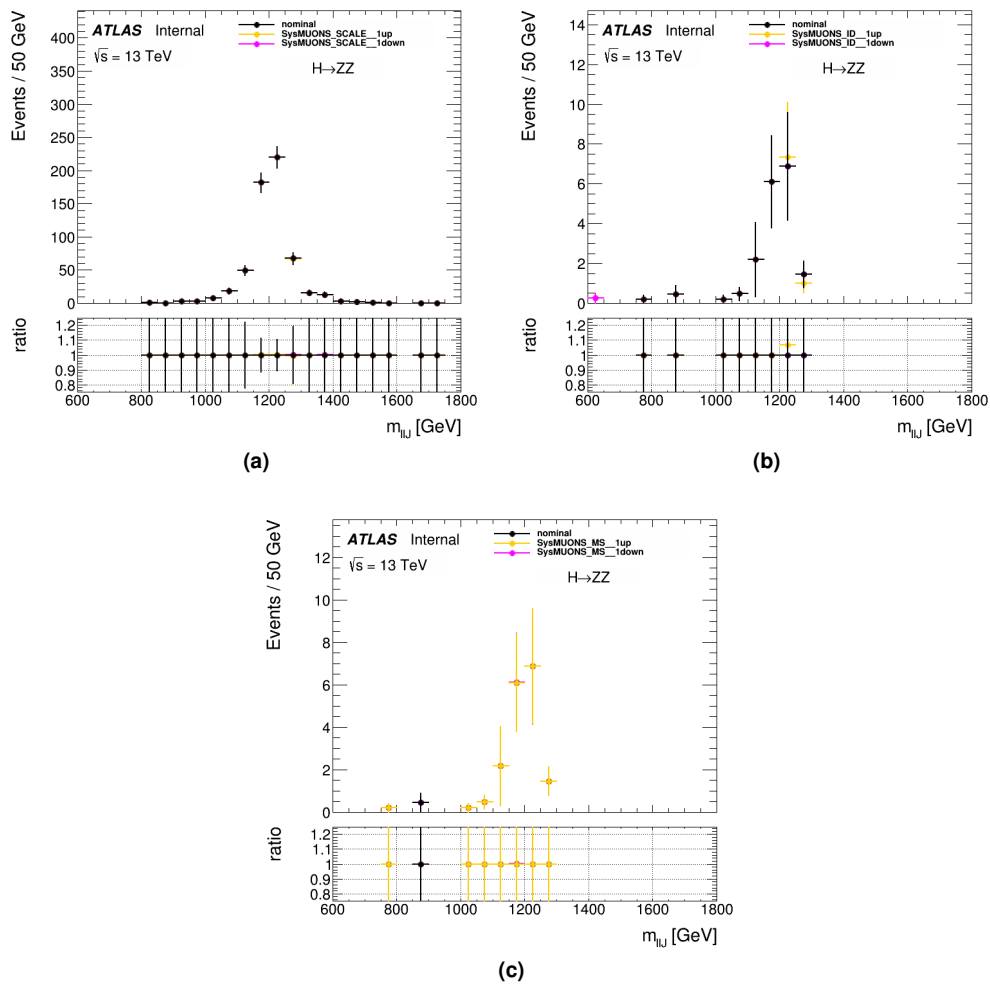


Figure 4.29: Impact of muon momentum scale (a), ID track resolution (b) and MS track resolution (c) uncertainties on m_{ll} distribution in the merged high purity signal region for spin-0 signal samples.

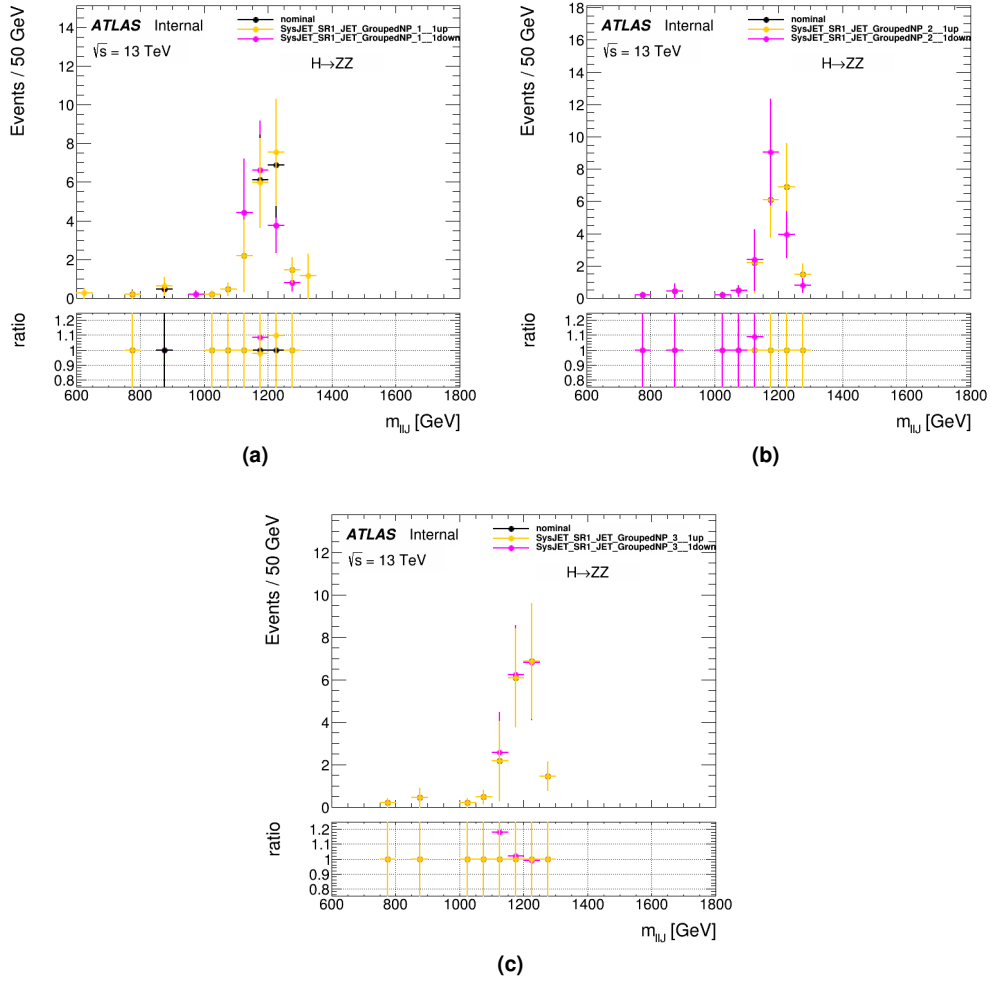


Figure 4.30: The m_{lljj} distribution varied up and down for small-R jet energy scale uncertainties: (a) JET_SR1_JET_GroupedNP_1 (b) JET_SR1_JET_GroupedNP_2 (c) JET_SR1_JET_GroupedNP_3. Spin-0 signal sample at 1.2 TeV in the resolved signal region is shown here.

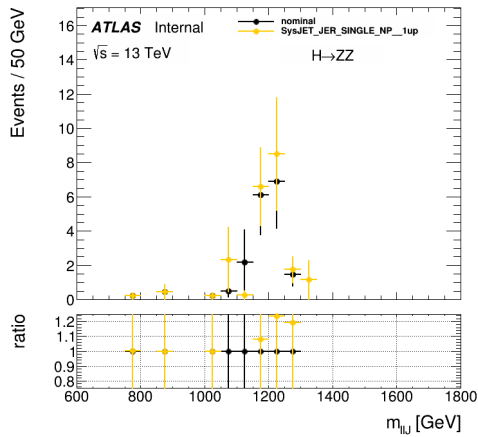


Figure 4.31: The m_{lljj} distribution varied up and down for small-R jet energy resolution uncertainty. Spin-0 signal sample at 1.2 TeV in the resolved signal region is shown here.

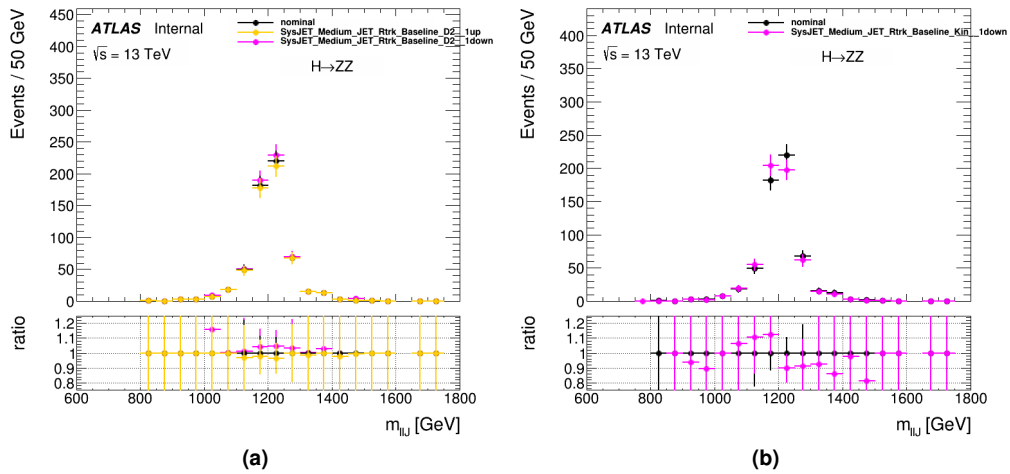


Figure 4.32: The m_{ll} distribution varied up and down for large-R jet energy scale uncertainties: (a) Medium_JET_Rtrk_Baseline_D2 (b) Medium_JET_Rtrk_Baseline_Kin. Spin-0 signal sample at 1.2 TeV in the merged high purity signal region is shown here.

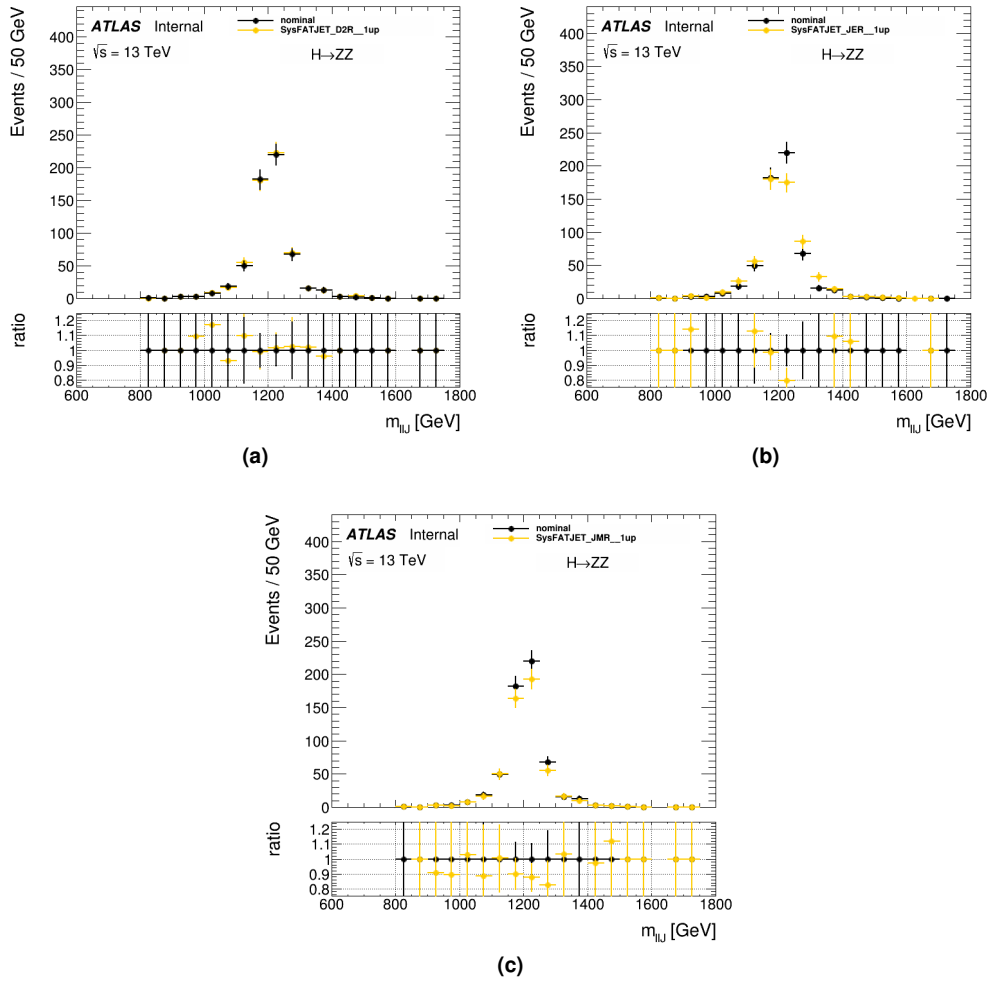


Figure 4.33: The $m_{l,l}$ distribution varied up and down for large-R jet resolution uncertainties: (a) substructure $D_2^{(\beta=1)}$ resolution (b) jet energy resolution (c) jet mass resolution. Spin-0 signal sample at 1.2 TeV in the merged high purity signal region is shown here.

4.8.2 Background Modeling Uncertainties

Several systematics have been evaluated to take into account the uncertainties on the modeling of backgrounds. These uncertainties were derived by looking at the same background processes from different Monte Carlo generators. These systematics are taken as shape variations on the nominal m_{lljj} and m_{llJ} shapes.

The Z+jets modelling uncertainty will be taken into consideration using the data driven background estimation method described in Section 4.6.1.

The data-driven estimations of the Z control region is then fitted with a functional form, in a procedure very similar to the smoothing of the Z+jets background explained in section 4.6.1. The reduced χ^2 obtained for each channel is very close to 1.

After the fit is performed, we use the functional form to fill the histogram in the corresponding signal region. The final smoothed histogram will take directly the data driven estimate points values as they are up to the mass, signal region dependant, where the residue of the functions start being smaller. From that threshold onwards, the functional form is used to set the bin content, by taking the integral of the functional form in the range corresponding to the lower and upper values of the bin, and dividing by the bin width. The distribution which we get using this procedure can be seen in Fig. 4.34, as the blue line. The black line in the same figure is the smoothed Z+jets background based on the MC. To get the red variation in Fig. 4.34, a symmetrisation of the uncertainty is performed: bin by bin of the m_{llJ} distribution, we take the difference between the nominal distribution and the data-driven estimate, and apply in the opposite direction with respect to the nominal distribution. In this way, we can get a symmetric uncertainty envelope around the nominal Z+jets background estimation.

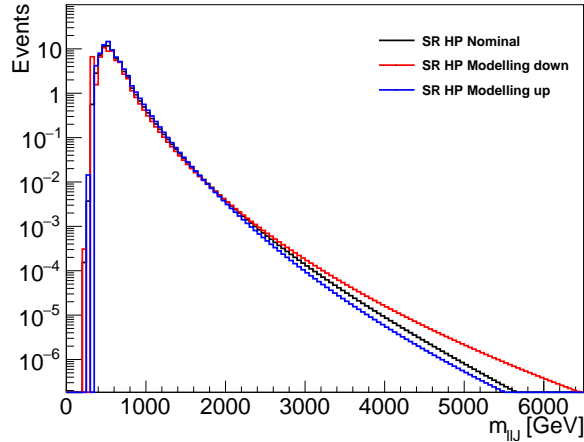


Figure 4.34: The Monte Carlo nominal Z+jets estimation (black line), and the data driven derived modelling systematics (blue and red lines), for the merged high purity signal region, in the ggF spin 0 category.

4.8.3 Signal uncertainties

Additional systematics are introduced due to modeling differences between various signal Monte Carlo generators. The PDF uncertainties are estimated by taking the acceptance difference due to PDF error sets and the difference between choice of PDF sets.

The uncertainties due to ISR/FSR are also estimated by varying relevant parameters in PYTHIA 8. A flat uncertainty of 3% for Higgs signals and 5% for Graviton signals are used in this analysis.

4.8.4 Summary of uncertainties

The impact of systematic uncertainties on the signal presence has been evaluated individually for each uncertainty and in logical groups organized by physics object (e.g. muons, electrons, jets, etc.) for three signal mass points, $m_{NWH} = 400, 700, \text{ and } 1600$, where each has been injected with a cross section of $\sigma = 20 \text{ fb}$. Table 4.6 shows a brief summary of leading groups of systematic uncertainty on the determination of μ , the magnitude of expected signal evaluated for a narrow width scalar of signal mass of 700 GeV with a cross section of $\sigma = 20 \text{ fb}$. The total uncertainty on μ is found to be $\pm 7 \text{ fb}$ for the 700 GeV signal.

	Uncertainties on μ , ggF $m_H = 700 \text{ GeV}$
Large-R Jet Resolution	18%
Large-R Jet Scale	13%
Alpha Modeling	9%
Background Normalization	6%
E/ γ	6%
Muons	6%

Table 4.6: The dominant uncertainties on the ggF scalar signal hypothesis, $M_H = 700 \text{ GeV}$. The numbers represent the uncertainty relative to the total uncertainties on the determination of signal cross section, μ .

4.9 Statistic procedure: the profile likelihood fit

The statistical treatment of this analysis uses a combined profile likelihood fit to binned discriminants in all categories and regions simultaneously based on the framework described in Refs. [139, 140, 141].

The binned likelihood function is constructed as the product of Poisson probability terms,

$$\text{Pois}(n|\mu S + B) \left[\prod_{b \in \text{bins}} \frac{\mu \nu_b^{\text{sig}} + \nu_b^{\text{bkg}}}{\mu S + B} \right], \quad (4.8)$$

where μ , a signal strength parameter, multiplies the expected signal yield ν_b^{sig} in each histogram bin b , and ν_b^{bkg} represents the background content for bin b . The dependence of the signal and background predictions on the systematic uncertainties is described by a set of nuisance parameters (NP) θ , which are parameterized by Gaussian or log-normal priors; the latter are used for normalization uncertainties in order to maintain a positive likelihood. The expected numbers of signal and background events in each bin are functions of θ and parameterized such that the rates in each category are log-normally distributed for a normally distributed θ .

The priors act to constrain the NPs to their nominal values within their assigned uncertainties. They are implemented via so-called penalty or auxiliary measurements added to the likelihood which will always increase when any nuisance parameter is shifted from the nominal value. The likelihood function, $\mathcal{L}(\mu, \theta)$, is therefore a function of μ and θ .

The nominal fit result in terms of μ and σ_μ is obtained by maximising the likelihood function with respect to all parameters. This is referred to as the maximised log-likelihood value, MLL. The test statistic q_μ is then constructed according to the profile likelihood: $q_\mu = 2 \ln(\mathcal{L}(\mu, \hat{\theta}_\mu) / \mathcal{L}(\hat{\mu}, \hat{\theta}))$, where $\hat{\mu}$ and $\hat{\theta}$ are the parameters that maximise the likelihood (with the constraint $0 \leq \hat{\mu} \leq \mu$),

and $\hat{\theta}_\mu$ are the nuisance parameter values that maximise the likelihood for a given μ . This test statistic is used to measure the compatibility of the background-only model with the observed data and for exclusion intervals derived with the CL_s method [142, 143]. The limit set on μ is then translated into a limit on the signal cross section times branching ratio, $\sigma \times \text{BR}(H \rightarrow ZZ \rightarrow \ell\ell qq)$, using the theoretical cross section and branching ratio for the given signal model.

The analysis discriminating distributions are arranged as the outer product of category, region, regime, and subregime. Here category refers to the selection for VBF or ggF signal, region refers to signal (SR) and control regions (CR), regime refers to the merged and resolved jet analysis objects used in selection, and subregime refers to 01-tag and 2-tag split for regular jets and W/Z-tagged vs. low-purity selection for large-R jets. For each of these selections, the input to the likelihood is the final ZZ invariant mass distribution: $m_{\ell\ell jj}$ in the resolved regime and $m_{\ell\ell J}$ in the merged regime.

The overarching principle of the analysis design is to provide a Z control region from the two-jet mass side bands of each signal region in order to normalize the backgrounds in the fit. This strategy serves the analysis well with the addition of a top CR made from the tagged subregime but requiring an $e\mu$ -pair instead of a matching lepton pair. Minor backgrounds are taken from MC simulation, normalized to the cross-sections, whereas the primary backgrounds Z +jets and top are constrained entirely by the fit.

The complete list of regions used in the fit is shown in Table 4.7.

Cat.	Region	$llqq$ channel			
		Resolved		Merged	
		untagged	tagged	W/Z tagged	low purity
ggF	SR	$m_{\ell\ell jj}$	$m_{\ell\ell jj}$	$m_{\ell\ell J}$	$m_{\ell\ell J}$
	ZCR	$m_{\ell\ell jj}$	$m_{\ell\ell jj}$	$m_{\ell\ell J}$	$m_{\ell\ell J}$
	TopCR	—	$m_{\ell\ell jj}$	—	—
VBF	SR	$m_{\ell\ell jj}$		$m_{\ell\ell J}$	$m_{\ell\ell J}$
	ZCR	$m_{\ell\ell jj}$		$m_{\ell\ell J}$	$m_{\ell\ell J}$

Table 4.7: Summary of the regions entering the likelihood fit and the distribution used in each. Rows with “—” indicate that the region is not included in the fit. “SR” stands for the signal regions and “CR” for the control regions.

A number of fit strategies have been compared to determine the correlation scheme of the floating parameters. The fit values obtained from 4 schemes are shown in Table 4.8.

	Nominal Fit	Split Z	Split VBF	Single $t\bar{t}$ bar
Resolved Z	0.99 ± 0.05	0.99 ± 0.05	1.00 ± 0.03	0.99 ± 0.05
$Z + b$	1.20 ± 0.11	1.19 ± 0.11	1.19 ± 0.09	1.20 ± 0.11
Merged Z	1.10 ± 0.04	—	1.08 ± 0.05	1.10 ± 0.04
$t\bar{t}$ bar	1.16 ± 0.06	1.16 ± 0.06	1.16 ± 0.05	1.16 ± 0.06
VBF-ggF ratio	0.80 ± 0.06	0.82 ± 0.06	—	0.80 ± 0.06
Low Purity Z	—	1.06 ± 0.04	—	—
High Purity Z	—	1.06 ± 0.06	—	—
VBF Merged Z	—	—	0.87 ± 0.06	—
VBF Resolved Z	—	—	0.95 ± 0.11	—

Table 4.8: Best-fit values of the global normalization factors from the fit to all of the regions in the analysis for various normalization schemes.

All systematic uncertainties enter the profile likelihood fit as nuisance parameters (NPs). Two different types of nuisance parameters are used: floating parameters and parameters with priors.

For the most significant backgrounds, those which the analysis is designed to constrain, no prior probability distribution is assigned to the normalization and the contribution are therefore floating.

The fit contains four freely-floating normalization parameters that are constrained by the signal and control regions described above:

Signal: Signal strength.

Background: The following scale factors are used for background in different categories:

Zresolved Normalization for Z +jets in the resolved regimes.

Zb Normalization for $Z + bb$ in the resolved regimes.

Zmerged Overall Z boson production normalization. Note: since the merged category selects a very different phase space, the normalization is separate from the resolved case.

Top Top normalization.

VBF-ggF Single floating ratio between all Z +jets normalization in the merged and resolved regimes.

A nuisance parameter with a prior corresponds to a systematic uncertainty where there is a prior constraint on the value of the parameter from designated studies. The fit contains XX nuisance parameters from experimentally-derived uncertainties (see) and 7 nuisance parameters from alpha modeling uncertainties (see), in addition to the floating normalization parameters. Nuisance parameters from signal acceptance uncertainties, due to PDF and ISR/FSR, are also included in the fit. A ranking of NPs according to impact on the parameter of interest is shown in Fig. 4.35.

The normalizations of the $Z + \text{jets}$ background components that are not floating in the fit are taken from Monte Carlo, where an uncertainty has been assigned to the ratio of their normalizations to the normalization of the $Z + bb$ component for the case of $Z + b^*$. For $Z + c^*$ the prior uncertainty is applied to absolute normalization. These priors are assigned the following values:

- $Z + bc/Z + bb$ ratio: 12%
- $Z + bl/Z + bb$ ratio: 12%
- $Z + cc$: 30%
- $Z + cl$: 30%

The statistical uncertainties for the background MC samples are taken into account in the profile likelihood using a light weight version of the Barlow-Beeston method as implemented in HistFactory [144]. This adds an extra nuisance parameter representing the statistical uncertainty on the total MC background in each bin, which is completely uncorrelated across bins. These nuisance parameters are not added to all bins but only those bins where the relative statistical uncertainty in the bin is above the threshold of 5%.

4.10 Results

This section describes the results of the analysis. Figs. 4.36-4.43 show the invariant mass distributions in all regions after the unconditional fit has been applied. Table 4.9 shows the yields of the Standard Model background and data in the signal regions. The observed distributions of the final discriminants, $m_{\ell\ell J}$ for the merged analysis and $m_{\ell\ell jj}$ for the resolved analysis, of the four signal regions of the ggF $H \rightarrow ZZ$ search are compared with the background expectation in Fig. 4.37-4.39-4.41-4.42. The data distributions are reasonably well reproduced by the background contributions in all these distributions. The distributions for the graviton search are similar. The largest deviations are an excess at approximately 500 GeV in the $m_{\ell\ell jj}$ distribution of the untagged category of the resolved analysis. The excess is estimated to have a significance of 2.75σ local and 1.4σ global. No such excess is seen in other categories. The largest deficit is at approximately 850 GeV with a global significance of 2.8σ .

	High P.	Low P.	VBF High P.	VBF Low P.	Untagged	VBF Resolv.	Tagged
Top	7.38 ± 0.92	46.99 ± 4.41	0.67 ± 0.14	3.57 ± 1.43	532.69 ± 54.60	25.45 ± 2.32	362.97 ± 14.99
Diboson	49.33 ± 4.00	212.70 ± 13.65	4.43 ± 1.74	19.42 ± 1.91	379.28 ± 24.39	10.83 ± 1.58	17.37 ± 2.59
Z	2057.63 ± 40.68	16210.18 ± 129.27	68.55 ± 4.59	458.74 ± 19.59	31510.40 ± 181.42	403.31 ± 19.81	913.69 ± 32.79
Zl	-	-	-	-	23779.11 ± 932.17	-	13.09 ± 4.43
Zbb	-	-	-	-	287.16 ± 46.62	-	791.86 ± 35.20
Zbc	-	-	-	-	179.58 ± 25.98	-	62.50 ± 12.64
Zbl	-	-	-	-	2589.17 ± 373.30	-	25.70 ± 10.96
Zcc	-	-	-	-	631.98 ± 187.96	-	12.53 ± 8.60
Zcl	-	-	-	-	4043.40 ± 926.98	-	8.01 ± 3.95
Total	2114.34 ± 41.66	16469.89 ± 127.80	73.65 ± 5.12	481.74 ± 18.96	32422.40 ± 172.74	439.59 ± 20.57	1294.02 ± 31.36
Data	2124	16499	82	467	32430	443	1265

Table 4.9: Best-fit values of the global yields for the Standard Model backgrounds from the background-only ($\mu = 0$) fit, as well as the total number of data candidates in all signal regions.

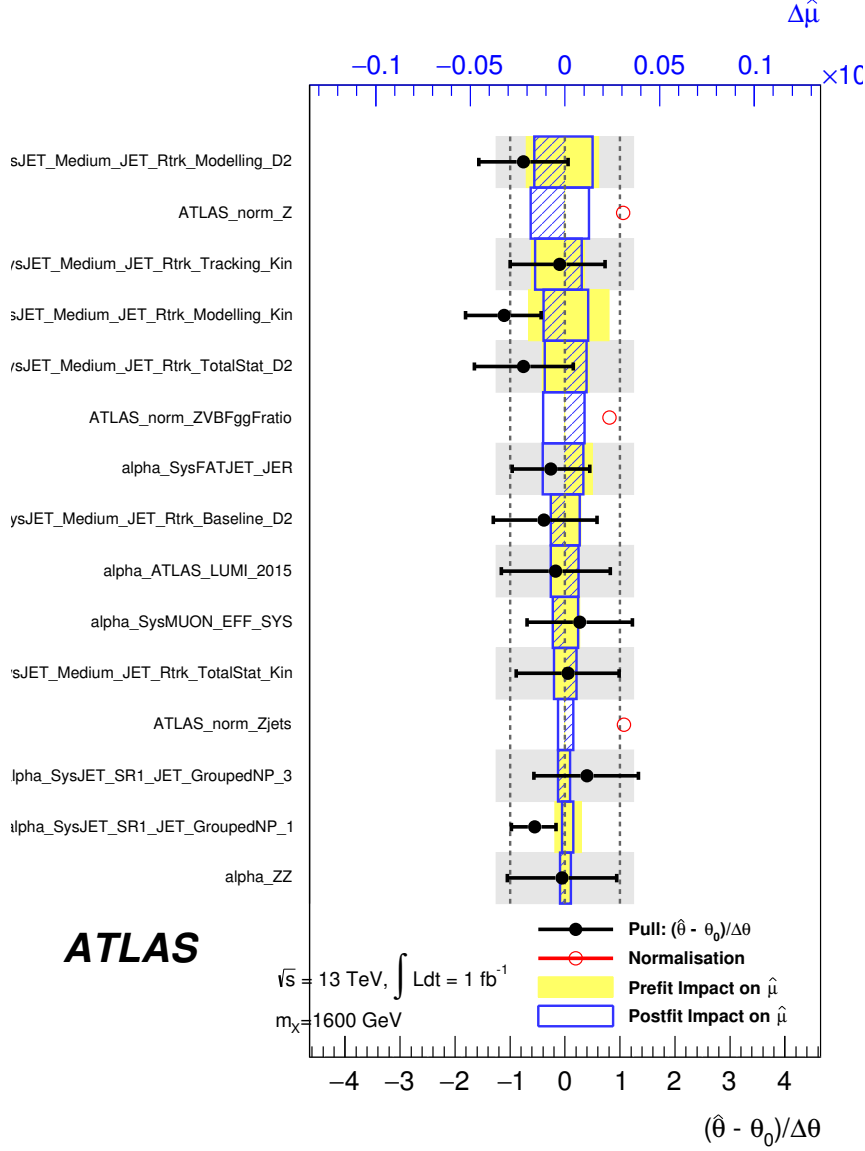


Figure 4.35: Ranking of NPs according to impact on the parameter of interest for narrow width scalar with mass of 1600 GeV.

In the absence of a signal, constraints on the production of a heavy resonance decaying to ZZ pairs are derived. The exclusion limits are calculated with a modified frequentist method [145], also known as CL_s , using the \tilde{q}_μ test statistic in the asymptotic approximation [142, 146].

The observed and expected 95% confidence level (CL) upper limits on $\sigma \times \text{BR}$ as functions of the resonance mass are shown in Fig. 4.44 in the mass range between 300 – 5000 GeV for $H \rightarrow ZZ$ of ggF and VBF processes and between 500 – 5000 GeV for HVT $W' \rightarrow ZW$ and RS graviton $G^* \rightarrow ZZ$ production.

The observed limit on $\sigma \times \text{BR}$ varies from 1.28 (0.6) pb at 300 GeV to 6.2 (5.2) fb at 3000 GeV for ggF (VBF) $H \rightarrow ZZ$ and from 730 fb at 500 GeV to 6.7 fb at 5000 GeV for RS graviton $G^* \rightarrow ZZ$. These limits are considerably tighter than those of early searches [17, 116]. Theoretical predictions for $\sigma \times \text{BR}$ of the RS graviton $G^* \rightarrow ZZ$ are overlaid in Fig. 4.44. The observed (expected) limits exclude the RS graviton lighter than 1035 (1045) GeV.

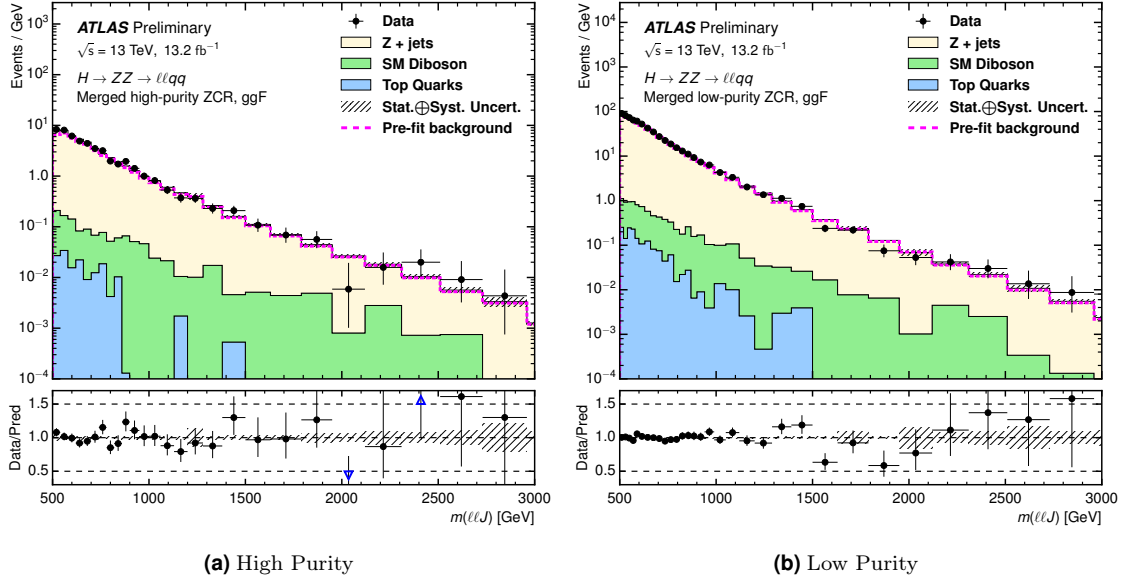


Figure 4.36: Post-fit distributions of Boosted ggF ZCRs in the H analysis.

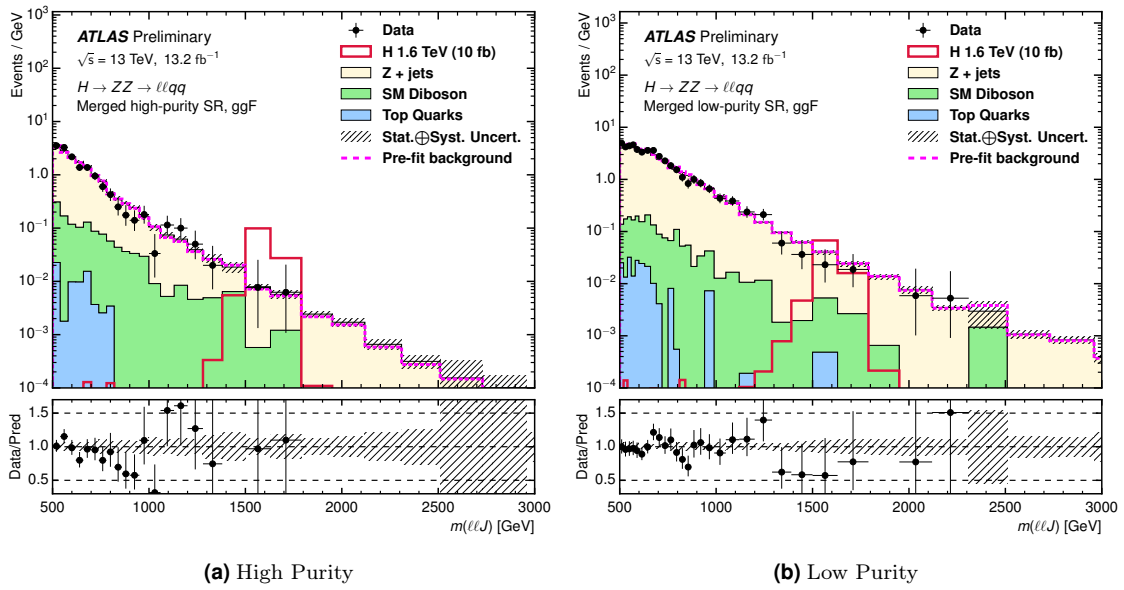


Figure 4.37: Post-fit distributions of Boosted ggF SRs in the H analysis.

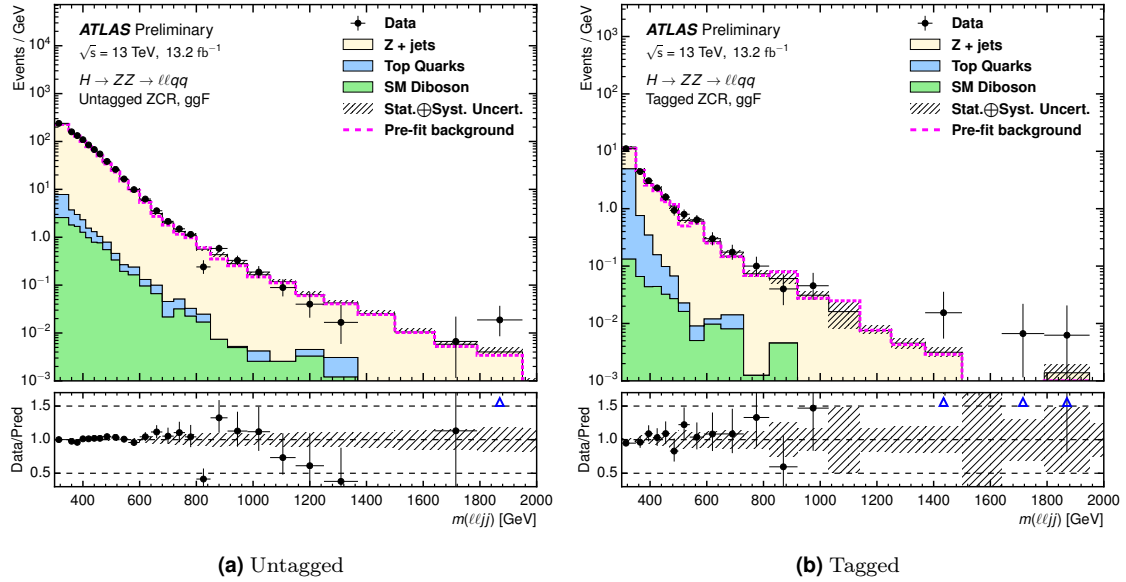


Figure 4.38: Post-fit distributions of Resolved ggF ZCRs in the H analysis post-fit.

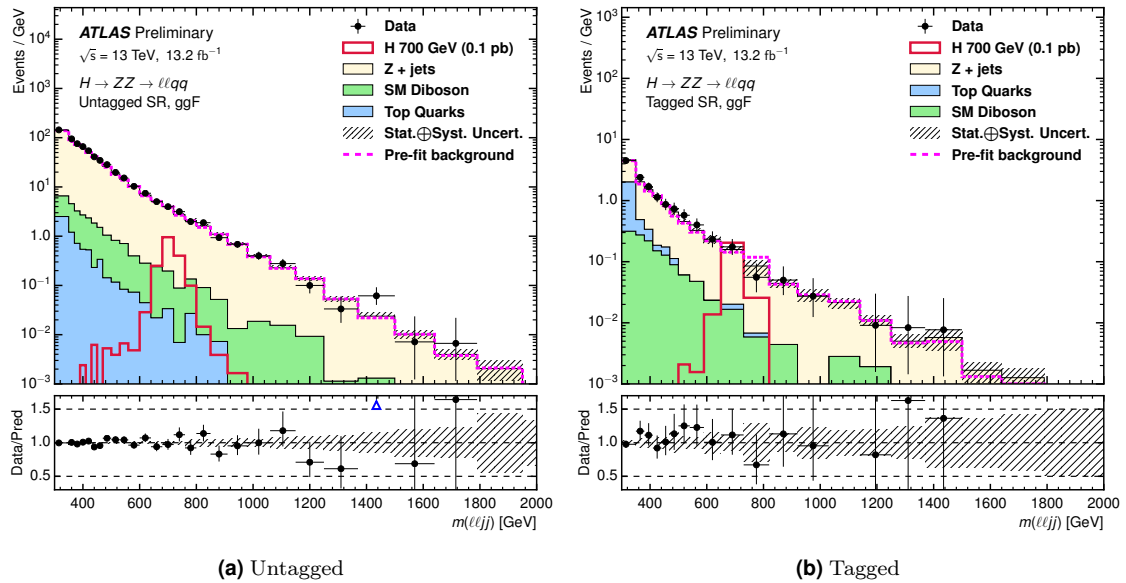


Figure 4.39: Post-fit distributions of Resolved ggF SRs in the H analysis.

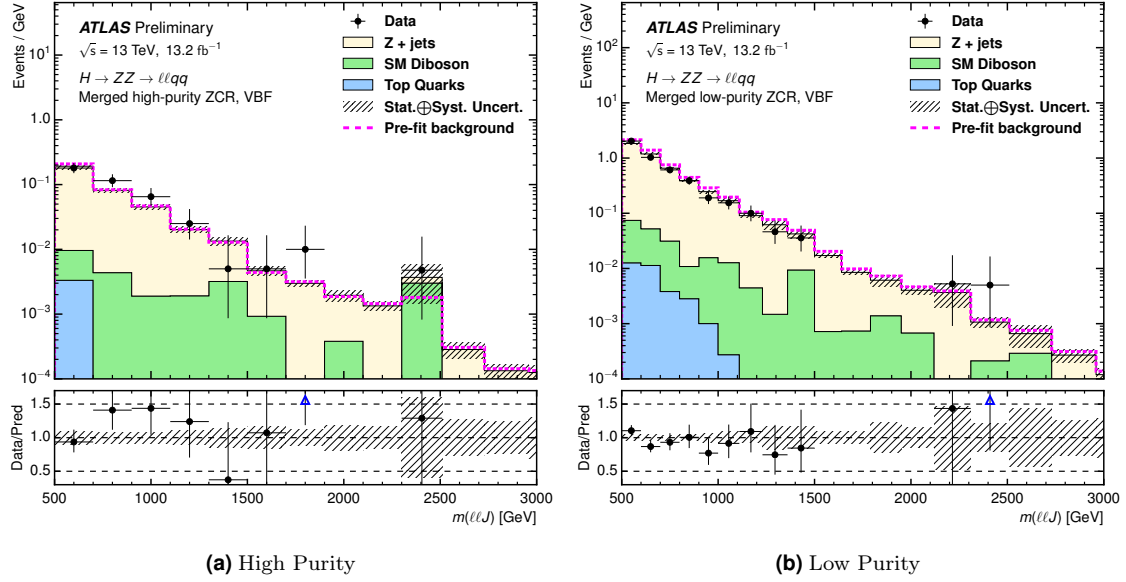


Figure 4.40: Post-fit distributions of Boosted VBF ZCRs in the H analysis.

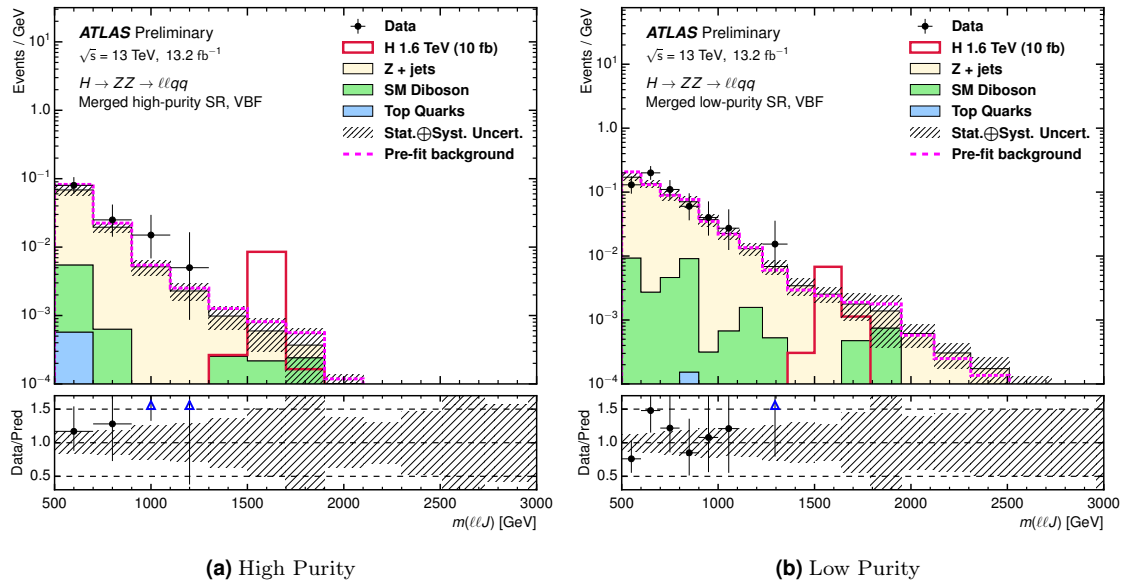


Figure 4.41: Post-fit distributions of Boosted VBF SRs in the H analysis.

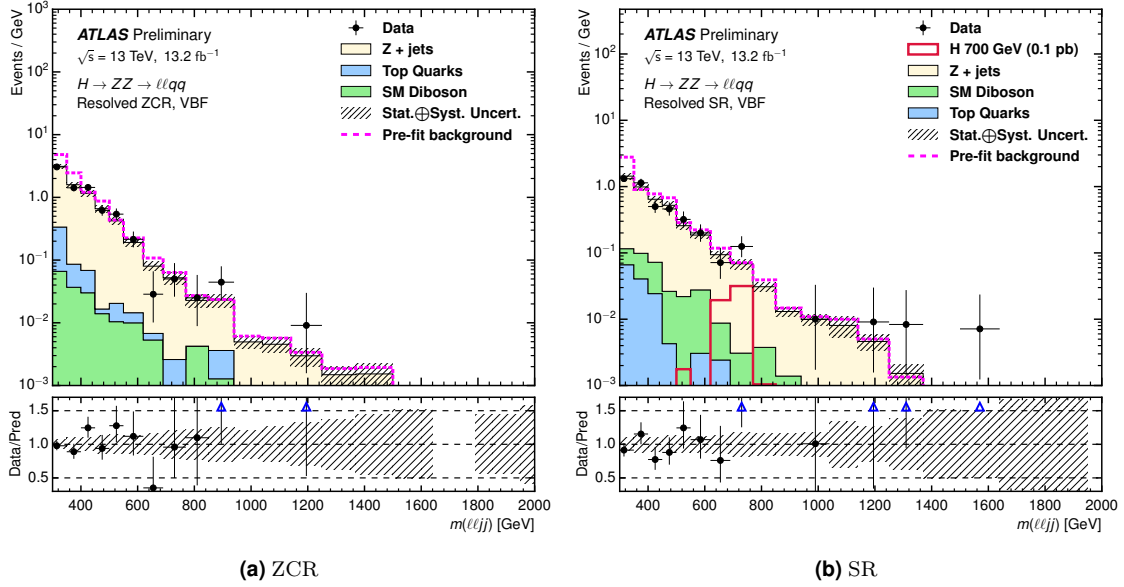


Figure 4.42: Post-fit distributions of VBF resolved regions in the H analysis post-fit.

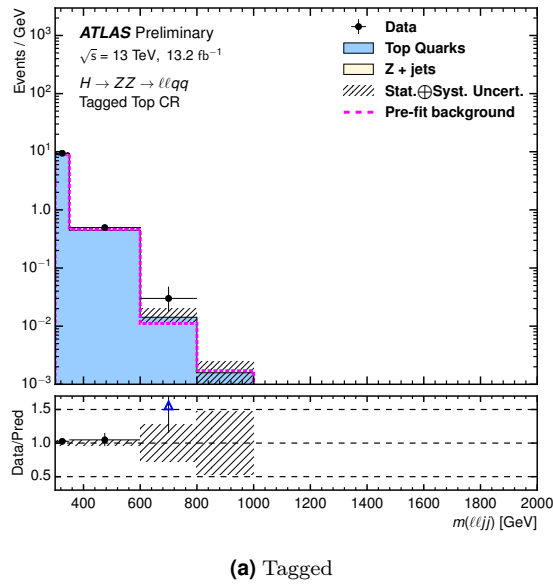


Figure 4.43: Post-fit distribution of Top CR in the H analysis.

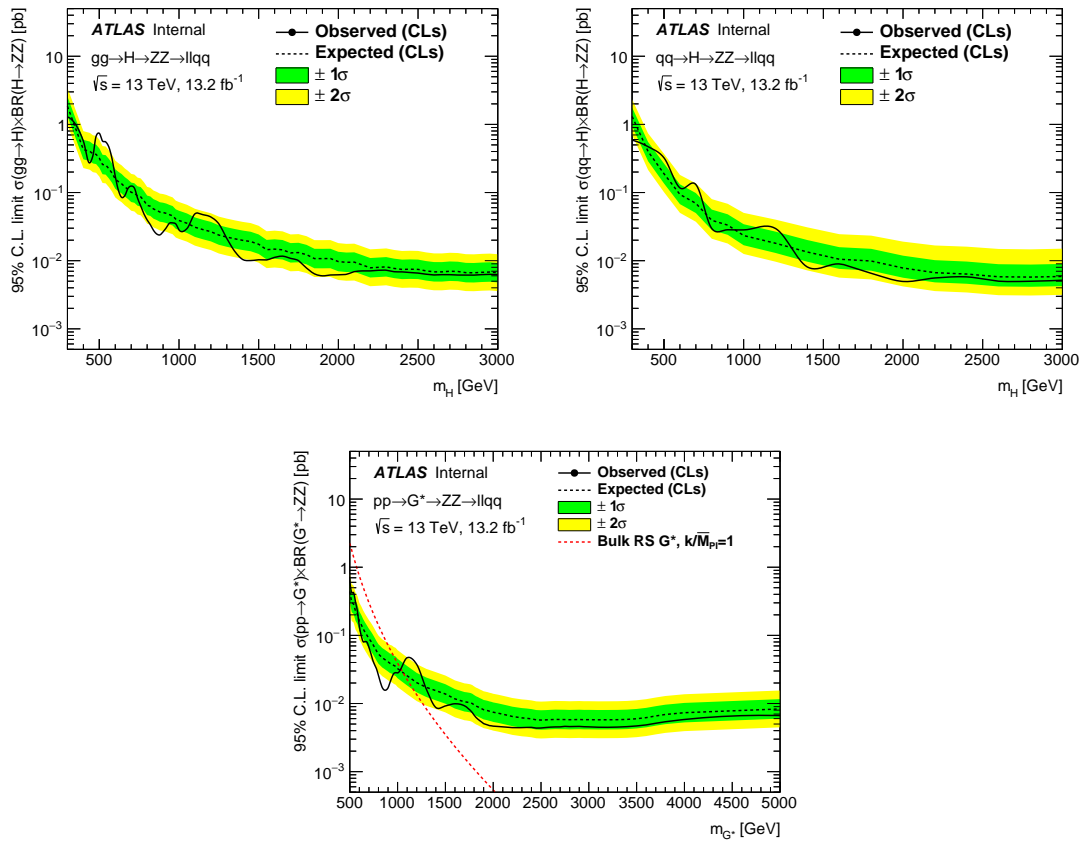


Figure 4.44: Expected and observed limits on $\sigma \times BR$ for (a) narrow-width scalar (ggF) (b) narrow-width scalar (VBF) (c) spin-2 Graviton production.

Conclusions

Many models predict the existence of a heavy spin-0 neutral Higgs boson (two-Higgs-doublet model (2HDM) [7] and the electroweak-singlet (EWS) model) or a spin-2 graviton (warped extra dimensions model [9, 10]) that can decay to a pair of Z bosons.

My thesis has been dedicated to the search for an extra heavy resonance in the $ZZ \rightarrow \ell\ell qq$ ($\ell = e, \mu$) decay channels, for a diboson mass in the range between 300 and 5000 GeV. The searches have been performed using proton-proton collision data produced at $\sqrt{s} = 13$ TeV and recorded by the ATLAS detector at the LHC in the 2015 and 2016 data-taking corresponding to a combined integrated luminosity of 13.2 fb^{-1} . The results of the search have been interpreted for a narrow width "Standard Model-like" Higgs boson and for a Randall-Sundrum graviton model (spin-2).

In my analysis I studied final states with one Z boson decaying either to a pair of charged leptons and the other Z boson decaying to a pair of quarks, identified either as two separate jets or as one large-radius jet. The resolved reconstruction attempts to identify two separate small-radius jets (small- R jet, or j) of hadrons from the $Z \rightarrow qq$ decay, while the so called merged reconstruction uses advanced jet-substructure techniques to identify the $Z \rightarrow qq$ decay reconstructed as a single large-radius jet (large- R jet, or simply J). The latter is expected when the resonance mass is significantly higher than the Z boson mass. In this case, the qq pair from the Z boson decay can be collimated and hadrons from the two quarks overlap in the detector. For this reason they are more efficiently reconstructed as a single large- R jet ("merged selection").

An important contribution to the production of scalar signals is the vector boson fusion process (VBF). In this process, two vector bosons are radiated from quarks in the colliding protons, which then produce a heavy particle through their normal interaction vertex. For the Standard Model Higgs boson, VBF production accounts for roughly 10% of the total production cross section.

My thesis has been focused on the optimization of the event selection and on the characterization of the VBF component and it has been part of a more general analysis for the searches of heavy resonances in diboson decays [20]. VBF production is characterized by extra jets in the event: usually jets in the forward section of the detector and with a large separation in pseudorapidity between them. To select VBF jets, I decided to use only two variables: the invariant mass of the jet pair m_{jj}^{tag} , and the absolute value of the difference between their pseudorapidities $|\Delta\eta_{jj}^{\text{tag}}|$. After having identified the two small- R or one large- R jet from the boson decay, the VBF jets are selected as the pair of remaining small- R jets that have opposite pseudorapidity signs and have the highest invariant mass. One of my main tasks for this thesis have been the optimization of the VBF jet selection that has been documented in 4.5.

My work on the optimization of the event selection consisted of a detailed study to the event categorization and also the event prioritization. A first study has been made in categorizing an event as either ggF or VBF. Selecting ggF or VBF one must consider the order in which you select the jets that come from the $Z \rightarrow q\bar{q}$ from the resonance decay and the jets that come from the valence quarks in the colliding protons. In the categorization scheme for this analysis, the decision to first find the reconstructed Z boson, then to select the VBF jets was made for two reasons: the expected limits from selecting the VBF jets second was shown to be 10% stronger than the other order, and, selecting the VBF jets second allows for the $Z \rightarrow q\bar{q}$ selection to be consistent for all signal selections, including those which do not have a ggF/VBF split.

The prioritization of the events is important in particular at intermediate masses of the signals ($500 \leq m_H \leq 800$ GeV) where boosted and resolved topologies overlap. Above and below these

signal masses hadronic decays of the $Z \rightarrow q\bar{q}$ are reconstructed primarily as either merged or resolved, respectively, but small differences in signal to background significance are found over the full mass range. Studies have been performed to maximize both signal acceptance and the sensitivity using different designs of event "recycling" methods (see section 4.7). The recycling strategy is considered to be superior to a fixed cut strategy on the basis of saving more signal events, no matter the cut optimization. Spin-0 and spin-2 models were all subjected to the three "recycling" methods in an attempt to arrive at the same strategy that can be used for simplicity.

A profile-likelihood-ratio test statistic is used to measure the compatibility of the background-only hypothesis with the observed data and to test the hypothesis of a heavy resonance, with its production cross section times branching ratio to ZZ , $\sigma \times \text{BR}$, as the parameter of interest. A maximum likelihood fit is made to the observed binned distributions of the final discriminants, $m_{\ell\ell J}$ or $m_{\ell\ell jj}$, in the signal categories and control regions simultaneously.

The data are found to be consistent with the background expectations and no evidence for heavy resonance production is observed. In the absence of a signal, constraints on the production of a heavy resonance decaying to ZZ pairs are derived. Upper limits at 95% CL on the production cross section times branching ratio as a function of the resonance mass are derived for $H \rightarrow ZZ$ in models with an extended Higgs sector and for $G^* \rightarrow ZZ$ in the context of the bulk Randall-Sundrum model of warped extra dimensions. The observed limit on $\sigma \times \text{BR}$ varies from 1.28 (0.6) pb at 300 GeV to 6.2 (5.2) fb at 3000 GeV for ggF (VBF) $H \rightarrow ZZ$ and from 730 fb at 500 GeV to 6.7 fb at 5000 GeV for RS graviton $G^* \rightarrow ZZ$. These limits are considerably tighter than those of early searches [17, 116]. The observed (expected) limits exclude the RS graviton lighter than 1035 (1045) GeV.

Bibliography

- [1] **ATLAS** Collaboration, Phys. Rev. B **716** (2012) **ATLAS**, *Collaboration, Observation of a new particle in the search for the Standard Model Higgs boson with the ATLAS detector at the LHC*, Phys. Lett. **B716** (2012) 1-29, arXiv:1207.7214 [hep-ex].
- [2] **CMS** Collaboration, *Observation of a new boson at a mass of 125 GeV with the CMS experiment at the LHC*, Phys. Lett. **B716** (2012) 30-61, arXiv:1207.7235 [hep-ex].
- [3] **ATLAS** Collaboration, Eur. Phys. J. **C76** (2016) 6.
- [4] **ATLAS** Collaboration, Eur. Phys. J. **C75** (2015) 476.
- [5] **CMS** Collaboration, Eur. Phys. J. **C75** (2015) 212.
- [6] **CMS** Collaboration, Phys. Rev. **D92** (2015) 012004.
- [7] Branco, G. C. and Ferreira, P. M. and Lavoura, L. and Rebelo, M. N. and Sher, Marc and Silva, Joao P., Phys. Rept. 516 (2012) 1-102.
- [8] A. Hill and J. J. van der Bij, Phys. Rev. **D36** (1987) 3463-3473.
- [9] Randall, Lisa and Sundrum, Raman, Phys. Rev. Lett. **83** (1999) 3370-3373.
- [10] Davoudiasl, H. and Hewett, J. L. and Rizzo, T. G., Phys. Lett. **B473** (2000) 43-49.
- [11] **ATLAS** Collaboration, Eur. Phys. J. **C75** (2015) 69.
- [12] **ATLAS** Collaboration, Eur. Phys. J. **C76** (2016) 45.
- [13] **ATLAS** Collaboration, JHEP **12** (2015) 055.
- [14] **CMS** Collaboration, JHEP08 (2014) 173.
- [15] **CMS** Collaboration, JHEP10 (2015) 144.
- [16] **ATLAS** Collaboration, ATLAS-CONF-2015-068 (2015) <https://cds.cern.ch/record/2114840>.
- [17] **ATLAS** Collaboration, ATLAS-CONF-2015-071 (2015) <https://cds.cern.ch/record/2114843>.
- [18] **ATLAS** Collaboration, CERN-EP-2016-106 arXiv 1606.04833 (2016).
- [19] **CMS** Collaboration, CMS-PAS-EXO-15-002 <https://cds.cern.ch/record/2117062>.
- [20] **ATLAS** Collaboration, ATLAS-CONF-2016-082 (2016) <https://atlas.web.cern.ch/Atlas/GROUPS/PHYSICS/CONFNOTES/ATLAS-CONF-2016-082/>
- [21] **ATLAS** Collaboration, JINST **3** (2008) S08003.
- [22] S. L. Glashow, *Partial-symmetry of weak interactions*, Nucl. Phys. **22** no. 4, (1961) 579.
- [23] S. Weinberg, *A model of leptons*, Phys. Rev. Lett. **19**, (1967) 1264.

- [24] A. Salam, *Weak and electromagnetic interactions*, in *Elementary particle theory: relativistic groups and analyticity*, NN. Svartholm, ed., p.367, Almqvist & Wiksell, 1968, Proceeding of the eighth Nobel Symposium.
- [25] G. Hooft and M. Veltman, *Regularization and Renormalization of Gauge fields*, Nucl. Phys. **B44**, (1972) 189.
- [26] Particle Data Group Collaboration, K. Nakamura et al., Review of particle physics, J. Phys. **G37** (2010) 075021. 10, 54, 58, 101.
- [27] F. Halzen and A. D. Martin, *Quarks and Leptons: An Introductory Course in Modern Particle Physics*. John Wiley and Sons, (1984) 11.
- [28] P. Dirac, *The Quantum Theory of the Electron*, Proc. Royal. Soc. **A117** (1928) 610624
- [29] C.N. Yang and R.L. Mills, *Conservation of isotopic spin and isotopic gauge invariance*, Phys. Rev. **96** (1954) 191-195
- [30] N. Cabibbo, Unitary Symmetry and Leptonic Decays, Phys. Rev. Lett. **10** (1963) 531533.
- [31] Peter W. Higgs, *Broken Symmetries and the Masses of Gauge Bosons*. Physical Review Letters **13** (1964).
- [32] F. Englert, R. Brout, *Broken Symmetry and the Mass of Gauge Vector Mesons*. Physical Review Letters **13** (1964).
- [33] C. R. Hagen G. S. Guralnik, T. W. B. Kibble, *Global Conservation Laws and Massless Particles*. Physical Review Letters **13** (1964).
- [34] Gerald S. Guralnik. *The History of the Guralnik, Hagen and Kibble development of the Theory of Spontaneous Symmetry Breaking and Gauge Particles*. International Journal of Modern Physics **A24** (2009).
- [35] J. Goldstone, *Field theories with superconductor solutions. Il Nuovo Cimento (1955-1965)*,**19** 154-164, 1961. 10.1007/BF02812722.
- [36] Y. Nambu. *Quasi-particles and gauge invariance in the theory of superconductivity*. Phys. Rev., **117**. 648-663 (1960).
- [37] J. Goldstone, A. Salam, and S. Weinberg. *Broken symmetries*. Phys. Rev., **127**. 965-970 (1962).
- [38] T. Hambye, K. Riesselmann, *Matching conditions and Higgs boson mass upper bounds reexamined*, Phys. Rev. **D55** (Jun, 1997) 7255-7262.
- [39] H. Georgi et al., Phys. Rev. Lett **40** (1978) 692; S.L. Glashow, D.V Nanopoulos, A. Yildiz, Phys. Rev. **D18** (1978) 196; K. Hikasa, Phys. Lett. **B164** (1985) 341.
- [40] J.F. Gunion et al., Phys. Rev. **D34** (1986) 101; J. Gunion, G. Kane, J. Wudka, Nucl. Phys. **B299** (1988) 231; M. Dittmar, H. Dreiner, Phys. Rev. **D55** (1997) 167.
- [41] A. Duperrin, arXiv:0805.3624 [hep-ph].
- [42] V. Barger et al., Phys. Rev. **D44** (1991) 1426; D. Rainwater, D. Zeppenfeld JHEP 9712 (1997) 5.
- [43] *CMS* Collaboration, Physics TDR, CERN/LHCC/2006-021 (2006).
- [44] **ATLAS** Collaboration, *Updated ATLAS results on the signal strength of the Higgs-like boson for decays into WW and heavy fermion final states*, ATLAS-CONF-2012-162 (2012).
- [45] **ATLAS** Collaboration, *Higgs to Diphoton*, ATLAS-CONF-2013-012 (2013).

- [46] **ATLAS** Collaboration, *SM H to $ZZ(*)$ to $4l$* , ATLAS-CONF-2012-169 (2013).
- [47] J. R. Ellis, G. L. Fogli, *New bounds on $m(t)$ and first bounds on $M(H)$ from precision electroweak data*, Phys. Lett. **B249** (1990) 543; J. R. Ellis, G. L. Fogli, E. Lisi, *Bounds on $M(H)$ from electroweak radiative corrections*, Phys. Lett. **B274** (1992) 456 and *Indirect bounds on the Higgs boson mass from precision electroweak data*, Phys. Lett. **B318** (1993) 148.
- [48] Torbjorn Sjostrand, Stephen Mrenna, Peter Z. Skands, *PYTHIA 6.4 Physics and Manual*. JHEP, 0605:026, (2006).
- [49] G. Corcella, I.G. Knowles, G. Marchesini, S. Moretti, K. Odagiri, et al. *HERWIG 6: An Event generator for hadron emission reactions with interfering gluons (including supersymmetric processes)*. JHEP, 0101:010, (2001).
- [50] G. Corcella, I.G. Knowles, G. Marchesini, S. Moretti, K. Odagiri, et al. *HERWIG 6.5 release note*. (2002).
- [51] J.M. Butterworth, Jeffrey R. Forshaw, M.H. Seymour. *Multiparton interactions in photoproduction at HERA*. Z.Phys., **C72**:637 646, (1996).
- [52] P. Calafiura, W. Lavrijsen, C. Leggett, M. Marino, D. Quarrie. *The athena control framework in production, new developments and lessons learned*. Computing in High-Energy Physics (CHEP '04), (2005) 456-458.
- [53] M. Bahr, S. Gieseke, M.A. Gigg, D. Grellscheid, K. Hamilton, et al. *Herwig++ Physics and Manual*. Eur.Phys.J., **C58** (2008) 639-707.
- [54] M. Bahr, S. Gieseke, M. H. Seymour, *Simulation of multiple partonic interactions in Herwig++*. Journal of High Energy Physics, (2008) 7:76.
- [55] M.L. Mangano, M. Moretti, F. Piccinini, R. Pittau, A.D. Polosa. *ALPGEN, a generator for hard multiparton processes in hadronic collisions*. JHEP, 0307:001 (2003).
- [56] S. Frixione, B.R. Webber. *Matching NLO QCD computations and parton shower simulations*. JHEP, 0206:029 (2002).
- [57] S. Frixione, P. Nason, B.R. Webber. *Matching NLO QCD and parton showers in heavy flavor production*. JHEP, 0308:007 (2003).
- [58] S. Frixione, P. Nason, C. Oleari. *Matching NLO QCD computations with Parton Shower simulations: the POWHEG method*. JHEP, 0711:070 (2007).
- [59] T. Cornelissen, M. Elsing, S. Fleischmann, W. Liebig, E. Moyses, A. Salzburger. *Concepts, Design and Implementation of the ATLAS New Tracking (NEWT)*. Technical Report ATL-SOFT-PUB-2007-007. ATL-COM-SOFT-2007-002, CERN, Geneva, (2007).
- [60] R. e. Kalman, *A new approach to linear filtering and prediction problems*. Journal of Basic Engineering 82 (1): 35-45. (1960). Retrieved 2008-05-03.
- [61] **ATLAS** Collaboration. *Performance of the ATLAS Inner Detector Track and Vertex Reconstruction in the High Pile-Up LHC Environment*. Technical Report ATLAS-CONF-2012-042, CERN, Geneva, (2012).
- [62] **ATLAS** Collaboration. *Performance of primary vertex reconstruction in proton-proton collisions at $\sqrt{s} = 7$ TeV in the ATLAS experiment*. Technical Report ATLAS-CONF-2010-069, CERN, Geneva, (2010).
- [63] Georges Aad et al. *Electron performance measurements with the ATLAS detector using the 2010 LHC proton-proton collision data*. Eur.Phys.J., **C72**:1909, (2012).

- [64] **ATLAS** Collaboration, *Detector and Physics Technical Design Report*, Vol.1, CERN-LHCC-99-14 (1999).
- [65] G. Aad et al. *Electron performance measurements with the ATLAS detector using the 2010 LHC proton-proton collision data*, Eur.Phys.J., **C72**:1909, (2012).
- [66] M. Aharrouche et al. *Measurement of the response of the ATLAS liquid argon barrel calorimeter to electrons at the 2004 combined test-beam. Nuclear Instruments and Methods in Physics Research Section A: Accelerators, Spectrometers, Detectors and Associated Equipment*, 614(3):400-432, (2010).
- [67] E. Abat, J. M. Abdallah, T. N. Addy, P. Adragna, M. Aharrouche, A. Ahmad, T. P. A. Akesson, M. Aleksa, C. Alexa, K. Anderson, et al. *Combined performance studies for electrons at the 2004 ATLAS combined test-beam*. Journal of Instrumentation, 5:11006, November (2010).
- [68] **ATLAS** Collaboration, *Expected electron performance in the ATLAS experiment*, Tech. Rep. ATL-PHYS-PUB-2011-006, CERN, Geneva, (2011).
- [69] **ATLAS** Collaboration, *Electron performance measurements with the ATLAS detector using the 2010 LHC proton-proton collision data*. arXiv:1110.3174 (2012, v2).
- [70] **ATLAS** Collaboration, *Jet energy measurement with the ATLAS detector in proton-proton collisions at $\sqrt{s} = 7$ TeV* CERN-PH-EP-2011-191. Submitted to Eur. Phys. J. C.
- [71] M. Cacciari, G.P. Salam, G. Soyez. *The Anti- k_t jet clustering algorithm*. JHEP, 0804:063 (2008).
- [72] Stephen D. Ellis, Davison E. Soper. *Successive combination jet algorithm for hadron collisions*. Phys.Rev., **D48**:3160-3166 (1993).
- [73] M. Wobisch, T. Wengler. *Hadronization corrections to jet cross-sections in deep inelastic scattering*. arXiv:hep-ph/9907280v1 (1998).
- [74] **ATLAS** Collaboration. *Jet energy resolution and selection efficiency relative to track jets from in-situ techniques with the ATLAS Detector Using Proton-Proton Collisions at a Center of Mass Energy $\sqrt{s} = 7$ TeV*. Technical Report ATLAS-CONF-2010-054, CERN, Geneva, (2010).
- [75] P. Adragna et al. *Testbeam studies of production modules of the ATLAS Tile Calorimeter*. Nucl. Instrum. Meth., **A(606)**:362-394 (2009).
- [76] J. Pinfold et al. *Performance of the ATLAS liquid argon endcap calorimeter in the pseudorapidity region in beam tests*. Nuclear Instruments and Methods in Physics Research Section A: Accelerators, Spectrometers, Detectors and Associated Equipment, 593(3):324-342 (2008).
- [77] **ATLAS** Collaboration. *Inputs to Jet Reconstruction and Calibration with the ATLAS Detector Using Proton-Proton Collisions at $\sqrt{s} = 900$ GeV*. Technical Report ATLAS-CONF-2010-016, CERN, Geneva (2010).
- [78] **ATLAS** Collaboration. *Commissioning of the ATLAS high-performance b -tagging algorithms in the 7 TeV collision data*. Technical Report ATLAS-CONF-2011-102, CERN, Geneva (2011).
- [79] De Palma, M. et al., ALEPH: Technical Report 1983 - CERN-LEPC-83-2.
- [80] Bartl, W. et al., DELPHI: Technical Proposal - DELPHI-83-66-1.
- [81] von Dardel, G., Walenta, A. H., Lubelsmeyer, K., Deutschmann, M., Leiste, R., et al. L3 Technical Proposal. (1983). See the BOOKS subfile under the following call number: QCD197:E951.

- [82] THE OPAL DETECTOR. TECHNICAL PROPOSAL - LEPC-83-4.
- [83] Blair, R. et al. The CDF-II detector: Technical design report - FERMILAB-DESIGN-1996-01.
- [84] Abazov, V. et al. D0 Run IIB upgrade technical design report (2002).
- [85] The CDF and D0 collaborations, "Updated Combination of CDF and D0 Searches for Standard Model Higgs Boson Production with up to 10.0 fb⁻¹ of Data", FERMILAB-CONF-12-318-E; CDF Note 10884; D0 Note 6348, arXiv:1207.0449.
- [86] J. Beringer et al. (Particle Data Group), Phys. Rev. D **86**, 010001 (2012).
- [87] **ATLAS** Collaboration, CERN/LHCC 97-21 (1997).
- [88] **ATLAS** Collaboration, CERN/LHCC 97-19 (1997).
- [89] **ATLAS** Collaboration, CERN/LHCC 97-20 (1997).
- [90] **ATLAS** Collaboration, ATLAS Trigger Performances, ATL-COM-PHYS-2008- 067, CERN (2008).
- [91] **ATLAS** Collaboration, *Selection of jets produced in proton-proton collisions with the ATLAS detector using 2011 data*, ATLAS-CONF-2012-020 (2012).
- [92] **ATLAS** Collaboration, *Jet energy resolution and reconstruction efficiencies from in-situ techniques with the ATLAS Detector Using Proton-Proton Collisions at a Center of Mass Energy $\sqrt{s} = 7$ TeV*, ATLAS-CONF-2010-054 (2010).
- [93] **ATLAS** Collaboration, *Commissioning of the ATLAS high-performance b-tagging algorithms in the 7 TeV collision data*, ATLAS-CONF-2011-102 (2011).
- [94] **ATLAS** Collaboration, *Performance of Missing Transverse Momentum Reconstruction in ATLAS with 2011 Proton-Proton Collisions at $\sqrt{s} = 7$ TeV*, ATLAS-CONF-2012-101 (2012).
- [95] G. Cowan, K. Cranmer, E. Gross, and O. Vitells, Eur. Phys. J. C **71**, 1554 (2011).
- [96] J. E. Kim, *Light pseudoscalars, particle physics and cosmology*, Phys. Rept. **150** (1987) 1-177.
- [97] H. E. Haber, G. L. Kane, *The search for supersymmetry: probing physics beyond the Standard Model*, Phys. Rept. **117** (1985) 75-263.
- [98] G. Branco, P. Ferreira, L. Lavoura, M. Rebelo, M. Sher, et al., *Theory and phenomenology of two-Higgs-doublet models*, Phys.Rept. **516** (2012) 1-102, arXiv:1106.0034 [hep-ph].
- [99] A. Djouadi, *The Anatomy of electro-weak symmetry breaking. II. The Higgs bosons in the minimal supersymmetric model*, Phys.Rept. **459** (2008) 1-241, arXiv:hep-ph/0503173 [hep-ph].
- [100] C.Y. Chen, S. Dawson, *Exploring two-Higgs-doublet models through Higgs production*, arXiv:1301.0309 [hep-ph].
- [101] J. Chang, K. Cheung, P.Y. Tseng, T.C. Yuan, *Implications on the heavy CP-even Higgs boson from current Higgs data*, arXiv:1211.3849 [hep-ph].
- [102] A. Drozd, B. Grzadkowski, J. F. Gunion, Y. Jiang, *Two-Higgs-doublet models and enhanced rates for a 125 GeV Higgs*, arXiv:1211.3580 [hep-ph].
- [103] W. Altmannshofer, S. Gori, G. D. Kribs, *A minimal-flavor-violating 2HDM at the LHC*, Phys. Rev. D **86** (2012) 115009, arXiv:1210.2465 [hep-ph].
- [104] D. S. Alves, P. J. Fox, N. J. Weiner, *Higgs signals in a type-I 2HDM or with a sister Higgs*, arXiv:1207.5499 [hep-ph].

- [105] **CDF** Collaboration, T. Aaltonen et al., *Search for a two-Higgs-boson doublet using a simplified model in $p\bar{p}$ collisions at $\sqrt{s} = 1.96$ TeV*, arXiv:1212.3837 [hep-ex].
- [106] **CDF** Collaboration, T. Aaltonen et al., *Search for Higgs bosons predicted in two-Higgs-doublet models via decays to tau lepton pairs in 1.96 TeV p anti- p collisions*, Phys.Rev.Lett. **103** (2009) 201801, arXiv:0906.1014 [hep-ex].
- [107] P. Ferreira, R. Santos, M. Sher, J. P. Silva, *Implications of the LHC two-photon signal for two-Higgs-doublet models*, Phys.Rev. **D85** (2012) 077703, arXiv:1112.3277 [hep-ph].
- [108] **ATLAS** Collaboration, *Muon reconstruction performance of the ATLAS detector in proton-proton collision data at $\sqrt{s} = 13$ TeV*, CERN-EP-2016-033.
- [109] **ATLAS** Collaboration, *Expected performance of the ATLAS b -tagging algorithms in Run-2*, ATLAS-NOTE-2015-022.
- [110] A. Hill and J. van der Bij, *Strongly interacting singlet-doublet Higgs model*, Phys.Rev. **D36** (1987) 3463.
- [111] G. Branco et al., *Theory and phenomenology of two-Higgs-doublet models*, Phys. Rept. **516** (2012) 1, arXiv: 1106.0034 [hep-ph].
- [112] N. Kauer and C. O'Brien, *Heavy Higgs signal-background interference in $gg \rightarrow VV$ in the Standard Model plus real singlet*, Eur. Phys. J. **C75** (2015) 374, arXiv: 1502.04113 [hep-ph].
- [113] D. Pappadopulo et al., *Heavy Vector Triplets: Bridging Theory and Data*, JHEP **1409** (2014) 060, [Inspire], eprint: 1402.4431.
- [114] L. Randall and R. Sundrum, *A Large mass hierarchy from a small extra dimension*, Phys.Rev.Lett. **83** (1999) 3370, arXiv: hep-ph/9905221 [hep-ph].
- [115] K. Agashe et al., *Warped Gravitons at the LHC and Beyond*, Phys.Rev. **D76** (2007) 036006, arXiv: hep-ph/0701186 [hep-ph].
- [116] **ATLAS** Collaboration, ATLAS-CONF-2016-016 <https://cds.cern.ch/record/214100>.
- [117] **ATLAS Collaboration**, The ATLAS Simulation Infrastructure, Eur. Phys. J. **C70** (2010) 823, arXiv: 1005.4568 [physics.ins-det]
- [118] S. Agostinelli et al., GEANT4: A Simulation toolkit, Nucl. Instrum. Meth. **A506** (2003) 250.
- [119] T. Gleisberg et al., Event generation with SHERPA 1.1, JHEP **0902** (2009) 007, arXiv: 0811.4622 [hep-ph]
- [120] S. Alioli et al., NLO single-top production matched with shower in POWHEG: s- and t-channel contributions, JHEP **09** (2009) 111, [Erratum: JHEP02,011(2010)], arXiv: 0907.4076 [hep-ph].
- [121] P. Artoisenet et al., Automatic spin-entangled decays of heavy resonances in Monte Carlo simulations, JHEP **1303** (2013) 015, arXiv: 1212.3460 [hep-ph].
- [122] Sjostrand, Torbjorn and Mrenna, Stephen and Skands, Peter Z., PYTHIA 6.4 Physics and Manual, JHEP **0605** (2006) 026, arXiv: hep-ph/0603175.
- [123] P. Z. Skands, Tuning Monte Carlo Generators: The Perugia Tunes, Phys. Rev. **D82** (2010) 074018, arXiv: 1005.3457 [hep-ph].
- [124] M. Czakon and A. Mitov, Top++: A Program for the Calculation of the Top-Pair Cross-Section at Hadron Colliders, Compt/ Phys. Commun. (2014) 2930, arXiv: 1112.5675 [hep-ph].
- [125] T. Sjostrand, S. Mrenna and P. Z. Skands, A Brief Introduction to PYTHIA 8.1, Comput. Phys. Commun. **178** (2008) 852, arXiv: 0710.3820 [hep-ph].

- [126] J. Alwall et al., The automated computation of tree-level and next-to-leading order differential cross sections, and their matching to parton shower simulations, JHEP 07 (2014) 079, arXiv: 1405.0301 [hep-ph].
- [127] ATLAS Collaboration, Muon reconstruction performance in early 13 TeV data, (2015), url: <https://cds.cern.ch/record/2047831>.
- [128] ATLAS Collaboration, Measurement of the muon reconstruction performance of the ATLAS detector using 2011 and 2012 LHC proton-proton collision data, Eur. Phys. J. C74 (2014) 3130, arXiv: 1407.3935 [hep-ex].
- [129] ATLAS Collaboration, Jet Calibration and Systematic Uncertainties for Jets Reconstructed in the ATLAS Detector at $\sqrt{s} = 13$ TeV, (2015), url: <https://cds.cern.ch/record/2037613>.
- [130] ATLAS Collaboration, Tagging and suppression of pileup jets with the ATLAS detector, (2014), url: <https://cds.cern.ch/record/1700870>.
- [131] ATLAS Collaboration, Calibration of the performance of b-tagging for c and light-flavour jets in the 2012 ATLAS data, (2014), url: <http://cds.cern.ch/record/1741020>.
- [132] M. Cacciari, G. P. Salam and G. Soyez, The Anti-k(t) jet clustering algorithm, JHEP 04 (2008) 063, arXiv: 0802.1189 [hep-ph].
- [133] ATLAS Collaboration, Identification of Boosted, Hadronically Decaying W Bosons and Comparisons with ATLAS Data Taken at $\sqrt{s} = 8$ TeV, (2015), arXiv: 1510.05821 [hep-ex].
- [134] ATLAS Collaboration, Identification of boosted, hadronically-decaying W and Z bosons in $\sqrt{ss} = 13$ TeV Monte Carlo Simulations for ATLAS, (2015), url: <https://cds.cern.ch/record/2041461>.
- [135] A. J. Larkoski, I. Moult and D. Neill, Power Counting to Better Jet Observables, JHEP 12 (2014) 009, arXiv: 1409.6298 [hep-ph].
- [136] A. J. Larkoski, I. Moult and D. Neill, Analytic Boosted Boson Discrimination, (2015), arXiv: 1507.03018 [hep-ph].
- [137] ATLAS Collaboration, Selection of jets produced in 13TeV proton-proton collisions with the ATLAS detector, (2015), url: <https://cds.cern.ch/record/2037702>.
- [138] ATLAS Collaboration, Electron efficiency measurements with the ATLAS detector using the 2012 LHC proton-proton collision data, (2014), url: <https://cds.cern.ch/record/1706245>.
- [139] ATLAS Collaboration, Combined search for the Standard Model Higgs boson in pp collisions at $\sqrt{ss} = 7$ TeV with the ATLAS detector, Phys. Rev. D86 (2012) 032003, arXiv: 1207.0319 [hep-ex].
- [140] L. Moneta et al., The RooStats Project, PoS ACAT2010 (2010) 057, arXiv: 1009.1003 [physics.data-an].
- [141] W. Verkerke and D. P. Kirkby, The RooFit toolkit for data modeling, eConf C0303241 (2003) MOLT007, arXiv: 0306116 [physics].
- [142] G. Cowan, K. Cranmer, E. Gross and O. Vitells, Asymptotic formulae for likelihood-based tests of new physics, Eur. Phys. J. C 71 (2011) 1554, arXiv: 1007.1727 [physics.data-an].
- [143] G. Cowan et al., Asymptotic formulae for likelihood-based tests of new physics, Eur. Phys. J. C71 (2011) 1554, [Erratum: Eur. Phys. J. C73, 2501 (2013)], arXiv: 1007.1727 [physics.data-an].
- [144] K. Cranmer et al., HistFactory: A tool for creating statistical models for use with RooFit and RooStats', tech. rep. CERN-OPEN-2012-016, New York U., 2012, url: <https://cds.cern.ch/record/1456844>.

- [145] A. L. Read, Presentation of search results: the CLs technique, *J. Phys. G* 28 (2002) 2693.
- [146] G. Cowan et al., Erratum to: Asymptotic formulae for likelihood-based tests of new physics, *Eur. Phys. J. C* 73 (2013) 1434.

Ringraziamenti

Vorrei con queste ultime righe ringraziare tutti coloro che hanno permesso la realizzazione di questo lavoro.

Questa tesi non rappresenta semplicemente il punto di arrivo del mio percorso da studente di Fisica, ma ha un significato ben più profondo. Questo lavoro si colloca in un progetto molto più ampio, di cui ho avuto la responsabilità ma soprattutto l'onore di portare avanti, progetto che vede questo lavoro di tesi non come un punto di arrivo bensì come il punto di lancio verso il mio futuro lavoro nell'ambito della Fisica delle Particelle. L'intero gruppo ATLAS di Napoli mi ha accolto e ha investito su di me come parte di esso per il futuro. Il mio impegno è stato enorme e lo sarà sempre, ma forse mai abbastanza per ripagare una tale fiducia.

Innanzitutto, un ringraziamento va al Prof. Leonardo Merola, senza il quale tutto ciò non sarebbe mai iniziato nè tantomeno realizzato. E' stato fondamentale non solo in questo progetto, nei miei due lavori di tesi con il gruppo ATLAS, ma anche nel mio intero percorso di studi; i tre corsi seguiti ed altrettanti esami sostenuti hanno contribuito con grande peso alla mia maturazione per lo studio e la comprensione della Fisica.

Un ringraziamento enorme va al Dr. Francesco Conventi ed alla Dr.ssa Elvira Rossi, mie guide ed angeli custodi in questo percorso; loro hanno permesso sì la realizzazione di questa tesi ma, soprattutto, la realizzazione di questo progetto così impegnativo, che solo grazie a loro poteva avere una reale possibilità di essere portato a termine e che senza di loro mi avrebbe fermato dopo i primi passi; invece, sono, siamo arrivati alla sua (quasi) conclusione e, loro lo sanno, i ringraziamenti non saranno mai sufficienti. Lavorando al loro fianco cerco, momento dopo momento, e cercherò sempre di fare mio quanto più possano insegnarmi; in questi anni ho potuto osservare non solo tanti aspetti di questo lavoro, così faticoso ma allo stesso tempo affascinante, ma anche principi fondamentali, sostegno, lavoro e fiducia di gruppo, che difficilmente credo potrò mai trovare altrove. Loro hanno creduto in me, io sono arrivato fin qui.

Ringraziamenti vanno al resto del gruppo ATLAS, a Francesco ed Arturo, il cui ruolo è stato fondamentale nella scrittura della tesi e non solo; a Mariaelena e Claudio, senza i quali non avrei portato a termine un esame e non solo di questo percorso (loro sanno quale).

Un ringraziamento agli amici di sempre, Pietro, Gaetano, Cristina e Federica, con i quali ho condiviso i pochi momenti di riposo di questi mesi.

Un ultimo ringraziamento va a mia madre, che, devo ammettere, questa volta ha dovuto sopportare uno dei miei lati più nervosi ed insopportabili, ma lei ci è abituata ormai, ed ad un'altra persona senza la quale non sarei qui oggi, nè come fisico nè come persona, lui sa chi è.

Grazie a tutti...
...ce l'abbiamo (quasi) fatta!